Master of Science Thesis

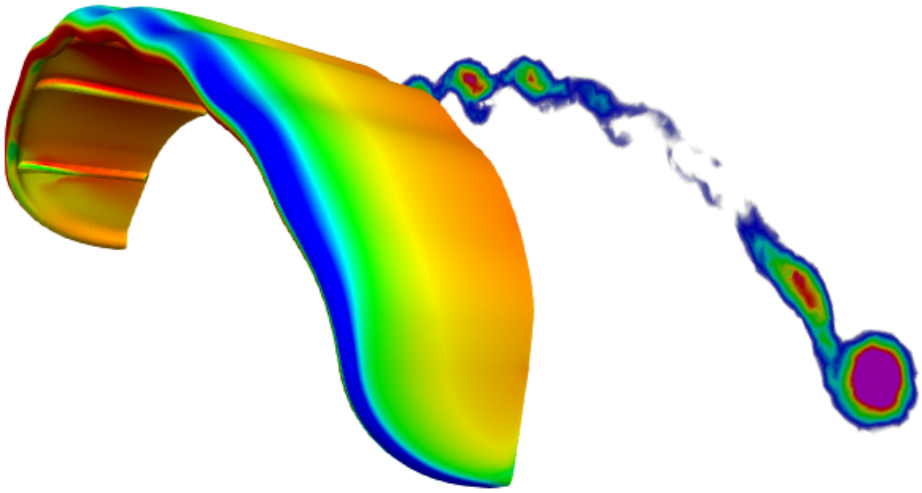

Steady-state RANS simulation of a leading edge inflatable wing with chordwise struts

G.H.M. Lebesque

December 15, 2020

Aerodynamics

TU Delft

Faculty of Aerospace Engineering

Delft University of Technology

Steady-state RANS simulation of a leading edge inflatable wing with chordwise struts

by

G.H.M. Lebesque

to obtain the degree of Master of Science

at the Delft University of Technology,

to be defended publicly on Tuesday December 15, 2020 at 10:00 AM.

Student number:	4304691	
Project duration:	March, 2020 – December, 2020	
Thesis committee:	Dr. A. Viré,	TU Delft, supervisor
	Dr.-Ing. R. Schmehl,	TU Delft, chair
	Dr. A. H. van Zuijlen,	TU Delft, reader
	MSc. M. A. M. Folkersma,	TU Delft, reader

An electronic version of this thesis is available at `http://repository.tudelft.nl/`.

TU Delft

Delft University of Technology

Summary

Airborne Wind Energy Systems (AWES) utilise flying devices that are tethered to the ground to reach altitudes far beyond the range of conventional wind energy systems. By doing so, they operate in regions of the atmospheric boundary layer where the wind power density is much higher. Therefore, these systems tap into an additional potential wind energy resource that can be used for renewable energy generation. Since Airborne Wind Energy (AWE) is still an emerging field of technology, it has not converged to a single design yet, hence research efforts are spread out over a large range of concepts. To categorise these concepts, they can be divided into two main classes. First, the ground-gen concepts, for which the conversion of wind energy to electrical energy takes place on the ground. Secondly, there are fly-gen concepts, for which the conversion is done on board of these flying devices.

A crosswind pumping kite power system is an AWE system that uses a flying tethered device for energy generation through a ground-based generator. The AWE research group of the TU Delft was one of the first to demonstrate the functioning of such a system. The spin-off Kitepower has continued the technological development of this concept towards a commercial product. The system uses a leading edge inflatable (LEI) wing that operates by alternating between a traction phase and a retraction phase. During the traction phase, the tether is reeled out, energy is generated and the loads on the wing are high. During the retraction phase, the tether is reeled back in and the loads will have to be minimised to limit energy consumption. This means the wing experiences a wide range of flow conditions with frequently changing incoming flow velocity, angle of attack and sideslip angle. As the wing is made of a flexible membrane, the shape is not fixed and will change under the aerodynamic loads applied to it. Therefore, the aerodynamic optimisation of such a wing forms a complex Fluid-Structure Interaction (FSI) problem.

As the recent study by Folkersma et al.[1] showed, it is possible to couple a structural and aerodynamic model for a flexible kite geometry. However, for the LEI wing subject of this study, which consists of an inflatable tubular frame supporting the canopy, there are still several aerodynamic aspects that require an in-depth study on their own. Therefore, this thesis will only focus on the aerodynamic analysis of the LEI V3A wing developed by Kitepower. The analysis is done through the use of steady-state Computational Fluid Dynamics (CFD) simulations with a rigid wing geometry. Similar work that was done previously used a simplified wing geometry without chordwise struts and only considered a limited range of flow conditions. In this study, these struts have been included in the geometry and their impact on the aerodynamic performance is assessed. In addition to this, the aerodynamic performance of the LEI wing under sideslip conditions is analysed. A hybrid meshing approach has been adopted to generate the computational domain. Simulations have been performed using a Reynolds-Averaged Navier-Stokes (RANS) solver with the $\gamma - \widetilde{\mathrm{Re}}_{\theta t}$ transition model. The overarching research aim of this project was to improve the correlation of these numerical simulations to available experimental data and to enhance the understanding of the aerodynamics of a LEI wing by considering a wider range of flow conditions.

Comparison of the force coefficient curves showed that the impact of the struts on the total aerodynamic performance is minimal. Throughout the whole range of flow conditions considered, the force coefficient curves showed similar trends and absolute values. Locally, there are differences in the flow fields, predominantly in the tip region on the pressure side of the wing. The change in aerodynamic performance as a function of the sideslip angle was concluded to be strong. An increase in the sideslip angle led to a drop in the lift coefficient and an increase in the drag coefficient. Averaged values of the force coefficients were in line with inputs of several numerical models. Comparison of the results to available experimental data showed agreement for a limited range of flow conditions. The differences between the results of the present study and available experimental data are believed to be caused by the experimental data processing methods, in-flight deformation of the wing and steering actuation.

Preface

First of all, I would like to thank my daily supervisor Axelle Viré for providing me with the opportunity to work on this interesting topic and for all the support I have received throughout this project. Secondly, I would also like to thank Roland Schmehl for all the support, answers to questions and discussions we had. Also a special thanks to Mikko for all the feedback you gave me. Your help and feedback have greatly improved the quality of my work.

Next, I would like to express my gratitude to all my friends for the great moments we shared over the past years, the good conversations we had and for helping me out when I needed it. A special mention should go to Tim for the years of friendship throughout the master's and for working so closely together with me on all projects. With our collaboration, we got the best out of each other and it got me through challenging times.

Furthermore, I would like to thank my parents and sisters for always being there and supporting me along the whole road that led to my graduation. I know that this has not always been easy. Last but not least, I would like to thank my girlfriend Madalina for her unconditional love and support.

G.H.M. Lebesque
Delft, December 2020

Contents

List of Figures

List of Tables

Acronyms

AWE Airborne Wind Energy

AWES Airborne Wind Energy Systems

CAD Computer-Aided Design

CFD Computational Fluid Dynamics

DNS Direct Numerical Simulation

FSI Fluid-Structure Interaction

GAMG Geometric agglomerated Algebraic MultiGrid

IMU Inertial Measurement Unit

KCU Kite Control Unit

LEI Leading Edge Inflatable

LES Large Eddy Simulation

LLM Lifting-Line Method

RANS Reynolds-Averaged Navier-Stokes

SIMPLE Semi-Implicit Method for Pressure Linked Equations

SIMPLEC Semi-Implicit Method for Pressure Linked Equations-Consistent

SST Shear Stress Transport

URANS Unsteady Reynolds-Averaged Navier-Stokes

VLM Vortex Lattice Method

Nomenclature

Greek symbols

α	Angle of attack	[°]
β	Sideslip angle	[°]
δ_{ij}	Kronecker delta	[−]
ϵ	Turbulent dissipation rate	$[m^2\,s^{-3}]$
μ	Dynamic viscosity	$[kg\,m^{-1}\,s^{-1}]$
ν	Kinematic viscosity	$[m^2\,s^{-1}]$
ν_T	Eddy viscosity	$[m^2\,s^{-1}]$
ω	Specific turbulent dissipation rate	$[s^{-1}]$
Ω_x	Vorticity	$[m\,s^{-1}]$
ρ	Density	$[kg\,m^{-3}]$
τ_w	Wall shear stress	$[kg\,m^{-1}\,s^{-2}]$

Latin symbols

A_{KCU}	Reference area of the KCU	$[m^2]$
A_{ref}	Reference area	$[m^2]$
A_{V3A}	Reference area of the LEI V3A	$[m^2]$
$A_{e,bridle}$	Effective area of the bridle line system	$[m^2]$
C_D	Drag coefficient	[−]
$C_{D,bridle}$	Drag coefficient of the bridle line system	[−]
$C_{D,cyl}$	Drag coefficient of a cylinder	[−]
$\widehat{C}_D$	Normalised drag coefficient	[−]
$C_{D,KCU_{tot}}$	Drag coefficient of the KCU	[−]
$C_{D,par}$	Parasitic drag coefficient	[−]
$C_{D,T_{tot}}$	Drag coefficient of the tether	[−]
C_f	Skin friction coefficient	[−]
C_L	Lift coefficient	[−]
$\widehat{C}_L$	Normalised lift coefficient	[−]
C_p	Pressure coefficient	[−]
$C_{p.T}$	Total pressure coefficient	[−]
c_{ref}	Reference chord	$[m]$
d	Bridle line diameter	$[m]$
D_{bridle}	Drag force on the bridle line system	$[N]$
d_T	Tether diameter	$[m]$

k	Turbulent kinetic energy	$[m^2\,s^2]$
L/D	Lift-to-drag ratio, aerodynamic efficiency	$[-]$
l_m	Turbulent length scale	$[m]$
L_{tet}	Average length of the tether	$[m]$
L_{bridle}	Total length of the bridle line system	$[m]$
p	Pressure	$[kg\,m^{-1}\,s^{-2}]$
Re	Reynolds number	$[-]$
Tu	Turbulence intensity	[%]
U_∞	Freestream velocity	$[m\,s^{-1}]$
u_τ	Friction velocity	$[m\,s^{-1}]$
V_n	Velocity component normal to the bridle line system	$[m\,s^{-1}]$
y^+	Non-dimensional wall distance	$[-]$

1 Introduction

With global warming becoming an increasingly serious issue for the environment year-on-year, energy generation is an industry where still big differences have to be made. With around 80% of the world's energy still relying on fossil fuels [2], it is clear that the potential for renewable and more sustainable energy production is huge. One source of renewable energy is the wind, which forms a large part of the world's renewable energy resources. It is still up for debate how much the realisable potential of this resource is. Various studies have tried to estimate the wind energy potential available [3–6], leading to estimates ranging from 32 EJ/year to 3024 EJ/year. While conventional wind turbines keep increasing in size to utilise some of this wind energy potential [7], the emerging field of Airborne Wind Energy (AWE) is gaining traction as well.

1.1. Airborne Wind Energy

AWE is fundamentally different in its approach to energy extraction compared to conventional wind energy. While many different concepts exist, the most common concepts involve energy extraction through the use of a kite or aircraft that is connected to the ground via a tether [8]. This means they can operate at altitudes much higher than the operational height of conventional wind turbines. As the atmospheric boundary layer of the earth decreases the velocity at lower altitudes, there is a potential for Airborne Wind Energy Systems (AWES) to benefit from higher wind power densities. Furthermore, the wind energy is less fluctuating at higher altitudes, meaning that higher capacity factors can be achieved and lower intermittency will be experienced [9].

In 1980, Loyd published a paper titled Crosswind Kite Power [10] in which the idea of wind power production through the use of kites in crosswind motion was described. This fundamental idea formed the basis for the analysis of potential AWES. His reasoning behind this was that the most efficient part of a wind turbine is usually the outer area of the blades. It was estimated that around half of the total power of a wind turbine is produced by the outermost 30% of the blades [8]. So if it would be possible to only use this more efficient outer area, without all the structure and material of a conventional wind turbine, higher aerodynamic efficiencies could be achieved at a lower cost. The benefit that a kite flying crosswind motions has, over the operation of a simple kite, is a much stronger scaling of power harvesting with the lift-to-drag ratio. Therefore, much higher efficiencies can be achieved with a well-designed kite that has a high lift-to-drag ratio.

For this crosswind kite concept, there are two main modes of operation. The first is the lift mode, where the lift force of the flying device acts as a pulling force on the tether. This means that tether gets reeled out during operation, this phase is called the traction phase. When the maximum tether length is reached, the kite has to be reeled back in during the retraction phase. The periodic alternation between these two phases also gives it the name pumping mode operation. Since the generator used for the energy conversion is stationed on the ground, this concept is also referred to as ground-based generation or ground-gen. Secondly, there are systems that operate in drag mode. For these systems, the conversion of energy happens on-board of the flying device through the use of e.g., turbines. The drag mode systems are also referred to as on-board generation or fly-gen concepts [11]. For more insight into different AWE concepts, the reader is referred to [11–14].

However, next to the benefit of tapping into an additional wind energy resource that is unreachable for conventional turbines, the lower material cost of these systems is a strong advantage as well. With the percentage of capital expenditure for the turbine and substructure & foundation ranging from 57% for floating offshore turbines to 72% for onshore turbines [15], it is clear how much these savings can add up when considering large-scale production. These cost-savings could be made because the whole support structure, tower and rotor-nacelle assembly are essentially replaced by a tether, generator and a flying device.

While there are clear advantages to the use of AWES, there are also some challenges still to overcome. The whole system should be able to operate autonomously for extended periods of time, without human intervention, to be economically viable. While the material and the cost needed for AWES is in general much less, the systems are more prone to wear and tear imposed by the environment [11]. At the moment, it is not well studied yet how long and under what conditions the AWES could operate before needing repairing or replacement. In addition to this, a new set of regulations will have to be developed that enforces certain safety and reliability standards for the operation of AWES [16]. Additionally, the ecological impact of AWES has been looked into for some specific cases [17], but all factors considered the bigger picture is not fully understood or validated yet. Nonetheless, the potential of AWE is evident and the contribution it could deliver to create a more sustainable future makes it well worth to develop the technology further.

1.2. Research context

Currently, the AWE research group at the TU Delft, together with the commercial spin-off Kitepower, is developing a crosswind pumping kite power system. This system consists of a Leading Edge Inflatable (LEI) wing that is connected to a ground-based generator. The system alternates between two phases, a traction phase and a retraction phase, during which the LEI wing experiences a wide range of flow conditions in terms of Reynolds number, angle of attack and sideslip [18]. Since the LEI wing is constructed of a flexible membrane, its shape will change depending on the aerodynamic loading that is applied to it. This makes optimising such a design a complex Fluid-Structure Interaction (FSI) problem.

As the recent study by Folkersma et al.[1] showed, it is possible to couple a structural and aerodynamic model for a flexible kite geometry. However, for the LEI wing subject of this study, which consists of an inflatable tubular frame supporting the canopy, there are still several aerodynamic aspects that require an in-depth study on their own. Therefore, this thesis will solely focus on the aerodynamic analysis of the LEI V3A wing developed by Kitepower. In recent years, advancements have taken place in the field of numerically modelling LEI wings using Computational Fluid Dynamics (CFD). An example of this is the study by Folkersma et al.[19], which focused on a 2D LEI airfoil geometry. This study showed that transition modelling is necessary to predict the laminar flow phenomena at the lower end of the Reynolds number range for LEI wings. Demkowicz [20] developed a methodology for modelling a 3D LEI wing with RANS simulations by extending the simulation framework of Folkersma et al.[19]. One of the main conclusions of this study was that along the LEI wingspan, strong regions of crossflow could be observed on the pressure side of the wing. These crossflow regions impacted the recirculation behaviour behind the leading edge and seemed to be dependent on the shape of the LEI wing. The results were compared to the experimental study of Oehler et al.[21], but only matched within a narrow range of flow conditions.

There were two main points of improvement based on Demkowicz's study [20]. First, the LEI wing geometry was oversimplified by omitting the chordwise struts. Given the strong regions of crossflow on the pressure side of the wing, the impact of this simplification should be quantified. Second, the aerodynamic performance of the LEI wing under sideslip conditions was not considered. As experimental data shows, there are variations in sideslip angle throughout a pumping cycle [18]. Therefore, quantifying how this affects the aerodynamic performance is important. Insight into these two points could also lead to a more complete understanding of the currently observed differences between numerical and experimental data. Based on this, the research objective of this thesis was formed to be:

"To improve the correlation of RANS CFD simulations of a 3D LEI wing with experimental data by decreasing the geometrical discrepancy between the simulated and actual LEI wing and enhancing the understanding about the aerodynamic behaviour of flow around the LEI wing by extending the range of the flow conditions considered to include sideslip."

To fulfil the research objective, several research questions and sub-questions were defined. The research questions that will be answered during this thesis are:

1. *What is the impact of the inclusion of the chordwise struts on the aerodynamic performance and the flow field around a LEI wing when employing a 3D RANS CFD simulation?*

   In order to answer this question, several sub-questions have been formed to aid the research process.

   - To what extent are the aerodynamic coefficients affected by the inclusion of the struts?
   - What are the differences in the flow field and main flow features when comparing to the numerical results of the geometry without the struts?
   - What is the impact of this geometrical change on the correlation with available experimental data?

2. *How does the aerodynamic performance of a LEI wing change as a function of the sideslip angle?*

   In order to answer this question, several sub-questions have been formed to aid the research process.

   - How do the aerodynamic coefficients change as a function of the sideslip angle?
   - Is there a relationship between the Reynolds number and the magnitude of the impact the sideslip angle has on the aerodynamic performance?
   - What observations can be made regarding the flow field and main flow features around the LEI wing during sideslip?

1.3. Thesis outline

The outline of this thesis work is as follows. The literature review on the aerodynamics of LEI wings and past numerical and experimental studies will be presented in Chapter 2. The theory behind CFD that is relevant for the current study is summarised in Chapter 3. The pre-processing steps, such as the design of the Computer-Aided Design (CAD) model, generation of the computational mesh and simulation setup are discussed in Chapter 4. A detailed analysis and discussion of the simulation results and a comparison to existing numerical and experimental studies are presented in Chapter 5. Finally, in Chapter 6 the conclusions of the thesis are summarised and recommendations for future studies are given.

2

Literature review

In this chapter, the literature review of this thesis project will be presented. The flow conditions during operation and important geometrical aspects of the LEI wing are discussed in Section 2.1. This is followed by an in-depth discussion of previously done numerical studies on kites and LEI wings in Section 2.2. The results of several experimental studies will be presented in Section 2.3. Lastly, conclusions will be drawn based on this literature review in Section 2.4.

2.1. Aerodynamics of a LEI wing

The operation of a pumping kite power system consists of two main phases and transition phases between them. During the traction phase, the tether is reeled out, the load is high and energy is generated while the wing performs figure-of-eight crosswind motions. During the retraction phase, the tether is reeled back in and loads will have to be minimised to limit energy consumption. This means the wing experiences a wide range of flow conditions with frequently changing incoming flow velocity, angle of attack and sideslip angle. This flight path during such an operational cycle is visualised in Fig. 2.1. Throughout a pumping cycle, the performance of the whole system is dependent on several aspects such as the system control, structural dynamics, aerodynamics and flight dynamics [22].

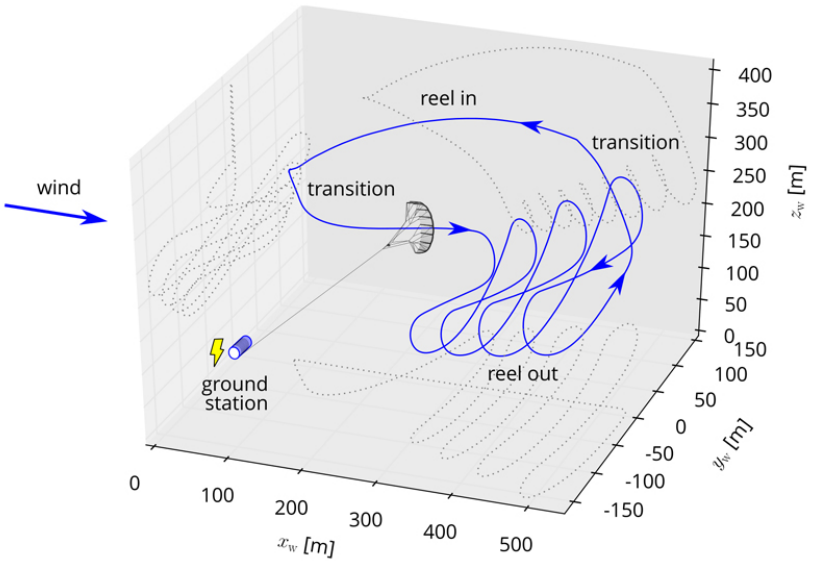

Figure 2.1: The flight path of a pumping kite power system as computed by Fechner [23].

A detailed analysis of the aerodynamic behaviour and modelling of LEI wings will be given in the upcoming sections. However, some of the more top-level parameters and effects will be briefly mentioned here. The aerodynamic performance of the LEI wing depends on the projected surface area, the lift-to-drag ratio, maximum wing loading and the depower capability [24]. However, for the lift-to-drag ratio, it is not enough to simply use the wing's coefficients, as the tether influences the aerodynamic efficiency as well. Thus, as Houska et al.[25] described, the effective lift-to-drag ratio is the lift force over the drag force of the wing and tether combined. The depower capability, sometimes referred to as the power setting, has the biggest influence on the pumping cycle efficiency. In the case of the LEI wing studied in this thesis, depowering happens through the extension of the power lines. This pitches the leading edge of the kite downwards, thereby decreasing the angle of attack and thus decreasing the lift and drag.

The experimental study by Oehler et al.[18], which will be discussed in greater detail in Section 2.3, showed the average conditions throughout an operational pumping cycle. The angle of attack range can be divided into the traction and retraction phase. The traction phase had angles of attack ranging from 6° to 16° and the retraction phase from −8° to 4°. During turning manoeuvres, there can be an angle between the heading direction of the LEI wing and the actual inflow angle, this is called the sideslip angle. This sideslip angle was measured to vary approximately by a maximum of ± 10° from the mean value of the heading. The maximum velocity the LEI wing experiences is when transitioning from the retraction to the traction phase. The apparent wind velocity is dependent on the heading of the kite and phase of the cycle but ranges from 12 to 22 m/s.

2.1.1. Geometry characteristics

The LEI wing experiences a wide range of aerodynamic conditions throughout an operational cycle. Due to the crosswind motion in the traction phase, both the apparent velocity and the Reynolds number will be high. To maximise the tether force, it will operate at high angles of attack, making it prone to stall. During the retraction phase, however, the wing no longer exploits the crosswind motion to increase the apparent wind velocity. Therefore, the perceived velocity and Reynolds number will be low, combined with a low angle of attack to minimise the lifting force that could cause an increase in the energy needed for the reel-in [22].

The design of the LEI wing subject of this study is shown in a partially depowered state in Fig. 2.2. Depowering is quantified through the inciated Δl, which can be seen as an extension of the rear suspension [18]. The wing consists of an inflatable leading edge, pressurised struts and a canopy in between the struts. While the leading edge and struts add some rigidity compared to, for example, a ram-air kite, it is still nothing like a rigid wing structure. The constantly changing flow conditions mentioned previously would already make a difficult design optimisation problem for a rigid wing, but having a LEI wing introduces additional challenges. The flexible membrane will change shape considerably under load changes and this will impact the aerodynamic performance and behaviour of the flow around the wing. Therefore, this can also be considered as an FSI problem. However, the main focus of this thesis will be on the aerodynamic modelling.

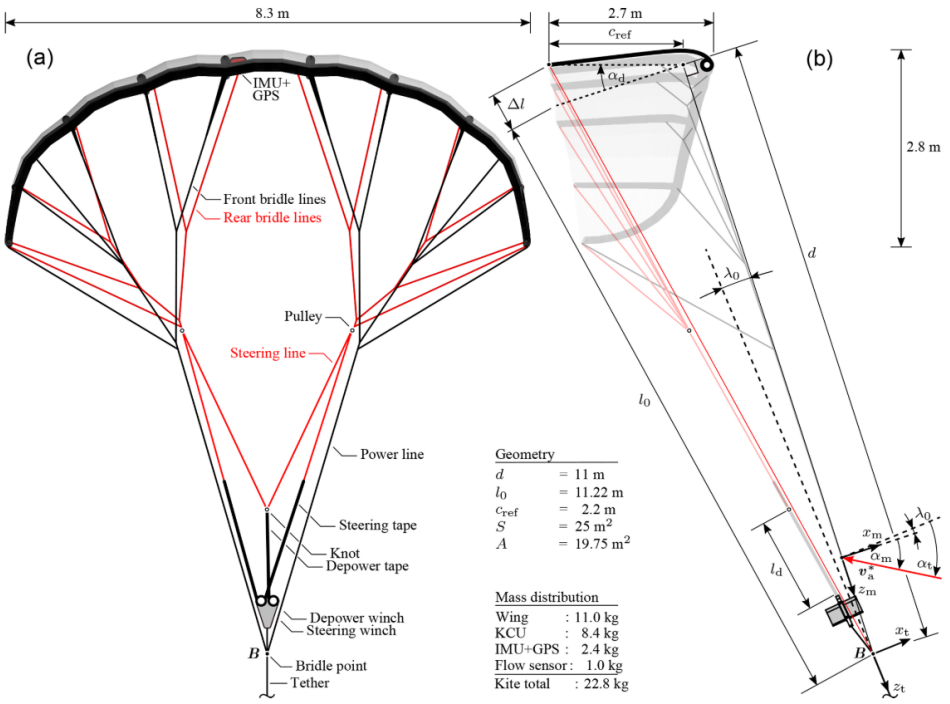

Figure 2.2: The Kitepower LEI V3A wing with bridle line system and Kite Control Unit (KCU) layout [18].

2.1.2. Laminar and turbulent flow

In Fig. 2.3, the flow topology and pressure distribution over a LEI wing airfoil are shown. There are a few flow characteristics that can be observed based on this. The suction side profile is similar to a conventional airfoil and is therefore susceptible to some common flow phenomena. First, there is a region where a laminar separation bubble could occur. While in many aircraft applications the Reynolds number is high enough to have fully developed turbulent flow, for the LEI wing this is not the case. The wide range of flow conditions makes the occurrence of a laminar boundary layer a possibility.

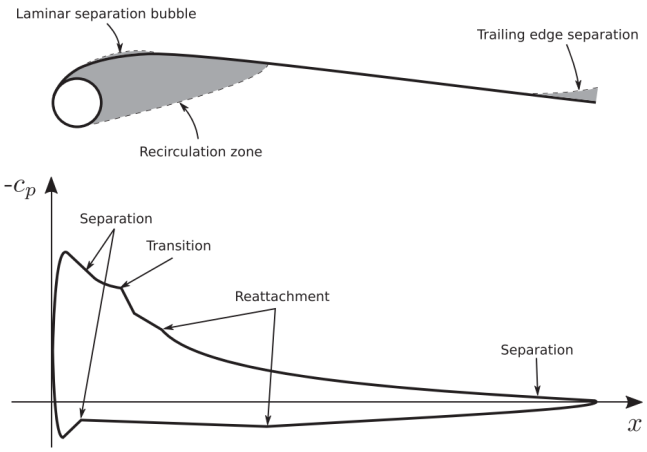

Figure 2.3: Flow topology and pressure distribution around a LEI wing airfoil [19].

A laminar boundary layer is not able to withstand an adverse pressure gradient in the same way as a turbulent boundary layer can [26]. Therefore, a laminar boundary layer will separate at lower angles of attack compared to a turbulent boundary layer. However, it is possible for the separated flow to transition and reattach to the surface. This will then lead to what is called a laminar separation bubble between the point the flow separated and the point it attaches again. This process is shown in Fig. 2.4. The three regions indicated on the LEI wing

airfoil geometry are studied on two-dimensional sails in [27]. The effect of the laminar separation bubble on the pressure profile can be seen in Fig. 2.3. A laminar separation bubble can influence the shape of the airfoil as perceived by the flow and it can be unstable. Consequently, it can strongly impact the aerodynamic performance of an airfoil [28]. The second region on the suction side is the trailing edge separation, which is a common type of separation observed for an airfoil at high angles of attack.

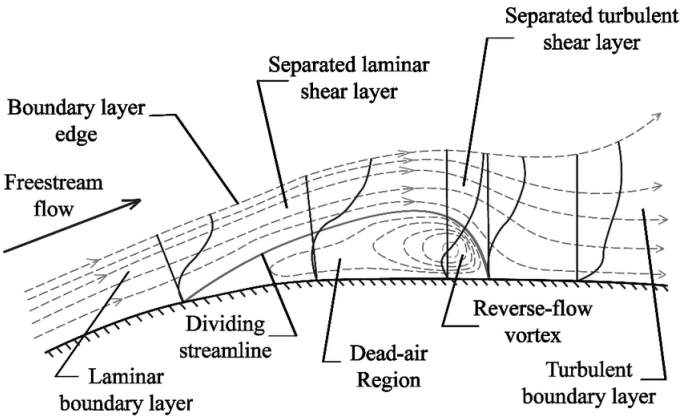

Figure 2.4: Sketch of a boundary layer experiencing a laminar separation bubble [29].

Where there are similar flow field phenomena for LEI wing airfoils and conventional airfoils on the suction side, the pressure side is not comparable. Due to the circular leading edge of a LEI wing airfoil, a recirculation zone will form behind it. The size of this circulation zone is dependent on the way the separation develops from the circular leading edge. Since a laminar and turbulent boundary layer have different separation behaviour, this can strongly impact the size of this recirculation zone [19]. In addition to this, the flow over a cylinder may experience drag crisis. The drag crisis occurs when the boundary layer transitions from laminar to turbulent leading to a delayed separation of the boundary layer. This results in a strong drop in the drag coefficient [30].

2.1.3. Flexible membranes

There have been multiple studies investigating the aerodynamic behaviour of flexible membranes for different applications [31–34]. These showed that there are some very distinct differences in the aerodynamic performance of flexible membranes when compared to rigid wings. Since the membrane is flexible, it will change shape according to the aerodynamic loading applied to it. So the effective camber of the airfoil is adjusting to the loading which suppresses the separation of the boundary layer on the suction side [26, 32]. Due to this delay in separation, the flexible membrane airfoil can reach higher lift coefficients, however, stall will occur much more abruptly [33]. The increase in lift coefficient and more abrupt stall behaviour of flexible membranes is shown in Fig. 2.5. In this figure, the lowest Batten stands for the highest flexibility. While this behaviour might be beneficial to obtain higher lift coefficients, the unpredictable stall behaviour could be a problem.

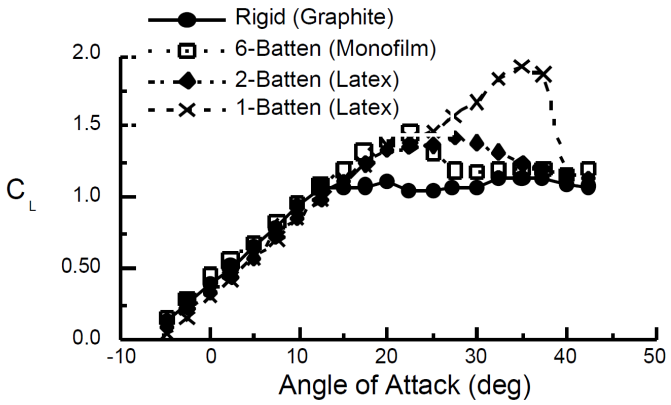

Figure 2.5: Comparison of the lift curves for rigid and flexible membrane wings [33].

In the thesis on membrane wings by Leuthold [34], the increase in lift coefficient was put in a category of trends for attached flow. Next to this, two non-linear flow trends for flexible membranes are discussed. The first one being low-lift hysteresis. Since the membrane is so susceptible to changes in the pressure forces, this can create hysteresis in cases where the overall lift is low. When the lift is low, a small change in loading can cause a large variation in the membrane causing the wing to reverse its shape. This could lead to a detrimental swing in lift force direction resulting in an uncontrollable LEI wing. The second non-linear flow trend is separation, which has been discussed in the previous subsection.

What the overview of this section shows is that the flow around a LEI kite is one with many different interactions. The changing conditions throughout the operational cycle, laminar and turbulent flow, separation and recirculation regions combined with fluid-structure interaction make for a complex computational and experimental problem.

2.2. Computational methods for kites and LEI wings

In this section, an overview of the different computational methods used for kite aerodynamic characterisation and design is given. Since more complex computational methods were only more recently used on 3D LEI wing geometries [20, 35, 36], part of this overview will also take flexible membranes and 2D LEI wing geometries into account. When looking into the assessment and prediction of the aerodynamic performance of LEI wings or flexible membranes there are several methods used. Generally speaking, the researcher has to make a trade-off between accuracy and computational resources. This decision can be based on the use case and application. For example, if the aim is to optimise a LEI wing geometry in a detailed way for certain specific flight conditions, one might be inclined to choose a more complex and accurate method. However, if the aerodynamic model is part of a bigger system that requires only ballpark figures, such detailed calculations are not necessary.

2.2.1. Aerodynamic models included in dynamic models

This implementation of simplified aerodynamic models often takes place in dynamic models where the focus lies on energy prediction, design of control systems or optimisation [37, 38]. Next to this, there are experimental methods that focus on the estimation of aerodynamic parameters, these will be discussed later in Section 2.3.

The approach used by Fechner et al.[37] modelled the LEI wing and tether as a particle system through discrete point masses connected by spring-dampers. Three of these points represented the LEI wing's surface on which the aerodynamic forces are applied as shown in Fig. 2.6. Since one of the requirements of this model was the capability of real-time running, it could not include very complex aerodynamic calculations. The computational model made use of an atmospheric model based on the power-law to determine the wind speed at the height of the kite and the tether segments. Through the state space parameters, the angle of attack is determined at each of the three aerodynamic surfaces corresponding to the points. Then the lift and drag forces are determined using reference data for stalled and attached flow over airfoils and applying a correction for LEI wing. So, while the four-point model includes the kinematics of steering and sideslip to

determine state values at the points, there is no assessment of aerodynamic performance based on the actual LEI wing geometry. All that is done is using some airfoil reference data and corrections that take the angle of attack as input. An extension on this model, made with a three-point mass model rather than four points to incorporate turning, was constructed in [39].

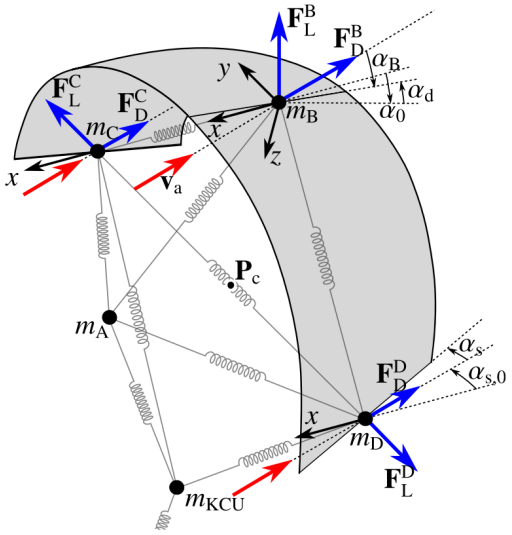

Figure 2.6: Four-point spring-damper model as used by Fechner et al.[37].

In a study done by van der Vlugt et al.[38], analytical equations were used for the traction, retraction and transition phases. The main aim was predicting the power generated during a complete pumping cycle. In this model, the crosswind manoeuvres were not resolved and the flight trajectory was idealised. Experimental data sets were used to determine the aerodynamic coefficients and the lift-to-drag ratio. The model showed very high sensitivity to the quality of the reference data, meaning that for example, correct values of wind speed at the kite are essential for accurate results.

Breukels developed a kite simulation toolbox that included the tether, beams and foils in a multi-body approach [40]. A LEI wing is divided into several chordwise elements which simplify the airfoil canopy to a single chordwise wire. On the chordwise elements of the wire, a force distribution is imposed. For the total aerodynamic force, the sum of all spanwise elements is taken. For each of the local elements, the aerodynamic coefficients are determined through an algorithm consisting of several parameters. The output of this algorithm will deliver the camber, angle of attack and airfoil thickness. The numerical data for the airfoils with these specific camber, angle of attack and thickness characteristics was generated through 2D RANS CFD simulations, a method that will be discussed in greater detail later. The airfoils are divided into 6 nodes at which the integral aerodynamic forces are applied through weighting functions. However, for the set of boundary conditions, there exist infinitely many coefficients that satisfy the equations, which makes it a rather arbitrary process.

2.2.2. Potential flow methods

A different approach to assess the aerodynamic performance is based on potential flow theory. Potential flow methods usually rely on a few assumptions to come to simplified equations to describe the flow field. The first is that the flow is irrotational, i.e. the fluid particles themselves are not rotating. Second, the flow around the bodies that is far enough off the surface can be treated as inviscid. Quite often the flow is also assumed to be incompressible.

The most simple version of this is a 2D panel method. In a 2D panel method, the surface contour of an airfoil is discretized into singularity panels. These singularity panels can be sources, doublet or vortices. It is also possible for the distribution to vary linearly or quadratic over a panel. By using a non-permeability boundary condition at the surface and the Kutta-condition at the trailing edge the system of equations can be solved. In this way, the lift coefficient and pressure distribution over an airfoil can be determined [41]. This method

can be extended to 3D as Lifting-Line Method (LLM) or Vortex Lattice Method (VLM) through use of the Biot-Savart law. A detailed overview of the implementation of these methods can be found in several references such as [42–44].

However, an issue with these methods is that by default they do not include viscous effects and are unable to model flow separation. As discussed in the previous section, flow separation is a reoccurring phenomenon on LEI wing. Therefore, it would be necessary to either use potential flow for viscous fluids, which is a possibility [45] or to apply viscous corrections. These viscous corrections can account for common effects such as boundary layer displacement [46] and separation [47], but often these methods still need experimental input such as the location of the separation point.

Several applications to yacht sails are already reviewed by Demkowicz [20] and Deaves [35], therefore, only applications to kites and LEI wings will be discussed here. In the study done by Gaunaa et al.[48], a new method was proposed that combines a VLM with 2D airfoil data through an algorithm to correct for viscous effects and thickness of airfoils. This algorithm was based on a modification of the concept introduced in [49] where it was used for corrections of wind tunnel interference. The results of this method were then compared to the results of an in-house developed RANS CFD code. The kite geometry used was a simple kite shape as shown in Fig. 2.7 consisting of a NACA64-418 airfoil.

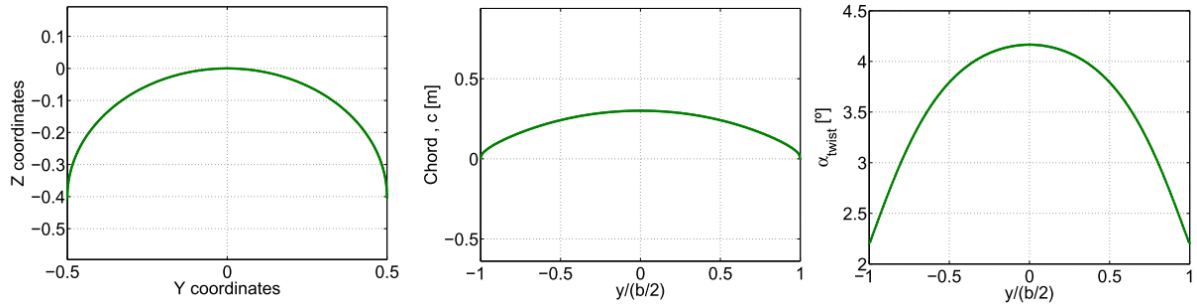

Figure 2.7: Spanwise shape, chord distribution and twist distribution of a simple kite as used by Gaunaa et al.[48].

First, the results for zero sideslip angle are shown in Fig. 2.8. In the graphs, a comparison is made between standard VLM, the VLM with the algorithm and CFD. It can be observed that the lift coefficients agree fairly well for the algorithm and CFD case, thus that the viscous correction does seem to have its intended effect. For the drag coefficient, the VLM with algorithm seems to underperform slightly at higher pitch angles, but the author did not give a direct explanation for this. The lift-to-drag coefficient curve shows a much better match to CFD for the VLM with the algorithm.

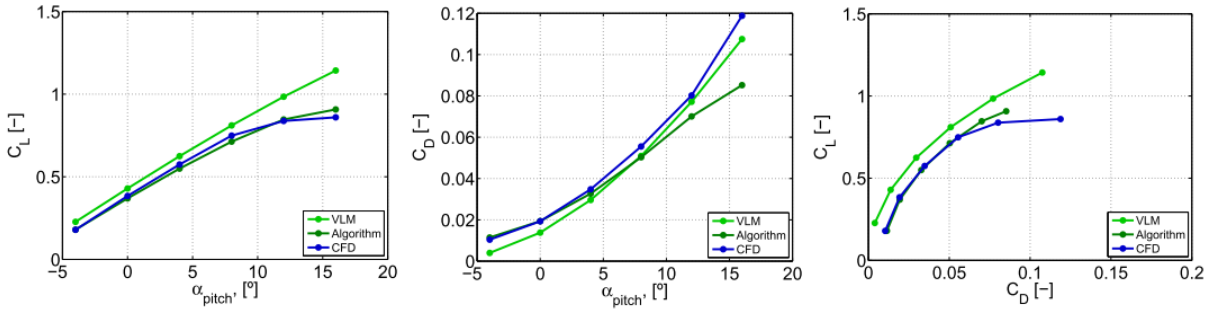

Figure 2.8: The lift (left) and drag (centre) curves and the drag polar (right) for three different computational methods [48].

The second results are those with a pitch angle of 0°, for which the angle of attack is higher than zero, and different sideslip angles. The results are shown in Fig. 2.9. These offer an interesting view on the performance impact the sideslip angle could have. While the VLM with the algorithm is close to CFD for all coefficients, it shows large deviations for sideslip angles above 8°. Which most likely corresponds to large areas of flow

separation around the kite. Therefore, it seems that for higher sideslip angles, a VLM method with viscous correction is not able to properly match higher fidelity methods such as CFD.

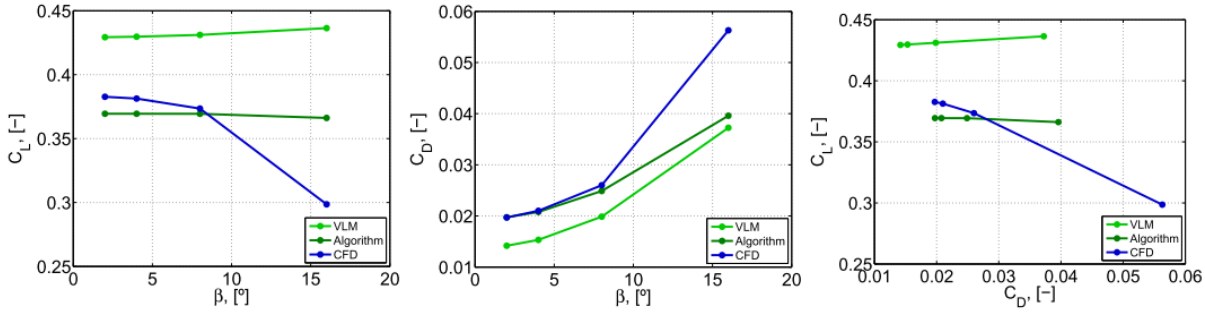

Figure 2.9: The lift (left) and drag (centre) coefficient vs. sideslip angle and the drag polar (right) for three different computational methods [48].

Another study that made use of an adjusted VLM method was by Leuthold [34]. The study aimed to develop a multiple wake VLM that could deal with more than one separation region on a three-dimensional surf kite. When comparing these results to the 3D RANS CFD simulations done by Deaves in [35], it showed that the adjusted VLM method over predicted the lift coefficient. Furthermore, it highlighted that for attached flow the drag coefficient increase is under predicted. In addition to this, the model had difficulties predicting reattachment and required a very high resolution to fulfil the set model constraints. With separation and reattachment occurring frequently throughout a pumping kite cycle, the inability to accurately predict this forms a strong limitation on this method.

Next to this, potential flow methods can also be used to determine corrections for induced flow velocity during experimental testing [18]. A schematic sketch of such an implementation is shown in Fig. 2.10. The kite is represented by three straight lifting line vortex filaments, one representing the main surface and two representing the tip surfaces. Since it is possible to use superposition for potential flows, the induced velocities of the filaments at the measurement location can be added up. In this specific case, it was proven that the measurement location could be considered as freestream based on the induced velocity through lifting line theory.

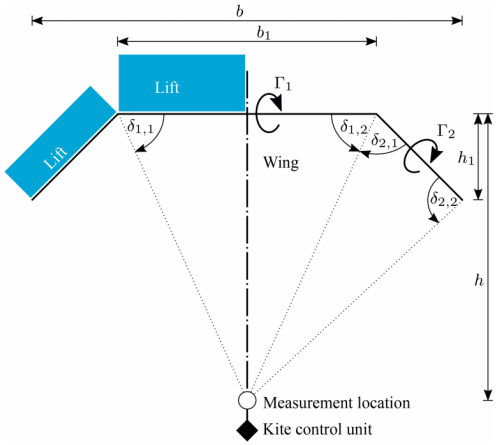

Figure 2.10: Lifting line model of a kite used for induced flow velocity at measurement location [18].

The cases discussed above show that potential flow methods, while effective for some cases, have some serious limitations for the application to 3D LEI wings. In the attached flow regime, the results of the potential flow methods agree fairly well with higher fidelity methods such as CFD. Even though the models presented made use of viscous corrections and more advanced multiple separation approaches, they still failed to capture the trends at higher angles of attack. At these higher angles of attack, the viscous effects play a dominant

role and separation and reattachment are very likely to occur. Furthermore, the results for different sideslip angles showed very large discrepancies between potential flow methods and CFD for higher sideslip angles. Both Ruppert [50] and Oehler et al. [18] presented experimental results that made it evident that the LEI wing will experience a range of sideslip angles throughout its operation. Therefore, being able to predict the LEI wing's performance in these conditions could prove valuable during design and analysis.

2.2.3. Computational Fluid Dynamics

Since the LEI wing goes through a wide range of flow conditions, it is important to assess the performance throughout this range. As the previous section showed, potential flow methods have difficulty dealing with separation, reattachment and sideslip. Furthermore, they do not include the transition from laminar to turbulent flow, a phenomenon that has a strong impact on the flow behaviour as shown earlier in Section 2.1.2. A computational method that is able to better deal with these aspects is CFD. This section will not be an extensive overview of CFD methods applied to different flexible membranes and kite geometries. For this, the reader is referred to the literature reviews in the studies of Deaves [35] and Demkowicz [20]. In this section, only results that are deemed relevant in terms of geometrical or methodological similarity will be discussed. However, before doing so, a short review of CFD methods will be given.

Through the use of CFD, an engineer or researcher can model and resolve a fluid flow problem numerically by approximating partial differential equations [51]. The work cycle of CFD usually can be subdivided into several types of modelling. These are physical, mathematical and numerical modelling. Physical modelling focuses on the fluid problem at hand and the assumptions that can be used for this. Fundamentally, the equations used for the physical modelling of fluid flows are the conservation laws for mass, momentum and energy. The equations used to represent the motion of fluids, based on these conservation laws, are known to be the Navier-Stokes equations [52]. While for a few very simple flow cases it is possible to derive an analytical solution of the Navier-Stokes equations [53], normally numerical methods are needed to solve the equations. If a fluid flow is considered turbulent or a transition to turbulence takes place, it will have an influence on the range of turbulent scales present in the flow. Turbulence is characterised by different length scales with the largest being the integral length scale and the smallest the Kolmogorov length scale [54]. In order to fully represent the flow field as accurately as possible, the equations have to be resolved until the smallest Kolmogorov scales.

When all of the turbulent scales are fully and explicitly resolved the simulation is considered a Direct Numerical Simulation (DNS) [55]. However, the computational cost associated with resolving all the turbulent length scales increases with Re^3. Therefore, it is currently unfeasible to use DNS to model high Reynolds number flows. While a DNS study has been done on a LEI wing by Coudou [36], the Reynolds numbers considered were too low to get representative conclusions that translate to in-flight conditions. Thus, fully resolving all turbulent length scales is not possible at the moment. Therefore, other methods have been developed that introduce further modelling into the Navier-Stokes equations. These methods rely on modelling (part) of the turbulent spectrum. One of these methods is Large Eddy Simulation (LES), in which the large scales of the turbulent spectrum are resolved and the smaller scales are modelled using a subgrid-scale model [56]. While this somewhat removes the heavy scaling with Reynolds number, it still requires a refined spatial and temporal discretization to properly represent the resolved turbulent effects. Therefore, the computational resource required for this approach is still relatively high and not feasible for most applications where reasonable turnaround times are required.

The method that is most widely used in industry is RANS. In these models, all the turbulence is modelled and only the mean flow is resolved. The RANS equations are obtained by substituting a decomposition of a mean and fluctuating part into the Navier-Stokes equations and subsequently taking the ensemble average [57]. However, this introduces a Reynolds-stress term which needs additional equations to ensure closure of the whole system. The equations that provide this closure are turbulence models, which model the effects of the turbulent fluctuations on the mean flow. Even with the additional equations, RANS simulations do not require the computational resources that are normally necessary for LES and DNS. However, RANS turbulence models do have their downsides in terms of predicting the separation and reattachment behaviour [58] and accuracy. Alternatively, Unsteady Reynolds-Averaged Navier-Stokes (URANS) methods have been tested to predict flows in which shedding of vortices occurs such as the study done by Yao et al.[59]. In this study, the time-averaged streamwise velocity solution and flow structures of a URANS simulation matched fairly well to experimental data at similar planes. In another study done by Schiavetta et al.[60], it was shown that URANS

was able to predict some of the low-frequency transient movement of vortical structures. Most of the common turbulence models will assume fully turbulent flow. This means that none of the laminar flow effects can be modelled. However, by incorporating an additional transition model into the equations it is still possible to capture and model laminar to turbulent transition and behaviour. The model that will be used in this thesis is the $\gamma - \widetilde{\mathrm{Re}}_{\theta t}$ transition model which adds two additional equations to the k-ω Shear Stress Transport (SST) model. This model has been able to predict laminar flow phenomena in the studies by Folkersma et al.[19] and Demkowicz [20] on 2D and 3D LEI wing geometries. More details about RANS simulations in general, turbulence modelling and transition modelling will be discussed in Chapter 3.

2D RANS CFD Study

In this section, a relevant 2D CFD simulation will be discussed. Folkersma et al.[19] performed a 2D steady-state RANS simulation with transition modelling on a LEI wing airfoil. It uses the k-ω SST turbulence model from [61] and is combined with a $\gamma - \widetilde{\mathrm{Re}}_{\theta t}$ transition model from [62].

The study focused on two different geometries, a validation study on a sailwing and a LEI wing airfoil. The sailwing reference data comes from the study done in [63]. The sailwing in this study is build up out of two steel elements, a cylinder forming the leading edge and a curved plate. Since it is not one formed element, there is a small imperfection where the two elements meet on the suction side. This geometry was recreated and simulations were run with and without the transition model, the lift and drag coefficients are shown in Fig. 2.11. It can be seen that the simulation with the transition model matches the experimental data better than the simulation without transition model.

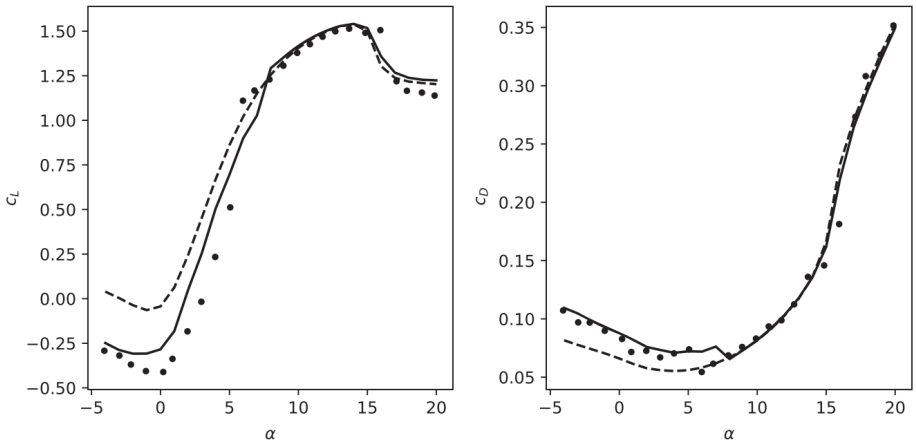

Figure 2.11: Lift (left) and drag (right) coefficients of a sailwing (experimental data is indicated by the dots, the simulation with transition model by the solid line and simulation without transition model by the dashed line) [19].

When looking at the drag coefficient, it is also visible that the simulation without transition model seems to underpredict the drag for angles of attack below approximately 8°. This can be explained by the fact that without a transition model the flow will always be turbulent. As discussed in Section 2.1.2, a turbulent boundary layer will be more resistant to separation. In the simulation with the transition model, the boundary layer flow can be laminar and therefore more prone to separation. The experimental tests were done with a chord length based Reynolds number of 10^5 and at low turbulence intensity. This relatively low Reynolds number is the reason that one can observe the jump the in lift and drag coefficient at 6° angle of attack in the experimental data. The increase in the angle of attack can lead to a more adverse pressure gradient experienced by the boundary layer earlier on, which in turn can cause an earlier transition [64]. This earlier transition then means that the boundary layer is turbulent and more resistant to separation. It essentially decreases the separation, thereby decreasing the pressure drag and increasing the lift [65].

After this validation study on a sailwing airfoil, a LEI wing airfoil geometry has been studied. The Reynolds number range from 10^5 to $5 \cdot 10^7$ has been chosen since it represents the full operational range from the lower end retraction phase to the higher end traction phase. The lift and drag coefficient curves for the LEI wing airfoil without transition model are shown in Fig. 2.12. These results show trends one normally observes on airfoils [66] with increasing Reynolds number the drag coefficient decreases, the lift curve shifts upwards and

a higher maximum lift coefficient can be obtained at higher angles of attack.

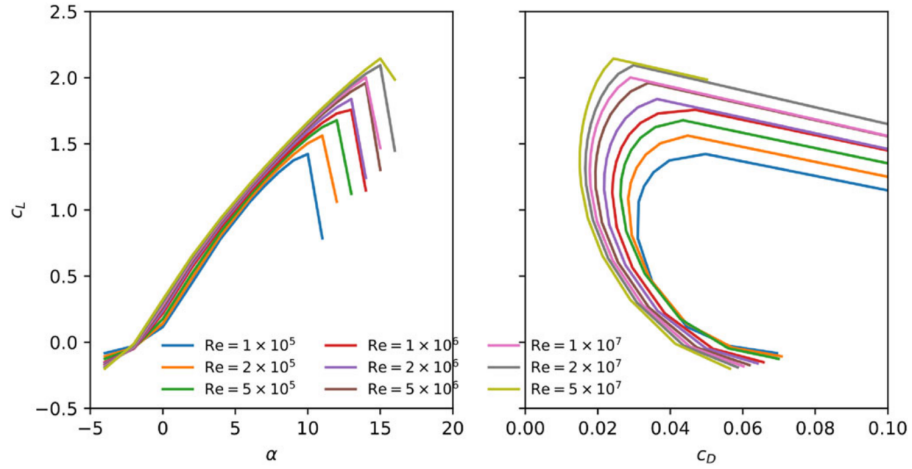

Figure 2.12: The lift curves (left) and drag polars (right) of a LEI airfoil for several Reynolds numbers without transition modelling [19].

The results with the transition model, shown in Fig. 2.13, reveal considerable changes with respect to the previous results. There is a much larger spread in both lift and drag coefficients for the whole range of Reynolds numbers. At the lower Reynolds numbers, the lift coefficient is lower and the drag coefficient is higher compared to the fully turbulent case. The change in values comes from the larger laminar separation bubble on the suction side of the LEI kite as shown in Fig. 2.14. As also shown in the figure, the laminar separation bubble disappears again for $\mathrm{Re} = 5 \cdot 10^5$. Thus, these flow field changes explain the large differences in the curves at the lower end of the Reynolds number range. Furthermore, it is interesting to observe that unlike the fully turbulent case, the highest Reynolds number does not lead to the highest maximum lift coefficient. Folkersma et al.[19] explained this by the fact that for the $\mathrm{Re} = 5 \cdot 10^6$ the flow still has a partly laminar boundary layer, whereas for higher Reynolds numbers it immediately transitions to a turbulent boundary layer.

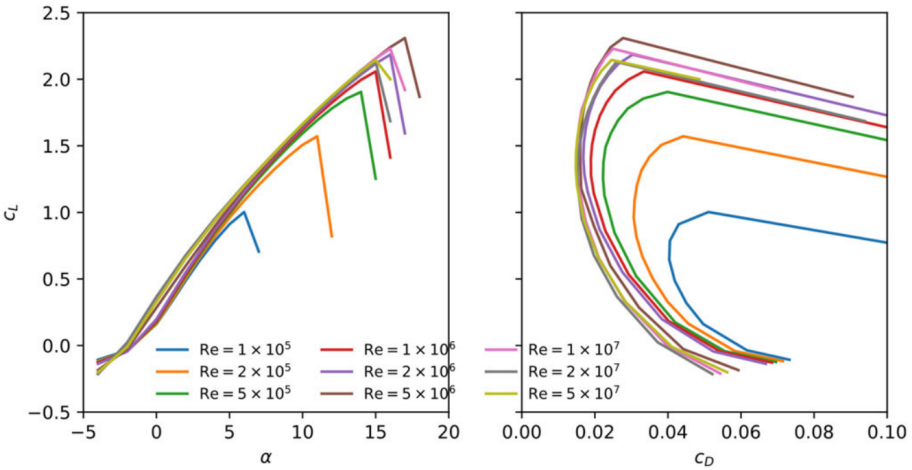

Figure 2.13: The lift curves (left) and drag polars (right) of a LEI airfoil for several Reynolds numbers with transition modelling [19].

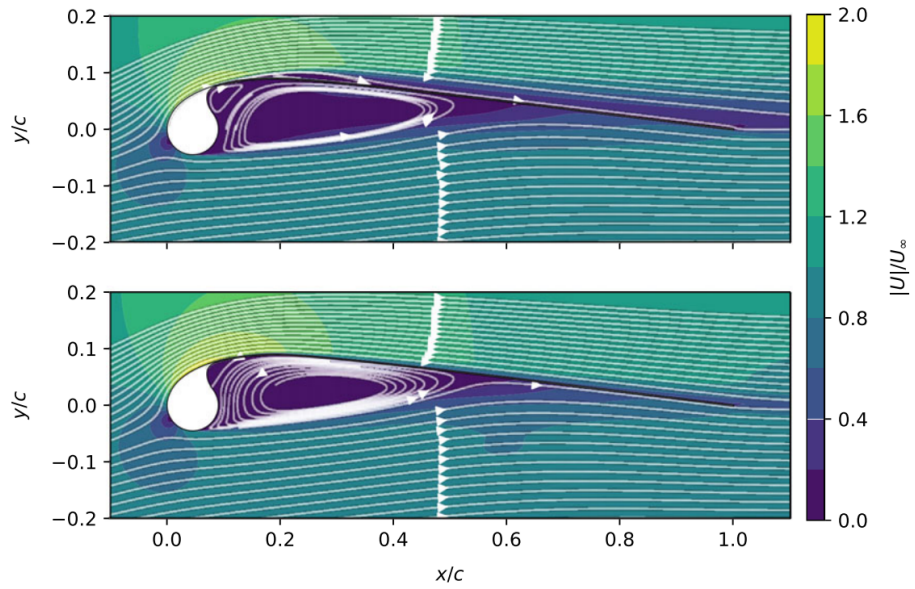

Figure 2.14: Streamlines along a LEI airfoil together with the normalised flow velocity for simulation with transition modelling. Both at $\alpha = 6^{\circ}$, Re = 10^5 (top) and Re = $5 \cdot 10^5$ (bottom) [19]

The conclusions from this study were that at lower Reynolds numbers, it is necessary to use transition modelling to properly model the flow field. Laminar separation was present on both sides of the LEI wing airfoil at lower Reynolds numbers. Furthermore, it showed that when using a transition model, the highest aerodynamic efficiency was not achieved at the high Reynolds as happened for the fully turbulent simulation. At larger Reynolds numbers, the flow behaves similar to the fully turbulent simulation, as would be expected.

3D RANS CFD studies

Deaves [35] performed a 3D steady-state RANS simulation of a LEI wing. This was based on the V2 LEI kite of the Kitepower group, the predecessor of the design studied in this thesis. It used a k - ω SST turbulence model without transition model. A first step in the study was validating the simulation setup in 2D for a NACA0012 airfoil. Validating the simulation settings in this way and then extrapolating this as correct to 3D seems a bit questionable. The reason for this is that turbulent fluctuation components will always be three dimensional [67], thus the case is validated using a simulation that does not take everything into account. In addition to this, the flow over an airfoil of a LEI wing has very different characteristics than that over a conventional airfoil. Nonetheless, it is understandable that due to the lack of other validation data, these 2D results are used. The results of the 2D validation simulation will not be discussed here.

The 3D steady-state RANS simulation used the V2 LEI kite and the results will be discussed here. A comparison was done between classic planar wing lifting line theory and the integral lift and drag coefficients of the LEI wing. The first observation was that when the angle of attack surpassed 4° , the CFD results started to deviate from lifting line theory. This is explained by the presence of the recirculation zone on the pressure side behind the leading edge, which reduces the effective camber. The second observation was that the point of minimum drag coefficient did not coincidence with the point of zero lift, this was again explained by the same reasoning.

The performance of the LEI was assessed by looking at $C_L^3/C_{D,eff}^2$, which is an important performance parameter of a pumping cycle kite power system. The effective drag coefficient $C_{D,eff}$ is made up of the drag coefficient of the kite itself and the parasitic drag of the tether and bridle system. It was decided to compute $C_L^3/C_{D,eff}^2$ against the angle of attack for several parasitic drag values, as shown in Fig. 2.15. It can be observed that the LEI wing's peak performance is between 14° and 20° angle of attack depending on the parasitic drag value assumed.

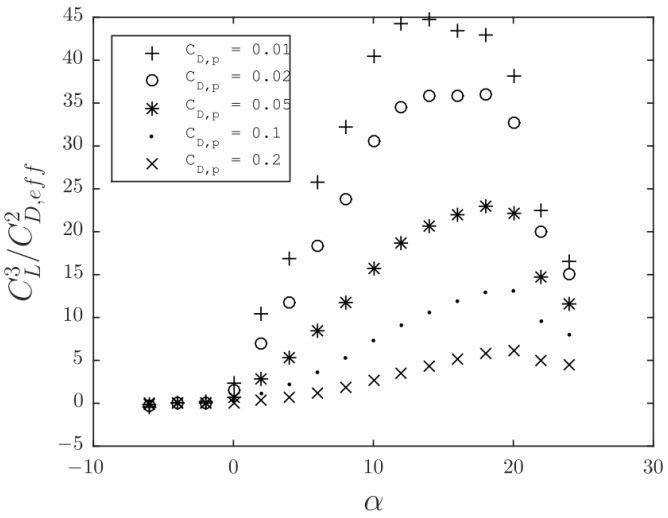

Figure 2.15: Performance curves for different values of the parasitic drag vs. angle of attack [35].

Another interesting analysis that was done revolved around the separation on both the pressure and suction side of the LEI wing. Starting with the suction side shown in Fig. 2.16, where the streamwise wall shear stress is plotted on the surface. When flow reversal or separation at the surface takes place the wall shear stress will go from positive to negative, just as shown previously in Fig. 2.4. As can be seen from these surface plots, already from 16° angle of attack there is some separation at the LEI wing's tip region. With an increase in the angle of attack, there are regions of reversed flow and separation on the surface, however, these regions differ for different angles of attack. It seems that the transient behaviour of the flow around the kite is impacting the steady-state solution convergence. Deaves [35] does not give a clear reason for this behaviour or the start of the separation point, but also indicates solution convergences issues at higher angles of attack due to unsteady phenomena. Other reasons mentioned by the author are decreased downwash in particular areas and variation in the LEI wing's cross-section, however, both statements are not backed up by quantitative or qualitative data.

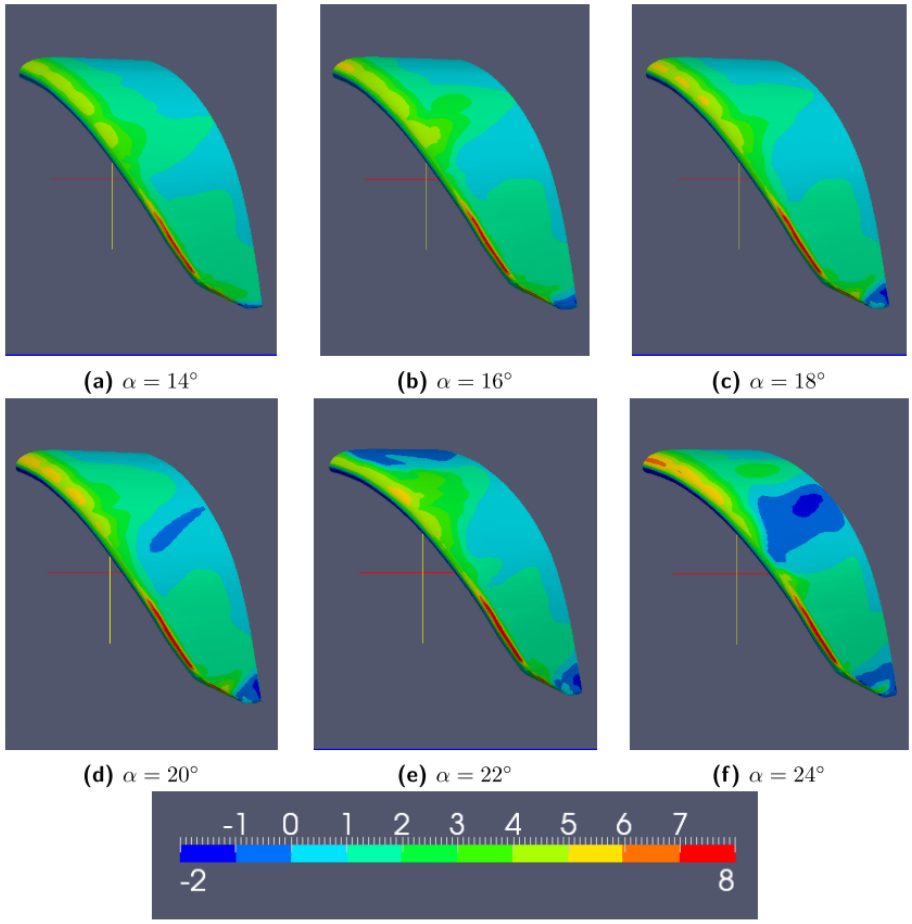

(a) $\alpha = 14°$ **(b)** $\alpha = 16°$ **(c)** $\alpha = 18°$

(d) $\alpha = 20°$ **(e)** $\alpha = 22°$ **(f)** $\alpha = 24°$

(g) Color legend, $\tau_{w,z}/\rho$ $[\mathrm{m}^3/\mathrm{s}^2]$

Figure 2.16: Wall shear stress on the suction side of the LEI V2 wing [35].

The pressure side of the LEI wing also showed large regions with separated or reversed flow as shown in Fig. 2.17. The general trend on the pressure side is that with an increase in the angle of attack, the recirculation area decreases. This behaviour is in line with the study done by Folkersma et al.[19], where the same recirculation area trend was observed. Since that was a 2D LEI wing airfoil study, the results of that can be best compared to the results close to the symmetry plane of the 3D simulation. However, since the 3D simulation did not use transition modelling, only the results without transition modelling should be used for comparison. It is interesting to note that the region where separation or recirculation is still present at higher angles of attack does seem to coincidence with the region of highest separation on the suction side.

The most important conclusions regarding the flow solution made in [35] were the following. Large angles of attack cause the CFD to become unstable to the point that no solution could be found. Throughout the whole angle of attack range, there is some separation or recirculation present on the pressure side of the airfoil, whereas on the suction side separation exists at higher angles of attack only. Depending on the parasitic drag of the tether and bridle line system, the maximum power for the LEI wing is generated between 14° and 20° angle of attack.

In addition to this, several recommendations for future studies were given. Since a highly simplified LEI wing geometry was used, this has consequences for the flowfield around the kite. The removal of the struts and geometric modification of the tip is expected to make a considerable impact on the results. The use of a solely turbulent simulation is questioned and how the transition from laminar to turbulent could affect the results and their correlation with experimental data. In addition to this, suggestions are made for the use of unsteady simulations to analyse transient flow effects. Also, the fact that a rigid LEI wing shape is used, whereas in reality it is a flexible structure that deforms under the load of the aerodynamics forces is mentioned. Finally, several other factors are mentioned such as variation in Reynolds number, the sideslip

angle and other dynamic flow phenomena could have a strong impact on the results.

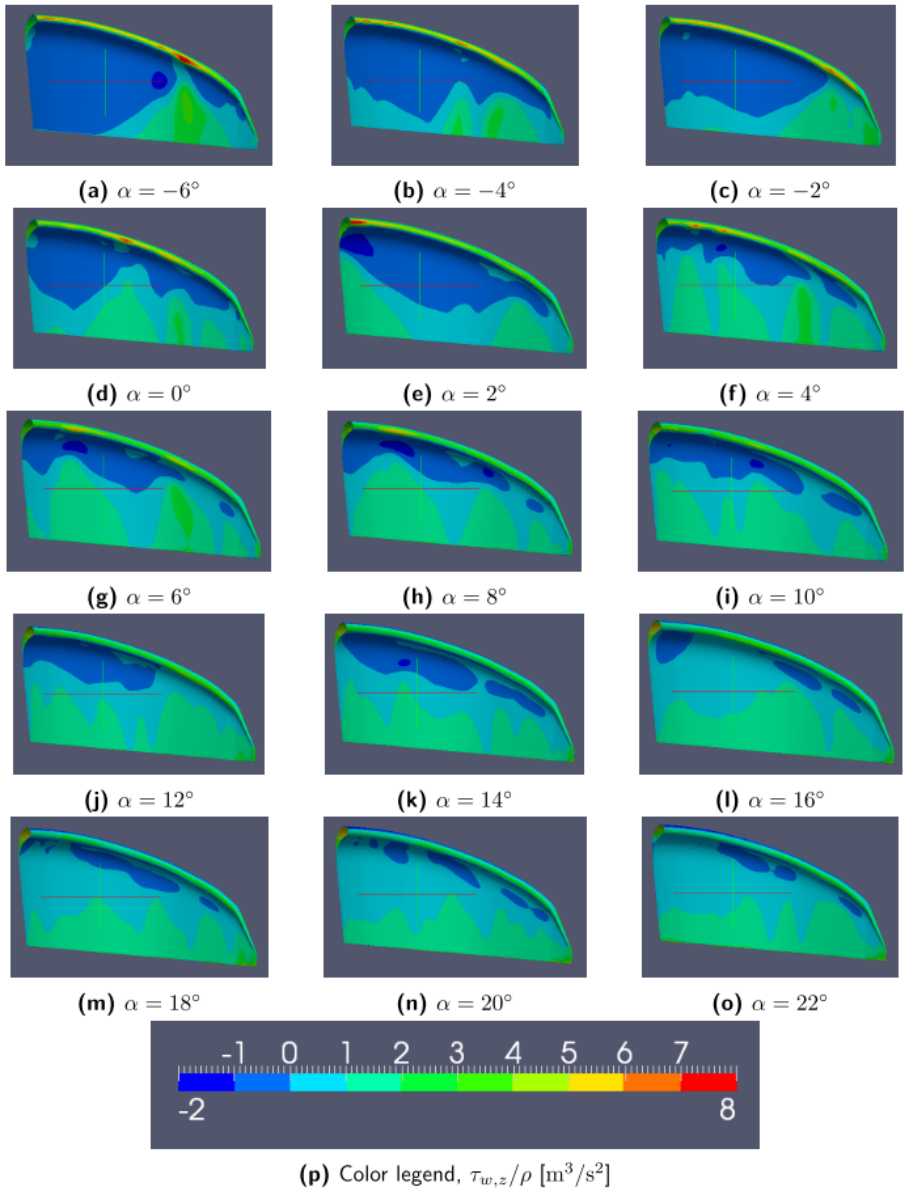

Figure 2.17: Wall shear stress on the pressure side of the LEI V2 wing [35].

The above study was a few years later followed up by Demkowicz [20], by using the setup of Folkersma et al.[19] and extending it to 3D. The results of this most recent study will be discussed here. Where the 3D study shown above used the LEI V2 kite by Kitepower, this more recent study used the LEI V3A wing design. Since this study used the 2D simulation set-up as a basis, the simulations are run for the same Reynolds number range of Re = 10^5 to Re = $15 \cdot 10^6$ and the angle of attack is varied between $-5°$ and $24°$. Furthermore, it used the $k-\omega$ SST turbulence model with and without the $\gamma - \tilde{\mathrm{Re}}_{\theta t}$ transition model.

The integral lift and drag coefficient of the LEI wing are shown in Fig. 2.18 for the case with transition modelling. The first observation that is in line with the 2D simulation is that at the lowest Reynolds number the stall happens early on around 6° angle of attack. The same trends in terms of decreasing the laminar separation bubble on the suction side were present in the 3D simulation as well. The trend of increasing maximum lift coefficient with Reynolds number also does not hold here using transition modelling. The maximum lift coefficient occurs at $1 \cdot 10^6$, whereas in the case of a turbulent simulation the maximum lift coefficient peaks at the highest Reynolds number. A potential reason for this, as given by Folkersma et al.[19], is the favourable

combination of a small laminar separation bubble and long laminar boundary layer. For higher Reynolds numbers earlier transition to a turbulent boundary layer takes place, which results in a lower maximum lift coefficient due to decambering and a higher drag coefficient.

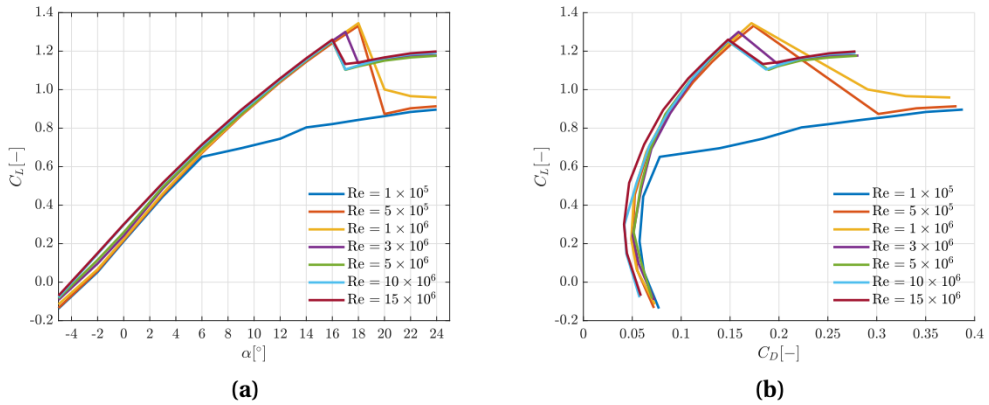

Figure 2.18: The lift (a) and drag (b) curves for the LEI V3A wing with transition modelling [20].

The flow field analysis was done for a common flight condition of 12° angle of attack at Re = $3 \cdot 10^6$. In Fig. 2.18, the wake contours and streamlines of the flow field around the LEI wing are shown. From the contours, one can observe that the pressure differential between the pressure and suction surface of the LEI wing causes the generation of vorticity. This vorticity is responsible for the in and outwash seen in the left plot. The decay in vorticity can be observed behind the LEI wing based on the contours in the right plot. When analysing the skin friction coefficient on the pressure surface of the LEI wing, it showed that recirculation zones behind the leading edge varied in size along the span. A statement was made that the pattern of the recirculation areas behind the leading edge could be attributed to the geometrical shape of the LEI wing itself. Regions of positive and negative circulation in spanwise direction alternate and influence the recirculation regions in the streamwise direction. When on the border between a negative and positive spanwise circulation region the flow moves towards the surface, the recirculation at the surface decreases. When the flow on the border of two spanwise circulation regions moves away from the surface, the recirculation zone on the surface increases.

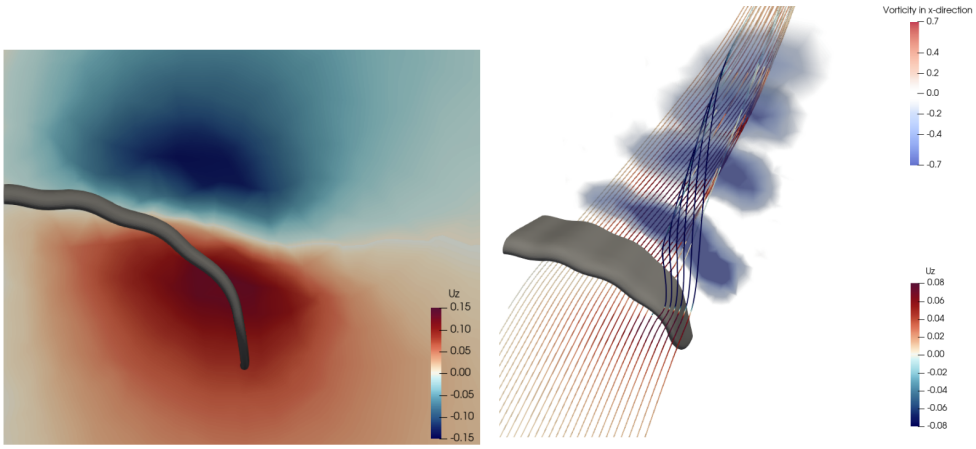

Figure 2.19: Spanwise velocity contours behind LEI V3A wing (left) streamlines coloured by streamwise velocity and vorticity contours behind the LEI V3A wing (right) [20].

Since this study included transition modelling, the analysis of separation can lead to better insights into the behaviour of the flow over the LEI wing. The lift and drag coefficient polars with and without transition modelling are compared in Fig. 2.20. Generally speaking, there was not a well-defined trend observed with consistent offsets between the results with and without transition modelling. For the highest Reynolds num-

ber the results matched the closest, one could argue that this makes sense as the higher the Reynolds number the earlier the laminar flow transitions to turbulent.

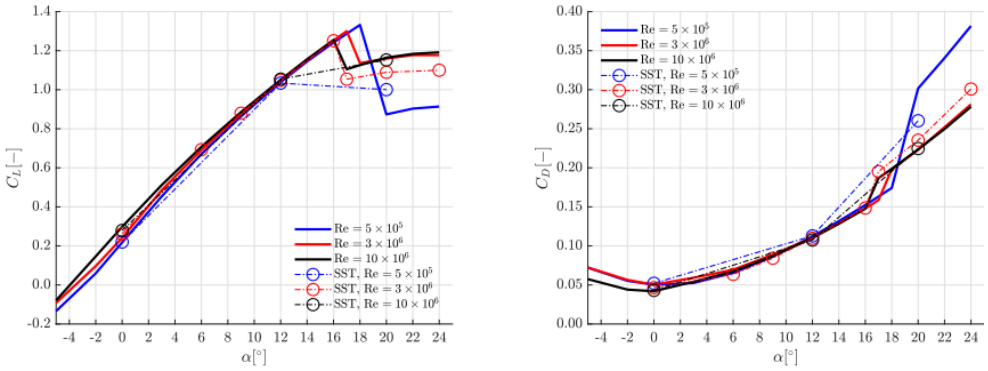

Figure 2.20: Lift and drag curves for several Reynolds numbers with and without (SST) transition modelling [20].

With transition modelling, a laminar separation bubble was visible at lower Reynolds numbers. Furthermore, the simulations showed different trends in skin friction over the surface of the LEI wing. Without transition modelling, the trend of skin friction over the surface stayed the same, with only the magnitudes changing. The difference between the flow over the LEI wing with and without transition modelling at low Reynolds number is shown in Fig. 2.21. In addition to this, the circulation zones along the span on the pressure side of the LEI wing also changed. Without transition modelling, these areas seemed to be thinner and the location of occurrence was different as well.

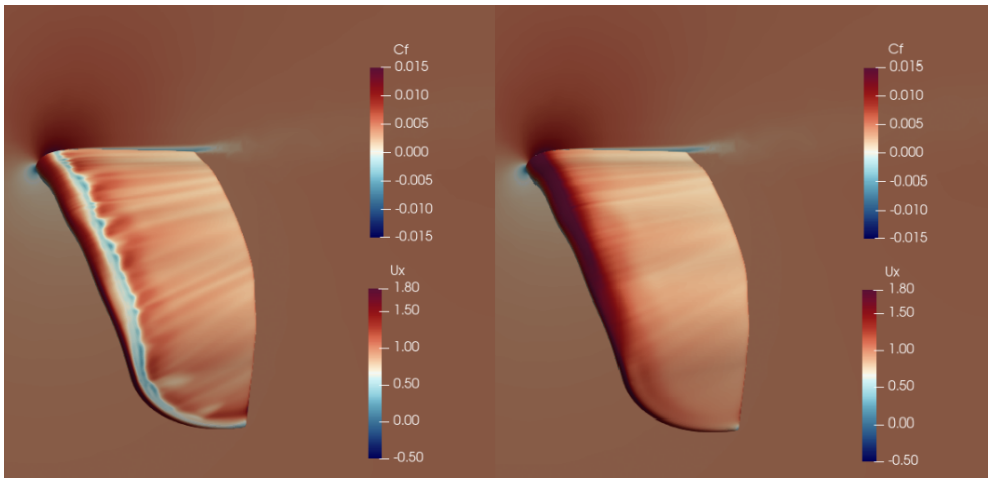

Figure 2.21: Skin friction with transition modelling (left) and without transition modelling (right) [20].

Compared to the values of several numerical models, the lift coefficient seemed to come quite close. However, for the drag coefficient the difference between the CFD results and the other numerical models was larger. Furthermore, the lift curve slope of the experimental data was much steeper. Two reasons given for this were the effect of the changing camber and wing surface area due to deformation in-flight. The lift-to-drag ratio of the CFD results matched the best available experimental data better than previous studies, however, it still had a considerable offset for most of the range.

Some of the conclusions made by Demkowicz [20] were as follows. At lower Reynolds numbers, laminar separation is present on both the suction and pressure side of the LEI wing and a laminar separation bubble is observed on the suction side of the LEI wing. When the Reynolds number is higher than $10 \cdot 10^6$ a very early transition to a turbulent boundary layer happens and a fully turbulent approximation would be valid. At the same higher Reynolds numbers, drag crisis has been observed which leads to the delay in flow separation of the cylindrical leading edge of the kite. For the tested flight conditions, strong crossflow was present which

influenced the recirculation behind the leading edge. The results also showed that at low Reynolds number, transition modelling is necessary to account for the actual flow dynamic interactions.

One of the first and most logical recommendations for future studies is increasing the geometric complexity of the model, more specifically including the chordwise struts. Since this study observed strong crossflow that influenced the recirculation zones on the pressure side, it is expected that the struts can have a large influence in altering this effect. Furthermore, there were no simulations done with non-zero sideslip angles, even though sideslip angle variation is present in real flight. Thus, simulations with a non-zero sideslip angle could be done.

Comparison between two 3D RANS CFD studies

Comparing the two computational methods of Deaves [35] and Demkowicz [20], the first thing that stands out is the fact that they did not come to the same conclusion regarding transition modelling. A likely reason for this is that the test case that was used by Deaves [35] on a NACA0012 airfoil was not fit for determining the benefits of transition modelling on a LEI wing. As explained before, the fact that a normal airfoil geometry has very different flow characteristics than a LEI wing airfoil makes extrapolating conclusions based on this a bit questionable. Since Folkersma et al.[19] showed that for LEI wing airfoils the trends observed with and without transition modelling did change considerably, testing this method on a LEI wing was worthwhile. On a three-dimensional LEI wing, the impact of transition modelling on the integral force coefficient seemed not very consistent. This could be due to the inherently transient nature of the flow field around the LEI wing. Nonetheless, at the lowest Reynolds number tested, it was clear that a fully turbulent simulation led to a wrong prediction of separation that influenced both the integral lift and drag coefficients. Furthermore, analysis of the skin friction coefficients over the LEI wing showed strong variation with Reynolds number when transition modelling is used. This shows that the impact of transition modelling can most likely not be neglected on a LEI wing.

The second part on which the two studies can be compared is the pre-processing approach. In terms of meshing domain, both studies made use of expected symmetry of the flow field at the centerline of the LEI wing. However, a very different pre-processing approach is used between the two studies. The original LEI wing geometry was made in the kite software SurfPlan and had to be transformed to a geometry format that the meshing software Pointwise could handle. Deaves [35] did these steps in SurfPlan, whereas Demkowicz [20] used a CAD package called Rhinoceros to prepare the geometry. The latter is the more preferred method as it gives more control over the preparation, tweaking and cleaning of the CAD model. Especially when looking surface mesh of the kite, it shows that the geometry made by Demkowicz [20] is much smoother around the tip versus a wrap with discontinuous surface edges as applied by Deaves [35]. As the anhedral curved shaped of the LEI wing poses difficulties for using a fully structured mesh, there has to be a transition region between the high aspect ratio prism layer cells at the surface of the ELI wing to an unstructured mesh. The method used by Deaves [35] relied on joining a far-field unstructured mesh with a structured boundary layer mesh. This led to highly skewed cells with orthogonality problems at the transition between the two meshes. Due to this, Deaves stated that the use of corrections was needed to ensure the stability of the solution, significantly increase the computational cost. In addition to this, it is likely that this would contribute to numerical errors in the solution. To mitigate some of these issues the approach taken by Demkowicz [20] is based on a special meshing algorithm named T-Rex [68]. Using this algorithm, a hybrid mesh can be created that is automated by Pointwise in such a way that the user can ensure sufficient cell quality is obtained. In addition to this, LEI wing geometry surface mesh was divided into a structured and unstructured part. The region around the tip is unstructured to be able to deal with the curvature in this area. The rest of the LEI wing surface mesh is structured. The impact of the mesh parameters was analysed well, and therefore this approach would get preference over the pre-processing approach used by Deaves [35].

The underlying issues with the mesh quality also showed itself in the numerical solution in terms of convergence for the study of Deaves [35]. The amount of non-orthogonal corrections needed for every case were higher than the maximum used by Demkowicz [20]. This eventually led to on average 8 times the amount of iterations necessary and unconverged integral force coefficients for most angles of attack. Even though there were some differences in the numerical schemes used, the mesh was most likely the biggest contributor to this.

In terms of actual results, a comparison becomes quite difficult. The fact that Deaves [35] used a different LEI wing version, only ran simulations for Re = $6 \cdot 10^6$ and did not include transition modelling means no like for

like comparison is possible. However, when comparing the integral force coefficients for both studies without transition modelling and the closest matching Reynolds number, still a few observations can be made. The maximum lift coefficient in [20] is higher and occurs at a lower angle of attack. Furthermore, the drag coefficient is higher for every angle of attack. This could be due to the fact that the higher lift also leads to higher induced drag [69]. In Deaves study [35], no strong drop in lift coefficient is observed even at higher angles of attack, the lift curve just flattens off.

Limitations of the current 3D RANS CFD studies

Based on the above comparison, it can be concluded that the approach and method used by Demkowicz [20] would be preferred over the one of Deaves [35]. However, even the former study left room for improvement in several directions.

The first big step forward could be taken with the geometry of the LEI wing itself. As Demkowicz [20] indicated, the geometry of the kite was greatly simplified to make the CAD and meshing process easier to do. By doing this, it was possible to make a good step forward in the mesh quality of a three-dimensional LEI wing and it was possible to lay the foundations of a new methodology for three-dimensional LEI wing meshing. However, since the study showed that there are strong crossflow interactions present and that the regions of recirculation are influenced by the wavy shape of the LEI wing, it is expected that including more details in the geometry can significantly impact the flow field. To highlight this, a plot of the crossflow zones along the span is given in Fig. 2.22, in which the circulation direction is indicated by the arrows. From this, it is evident that the inclusion of the chordwise struts will have a large impact on crossflow behaviour and the recirculation zones behind the leading edge of the LEI wing.

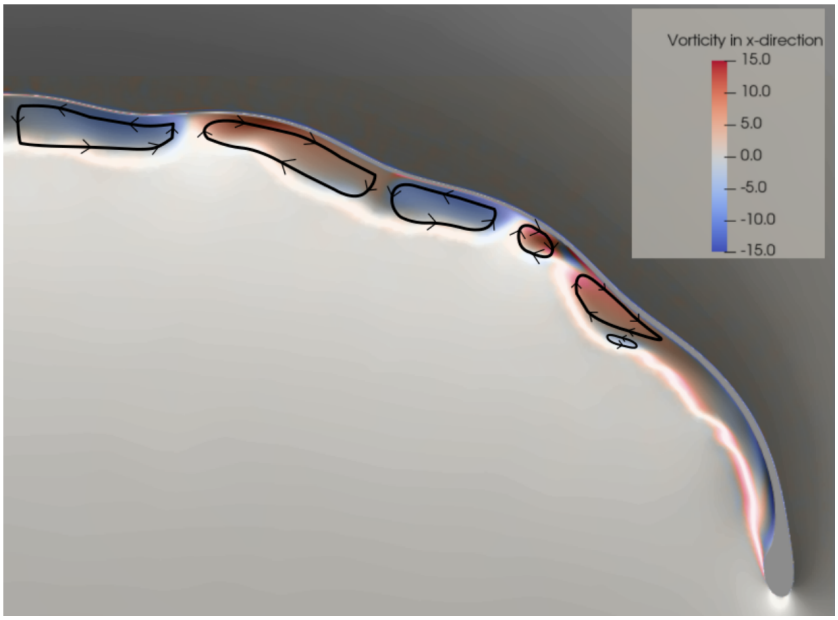

Figure 2.22: Recirculation regions along the span of the LEI V3A wing at x = 0.3 [20].

Another key flow condition of which the understanding of the flow around the LEI wing is currently lacking is sideslip. The CFD results presented by Gaunaa et al.[48] showed that aerodynamic performance quickly diminished when non-zero sideslip angles where considered. However, no further details of this study or the simulations done could be found. Apart from these results, no computational results have been found on similar geometries. Some experimental studies looked into the effect of sideslip on delta wings [70] or low aspect ratio wings [71], but none of these results could be representative for a LEI wing. However, the sideslip angle can be non-zero on several occasions throughout the pumping cycle as Oehler et al.[18] showed. Therefore, more knowledge about the effect of the sideslip angle on the aerodynamic performance of a LEI wing could potentially explain more about certain performance variations seen in experimental testing.

The inherently unsteady nature of the recirculation zones around the LEI wing mean that when averaging

out the result, as done in RANS simulations, many intricacies of the transient flow field are overlooked. As Demkowicz [20] also showed, there could be some unsteady behaviour present in the flow field. A way to get a bit more insight into this unsteady behaviour would be through URANS simulations. It has been shown that URANS simulations can predict some of the low-frequency transient vortices [60]. One problem is the steep ramp-up in computational resources needed with URANS simulations. It is reported it can take up to two times longer to run a URANS simulation for a simple vehicle geometry [72].

The last point that can be mentioned is about the geometry itself being rigid and not true to the actual shape of the LEI wing. Throughout the pumping cycle, the wing will constantly deform as an effect of the aerodynamic loads applied on it and vice versa. Before resorting to FSI simulations, it could for example be possible to have two separate geometries, one for the traction phase and one for the retraction phase. Running simulations with these geometries could decrease the geometrical discrepancy that now exists.

While there are other points mentioned by Demkowicz [20] such as using different transition models, varying boundary conditions and mesh settings, the points mentioned above are expected to have a bigger impact. This is also due to the fact that playing around in the margin of CFD simulation settings will be hard without proper reference data. One can change a boundary condition or slightly improve the mesh quality, but if there is no actual quantitative data available to correlate with then the amount that can be learned by tweaking in these fine margins is limited.

2.3. Experimental methods and results

Even though the increase in computational power has made RANS CFD simulations accessible for most research. These computational methods still deal will plenty of challenges and limitations which cannot be resolved without moving to higher fidelity methods. However, the use of these higher fidelity methods would lead to an excessive increase in computational resources and is therefore not feasible at this point in time. Thus, the only real physically accurate representation of a LEI wing's performance can be obtained through experimental testing. However, these experimental methods also deal with challenges and limitations which will also be discussed in this section.

When a researcher or engineer wants to obtain information about the flow field around a certain geometry or lifting device it is quite common to resort to wind tunnel testing. The benefits of using a wind tunnel lie in the fact that one is observing the real flow field as it happens and it is possible to extract a large amount of data from a test [73]. Since it is not possible to test a full-scale aircraft wing, as you could with CFD, in a wind tunnel a scaled-down version is often used. Scaling down the problem means that similarity parameters need to be kept constant to ensure that the flow field interactions in the wind tunnel and in the real world can be considered similar. However, this is where one of the issues lies for testing LEI wings or kites in a wind tunnel. Since LEI wings are flexible membranes, the down-scaling should be done in such a way that both the aerodynamic and structural characteristics are adequately scaled, which would be very difficult to achieve [18]. In a study by de Wachter [74], a full-scale ram-air wing was subjected to tests in two wind tunnels to study the structural and aerodynamic behaviour of the kite. Through photogrammetry, a CAD model of the ram-air kite under certain loading conditions was created. This CAD model was then used for several 3D RANS CFD simulations, however, the results were reported to be quite far off the wind tunnel data. This was supposedly caused by wind tunnel wall effects and the fact that the CFD simulations were not done in a wind tunnel domain. Even though this was a relatively small kite, it still took up a large part of the wind tunnel's cross-section, as can be seen in Fig. 2.23. Therefore, it is clear that wind tunnel testing of large LEI wings without down-scaling would not be possible. This, combined with the difficulties of down-scaling the structural properties of the flexible membranes of a LEI wing, makes wind tunnel testing currently unfeasible. For more information on wind tunnel testing and experimental methods, the reader is referred to [73].

Figure 2.23: Ram-air kite during wind tunnel test [74].

Because of the above indicated reasons, many experimental studies on LEI wings and kites have focused on full-scale in-flight measurements [18, 21] or alternative tests such as towing [75, 76] or the use of a rotating arm [77].

Stevenson et al.[77] designed a circular flight system that could be used to determine the lift-to-drag ratio of a given kite. However, since circular testing is not the same as testing in real flight conditions, there are a few caveats with this method. These are the fact that the weight of the kite acts in a different plane than the lift and drag force do, the circular motion causes a centrifugal force and the tether will not have real flight dynamic behaviour. The results did not match other car-based tests done with the same kite. However, the author argued that it would be still a useful tool to compare different configurations of kites with respect to each other using the same method. Nonetheless, this method does not give deeper aerodynamic insights that can prove valuable in designing the next iteration. Comparison to CFD would be limited to only the lift-to-drag ratio value, which is not enough to gain a better understanding of the aerodynamics trends.

Another method that is used for the assessment of the aerodynamic performance of LEI wings and kites is by towing it with a car. The basic idea behind these towing tests is to use the car's velocity to move the kite through the air. In the most recent towing study by Hummel et al.[76] the system consisted of a car, a test bench, the kite and several sensors and measurement systems. The schematic overview of the system is given in Fig. 2.24.

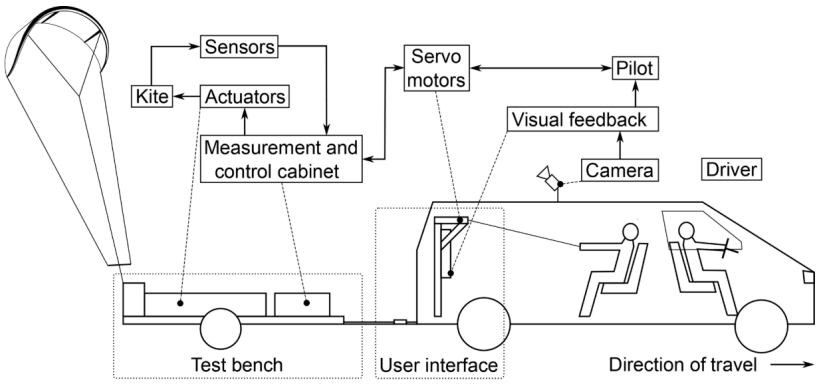

Figure 2.24: Schematic overview of the towing test setup as used by Hummels et al.[76].

In order to convert the raw data into aerodynamic parameters and coefficients, a dynamic model was devel-

oped. The post-processed data of Costa [75] was fitted with polynomials and several different filters and the results are shown in Fig. 2.25. It can be seen that the lift, drag and lift-to-drag ratios vary for the different fitting methods. Improvements could be made to this by measuring the angle of attack more accurately, the wind speed of the kite itself and extending the mathematical model behind it.

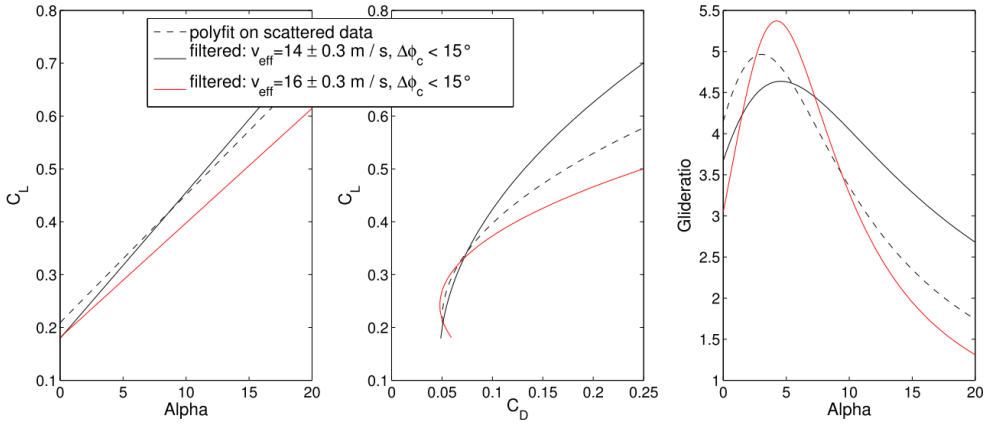

Figure 2.25: Fitted data for lift curve (left), drag polar (middle) and lift-to-drag ratio (right) [75].

Hummel et al.[76] performed a more advanced version of this is study. The testing procedure was more automated and most of the real kite system was included such as the common steering input device. This allowed testing in a more controlled manner with a linear power manoeuvre. Through the use of this novel set-up, the aerodynamic coefficients and lift-to-drag ratio of several kites were determined for different power settings. The aerodynamic efficiency and lift curves as a function of the power setting are shown in Fig. 2.26. These results have not undergone filtering or post-processing such as the towing results of the previous study. The test set-up has proven that it is possible to assess the performance of kites relative to each other by testing them in an automated and controlled way. However, the only manoeuvre done in this test was the linear power manoeuvre, and therefore it is still a very isolated result that might not transform to crosswind motion with similar trends. Furthermore, for comparison to CFD, it would be good to have lift and drag curves as a function of angle of attack as the power setting is not something that can be output from CFD.

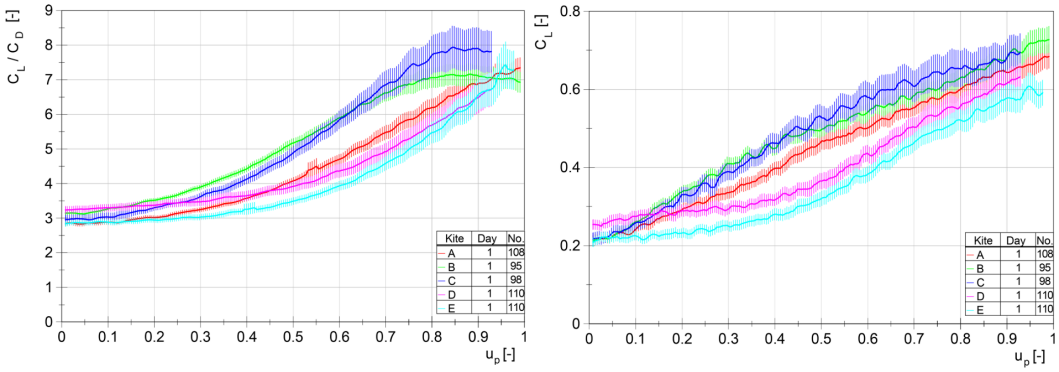

Figure 2.26: The lift-to-drag ratio (left) and lift coefficient (right) as a function of power setting for different kite models [76].

While both methods can provide some useful data to compare different kite designs, they still have some inherent limitations [21]. First, there is a limitation on the traction force due to the design of the platform, therefore, it is not possible to achieve traction loading as high as encountered during real flight. Second, since the wind is not measured close to the kite, variations in wind speed will lead to variations in the determined coefficients. Third and last, based on a measurement set-up that is situated on the ground, it is hard to quantify the effect of tether sag during operation or to determine the lift-to-drag ratio for movements such as crosswind figure eights. The last experimental method that will be discussed is one that tries to solve these problems, this is in situ testing.

The first introduction to the concept of using an onboard measurement setup for LEI wings was given in [21]. The apparent flow velocity and inflow angles are measured at the bridle lines in a position that is not influenced by the induced velocity of the LEI wing itself. Ideally, during the reel-out phase, the LEI wing operates near maximum power, represented by the power setting $u_p = 1$. At this setting, the lift-to-drag ratio and lift coefficient will be highest. The study showed that when the power ratio is close to 1, the LEI wing is in its traction phase and the lift-to-drag ratio is high. When the power ratio is low, the LEI wing is in its retraction phase and the lift-to-drag is considerably lower.

A more detailed study using in situ measurements has been done by Oehler et al.[18]. The first important conclusion that could be drawn from the results was that without in situ measurements it is very hard to achieve accurate estimates for parameters. When the results were compared to the study done by Ruppert [50], which only used GPS and Inertial Measurement Unit (IMU) data, the determined range for angle of attack and sideslip varied widely. In [18], the angle of attack throughout the traction phase ranged from 6° to 16° and the sideslip angle had a maximum deviation of 10°. In Fig. 2.27, the filtered data for lift-to-drag ratio vs. angle of attack including power setting is shown. For angles of attack between 5° and 16°, the lift-to-drag ratio is high and the relative power setting is high. Therefore, this region can be identified as the traction phase. For the angles of attack between −8° and 4°, the lift-to-drag ratio is low and the relative power setting is also low. Therefore, this region can be identified as the retraction phase. Generally speaking, when the relative power setting is high, the lift-to-drag ratio is high and vice versa. This also clearly shows from Fig. 2.28, where the oscillations in lift-to-drag ratio at high power settings correspond to turning manoeuvres.

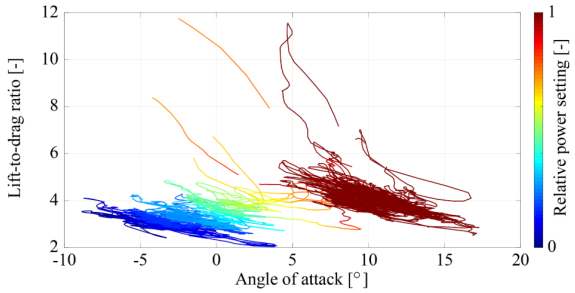

Figure 2.27: Lift-to-drag ratio vs. angle of attack coloured for relative power setting [18].

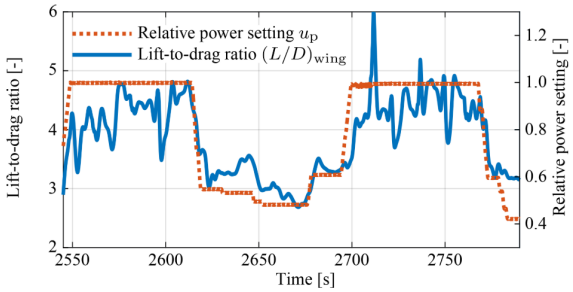

Figure 2.28: Lift-to-drag ratio over a certain period of time during testing with the accompanying relative power setting [18].

Demkowicz [20] made a comparison between the CFD results and several experimental methods, the graph of this is shown in Fig. 2.29. This highlights that there are also large differences between the results of the experimental methods for the lift-to-drag ratio vs. the angle of attack. Since both Ruppert [50] and Fechner et al.[37] used different definitions of the angle of attack, corrections were needed and comparison becomes difficult.

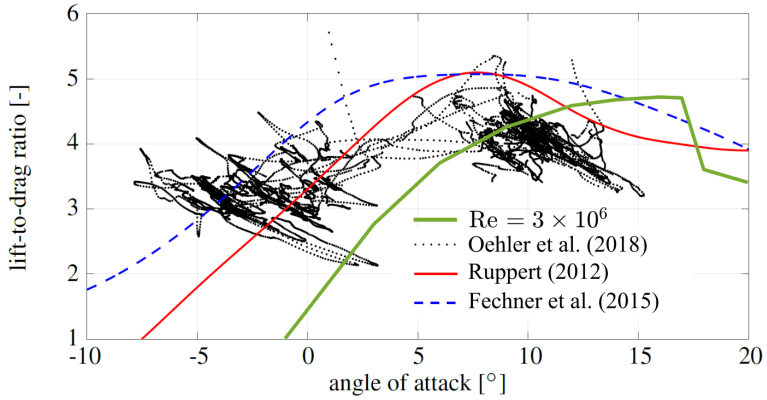

Figure 2.29: Experimental data of the lift-to-drag ratio compared to different experimental studies and CFD (green) [20].

One other interesting result was derived from looking at the lift coefficient vs. the angle of attack depending

on the LEI wing heading. As can be seen in Fig. 2.30, there is a large variability of the lift coefficient and angle of attack depending on if the LEI wing is heading up or down. When the LEI wing is heading down, its velocity increases and to keep the tether force constant the angle of attack and hence lift coefficient decrease. When the LEI wing is heading up, the opposite is true.

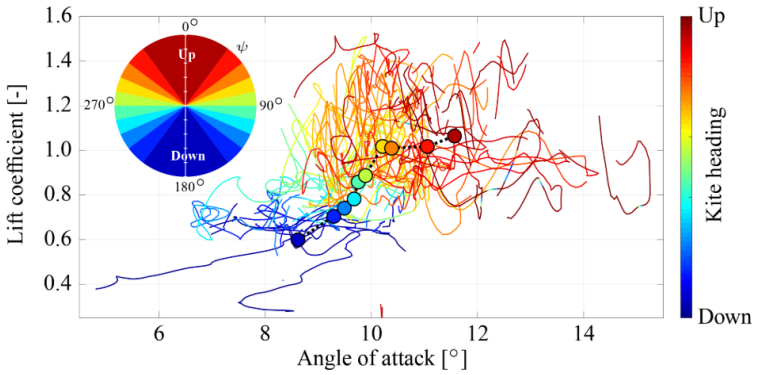

Figure 2.30: Lift coefficient vs. angle of attack coloured by different heading directions of the LEI V3A wing [18].

2.4. Conclusions of literature review

In this chapter, the aerodynamics of LEI wings has been discussed in detail. Based on this literature review, several conclusions can be drawn regarding flow field around a LEI wing, the current state-of-the-art numerical simulations and experimental studies of LEI wings.

First, the conclusions about the flow field around a LEI wing. What is evident is that the flow around a 3D LEI wing includes many different phenomena and interactions. Laminar and turbulent flow regions occur on both the pressure and suction side. On the suction side, a laminar separation bubble can be present of which the occurrence, position and strength are dependent on the Reynolds number and the angle of attack. At higher Reynolds numbers, the transition can happen very early which prevents such a laminar separation bubble from forming. On the pressure side, a large recirculation zone exists behind the leading edge of the LEI wing. The size of this recirculation zone is also a function of the Reynolds number and the angle of attack. At lower Reynolds numbers, separation can happen off a laminar boundary layer, which can be more severe. Furthermore, results showed that with increasing Reynolds number, the recirculation zone decreased for a fixed angle of attack [19]. The most recent study on a 3D LEI wing done by Demkowicz [20] showed the presence of strong 3D crossflow effects and a changing recirculation pattern along the span.

In terms of numerical modelling, the consensus based on the studies discussed in this literature review is that CFD simulations are currently the best numerical method for analysing the flow around LEI wings. While RANS methods have their limitations, they are at the moment still the best trade-off between computational resources and the accuracy of the results. In addition to this, transition modelling is needed to properly model the flow phenomena at lower Reynolds numbers. The foundation for this was laid by the 2D LEI wing study done by Folkersma et al.[19] and then followed-up by a 3D LEI wing study by Demkowicz [20]. Furthermore, Demkowicz [20] showed that it is possible to develop a methodology to mesh a 3D LEI wing and obtain numerical results without doing too many concessions on mesh and simulation settings. Through the use of a hybrid meshing approach and the T-rex algorithm in Pointwise, a satisfactory mesh quality could be obtained. Some transient behaviour was observed in the residuals, however, this did not affect the convergence of most simulations too much. While in reality, the flexible membrane of a LEI wing will lead to an intricate FSI problem, most modelling efforts based on CFD have focused on rigid geometries. This choice is justified by the otherwise high computational cost of a coupled fluid-structure model. If one would want to model the 3D LEI wing as a FSI problem, the geometry would have to be simplified which means the geometry itself becomes less representative. Since the aerodynamic flow around LEI wings is not studied extensively yet, there is still a large potential for knowledge gain even from rigid geometries.

Even though good progress was made regarding numerical simulations of LEI wings by Demkowicz [20], the study still had some points of improvement. The first one being the fact that the chordwise struts were not included in the geometry. These struts are expected to have a strong impact on the crossflow interaction be-

haviour that was observed and might also have a large impact on the recirculation zones behind the leading edge. This in turn could lead to different values for the lift and drag coefficients. Thus, there is a potential for bringing the numerical results closer to the experimental data if the geometry includes more detail. Furthermore, the study only focused on zero sideslip angle conditions. In experiments, it showed that the LEI wing experiences moderate non-zero sideslip angles during the traction phase of the pumping cycle [18]. Therefore, simulating non-zero sideslip angles could provide more insight into flow conditions of which it is known the LEI wing will experience them in flight. One other point mentioned in the discussion was the unsteady nature of the flow around the LEI wing. This can cause low- and high-frequency transient movement which is currently simply averaged out by the RANS solver. By using URANS simulations it would be possible to model some of the low-frequency movements of the structures around the LEI wing. Insight into this transient behaviour could lead to a better picture of transient effects observed in experimental testing.

While there have been several attempts at gathering experimental data on LEI wings and kites, there are not many that can provide the much-needed validation data for CFD simulations. As wind tunnel testing of full-scale LEI wings is not feasible and scaling down all structural and aerodynamic characteristics is nearly impossible, data has been gathered outside the wind tunnel. The most important results were obtained by in situ flow measurements, which provided reference data for trends throughout a large angle of attack range [18]. Unfortunately, due to the nature of in-flight testing, none of the experimental studies has been able to provide quantitative flow field data.

3

Computational Fluid Dynamics

This chapter will discuss the theory behind CFD that is relevant to this study. This starts with an introduction to the RANS equations in Section 3.1. After this, several turbulence models are discussed in Section 3.2. The transition model used in this study is presented in Section 3.3. This is followed by a brief discussion on the discretisation of the fundamental equations in Section 3.4. Lastly, the approach to solving the RANS equations in OpenFOAM is outlined in Section 3.5.

3.1. Reynolds-Averaged Navier-Stokes equations

As has been discussed in the literature review of Chapter 2, the underlying equations for CFD methods are known as the Navier-Stokes equations. Assuming the fluid to be steady-state, incompressible and with constant density, the Navier-Stokes equations can be expressed using Einstein notation as Eq. (3.1) and Eq. (3.2). With u_i being the velocity, p the pressure, ν the kinematic viscosity and ρ the density.

$$\frac{\partial u_i}{\partial x_i} = 0 \tag{3.1}$$

$$u_j \frac{\partial u_i}{\partial x_j} = -\frac{1}{\rho}\frac{\partial p}{\partial x_i} + \nu \frac{\partial^2 u_i}{\partial x_j^2} \tag{3.2}$$

The usage of higher fidelity methods such as DNS and LES would require too many computational resources for the current type of study. Therefore, this study will make use of a steady-state RANS method, which solves the Navier-Stokes equations for the steady mean solution of the flow. In order to derive the RANS equations, several steps have to be taken. First, the Reynolds decomposition is introduced through equation Eq. (3.3) The idea behind this decomposition is that the solution $u(x,t)$ can be decomposed into a mean value $\overline{u}(x)$, which is time-averaged, and the fluctuations $u'(x,t)$ around the mean.

$$u(x,t) = \overline{u}(x) + u'(x,t) \tag{3.3}$$

This decomposition then has to be substituted into Eq. (3.1) and Eq. (3.2), which after time-averaging leads to the RANS equations as shown in Eq. (3.4) and Eq. (3.5). As can be seen, the substitution introduced a new term $\overline{u_i' u_j'}$, which is called the Reynolds stress tensor and it consists of six independent components. This term will account for the averaged effect the turbulent fluctuations have on the main flow field, however, it also includes the effect of the smoothing that is introduced through the Reynolds averaging [78]. The introduction of this Reynolds stress term leads to what is called the closure problem. The closure problem stands for the fact that, without modelling the Reynolds stress tensor, the RANS equations do not form a closed system. To close the system, empirical turbulence models will have to be introduced, which will be discussed in Section 3.2.

$$\frac{\partial \overline{u}_i}{\partial x_i} = 0 \tag{3.4}$$

$$\overline{u}_j \frac{\partial \overline{u}_i}{\partial x_j} = -\frac{1}{\rho}\frac{\partial \overline{p}}{\partial x_i} + \nu \frac{\partial^2 \overline{u}_i}{\partial x_j^2} - \frac{\partial \overline{u_i' u_j'}}{\partial x_j} \tag{3.5}$$

3.2. Turbulence modelling

As discussed in Section 3.1, the RANS equations do not form a closed system and the Reynolds stress tensor has to be modelled. This is done through turbulence modelling, which will be the topic of this section. The currently available turbulence models for the RANS equations can be subdivided into two main categories: eddy viscosity models and Reynolds stress models.

The eddy viscosity models are based on the turbulent-viscosity hypothesis, which draws an analogy between the interaction of the viscous stress and the Reynolds stress on the mean flow [52]. Using this assumption, Boussinesq proposed the hypothesis given in Eq. (3.6). In this relation, k is the turbulent kinetic energy, δ_{ij} the Kronecker delta and ν_T the eddy viscosity. When this term is substituted into Eq. (3.5), only the eddy viscosity is used to represent the effect of the Reynolds stress.

$$-\overline{u_i' u_j'} = \nu_T \left(\frac{\partial \overline{u}_i}{\partial x_j} + \frac{\partial \overline{u}_j}{\partial x_i} \right) - \frac{2}{3} k \delta_{ij} \tag{3.6}$$

This leads to the first main category of turbulence models, which are the eddy viscosity models. The eddy viscosity will be expressed as a function of the mean velocity field. The first model that was introduced for this was by Prandtl based on the mixing length proposition and shown in Eq. (3.7). In this equation, l_m represents the problem-dependent turbulent length scale. Models based on this proposition are also referred to as algebraic or zero-equation models. It is mainly effective within the boundary layer and not to be used for complex flows far away from the wall.

$$\nu_T = l_m^2 \left\| \frac{\partial \overline{u}_i}{\partial x_j} \right\| \tag{3.7}$$

As an improvement over this model, the Prandtl one-equation model was introduced, as shown in Eq. (3.8). One-equation refers to the fact that there is one additional transport equation to be solved, namely for the turbulent kinetic energy k. Downside of these zero- and one-equation models is that in both models, the mixing length is assumed to be constant throughout the flow. However, one can imagine that mixing length varies heavily dependent on the location in the flow field, especially for complex, three-dimensional flows.

$$\nu_T = l_m \sqrt{k} \tag{3.8}$$

The most widely used RANS turbulence models are the two-equation eddy viscosity models. The turbulent model used in this study is based on a two-equation eddy viscosity model. For these turbulence models, there are two additional transport equations to be solved. There are three turbulence models that will be treated in the upcoming subsections. Limitations of these two-equation models is that they assume that there exist an equilibrium between the production and dissipation of turbulence. This assumption does not hold everywhere in the flow field, such as the boundary layer. Furthermore, due to the fundamental assumption that the Reynolds stress is proportional to the mean shear rate, as shown in Eq. (3.6), there is no way to account for the effect of specific Reynolds stress terms. In addition to this, there are more model-specific limitations, which will be mentioned in their respective subsections. The three different two-equation eddy viscosity turbulence models that will be discussed are $k-\epsilon$, $k-\omega$ and $k-\omega$ SST. Where $k-\omega$ SST is a blend of the first two to combine the advantages of both.

Before presenting these turbulence models, the second main category of RANS turbulence models will be briefly discussed, these are the Reynolds stress models. As the limitations of eddy viscosity models can only be mitigated by using a fundamentally different approach, this is what the Reynolds stress models aim to

do. Rather than using Boussinesq hypothesis and either zero, one or two additional transport equations, all the terms of the Reynolds stress tensor are directly modelled by using transport equations. However, this is done by simplifying the exact Reynolds stress transport equations and introducing approximations. In theory, these models should give much better results for complex flows, but they have also have disadvantages. First, as they introduce at least six additional transport equations, they are computationally much more expensive than the two-equation eddy viscosity models. Secondly, stability cannot be easily guaranteed and convergence can be slow as well.

3.2.1. The $k-\epsilon$ turbulence model

The $k-\epsilon$ turbulence model is one of the most popular two-equation eddy viscosity models currently used in the industry [79]. It introduces a transport equation for the turbulent kinetic energy k and the turbulent dissipation rate ϵ. It was developed by Jones & Launder in 1972 [80]. Since then, many different variations on this model have been developed, which treat the coefficients and parameters in a slightly different manner. The version that has been implemented in OpenFOAM is not the model initially proposed by Jones and Launder, but rather the Standard $k-\epsilon$ model that was proposed later by Launder and Spalding [81]. The transport equations for the turbulent kinetic energy and the dissipation rate, for steady-state RANS in OpenFOAM, are given by Eq. (3.9) and Eq. (3.10), respectively.

$$\overline{u}_j \frac{\partial k}{\partial x_j} = \tau_{ij} \frac{\partial \overline{u}_i}{\partial x_j} - \epsilon + \frac{\partial}{\partial x_j} \left[\left(\nu + \frac{\nu_T}{\sigma_k} \right) \frac{\partial k}{\partial x_j} \right] \tag{3.9}$$

$$\overline{u}_j \frac{\partial \epsilon}{\partial x_j} = C_{\epsilon 1} \frac{\epsilon}{k} \tau_{ij} \frac{\partial \overline{u}_i}{\partial x_j} - C_{\epsilon 2} \frac{\epsilon^2}{k} + \frac{\partial}{\partial x_j} \left[\left(\nu + \frac{\nu_T}{\sigma_\epsilon} \right) \frac{\partial \epsilon}{\partial x_j} \right] \tag{3.10}$$

In these equations, the Reynolds stress tensor is given by Eq. (3.11), where S_{ij} represents the mean shear rate tensor. The eddy viscosity for this specific model is determined through Eq. (3.12). The values of the model constants are summarised in Table 3.1.

$$\tau_{ij} = 2\nu_T \left[S_{ij} - \frac{1}{3} \frac{\partial \overline{u}_k}{\partial x_k} \delta_{ij} \right] - \frac{2}{3} k \delta_{ij} \tag{3.11}$$

$$\nu_T = C_\mu \frac{k^2}{\epsilon} \tag{3.12}$$

Table 3.1: The $k-\epsilon$ turbulence model constants.

$C_{\epsilon 1}$	$C_{\epsilon 2}$	σ_k	σ_ϵ	C_μ
1.44	1.92	1.0	1.3	0.09

This turbulence model performs well for external aerodynamics applications where no strong adverse pressure gradients or separation is present [82]. This means that, in theory, it is not very well suited for the simulation of the flow around a LEI wing, as these phenomena do occur frequently.

3.2.2. The $k-\omega$ turbulence model

To overcome the shortcomings of the $k-\epsilon$ model, the $k-\omega$ model has been developed. This model is more accurate for boundary layer flows that experience an adverse pressure gradient [79]. It introduces a transport equation for the turbulent kinetic energy k and the specific turbulent dissipation rate ω. For the model introduced by Wilcox in 1988, the transport equations for turbulent kinetic energy and specific turbulent dissipation rate are given by Eq. (3.13) and Eq. (3.14), respectively.

$$\overline{u}_j \frac{\partial k}{\partial x_j} = \tau_{ij} \frac{\partial \overline{u}_i}{\partial x_j} - \beta^* \omega k + \frac{\partial}{\partial x_j} \left[\left(\nu + \sigma^* \nu_T \right) \frac{\partial k}{\partial x_j} \right] \tag{3.13}$$

$$\overline{u}_j \frac{\partial \omega}{\partial x_j} = \frac{\gamma \omega}{k} \tau_{ij} \frac{\partial \overline{u}_i}{\partial x_j} - \beta \omega^2 + \frac{\partial}{\partial x_j} \left[(\nu + \sigma \nu_T) \frac{\partial \omega}{\partial x_j} \right] \tag{3.14}$$

Again, the Reynolds stress tensor in these equations is defined by Eq. (3.11). However, for this model, the eddy viscosity ν_T is given by Eq. (3.15). The values of the model constants are given in Table 3.2.

$$\nu_T = \gamma^* \frac{k}{\omega} \tag{3.15}$$

Table 3.2: The $k-\omega$ turbulence model constants.

β	β^*	γ	γ^*	σ	σ^*
$\frac{3}{40}$	0.09	$\frac{5}{9}$	1.0	0.5	0.5

The drawbacks of this model are that it is very sensitive to, and dependent on, the prescribed freestream values of both the turbulent kinetic energy and the specific turbulent dissipation rate [79]. Thus, the final solution will change depending on these prescribed values, which is undesirable for simulations without experimental flow field data to tweak these parameters to.

3.2.3. The $k-\omega$ SST turbulence model

Both the $k-\epsilon$ and $k-\omega$ turbulence model have their advantages and disadvantages. To combine the advantages and mitigate the disadvantages, the $k-\omega$ SST model was developed. This model was first introduced by Menter in 1993 [61]. The main idea behind this model is to use the $k-\omega$ model near the wall and the $k-\epsilon$ model away from the wall. The way this is implemented is through a blending function. The version that has been implemented in OpenFOAM is the revised version presented in [83]. The transport equations for the turbulent kinetic energy k and the specific turbulent dissipation rate ω are given by Eq. (3.16) and Eq. (3.17), respectively.

$$\overline{u}_j \frac{\partial k}{\partial x_j} = \widetilde{P}_k - \beta^* k \omega + \frac{\partial}{\partial x_j} \left[(\nu + \sigma_k \nu_T) \frac{\partial k}{\partial x_j} \right] \tag{3.16}$$

$$\overline{u}_j \frac{\partial \omega}{\partial x_j} = \gamma \frac{\widetilde{P}_k}{\nu_T} - \beta \omega^2 + \frac{\partial}{\partial x_j} \left[(\nu + \sigma_\omega \nu_T) \frac{\omega}{x_j} \right] + 2 (1 - F_1) \sigma_{\omega 2} \frac{1}{\omega} \frac{\partial k}{\partial x_j} \frac{\partial \omega}{\partial x_j} \tag{3.17}$$

In these transport equations, $\widetilde{P}_k$ stands for the limited production term given by Eq. (3.18). This puts a limit on the production of turbulent kinetic energy and the specific turbulent dissipation rate. In this equation, P_k is given by Eq. (3.19).

$$\widetilde{P}_k = \min \left(P_k, 10 \beta^* k \omega \right) \tag{3.18}$$

$$P_k = \nu_T \frac{\partial u_i}{\partial x_j} \left(\frac{\partial u_i}{\partial x_j} + \frac{\partial u_j}{\partial x_i} \right) \tag{3.19}$$

The blending is implemented through two blending functions. The first can be seen in the specific turbulence dissipation rate transport equation, denoted as F_1, which corresponds to the blending function that is given by Eq. (3.20). Where CD_{kw} is defined as Eq. (3.21). This blending function F_1 will be equal to zero far away from the walls and close to unity in the boundary layer. This means that model constants will have to be interpolated between the values for $k-\epsilon$ and $k-\omega$, which is done by using Eq. (3.22). The values for α_1 and α_2 are given by the model constants presented in Table 3.3 and Table 3.4. The value for β^* is equal to the value presented in Table 3.2.

$$F_1 = \tanh\left\{\left\{\min\left[\max\left(\frac{\sqrt{k}}{\beta^* \omega y}, \frac{500\nu}{y^2\omega}\right)^4 \cdot \frac{4\rho\sigma_{\omega 2} k}{CD_{k\omega} y^2}\right]\right\}^4\right\} \tag{3.20}$$

$$CD_{kw} = \max\left(2\rho\sigma_{\omega 2}\frac{1}{\omega}\frac{\partial k}{\partial x_i}\frac{\partial \omega}{\partial x_i}, 10^{-10}\right) \tag{3.21}$$

$$\alpha = \alpha_1 F_1 + \alpha_2(1 - F_1) \tag{3.22}$$

The eddy viscosity for this turbulence model is defined by Eq. (3.23). In this relation for the eddy viscosity, the second blending function, F_2, is present. This blending function is given by Eq. (3.24), where $a_1 = 0.31$.

$$\nu_T = \frac{a_1 k}{\max(a_1\omega, \|S\| F_2)} \tag{3.23}$$

$$F_2 = \tanh\left[\left[\max\left(\frac{2\sqrt{k}}{\beta^*\omega y}, \frac{500\nu}{y^2\omega}\right)\right]^2\right] \tag{3.24}$$

Table 3.3: The $k-\omega$ SST turbulence model α_1 constants.

β_1	γ_1	σ_{k1}	σ_{k2}
0.075	5.0	0.85	1.0

Table 3.4: The $k-\omega$ SST turbulence model α_2 constants.

β_2	γ_2	$\sigma_{\omega 1}$	$\sigma_{\omega 2}$
0.0828	0.44	0.5	0.856

3.3. Transition modelling

As was discussed in the literature review of Chapter 2, both Folkersma et al.[19] and Demkowicz [20], showed that transition phenomena affected the flow field around the LEI wing. As this study will perform a direct comparison to the results of Demkowicz, the simulations done in this study will also account for these phenomena through the use of a transition model.

The transition model used in this study is the $\gamma - \widetilde{\mathrm{Re}}_{\theta t}$ model developed by Langtry and Menter in 2009 [62]. It is a correlation-based transition model, as opposed to a phenomenological transition model. This means that rather than attempting to model the real physical transition phenomenon, the effect is accounted for through empirical correlations. These empirical correlations are developed through the use of experimental data for different geometries and flow conditions. In this way, an attempt was made to develop a model that can be used for many different geometries and flow conditions.

The $\gamma - \widetilde{\mathrm{Re}}_{\theta t}$ transition model adds two additional transport equations to the previously discussed $k-\omega$ SST turbulence model, however, there are also a few modifications to the turbulence model itself. Both the production and destruction terms of the turbulent kinetic energy transport equation are modified as shown in Eq. (3.25). In this transport equation, $\widetilde{P}_k$ represented the limited production term given by Eq. (3.26) and $\widetilde{D}_k$ the limited destruction term given by Eq. (3.27).

$$\overline{u}_j \frac{\partial k}{\partial x_j} = \widetilde{P}_k - \widetilde{D}_k + \frac{\partial}{\partial x_j}\left((\nu + \sigma_k \nu_t)\frac{\partial k}{\partial x_j}\right) \tag{3.25}$$

$$\widetilde{P}_k = \min\left(P_k, 10\beta^* k\omega\right)\gamma_{\text{eff}} \tag{3.26}$$

$$\widetilde{D}_k = \min\left(\max\left(\gamma_{\text{eff}}, 0.1\right), 1.0\right) D_k \tag{3.27}$$

The first additional transport equation is for the intermittency factor γ, which is given by Eq. (3.28). The intermittency factor represents a probability that, at a certain location, the flow is turbulent. A value of 1 means

that the region is fully turbulent and a value of 0 stands for a fully laminar region. In this transport equation, P_γ is defined as Eq. (3.29), in which there are two new functions introduced F_{length} and F_{onset}.

$$\overline{u}_j \frac{\partial \gamma}{\partial x_j} = P_\gamma - D_\gamma + \frac{\partial}{\partial x_j}\left[\left(\nu + \frac{\nu_t}{\sigma_f}\right)\frac{\partial \gamma}{\partial x_j}\right] \tag{3.28}$$

$$P_\gamma = F_{\text{length}}\, c_{a1}\rho S\left[\gamma F_{\text{onset}}\right]^{0.5}\left(1.0 - c_{e1}\gamma\right) \tag{3.29}$$

F_{length} is an extensive empirical correlation for which the relations be found in [62], it controls the length of the transition regions based on the value of $\widetilde{\text{Re}}_{\theta t}$. F_{onset} is a function through which the onset location of the transition is determined and given by Eq. (3.30). The additional included functions and relations are given by Eq. (3.31) to Eq. (3.34), for which the empirical relation for $\text{Re}_{\theta c}$ can be found in [62], which is again dependent on $\widetilde{\text{Re}}_{\theta t}$.

$$F_{\text{onset}} = \max\left(F_{\text{onset2}} - F_{\text{onset3}}, 0\right) \tag{3.30}$$

$$F_{\text{onset1}} = \frac{\text{Re}_\nu}{2.193\,\text{Re}_{\theta c}} \tag{3.31}$$

$$F_{\text{onset2}} = \min\left(\max\left(F_{\text{onset1}}, F_{\text{onset}}^4\right), 2.0\right) \tag{3.32}$$

$$F_{\text{onset3}} = \max\left(1 - \left(\frac{R_T}{2.5}\right)^3, 0\right) \tag{3.33}$$

$$\text{Re}_\nu = \frac{y^2 S}{\nu}, \quad \text{R}_T = \frac{\text{k}}{\nu\omega} \tag{3.34}$$

The destruction term D_γ in the transport equation of the intermittency factor is given by Eq. (3.35), where $\|\Omega\|$ represents the magnitude of vorticity. In order to disable the destruction of intermittency at locations outside of the viscous sublayer or the laminar boundary, the function F_{turb} is defined by Eq. (3.36).

$$D_\gamma = c_{a2}\|\Omega\|\gamma F_{\text{turb}}\left(c_{e2}\gamma - 1\right) \tag{3.35}$$

$$F_{\text{turb}} = e^{\left(-\frac{\text{R}_T}{4}\right)^4} \tag{3.36}$$

The second transport equation is for transition onset local momentum thickness Reynolds number $\widetilde{\text{Re}}_{\theta t}$ and given by Eq. (3.37). In this equation, the production term $P_{\theta t}$ is given by Eq. (3.38), where $t = \frac{500\nu}{U^2}$. The function $F_{\theta t}$ defined as Eq. (3.39), with the additional included functions given by Eq. (3.40) to Eq. (3.42). The model constants of the $\widetilde{\text{Re}}_{\theta t}$ transition model are given in Table 3.5.

$$\overline{u}_j \frac{\partial \widetilde{\text{Re}}_{\theta t}}{\partial x_j} = P_{\theta \text{t}} + \frac{\partial}{\partial x_j}\left[\sigma_{\theta t}\left(\nu + \nu_t\right)\frac{\partial \widetilde{\text{Re}}_{\theta t}}{\partial x_j}\right] \tag{3.37}$$

$$P_{\theta t} = \frac{c_{\theta t}}{t}\left(\text{Re}_{\theta t} - \widetilde{\text{Re}}_{\theta t}\right)\left(1.0 - F_{\theta t}\right) \tag{3.38}$$

$$F_{\theta t} = \min\left(\max\left(F_{\text{wake}} \cdot e^{-\left(\frac{y}{\delta}\right)^4}, 1.0 - \left(\frac{\gamma - 1/c_{e2}}{1.0 - 1/c_{e2}}\right)^2\right), 1.0\right) \tag{3.39}$$

$$F_{\text{wake}} = e^{-\left(\frac{\text{Re}_\omega}{10^5}\right)^2} \tag{3.40}$$

$$\text{Re}_\omega = \frac{\omega y^2}{\nu} \tag{3.41}$$

$$\delta = \frac{375\Omega y \nu \widetilde{\mathrm{Re}}_{\theta t}}{U^2} \tag{3.42}$$

Table 3.5: The $\gamma - \widetilde{\mathrm{Re}}_{\theta t}$ transition model constants.

c_{e1}	c_{a1}	c_{e2}	c_{a2}	σ_f	$c_{\theta t}$	$\sigma_{\theta t}$
1.0	2.0	50.0	0.06	1.0	1.0	2.0

As mentioned at the beginning of this section, the $\gamma - \widetilde{\mathrm{Re}}_{\theta t}$ transition model has been used by Folkersma et al.[19] and Demkowicz [20] for studies on LEI wings. In both cases, it showed the capability to capture important flow features such as laminar to turbulent transition, laminar separation bubbles and drag crisis. Folkersma validated the results against experimental sailwing data and this showed better agreement at low Reynolds numbers than simply using the $k-\omega$ SST turbulence model alone. Gaunaa et al.[48] used the same transition model, combined with an in-house developed solver, for 3D RANS simulations of a simple kite geometry. Unfortunately, the impact of the transition model on the results was not discussed in that study.

3.4. Discretisation

The equations that were derived and presented in the previous sections are continuous and will have to be broken down into discrete functions to employ a numerical method. This is done by subdividing the domain into several cells or nodes and defining the discretised equations at each of these locations. The three discretisation methods that are most commonly used for CFD simulations are finite element, finite difference and finite volume [84]. The discretisation method that has been used for the CFD simulations in this study is the finite volume method. The main advantages of finite volume discretisations are that they ensure both local and overall conservation of the quantities and that they can handle complex, unstructured geometries very well [85].

The main idea behind the finite volume method is to decompose the computational domain into several finite volumes or cells. Each of these volumes will then be treated as a control volume on its own. The mean values are computed for every control volume throughout the time-stepping. In order to evaluate the balance of the fluxes of the finite volume surface, it is necessary to approximate the fluxes over each of the surfaces. To approximate these fluxes, quadrature rules are used, which make use of discrete values along the surfaces. As each cell will have a centre associated with it, the values of the conserved quantities can be interpolated to get the discrete values along the cell surfaces. These approximations will introduce numerical errors into the solution. The truncation error artificially increases the numerical diffusion of the scheme. The finite volume schemes chosen in this study are presented and discussed in Section 4.4.2.

3.5. Solving the Navier-Stokes equations in OpenFOAM

This section will only discuss the algorithm through which the Navier-Stokes equations are solved using OpenFOAM. The overview of all the solver and algorithm settings is given in Section 4.4.2. Several numerical methods can be used to solve the Navier-Stokes equations, such as pressure-correction methods, project methods, density-based method and precondition solvers [86]. The pressure-based method used in this study solves the equations in a segregated manner, which means all equations are solved sequentially, in contrast to a coupled manner where all equations are solved simultaneously. Depending on the type of flow and application, OpenFOAM offers several tailored flow solvers.

The solver that has been used throughout this study is called `simpleFoam`, which is a steady-state, incompressible solver that makes use of the Semi-Implicit Method for Pressure Linked Equations (SIMPLE) [87] algorithm to solve the continuity and momentum equations. This algorithm was first introduced in 1972 by Patankar & Spalding [88]. OpenFOAM also offers the usage of the slightly modified Semi-Implicit Method for Pressure Linked Equations-Consistent (SIMPLEC) algorithm. This version of the algorithm was introduced by Van Doornmaal and Raithby in 1984 [89]. In general, the setup of the algorithm is the same between SIMPLE and SIMPLEC. The differences lie in several derivation steps for the pressure equation, which results in SIMPLEC not needing under-relaxation on the pressure correction term. This will usually lead to faster con-

vergence. The SIMPLE algorithm in OpenFOAM consists of the following steps per iteration (as reproduced from [90]):

1. Advance to the next iteration $t = t^{n+1}$
2. Initialise $\mathbf{u}^{n+1}$ and p^{n+1} using latest available values of $\mathbf{u}$ and p
3. Construct the momentum equations
4. Under-relax the momentum matrix
5. Solve the momentum equations to obtain a prediction for $\mathbf{u}^{n+1}$
6. Construct the pressure equation
7. Solve the pressure equation for p^{n+1}
8. Correct the flux for ϕ^{n+1}
9. Under-relax p^{n+1}
10. Correct the velocity for $\mathbf{u}^{n+1}$
11. If not converged, go back to step 2

When this loop has converged to chosen tolerances, the transport equations for the turbulence and transition model are solved. Usually, multiple pressure corrections are done within one SIMPLE loop, this means repeating steps 6 to 9 multiple times before moving on. This is done as a stabilising step for meshes that have highly non-orthogonal cells.

4

Pre-processing and simulation setup

In this chapter, all the taken pre-processing steps will be discussed and the numerical simulation setup is presented. This starts with the design of the CAD model in Section 4.1. Following this, the meshing approach, mesh quality metrics and the final volume mesh itself are discussed in Section 4.2. The results of an extensive mesh convergence study will be discussed in Section 4.3. Lastly, the simulation setup and convergence monitoring is discussed in Section 4.4.

4.1. CAD Model

The CAD model will form the basis of the geometry that is used for mesh generation. When designing the model, it is important to keep this meshing step in mind, because otherwise mesh generation becomes a difficult task. It is best to prepare the CAD geometry in such a way that during the meshing stage, no geometrical alterations have to be done. In practice, this is not a sequential process, but rather an iterative process. Over several iterations, the CAD model is designed in such a way that the highest quality mesh can be achieved.

Since there was a CAD model for the LEI wing geometry without struts made by Demkowicz [20], this was used as a starting point for further development. A brief overview of the choices and steps made by Demkowicz will be discussed here. This is done to justify some of the different choices made in the approach of the current study compared to Demkowicz's study. While the final geometry was designed using Rhinoceros, the original LEI wing was designed in SurfPlan, which is an industry design tool for kites and LEI wings. A multitude of simplifications were made to develop a CAD geometry that was deemed simple enough to be meshed. The most important simplification was the removal of the struts. Doing this enabled Demkowicz to use Rhinoceros, as the whole geometry could be designed using a set of simple splines to define surfaces. For such an application, Rhinoceros is a very powerful tool. However, when more complex geometries are concerned, parameterisation becomes a necessity. Parameterisation was important for the current study as many iterations were done between the meshing and CAD software to get the design right. Without parameterisation, this would mean redesigning larger parts of the geometry every time a change was made. Therefore, the CAD model was imported into CATIA for further design and development.

A comparison between the lower surface of the CAD model used in the study by Demkowicz [20] and the current study is shown in Fig. 4.1. As can be seen, for the full LEI wing, a total of eight struts have been included in the geometry. The most important steps and design choices made to aid the meshing process are as follows:

- The struts were recreated using circular cross-sections
- A modular fillet has been formed between the struts and the surface of the wing
- The rear of the struts has been capped, i.e. closed off
- The main upper surface, excluding the tip surfaces, has been split up into eight surfaces

- The lower surfaces in between the struts have been split up into several surfaces

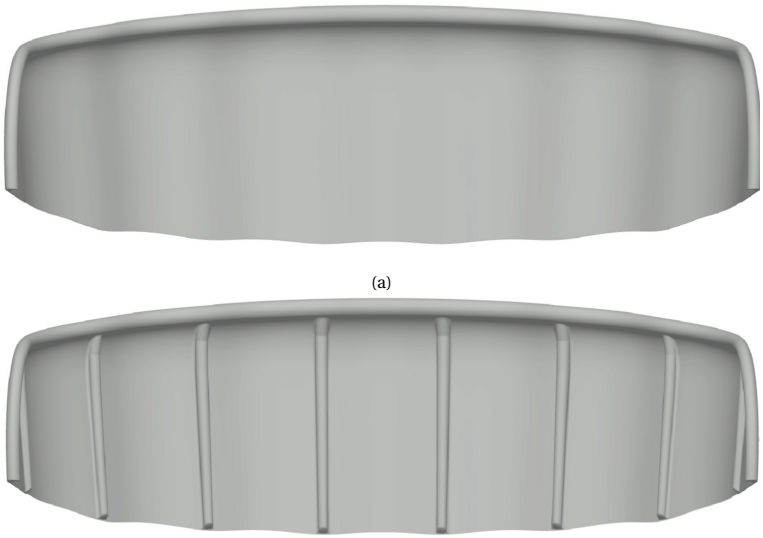

(a)

(b)

Figure 4.1: Lower side of the CAD geometry used in the study by Demkowicz [20] (a) and the current study (b).

These adjustments were done for several reasons. First, the geometry of the struts that were imported came from SurfPlan. This meant that the struts were not build up out of circular cross-sections, but rather polyline cross-sections. If no adjustments were made to this, then the result would have been non-smooth struts, which is not beneficial for mesh generation. Second, in reality, the struts have a sharp intersection/attachment to the main canopy surface. However, for meshing software, it is very challenging, if not impossible, to deal with such acute angles. Therefore, a fillet was formed around all the struts to turn this acute angle into a smooth radius curve. By doing so, the meshing process becomes more manageable since the intersection of extruded cells is less of an issue. A close up of this implementation can be seen in Fig. 4.2. Third, the struts of the SurfPlan geometry were open at the trailing edges. These trailing edges have been closed off to ensure no mesh cells were grown on the inside of the struts. The implementation of this is shown in Fig. 4.3.

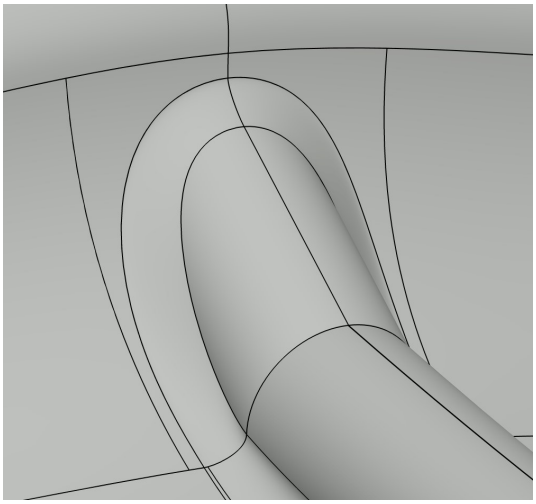

Figure 4.2: Integration of a strut with the wing surface around the leading edge.

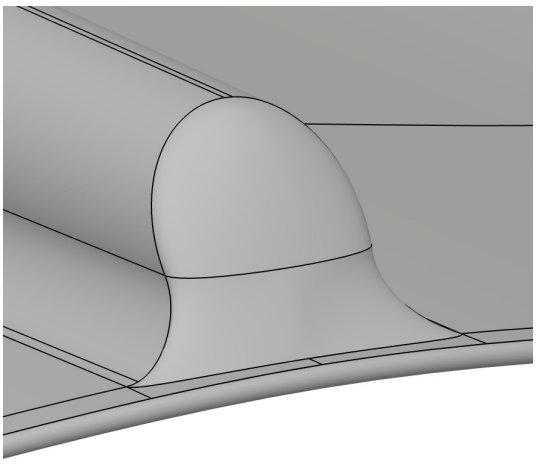

Figure 4.3: Closed off trailing edge section of a strut.

Last, after several iterations between Pointwise and CATIA, the basis for the mesh topology was made in CAD by subdividing the surfaces into several sections. This mesh topology is fundamentally different than the

approach that was taken by Demwkowicz [20]. Due to the increased complexity by adding the struts, it was initially not possible to use large structured surfaces. For reasons that will be explained in Section 4.2, it is preferable to have structured surfaces for higher mesh quality where possible. However, without subdividing the surfaces, the majority of the surface mesh would have been unstructured. Thus, this subdivision enabled the use of structured surfaces and meant unstructured surface meshing was only applied in regions where it was really a necessity. The upper side and lower side of the final LEI wing CAD geometry, with all surface edges visible, can be seen in Fig. 4.4.

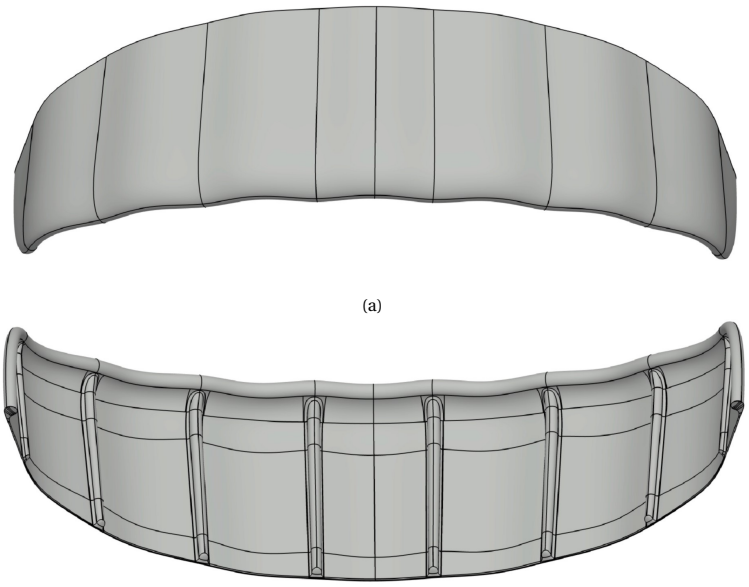

(a)

(b)

Figure 4.4: The upper side (a) and lower side (b) of the final CAD geometry with all surface edges visible.

4.2. Meshing

This section will discuss the steps and decisions taken to generate the final volume mesh. First, the meshing software Pointwise will briefly be discussed in Section 4.2.1. After this, the surface mesh topology and challenging areas will be highlighted in Section 4.2.2. The used volume mesh quality criteria are presented in Section 4.2.3. Last, a detailed overview of the volume mesh generation process and the final settings is given in Section 4.2.4.

4.2.1. Pointwise meshing software

While many different commercial and open source meshing software packages exist, the choice for Pointwise was based on two principles. First, the meshing of LEI wings has been a challenge in the past with, for example, an attempt by Deaves [35] leading to insufficient mesh quality and instability during solving. The direct predecessor of this study was done by Demkowicz [20], which managed to get mesh quality to a higher level in Pointwise. Given these previous challenges, there is a large risk associated with switching from one meshing software package to another. While a comparative study between several meshing software packages could have been done, the risk was that one ends up reinventing the wheel for the same application. Since the time frame of a master thesis is limited, it was therefore decided to use the same meshing software package used in the previously successful attempt in [20].

However, the choice for Pointwise can also be justified by the meshing capabilities it offers. When complex curved geometries such as a LEI wing are involved, the usage of a fully structured domain becomes difficult to implement. While it might be possible to generate a structured meshing topology, it often involves the usage of complex and time-consuming meshing strategies. It was shown by Morgut et al.[91], that for assessing the general performance of a geometry, a hybrid meshing approach is often just as good while being much easier to construct. Some of the benefits offered by structured meshing lie in the fact they offer

the highest level of quality and control (when implemented right), have better flow alignment, which should lead to better convergence and require less memory and time to solve compared to unstructured grids [92]. To still reap the benefits of a flow aligned mesh in the near-surface region, a hybrid meshing approach has been employed in this study. In hybrid meshing, the near-wall region is meshed with flow aligned structured hexahedrals, whereas further away from the surface the grid transitions to an unstructured grid. The hybrid meshing approach that is used in this study is the highly automated 3D anisotropic tetrahedral extrusion technique developed by Pointwise, also known under the shorter name T-Rex [93]. For the volume mesh, this starts with the placement of pyramids on the quadrilateral cells of the surface mesh. The height of this first pyramid is specific through the wall spacing. On top of this pyramid, four side pyramids are added to form one hexahedral cell. Then for all layers after the first one, there are 12 anisotropic tetrahedrons, which are combined into four prisms, which then merge into one hexahedral cells. In this way, the volume mesh can be extruded from the surface mesh. The strength of using the algorithm lies in the fact that it enables the user to generate high-quality, high aspect ratio, flow aligned hexahedral cells off the surface. These will then automatically transition to unstructured tetrahedrons once certain stopping criteria are reached.

4.2.2. Surface mesh

Before the volume mesh can be extruded, a high-quality surface mesh needs to be generated. In Pointwise, this surface mesh can consist of a combination of structured and unstructured surfaces. For the unstructured regions, a 2D version of the T-Rex algorithm can be used. To get the highest quality surface mesh possible, the final mesh topology is as shown in Fig. 4.5. As can be seen, the majority of the LEI wing surface mesh consists of structured surfaces, only the tip region, rear and front of the struts needed to be meshed unstructured. This mesh topology has been chosen such that the surface mesh is as uniform as possible. Using a fully unstructured surface mesh was possible, but this would lead to a lower overall mesh quality due to a loss of control over the final meshing result.

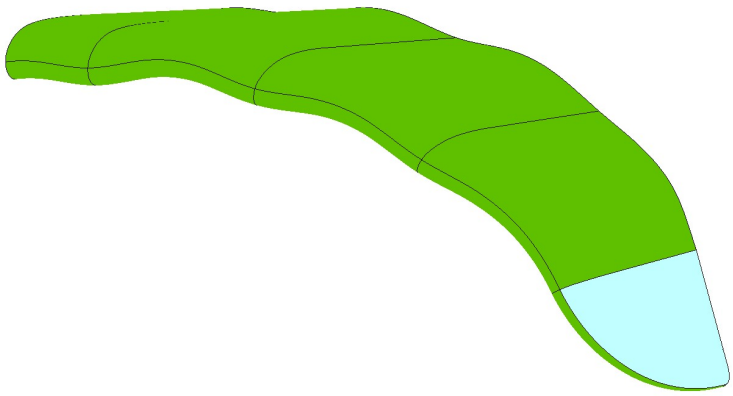

(a)

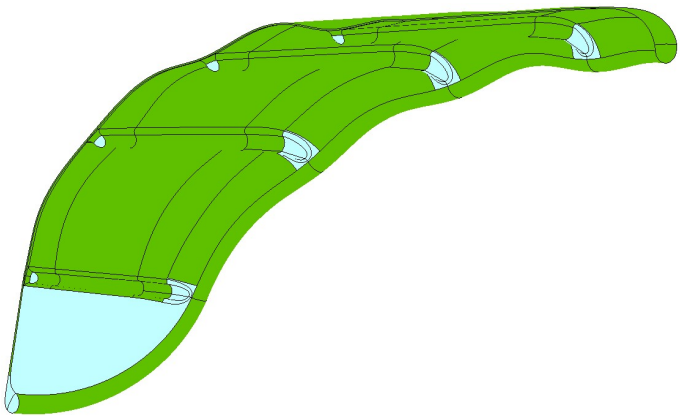

(b)

Figure 4.5: Upper side (a) and lower side (b) of the final surface mesh topology (green indicates structured surfaces and blue indicates unstructured surfaces).

In Pointwise, these surfaces mesh areas are called domains and each domain can have independent settings, which will influence how the volume mesh is extruded from the surface. It is a bottom-up approach meshing software, which means that it starts with defining the geometry from points and edges, these edges will form faces and these faces are combined to create volumes [94]. When the CAD surface is imported into Pointwise, the first step is to scale the model in such a way that the reference chord length at the symmetry plane represents one unit. This is done by scaling the geometry by $1/c_{ref}$, where $c_{ref} = 2.6m$. Having a length scale of unity simplifies the boundary condition setup later on. After this, one has to define connectors along all the edges in the geometry. These connectors consist of nodes, and the distribution of nodes can be influenced in several ways. It is the number of nodes along these connectors which determines how refined a domain will be. For structured domains, these nodes on opposite edges should be balanced, however, for unstructured domains, this does not have to be the case. An overview of the most challenging unstructured areas of the surface mesh is given in Fig. 4.6. In this figure, the connectors and their respective nodes are shown in blue. It can be seen that the surface mesh is quad-dominant. This is natural for the structured regions, but also the unstructured regions are made quad-dominant. This is through the use of the 2D T-Rex algorithm which has an option 'Advancing Front Ortho'. What this will do is rather than using triangles, as per normal unstructured surface meshing, it will create quad-dominant orthogonal fronts which are marched to the inner point of the domain. Only where these fronts meet the algorithm will form triangular cells to ensure a smooth merging of the fronts. This enables the user to create an unstructured surface mesh while maintaining some of the benefits of structured orthogonal meshing. Along the connectors of these domains, it is possible to define so-called boundary conditions. These boundary conditions can enforce a certain cell spacing height to ensure a smooth transition with other domains.

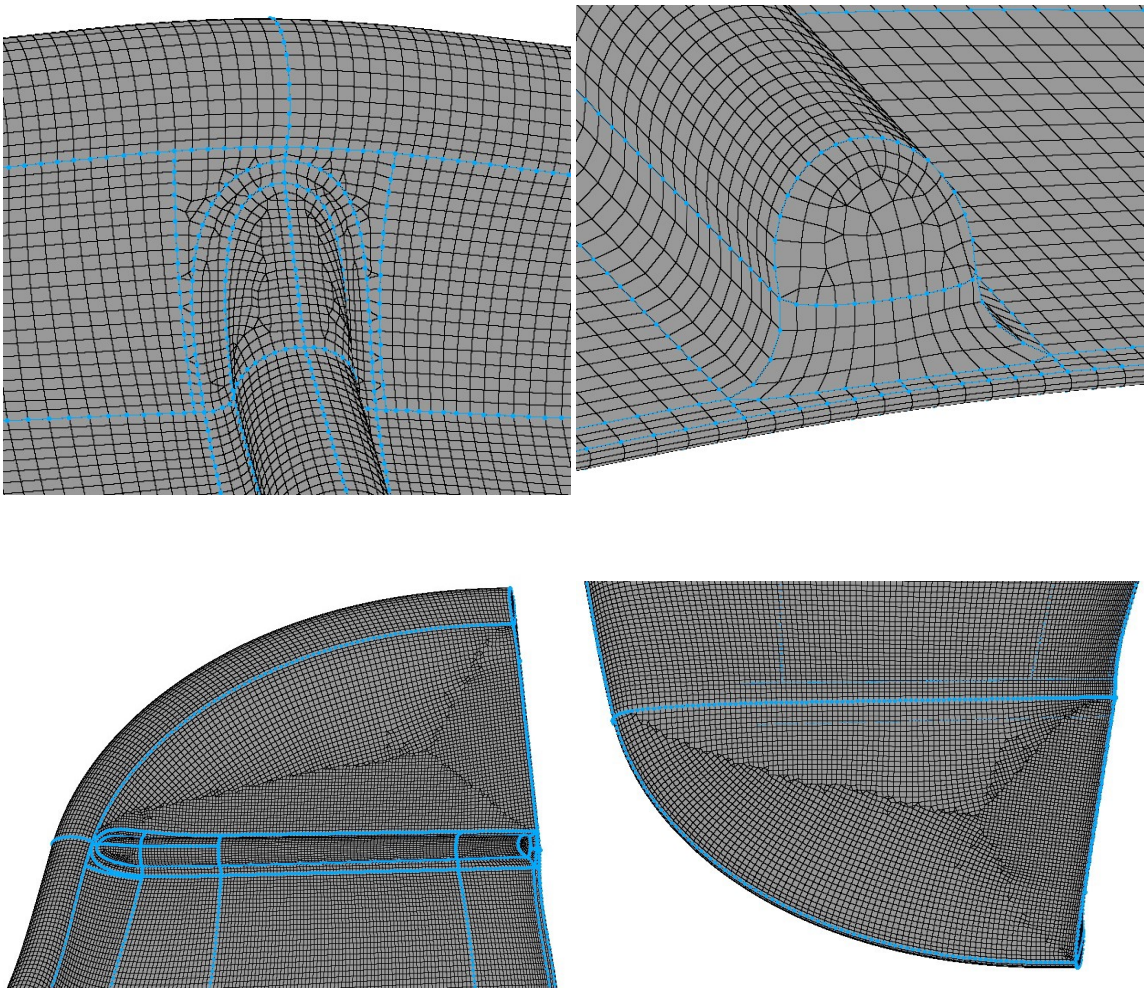

Figure 4.6: Close-ups of several unstructured surface mesh regions.

When designing this surface mesh topology, there were several surface mesh quality variables monitored such as area ratio, maximum included angle and skewness equiangle. While Pointwise does not give hard set limits and these variables, they do provide some guidelines. The area ratio is a measure of the maximum area ratio the cell shares with any of the adjacent cells. Pointwise states that a quad-dominant surface mesh with area ratios of eight to ten will still result in a high-quality volume mesh [95]. The maximum area ratio of the surface mesh was measured to be 7.57. The maximum included angle and skewness equiangle are both a measure of skewness. They are both relevant variables for the surface and volume mesh. For the surface mesh, the maximum included angle was measured to be 158, whereas for the skewness equiangle the maximum was 0.8. Pointwise indicates that it is recommended to keep the skewness equiangle below 0.8, but that depending on the solver, values of 0.9 are also acceptable [96]. An overview of the upper and lower side of the final surface mesh can be seen in Fig. 4.7. This clearly shows that the surface mesh is quad-dominant and very uniform around the majority of the geometry.

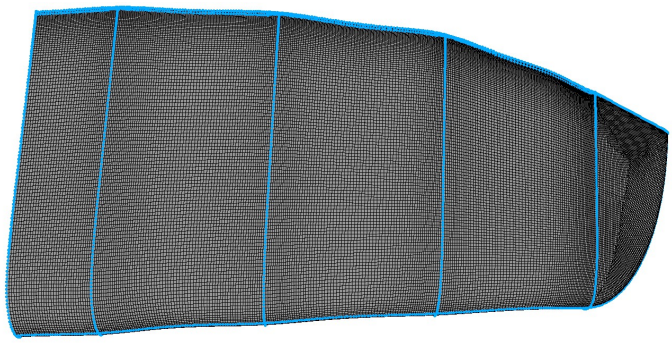

(a)

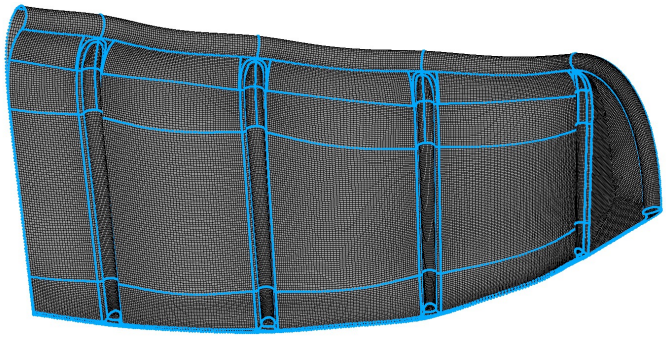

(b)

Figure 4.7: Upper side (a) and lower side (b) of the final surface mesh.

4.2.3. Volume mesh quality criteria

While the surface mesh is of high-quality up to Pointwise's standards, this does not automatically imply a good volume mesh as a result. The complex nature of the geometry presented some challenges for the volume mesh extrusion. While ideally all of the volume mesh keeps within the bounds of what is considered high-quality, in practice this was not possible. It was therefore not the focus to completely get rid of certain lower quality cells, but rather to reduce their occurrence to a minimum. This also meant sometimes making compromises in one region, which then might introduce a few lower quality volume cells somewhere, but lead to an overall reduction in the amount of lower quality volume cells.

To ensure a high-quality volume mesh and good stability and convergence when solving, several ideal targets were set. These targets were to keep:

- The number of severely orthogonal cells (> 70°) to a minimum
- The skewness of volume cells to a minimum (< 0.8 for skewness equiangle and skewness centroid)
- The volume ratios below 15

- The maximum included angle below 165°
- The aspect ratio of boundary layer cells in the order of 10^3

Non-orthogonal cells are a big contributor to errors in the solutions obtained by using the OpenFOAM solver [97]. The non-orthogonality angle will be zero when cells are perfect rectangles growing from a non-curved surface, such as a flat plate. However, a non-zero non-orthogonality angle forms when a cell is slightly skewed as shown in Fig. 4.8. The non-orthogonality angle is calculated by taking the angle between the vector perpendicular to the face shared by the cells and the vector connecting the centroids. When a cell is severely orthogonal, this angle will exceed 70 °. This misalignment can lead to a substantial error when a dot product of the gradient with the shared cell face is calculated. This predominantly shows itself for the diffusive terms in the Navier-Stokes equations [97].

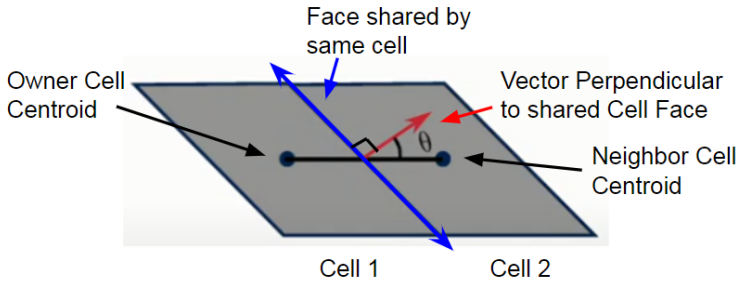

Figure 4.8: Example of the non-orthogonality angle definition between two cells [98].

A second contributor to errors in the solutions obtained through the usage of the OpenFOAM solver is the skewness of cells. The skewness is a direct result of the difference between the actual centre of the shared face and the intersection point of the cell centre vector with the shared face. High skewness causes numerical diffusion and it is most important for the computation of the convective derivatives. In Pointwise, there are several quality metrics which compute a measure of skewness in different ways. The three metrics that will be used in this study are equiangle skewness, centroid skewness and maximum included angle. The equiangle skewness takes the maximum ratio between the included angle of a cell and the angle of an equilateral element [96]. The centroid skewness is determined by subtracting the minimum dot product of the vector perpendicular to the cell face and the vector connecting the cell faces from 1 [99]. However, also the maximum included angle refers in a way to the skewness of a cell and is, therefore, taken into consideration. There are two reasons for considering multiple skewness measures. First, skewness is an important quality metric for solution stability and accuracy. Second, all metrics will deviate from each other, therefore, solely focusing on one might be too limited.

The maximum volume ratio of a cell is calculated by taking the maximum ratio with respect to the adjacent cells. High volume ratios can lead to interpolation errors which hamper both stability and accuracy [100]. The upper limit has been set based on comparisons in terms of residual and force convergence to Demkowicz's study [20]. This showed that increasing the maximum volume ratio from the previously set 10 to 15 did not introduce more instability or changes in force coefficients. A higher aspect ratio of the cells near the wall is necessary to accurately resolve the velocity gradient of the boundary layer near the wall. Again, there is no hard-set rule on what the aspect ratio of boundary layer cells should be as it is fully application dependent. The previous study by Demkowicz [20] showed that having the aspect ratio of boundary layer cells in the order of 10^3 resulted in an adequate resolution. Since the same computational approach and models will be used, it has been decided to aim for a similar range of aspect ratios near the wall.

4.2.4. Volume mesh

The Pointwise software offers the capability to examine the volume mesh quality based on several quality metrics. This capability has been utilised throughout the meshing process to constantly improve the quality of the final volume mesh. As has been shown in Section 4.1, the CAD model was divided into several surfaces to aid the meshing process. This was done based on analysing the quality of the volume mesh extrusion and targeting low-quality areas accordingly.

After the surface mesh was made, the half-domain volume mesh was generated first. Since part of the research will focus on flow conditions with zero sideslip angle, it is not necessary to use the full LEI wing geometry for all cases. The farfield was generated using a hemisphere with a radius of approximately 84 chord lengths. This farfield and the symmetry plane were the outer boundaries and the LEI wing geometry the inner boundary of the volume mesh. Generating the volume mesh was done using the 3D T-Rex algorithm, for which several mesh parameters have been tweaked to achieve the highest mesh quality. The T-Rex algorithm extrudes hexahedral cell fronts off the surface of the LEI wing into the volume, called a block in Pointwise. The extrusion will be terminated once either isotropy is reached, the cells fronts collide or one of the generated volume cells is below the set quality metrics. Once one of these criteria is met, the meshing algorithm will start generating tetrahedral cells in the remainder of the block. Having the algorithm stop extruding hexahedral cells in one location does not mean it automatically stops everywhere. An extrusion front can locally stop, whereas at other areas around the LEI wing the hexahedral cell extrusion continues. For the full-domain cases, which are needed for non-zero sideslip angle simulations, no symmetry plane was required and the domain was made up of a full sphere. The way Pointwise handles the symmetry plane for the half-domain case has shown that the algorithm does have its problems. These problems will be discussed later.

Much of the T-Rex algorithm is automated, but there are still several settings through which the user can influence the final mesh. This is through layer settings, cell types, advanced settings, skew criteria and smoothing. Starting with the layers where the max layers, full layers, and growth rate have to be set. The max layers represents the maximum amount of hexahedral cell layers that will be extruded off the surface. If the cells have not reached isotropy yet by the given layer, the extrusion front is automatically terminated. Full layers forces a minimum number of layers to be extruded, regardless of the criteria that are set. Pointwise has often difficulties with extrusion in the vicinity of the symmetry plane and this meant that this value could not be set to zero. The growth rate has a strong influence on the resolution of the boundary layer profile and extruded mesh topology. The cell type option has been set to 'All: Tets, Pyramids, Prisms and Hexes', which meant that the final mesh is allowed to consist of all these different types of cells.

The advanced settings are isotropic seed layers, collision buffer, aniso-iso blend and isotropic height. The isotropic seed layer influences the creation of layers of seed points in regions where the extrusion fronts have stopped before reaching isotropy due to violation of one of the quality criteria or layer settings. The additional seeding of points will still be terminated once isotropy in the seeding areas is reached. The setting ranges from 0 (no additional seeding) to 1 (maximum additional seeding), the difference between the two can be seen in Fig. 4.9.

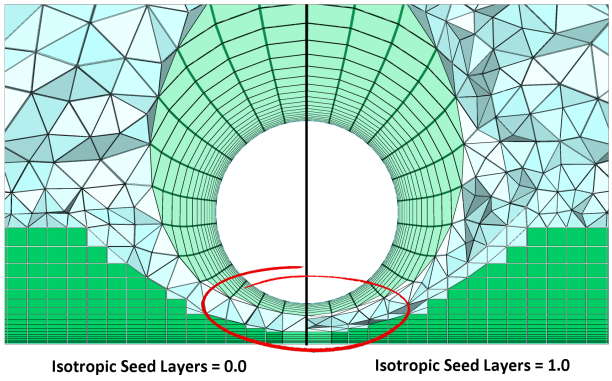

Figure 4.9: The effect of the isotropic seed layer setting [93].

The second advanced setting is the collision buffer, which defines how much of a buffer should be maintained between two fronts that grow into each others direction. It is expressed as a factor of the local cell size and should be a non-negative value. An example of the influence this has on the volume mesh is shown in Fig. 4.10.

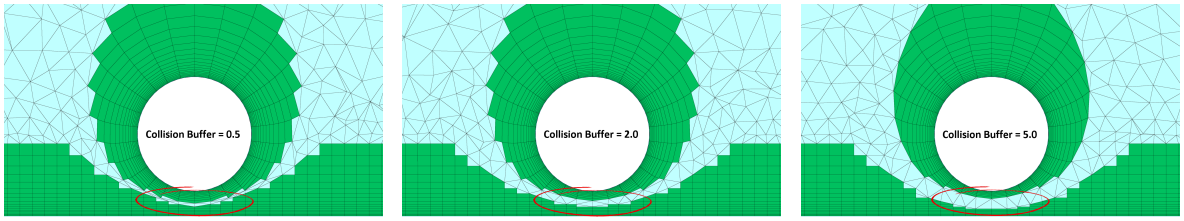

Figure 4.10: The effect of the collision buffer value on local volume mesh growth [93].

The aniso-iso blend determines the rate at which the anisotropic extruded T-Rex cells blend into isotropic cells. The blend works through locally decimating the extruded T-Rex cells while the algorithm progresses. A value of 0 means that no blending will be enforced and a value of 1 means maximum blending. The effect this has on the volume mesh is shown in Fig. 4.11, where it can be seen that isotropic cells (in yellow and blue) are grown in the areas within the anisotropic fronts (in green).

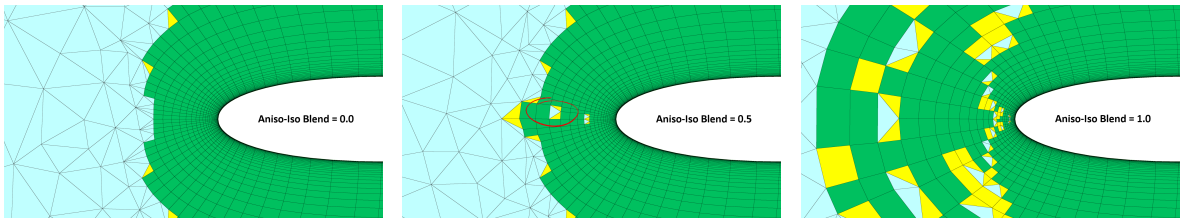

Figure 4.11: The influence of aniso-iso blend settings on extrusion of hexahedral cells [93].

The T-Rex algorithm offers the possibility to set upper limits on the values of certain skew criteria. While this sounds useful in theory, it was found that in practice this often leads to a lower quality mesh. Some areas are inherently of lower quality, which exacerbated when limitations were set on the skew criteria. Therefore, it was decided to not impose hard upper limits on these criteria, i.e. set them to 1. The final parameters settings of the T-Rex algorithm are shown in Table 4.1.

Table 4.1: Final T-Rex algorithm parameter settings.

Parameter	Value
Max. Layers	100
Full Layers	5.0
Growth Rate	1.15
Isotropic Seed Layers	0.0
Collision Buffer	0.8
Aniso-Iso Blend	0.0
Isotropic Height	1.2
Max. Angle	170°
Equi-volume, Equi-Angle and Centroid Skewness	1.0

Now considering the final volume mesh, starting with a mesh slice in the vicinity of the symmetry plane in Fig. 4.12. From this image, it can be seen that there is a very uniform extrusion of hexahedral cells originating from the surface of the LEI wing. Two areas of interest are the region behind the leading edge on the lower side of the wing and the trailing edge. It can be seen that in these two areas, the hexahedral cell fronts do not advance as far into the volume as in other regions. This can be explained by the fact that to deal with the curvatures in these regions, the surface mesh cell size is smaller here. Having smaller surface mesh cells influences the 3D T-Rex extrusion algorithm, as it will reach isotropy earlier. When isotropy is reached for the hexahedral cell front, the algorithm will automatically transition to tetrahedral cells. Furthermore, it can be

seen that the tetrahedra cells around the wing, expect for the transition region from structured to unstructured, have the same size. This is by design and achieved through volumetric mesh refinements which will be discussed in Section 4.3. In Fig. 4.13, the mesh topology around the whole LEI wing can be observed. Overall, the distribution of hexahedral layers around the wing looks uniform and it follows the shape of the wing including the struts very well. Different tetrahedral cell size regions can be observed, which will be discussed in further detail later on in Section 4.3.

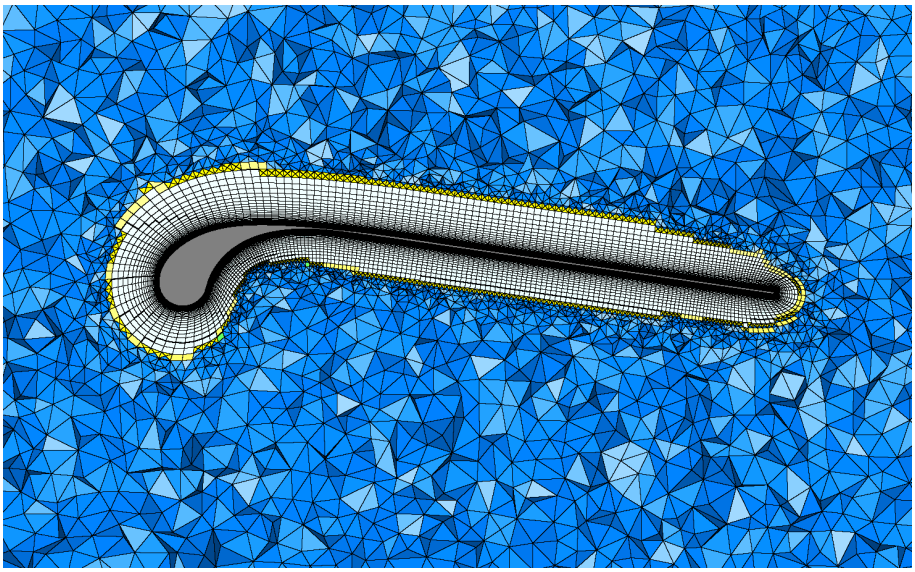

Figure 4.12: Volume mesh slice near the symmetry plane.

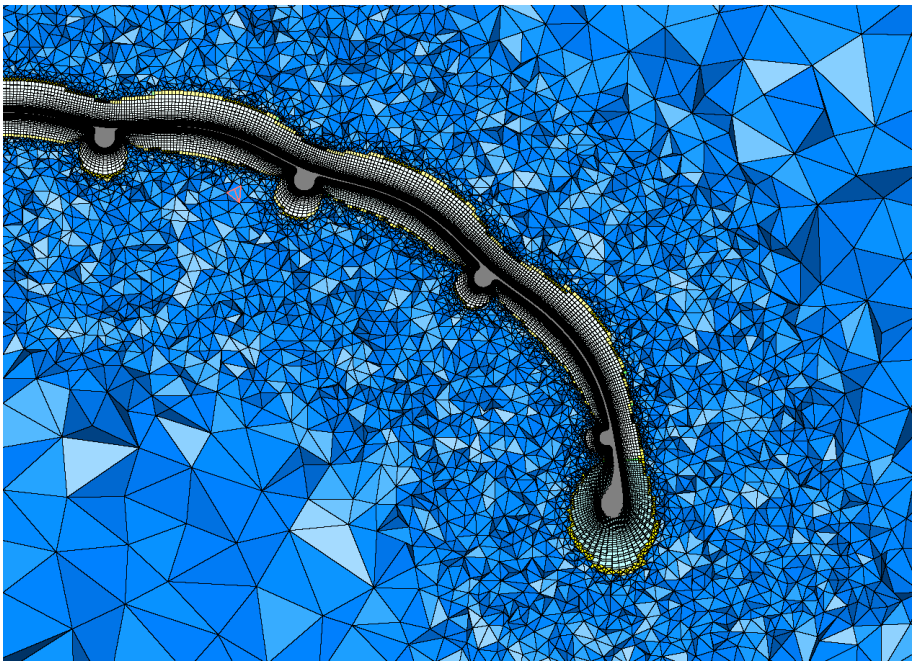

Figure 4.13: Volume mesh slice at x = 0.3.

While the above figures gave a good overview of the general mesh topology, there are several regions of interest that can use some further discussion. Starting with a close-up of a slice through the mesh around a strut in Fig. 4.14. In this figure, one can see the effect of the fillet between the surface of the LEI wing and the strut. Due to the introduced fillet, it is possible to extrude the flow aligned hexahedral cells all around the struts, in

a very uniform way. Without the introduced fillet, the cell fronts extruded from the strut and the main surface of the wing would clash almost instantly and extrusion would be locally terminated. A mesh slice over a strut in the leading edge area is shown in Fig. 4.15. Around the circular leading edge, the hexahedral cell fronts advance the furthest into the volume. This is due to the fact that the surface mesh cells are larger around the leading edge, which results in isotropy being reached later. The opposite is true for the area behind the leading edge over the front part of the strut. In order to properly resolve the geometry in this area, a much smaller surface mesh size was needed. This resulted in the hexahedral fronts reaching isotropy earlier. However, the mesh convergence study of Section 4.3 will show that this does not impact the results. In Fig. 4.16, the same slice is shown, but then a close-up at the rear of a strut. This highlights the fact that even over the rear of the struts, which has an unstructured surface mesh, the hexahedral cell extrusion is very consistent and uniform. Last, the extrusion around the tip region is shown in Fig. 4.17. This is a fairly complex area with a strut and several unstructured surface mesh fronts meeting. Despite this, the hexahedral extrusion is very consistent and uniform.

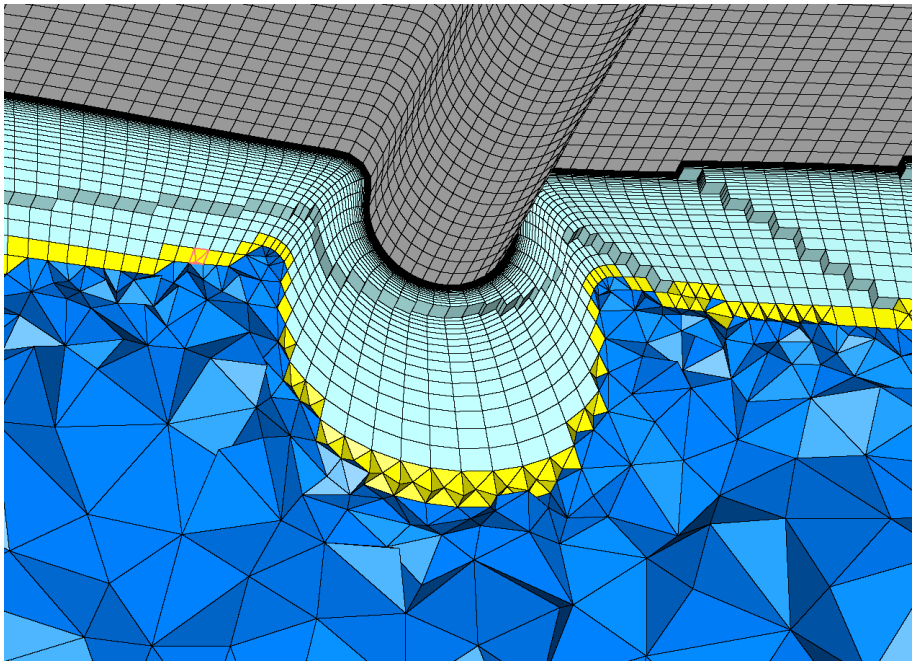

Figure 4.14: Volume mesh slice in the spanwise direction of a strut.

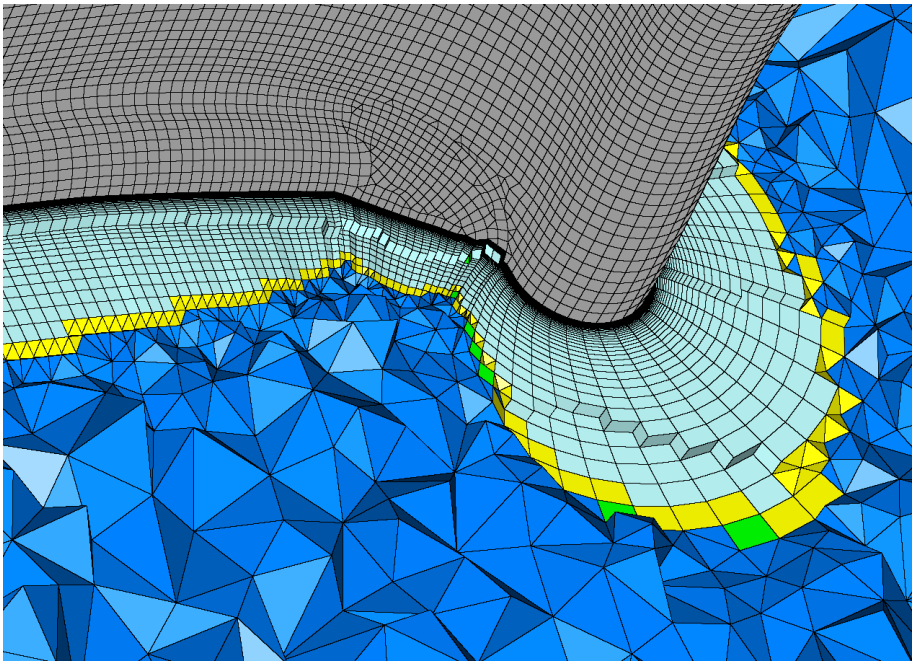

Figure 4.15: Volume mesh slice in the chordwise direction at the front of a strut.

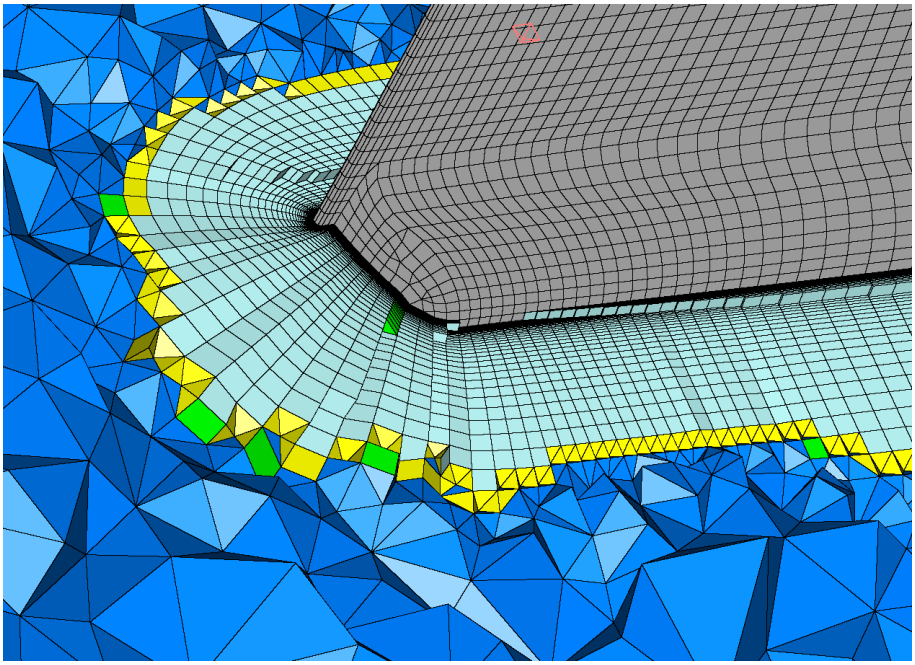

Figure 4.16: Volume mesh slice in the chordwise direction at the rear of a strut.

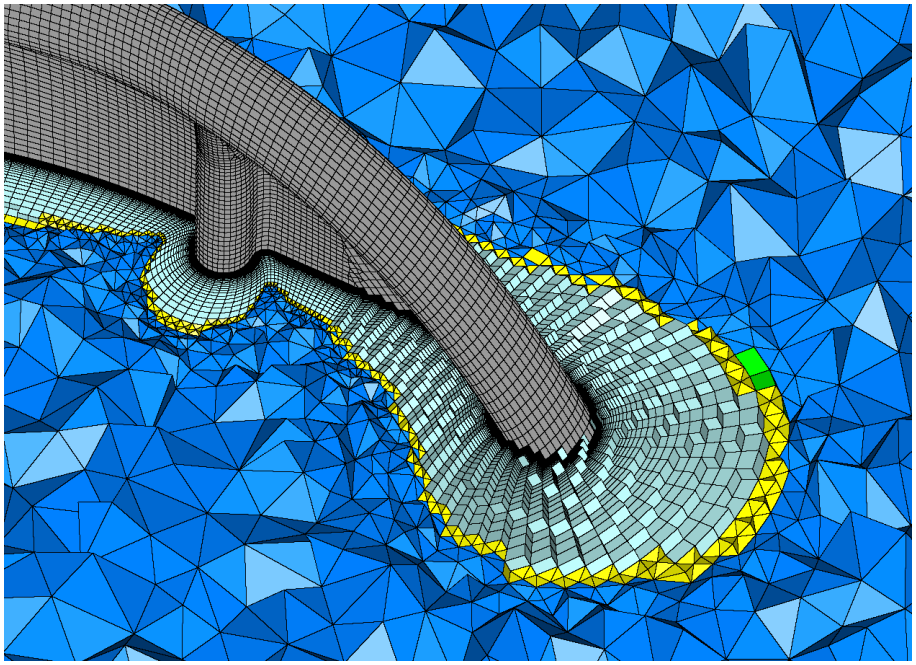

Figure 4.17: Volume mesh slice in the tip region.

In Fig. 4.18, a few of the mesh quality metrics are presented as histograms. The aim for the cell non-orthogonality was to keep the number of cells that were highly non-orthogonal (> 70°) to a minimum. As can be seen, there are quite some highly orthogonal cells, but this was also observed by Demkowicz [20]. Demkowicz showed that very close to the surface, there were many highly non-orthogonal cells. Upon consultation with Pointwise, it was concluded that this was due to some steps within the T-Rex algorithm and would always occur in high aspect ratio cells near the surface. When inspecting the mesh of the current study, it clearly showed that most of the highly non-orthogonal cells were close to the surface, which can be seen in Fig. 4.19. Demkowicz [20] tested two different meshes with different first cell heights. One very small first cell height, which had many non-orthogonal cells near the surface, and one with a larger first cell height, which did not have a lot of non-orthogonal cells near the surface. Through this analysis, he showed that these cells near the surface of the wing that were flagged as highly non-orthogonal did not negatively impact the results. The distribution of cell non-orthogonality in the histogram shows that most of the cells have a low non-orthogonality angle, with the average around 16°. Second, the cell skewness equiangle, which shows that in essence, the mesh quality is much higher than the cell non-orthogonality portrays. On the total cell count of 8.1 million, only 545 cells exceed the set upper bound target of 0.8. The histogram shows that the majority of the cells have very low skewness equiangle, with the average around 0.22. Third, the volume ratio. The target for the volume ratio was to keep the cells that have a higher volume ratio than 15 to a minimum. As can be seen, only 36 cells have a higher volume ratio than 15. Again, considering the total amount of cells in the mesh, this is a satisfactory result. Most of the cells have a very lower volume ratio, with the average around 1.3. The last mesh quality metric to be considered is the maximum included angle. The target was to keep cells with a maximum included angle higher than 165° to a minimum. Only 50 cells have failed to meet this target. On average, cells have a maximum included angle very close to 100°. Based on these mesh quality metrics, it can be concluded that even for such a complex and challenging geometry a good overall mesh quality has been achieved.

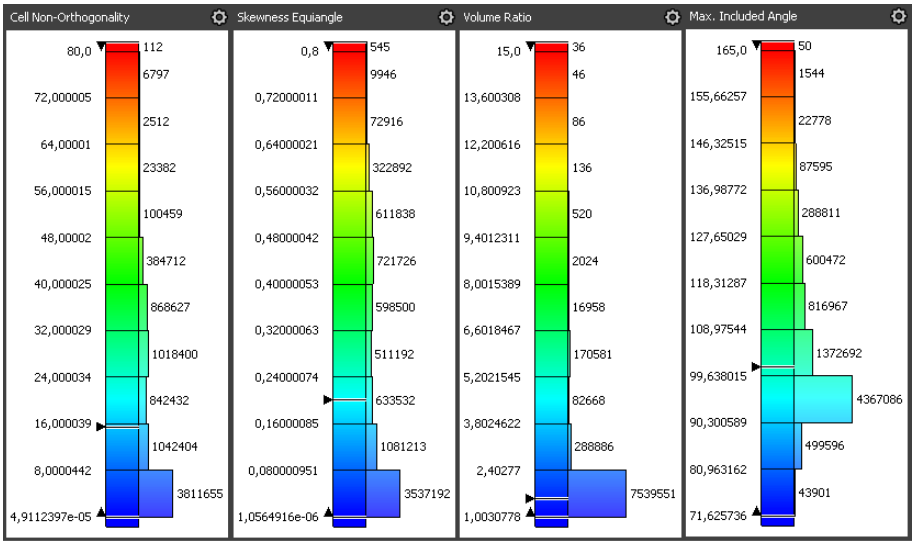

Figure 4.18: Volume mesh quality metrics.

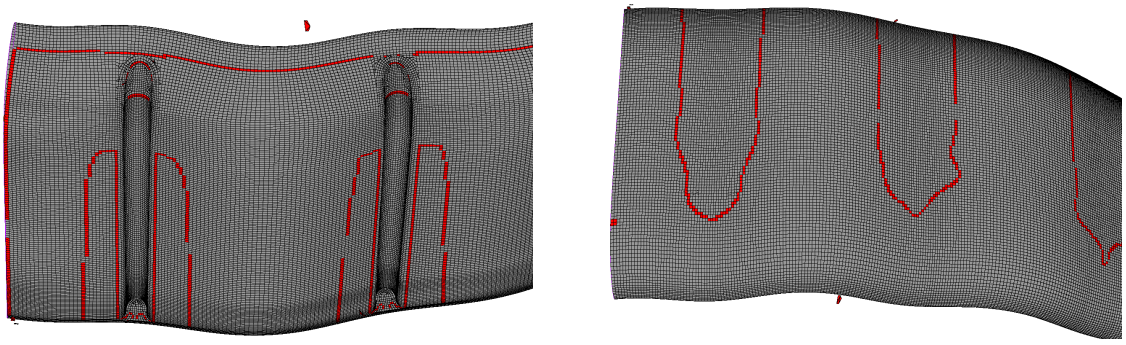

(a) (b)

Figure 4.19: Cell non-orthogonality for part of the lower surface (a) and the upper surface (b) where red cells indicate non-orthogonality angle > 70°.

As mentioned before, the Pointwise algorithm sometimes has difficulties with growing the hexahedral cells adjacent to the symmetry plane. Several attempts have been made to completely mitigate this, but it is simply a reoccurring problem and something that was also noted by Demkowicz [20]. To illustrate what is meant by this, a mesh slice of the half domain case and full-domain case are shown in Fig. 4.20. From this, it can be clearly seen that in the full-domain mesh, there is no issue with the layers collapsing at the centre section of the LEI wing. On the half-domain image, the symmetry plane is on the left side. This shows that the issue is not something with the quality of the surface mesh, but purely how Pointwise's algorithm deals with the symmetry plane boundary.

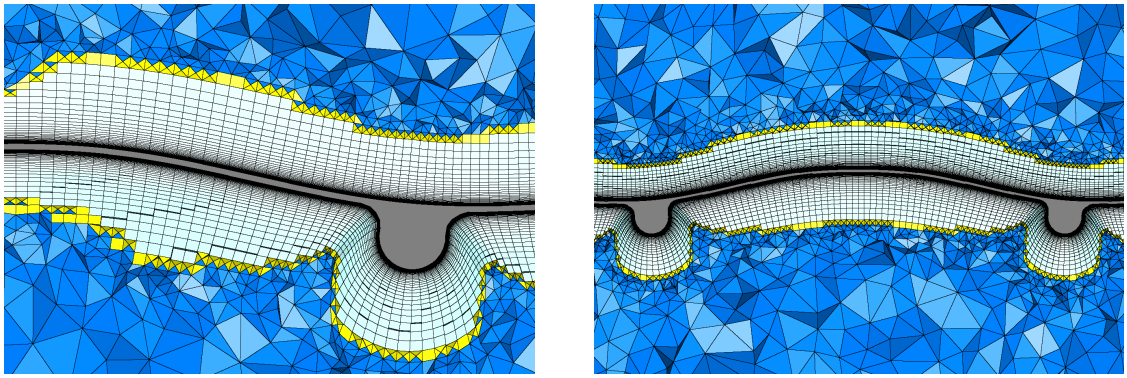

(a) (b)

Figure 4.20: Mesh slices at x = 0.97 for the half-domain (a) and full-domain (b) at the centre section of the wing.

4.3. Mesh convergence study

There are several sources of errors that impact the final solution of CFD simulations. One of these sources of error is the discretization of the mesh. Therefore, a mesh convergence study has been conducted for both the LEI wing itself as well as the volume mesh in the vicinity of the wing. All simulations for this mesh convergence study have been performed using steady-state RANS for $\mathrm{Re} = 3 \cdot 10^6$, $\alpha = 12$, $\beta = 0$ and with the $\gamma - \widetilde{\mathrm{Re}}_{\theta t}$ transition model.

Starting with the mesh convergence study on the LEI wing itself, which is done by increasing or decreasing the number of nodes along the connectors. However, as the 2D T-Rex algorithm is very sensitive to changes, the surface mesh regions that were meshed unstructured required an alternative approach. It was found that when changing the nodes along the connectors bounding the unstructured surface regions, the quality of the surface mesh and the resulting volume mesh diminished quickly. Therefore, the connectors along these regions have not been changed with the same percentage increments as the rest, to keep the volume mesh quality as high as possible. Next to this, the distribution of nodes along the spanwise direction of the fillets have been left unchanged as well. This has been done because otherwise the volume mesh quality actually deteriorated due to collision and skewness of the extruded cells fronts.

It was decided to do the refinements divided over five different levels, with the third level being the mesh that was generated initially. Thus, from this third level, there are two steps up and down in refinement. Each step represents a 10% change in nodes along the connectors with respect to the third level. The total cell count, simulation time and force coefficients for these different refinement levels are shown in Table 4.2. As can be seen, the changes in the lift and drag coefficients do not follow a very defined trend with refinement level.

Table 4.2: Cell count and simulation time for the different LEI wing refinement levels.

Level	1	2	3	4	5
Cell count [mil]	5.67	6.78	8.10	9.54	10.90
Simulation time [hrs]	4.3	4.9	5.7	6.5	9.5
C_L [-]	1.0524	1.0548	1.0532	1.0503	1.0515
C_D [-]	0.1109	0.1124	0.1095	0.1109	0.1092

In theory, errors such as numerical diffusion should decrease when moving to finer refinement levels. Therefore, the force coefficients will be normalised with respect to the last refinement level 5. This is done through the relation as shown in Eq. (4.1). The resultant graph of this normalisation is presented in Fig. 4.21. The lift coefficient does not seem to follow a trend that is proportional to the respective refinement levels. For all the chosen refinement levels, the lift coefficient stays within a very narrow range of less than 0.5% difference. The drag coefficient seems to be affected more by different refinement levels. However, as can be seen from the graph, the results do not portray a clear convergence between successive refinement level for the drag coefficient. One could argue that over the whole range of refinement levels, the trend is downwards, with drag

decreasing as the geometry of LEI wing is more refined.

$$\hat{C_L} = \frac{C_L}{C_{L,5}}, \quad \hat{C_D} = \frac{C_D}{C_{D,5}} \tag{4.1}$$

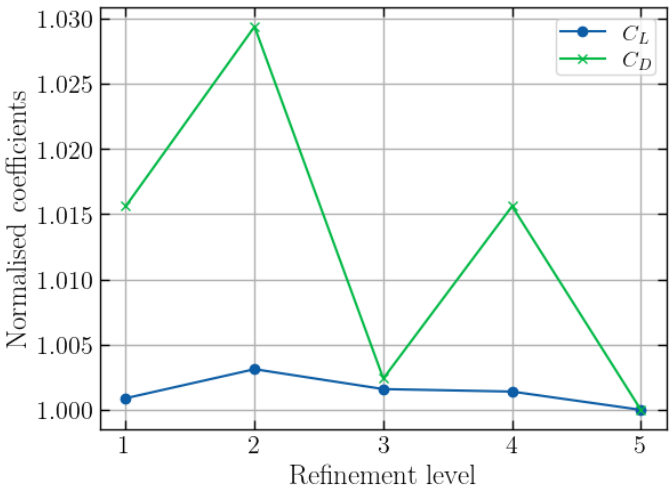

Figure 4.21: Normalised force coefficients for the surface mesh convergence study.

The difficulty with assessing mesh convergence based on a mesh generated in Pointwise lies in the high sensitivity to and a necessity for user input. While there are standards for high-quality surface meshes, in practice it was found that often a concession on a certain surface mesh region led to a higher quality volume mesh. This makes it very hard to achieve consistent meshing results when changing the refinement. It is possible that the lowest refinement level 1 is already adequate and that, therefore, no strong mesh convergence trend could be observed. However, it was not possible to get an even coarser mesh that still had acceptable mesh quality for CFD. While the aerodynamic coefficients are quite close to each other, the simulation time does scale strongly with the refinement levels. Next to this, post-processing effort and the amount of data being generated does also scale strongly with the refinement levels. Taking this into account, and the fact that the refinement level 3 had the highest quality volume mesh in terms of metrics, this mesh was selected for further study.

In the previous study done by Demkowicz [20], a similar observation regarding mesh convergence has been made. In his study, he argued that this could be due to the hexahedral extrusion fronts reaching isotropy earlier for a higher refinement level. This then meant that in his case, the mesh transitioned earlier to coarser isotropic tetrahedral cells, as shown in Fig. 4.22. Besides the refinement around the surface itself, it is also necessary to assess the impact of the refinement in the volume around the LEI wing. In the case of Demkowicz, no convergence study has been done on the volume mesh around the LEI wing. Naturally, and maybe a bit counter-intuitive, this meant that when refining the surface of the LEI wing more, the volume mesh in the vicinity of the surface actually became less refined. As the aerodynamic performance of the LEI wing is also assessed for high angles of attack near and beyond stall, it is important to have sufficient refinement for the regions where separation could occur. Inadequate refinement in regions of separation or the wake can have a strong influence on the result. This is due to the fact that these regions often experience strong variable pressure gradients [101]. Therefore, a volumetric mesh convergence study has been done as well to exclude dependence on these mesh regions.

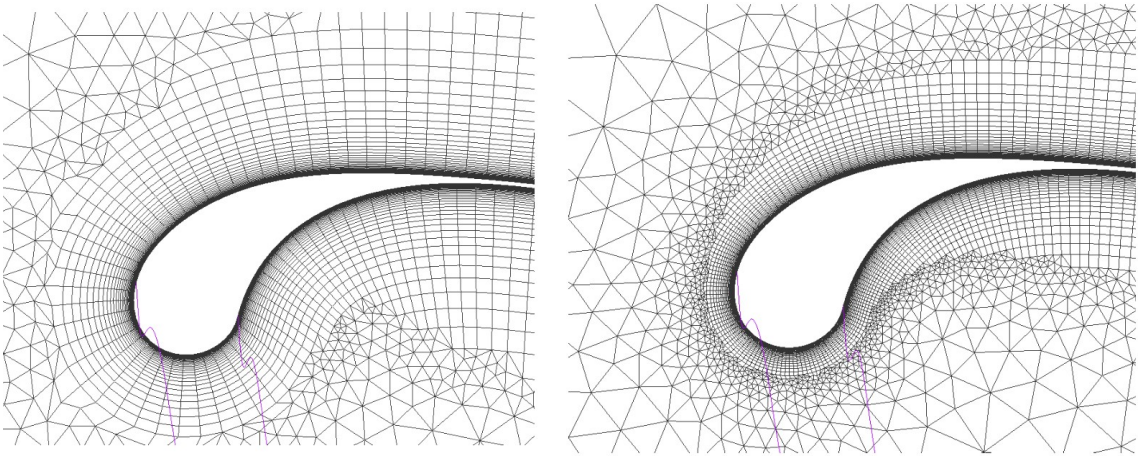

Figure 4.22: Visualisation of how the volume mesh becomes coarser when going from average (left) to high (right) refinement levels in the study by Demkowicz [20].

The goal of this volumetric mesh refinement study was to assess if and by how much the force coefficients are affected by refinements around the LEI wing. Next to this, the impact on the convergence behaviour has been assessed as well. However, the way convergence has been monitored will be discussed in Section 4.4.3. For this mesh convergence study, there were eight different refinement levels constructed. This was done using several refinement boxes, called source regions in Pointwise. For these source regions, a spacing and decay value had to be defined. The spacing value corresponds to the cell size and can be defined at two locations in the source volume. The decay value controls how quickly the size of the volume cells increases/decreases between these two points if different spacing values are chosen.

Several configurations have been tested divided over eight different refinement levels. To clarify what each of the levels represents, an overview of the different source regions used is given in Fig. 4.23. As can be seen, there are several combinations of source regions possible. The different refinement levels and their corresponding source region combinations and settings are given in Table 4.3. Since the LEI wing has been normalised with the chord length at the symmetry plane c_{ref} all sizes are relative to unity. For the cylindrical sphere settings, the first number indicates the setting at the centre of the frontal hemisphere and the second number indicates the setting at the rearward hemisphere. Ultimately, they can be seen as four different configurations: no refinement regions (config 0), small rectangular boxes (config 1), large rectangular boxes (config 2) and large rectangular boxes with spherical cylinder (config 3).

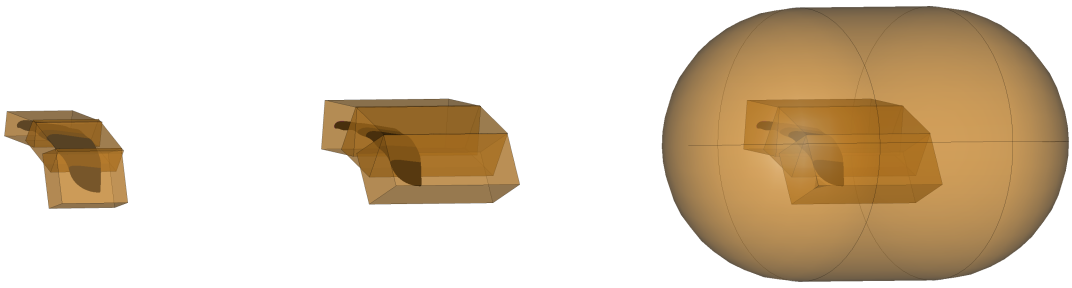

(a) (b) (c)

Figure 4.23: Different source regions configurations: config 1 (a), config 2 (b) and config 3 (c).

Table 4.3: Volumetric refinement levels (RL) and their respective settings.

	RL	Rectangles [-]	Sphere [-]
config 0	1	-	-
config 1	2	0.02	-
config 2	3	0.03	-
	4	0.025	-
	5	0.02	-
config 3	6	0.03	0.1 - 0.2
	7	0.025	0.1 - 0.2
	8	0.02	0.1 - 0.2

When plotting the lift and drag coefficient normalised against the most refined case (refinement level 8), the graph of Fig. 4.24 is obtained. From this graph, several conclusions can be drawn. First, in terms of absolute values, the percentage differences between all the cases are again minimal. With the exception of refinement level 1, the force coefficients stay within a range of 0.5% of each other. Second, while these differences might not be substantial, it does seem that there is a certain convergence trend for both the lift and drag coefficient. The refinement level 1 is furthest off from the final refinement level 8. After this, an increment of refinement level brings the lift coefficient closer, up to and including refinement level 5. From refinement level 5 onwards, it seems that the lift coefficient has converged. From refinement level 6 onwards, it seems that the drag coefficient is also converged. One could again argue that the differences are marginal, but this does not change the fact that there seems to be a stronger converging trend compared to the surface mesh refinement. Therefore, based on a balance of force coefficient convergence, simulation time and simulation stability, it has been decided to use refinement level 7 for all simulations. Thus, volumetric refinement level 7 has also been used for the surface mesh convergence study presented previously.

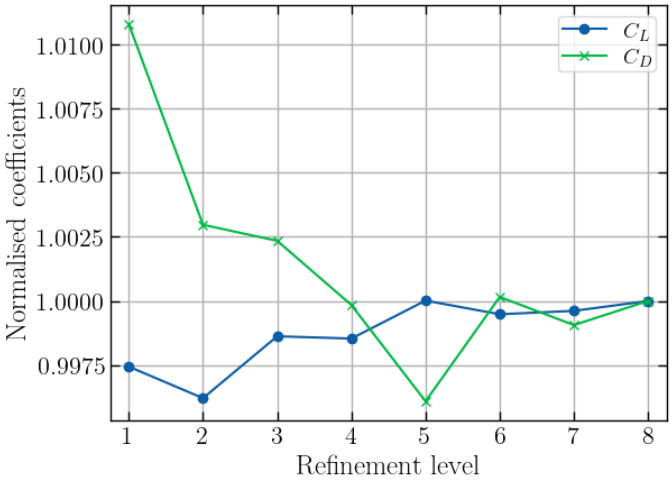

Figure 4.24: Normalised force coefficients for the volumetric mesh convergence study.

There are generally two options when considering the mesh in the near-wall region. First, one could use wall functions to mimic the boundary layer profile and obtain the resulting wall shear stress. In this case, the mesh requirements are less strict in terms of first cell height. Second, one could decide to resolve the boundary layer profile to the wall without the use of a wall function. In this case, a very small first cell height is necessary to accurately capture the velocity gradient near the wall and predict the wall shear stress correctly. One parameter that can be used when assessing the required first cell height is the dimensionless wall distance y^+, which is given by Eq. (4.2). Where y is the distance from the wall, ν is the kinematic viscosity and u_τ is the friction velocity defined by Eq. (4.3). To have a well resolved viscous sub-layer, the y^+ should be kept below 1. This condition is also important for the transition model used in this study. It was decided to use a first cell spacing that resulted in $y^+ << 1$, for all Reynolds numbers considered.

$$y^+ = \frac{y u_\tau}{\nu} \tag{4.2}$$

$$u_\tau = \sqrt{\frac{\tau_w}{\rho}} \tag{4.3}$$

4.4. Numerical simulation setup

As one of the most important aspects of the current study is the comparison to the previous study done by Demkowicz [20], a similar simulation setup and solver have been used. The solver used is the open source CFD toolbox OpenFOAM developed by ESI-OpenCFD [102]. The version used is the v2006 release, which was the most recent release upon starting this thesis project.

Currently, the only way to compare the simulation data to available experimental results is through the use of force coefficients. The coefficients that have been determined in this study are the lift, drag and sideforce coefficient. The way these are computed in OpenFOAM is through the relations shown in Eq. (4.4), Eq. (4.5) and Eq. (4.6). In these equations, L, D and S are the lift, drag and sideforce respectively, ρ is the density which is equal to 1, U_∞ is the freestream velocity which is also equal to 1.

$$C_L = \frac{2L}{\rho U_\infty^2 A_{ref}} \tag{4.4}$$

$$C_D = \frac{2D}{\rho U_\infty^2 A_{ref}} \tag{4.5}$$

$$C_S = \frac{2S}{\rho U_\infty^2 A_{ref}} \tag{4.6}$$

As can be seen, all force coefficients use the same reference area A_{ref} in OpenFOAM's calculation. This reference area is determined by taking the CAD model and projecting the area onto the ground plane. The reason for doing this, instead of taking the reference area from literature and scaling it, is that this way one can be sure the correct reference area is used. As OpenFOAM did not easily allow multiple reference areas to be defined, the sideforce coefficient had to be scaled afterwards using the relation shown in Eq. (4.7). This was necessary because of the assumed convention that the sideforce is calculated with the side projected area, which is determined by projecting the CAD model onto the symmetry plane. When discussing the results, C_S is the scaled parameter as shown in Eq. (4.7).

$$C_{S_{scaled}} = C_S \frac{A_{ref}}{A_{side}} \tag{4.7}$$

The LEI wing model itself has been scaled in such a way that the chord length at the symmetry plane represents one unit, i.e. all distances have been normalised with this chord length. For this chord length, different values circulate depending on the studies considered. Similarly to the reference areas, the physical chord length of the model in the current study was measured in CATIA and used for scaling.

As the simulation domains for both the half-domain and full-domain cases had a significant amount of cells, they needed to be decomposed into several sub-domains. Doing this allows optimal use of the parallelisation capabilities of OpenFOAM and can significantly decrease the solving time. Instead of solving the whole problem on one single CPU, the problem gets split-up into several sub-problems where the amount of sub-problems is equal to the number of CPU's used. In OpenFOAM, this is possible through defining several variables in a `decomposeParDict` file. The chosen decomposition method, scotch, tries to minimise the boundaries between the number of processors. The chosen amount of nodes and processors depended on the size of the simulation. All steady-state simulations have been run on a single node with 20 cores.

4.4.1. Boundary conditions and initial values

All cases are set up by using a reference file in which the turbulence model, boundary conditions and initial values are defined. For convenience, the velocity has been set to unity, which means that the initial velocity vector is defined through Eq. (4.8). Where i is the chordwise component, j is upwards and k is the spanwise component. Therefore, in the case that $\beta = 0$, the vector simply reduces to an i and j component. To indicate the calculation of the initial values, the subscript i is used for the variables in this section.

$$U_i = (i, j, k) = \big(cos(\beta)cos(\alpha),\ sin(\alpha),\ sin(\beta)\big) \tag{4.8}$$

An important similarity scaling parameter is the Reynolds number, which is defined by Eq. (4.9). In this equation, U represents the velocity, ρ the density, L the length scale, μ the dynamic viscosity and ν the kinematic viscosity. Since the density, velocity and length scale are unity, the initial kinematic viscosity is determined by rewriting Eq. (4.9). This means that the only required inputs are the: angle of attack, sideslip angle, Reynolds number, turbulence intensity and eddy viscosity ratio. Based on these inputs parameters, all initial values and boundary conditions can be determined.

$$Re = \frac{U \cdot \rho \cdot L}{\mu} = \frac{U \cdot L}{\nu} \tag{4.9}$$

The turbulent kinetic energy, given by Eq. (4.10), represents the mean kinetic energy of the eddies that exist in the turbulent flow. In this equation, Tu stands for the turbulence intensity expressed in percentages. The specific turbulence dissipation rate, given by Eq. (4.11), represents the rate at which the turbulent kinetic energy gets converted into thermal internal energy. In this equation, ν/ν_t stands for the eddy viscosity ratio.

$$k_i = \frac{3}{2}\left(U_i \frac{Tu}{100}\right)^2 \tag{4.10}$$

$$\omega_i = \frac{k_i}{\nu} \cdot \frac{\nu}{\nu_t} \tag{4.11}$$

Since transition modelling is used, two empirical correlations defined in [62] are used for the initial conditions. These are given by Eq. (4.12) and Eq. (4.13).

$$\widetilde{\mathrm{Re}}_{\theta t,i} = 1173.51 - 589.428\mathrm{Tu} + \frac{0.2196}{\mathrm{Tu}^2}, \text{ for } \mathrm{Tu} \leq 1.3 \tag{4.12}$$

$$\widetilde{\mathrm{Re}}_{\theta t,i} = 331.5(\mathrm{Tu} - 0.5658)^{-0.671}, \text{ for } \mathrm{Tu} > 1.3 \tag{4.13}$$

For the half-domain, a farfield boundary, a symmetry plane boundary and a LEI wing boundary are defined. The farfield boundary has the `inletOutlet` or `outletInlet` boundary type which allows an `inletValue` or `outletValue` to be defined. It is a mixed boundary condition for which the outflow is automatically treated as a zero gradient condition and can be used for all the variables in this study. The symmetry plane has the `symmetry` type boundary condition and can be used for all the variables. Last, the LEI wing surfaces were named walls, different boundary conditions were set depending on the variable. In the case of a full-domain, the symmetry plane is omitted and only the farfield and the LEI wing surfaces are the boundaries. An overview of all boundary condition types and initial values is given in Table 4.4.

Table 4.4: Boundary condition types and initial values for flow field and turbulence variables.

	Farfield type	Farfield value	Walls type	Walls value
p $[m^2/s^2]$	`outletInlet`	`outletValue` = 0 Initial value = 0	`zeroGradient`	-
U $[m/s]$	`inletOutlet`	`inletValue` = U_i Initial value = U_i	`fixedValue`	(0, 0, 0)
ν_t $[m^2/s]$	`calculated`	Initial value = 0	`nutkWallFunction`	Value = 0
k $[m^2/s^2]$	`inletOutlet`	`inletValue` = k_i Initial value = k_i	`fixedValue`	Initial value = 0
ω $[1/s]$	`inletOutlet`	`inletValue` = ω_i Initial value = ω_i	`omegaWallFunction`	Initial value = ω_i
$\widetilde{\mathrm{Re}}_{\theta t}$ [-]	`inletOutlet`	`inletValue` = $\widetilde{\mathrm{Re}}_{\theta t,i}$ Initial value = $\widetilde{\mathrm{Re}}_{\theta t,i}$	`zeroGradient`	-
γ [-]	`inletOutlet`	`inletValue` = 1 Initial value = 1	`zeroGradient`	-

4.4.2. Numerical schemes and solver control

For the steady-state simulation setup, several settings needed to be set to ensure solution stability and good convergence. All steady-state cases were run for a fixed amount of iterations, rather than defining a certain convergence tolerance for the set of equations. This was done to be able to observe the residuals and force coefficients over the same number of iterations. There are many different settings that the user can influence, however, the purpose of this study was not to perform a deep analysis of different OpenFOAM simulation settings. Therefore, most of the settings are similar to the ones used in the study by Demkowicz [20]. This choice has been made to ensure that when comparing the results of the two studies, the differences can be attributed to geometrical differences and are not caused by the OpenFOAM solver settings.

The two most important files for solution control in OpenFOAM are `fvSchemes` and `fvSolution`, which define the numerical schemes and solver settings respectively. For the numerical schemes, there are several categories that require inputs for steady-state simulations, these are as follows [103]:

- Time schemes
- Gradient schemes
- Divergence schemes
- Surface normal gradient schemes
- Laplacian schemes
- Interpolation schemes

The combination of numerical schemes is chosen in such a way that it ensures stability and convergence throughout the whole Reynolds number, angle of attack and sideslip angle range. All numerical schemes used for the steady-state simulations are summarised in Table 4.5, where the chosen schemes are written exactly as in the OpenFOAM setup.

The time scheme for a steady-state simulation is simply steady state, which sets all time derivatives to zero. The gradient schemes have been chosen to be of the Gauss linear type, which is the default setting provided by the OpenFOAM documentation. It uses central differencing to interpolate the values of the cell centres to the face centres that are required for the integration. The divergence schemes control all the divergence terms, excluding the Laplacian terms which are defined later on. The divergence terms appear for both non-advective and advective terms and it is, therefore, necessary to select the schemes per variable accordingly. The non-advective terms use Gauss linear, whereas the advective terms use either bounded Gauss linearUpwind default for velocity or bounded Gauss upwind for k, ω, γ, and $\widetilde{\mathrm{Re}}_{\theta t}$. The reason to go for bounded upwind schemes on the divergence terms follows from the need for stability at higher Reynolds numbers and angles of attack. The linear upwind is a second-order scheme and the upwind scheme is first order. The Laplacian terms use a Gauss linear corrected scheme. Since the domain and LEI geometry are not a simple rectangular shapes, there will be a fairly large amount of non-orthogonal cells in the domain. For such cases, OpenFOAM advises the use of the corrected settings for both the Laplacian terms and surface normal gradients [103]. An even more conservative setting would be limited corrected, which is advised when the corrected schemes could not provide sufficient stability, however, this was not necessary for this study.

Table 4.5: Numerical schemes used for the steady-state simulations.

Category	**Chosen scheme**
Time	steadyState
Gradient	Gauss linear
Divergence (U)	bounded Gauss linearUpwind default
Divergence ($k, \omega, \gamma, \widetilde{\mathrm{Re}}_{\theta t}$)	bounded Gauss upwind
Laplacian	Gauss linear corrected
Interpolation	linear
Surface normal gradient	corrected

All the solver control settings that are used for the steady-state simulations are summarised in Table 4.6. In the `fvSolution` file, the solvers of the equations, the tolerances and the algorithms are defined. The majority

of the settings is similar for the whole Reynolds number range, with the exception of two settings, which will be discussed later. Similar to the finite volume schemes, the terms described in the table are written exactly as the OpenFOAM setup.

The first settings are solver settings. For solving the pressure, a Geometric agglomerated Algebraic MultiGrid (GAMG) solver, with a Gauss-Seidel smoother is used. This solver operates under the algebraic multi-grid principle, where a coarse matrix is solved first and is used as a starting solution for the finer matrix. For all other variables, the smoothSolver is selected with an additional Gauss-Seidel smoother. The SIMPLE settings refer to some of the SIMPLE algorithm-specific settings. The working of the SIMPLE algorithm was explained in Chapter 3. Consistent set to yes means that rather than the default SIMPLE algorithm, the SIMPLEC variant is used. This algorithm should have a better convergence rate and does usually not require additional under-relaxation of the pressure correction term. Depending on the Reynolds number, a different number of non-orthogonal corrections is applied. These correctors are necessary to provide stability in the initial part of the simulations and their required number increases with Reynolds number. One corrector is used for the cases where $\mathrm{Re} \leq 3 \cdot 10^6$ and three correctors for $\mathrm{Re} = 15 \cdot 10^6$. Relaxation factors have been applied on all variables apart from the pressure, with the velocity at 0.9 and the other variables at 0.7. At the start of the steady-state simulations, a few potential flow non-orthogonal corrector steps are done to initialise the flow field. Again, these depend on the Reynolds number, with 10 correctors being used for $\mathrm{Re} \leq 3 \cdot 10^6$ and 30 correctors for $\mathrm{Re} = 15 \cdot 10^6$.

Table 4.6: Solver control settings used for the steady-state simulations.

Category	**Settings**
Solver (p)	GAMG; Gauss-Seidel smoother
Solver ($U, k, \omega, \gamma, \widetilde{\mathrm{Re}}_{\theta t}$)	smoothSolver; symmetric Gauss-Seidel smoother
SIMPLE	consistent: yes
	nNonOrthogonalCorrectors: 1 to 3
relaxationfactors	
U	0.9
$k, \omega, \gamma, \widetilde{\mathrm{Re}}_{\theta t}$	0.7
potentialFlow	nNonOrthogonalCorrectors: 10 to 30

4.4.3. Monitoring convergence

Keeping track of the convergence and stability of the simulations is done by monitoring the residuals and the force coefficients. An example of such a residual convergence plot is presented in Fig. 4.25. As has been mentioned before, all cases were run to a fixed amount of iterations. This was 4000 for the half-domain cases and 6000 for the full-domain cases. Most of the residuals fall around or below 10^{-7}. The only exception to this is the pressure and velocity in the z-direction, which usually settle slightly higher, but still well converged.

However, only monitoring the residuals is not sufficient as low residuals alone are not a good indicator of convergence. Therefore, the force coefficients were picked as quantities of interest and monitored in a similar way. For the half-domain cases, these were the lift and drag coefficient and for the full-domain cases, the sideforce coefficient was added to this as well. Monitoring these force coefficients is especially important for cases where residuals might be higher due to underlying transient effects, such as separation. This flow separation will introduce instability in the simulation which will then prevent the residuals converging to similar tolerances as, for example, Fig. 4.25. An example of this is given in Fig. 4.26, which is a case at high angle of attack and post-stall. It can be seen that the pressure residual is not able to reach similar residual convergence. However, when observing the force coefficient history of the simulation in Fig. 4.27 it can be seen that these stay stable enough to be considered converged.

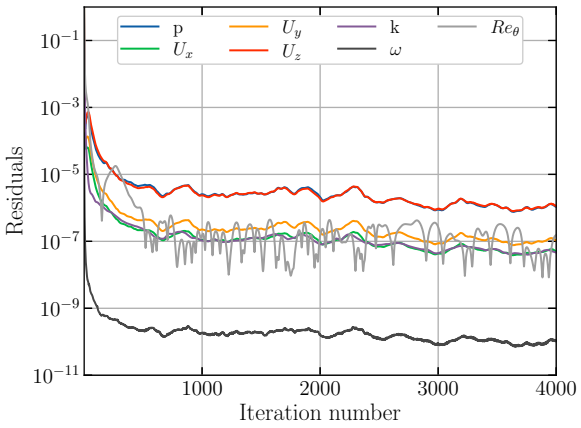

Figure 4.25: Residuals of a simulation at Re = $3 \cdot 10^6$ and $\alpha = 12°$.

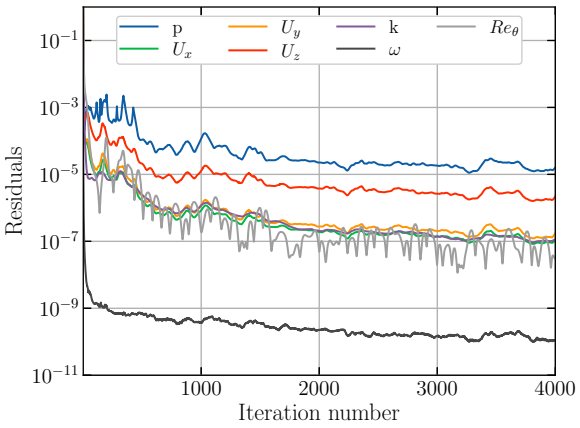

Figure 4.26: Residuals of a simulation at Re = $3 \cdot 10^6$ and $\alpha = 22°$.

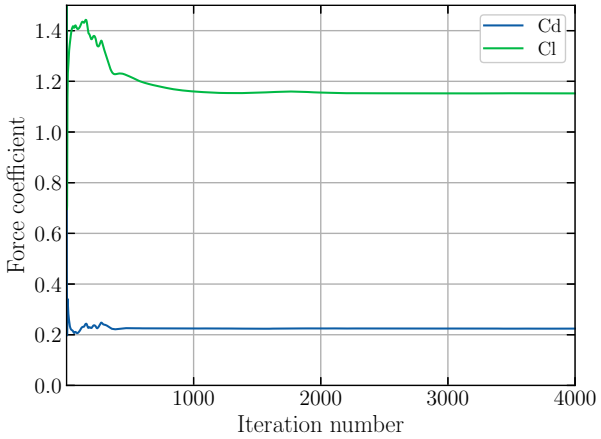

Figure 4.27: Force coefficients of a simulation at Re = $3 \cdot 10^6$ and $\alpha = 22°$.

5

Results and discussion

In this chapter, the numerical results will be presented and the aerodynamic performance of the LEI wing will be discussed. Starting with an overview of the used conventions, variables and their formulas in Section 5.1. In Section 5.2, the aerodynamic performance of the LEI wing under zero sideslip angle conditions is analysed. In addition to this, the impact of the struts under these conditions is assessed. The aerodynamic performance of the LEI wing during sideslip conditions, together with the impact of the struts under these conditions, is discussed in Section 5.3. Lastly, the results of the current study are compared to several other numerical and experimental studies in Section 5.4.

5.1. Conventions, variables and their formulas

This section will give a brief overview of several conventions used in this study. Furthermore, the definitions of certain variables are explained. If the definition of a used variable is unclear during the analysis, please refer back to this section. In addition to this, it is once more underlined that all results of the present study, discussed in this chapter, are obtained through steady-state RANS simulations using the $\gamma - \widetilde{\mathrm{Re}}_{\theta t}$ transition model. The domain has been scaled such that the chord length at the symmetry plane represents one length unit. The density and freestream velocity are also unity, which means the Reynolds number is controlled through setting the kinematic viscosity.

The global coordinate system of the current study is shown in Fig. 5.1. As can be seen, the positive x-direction is pointing downstream in chordwise direction, the positive y-direction is pointing upwards and the positive z-direction is pointing in the spanwise direction to the left side of the wing itself. When discussing the velocity components, these directions define the direction of positive velocity. In subfigure (a) of Fig. 5.1, the assumed convention for positive sideslip angle is indicated as well. This will be relevant for the analysis in Section 5.3.

(a) (b)

Figure 5.1: Top-down view (a) and side view (b) of the LEI wing with global coordinate system and positive sideslip angle convention.

In Fig. 5.2, the outline of the half-domain LEI wing is plotted. This is relevant for understanding how the spanwise pressure distribution plots are made that are used during the analysis. Where the chordwise pressure distribution can easily be plotted based on x-coordinates, the spanwise pressure distribution requires a different approach. Since the pressure distribution is a surface variable, plotting this along the spanwise direction will require a location. However, this causes issues with plotting because if just either the y or z coordinate is used, the graph will start self-intersecting in some regions due to the shape of the LEI wing. Therefore, the distances between each of the consecutive points for the upper and lower surface are computed. After this, the total arc length of the upper and lower surface is determined. The distances are then normalised by the respective total arc length and this results in the $arc_{n,u}$ coordinate for the upper surface and the $arc_{n,l}$ for the lower surface.

The approximate locations of the struts will be indicated on several spanwise pressure distribution plots using vertical lines. Please note that the location of the struts in these cases is normalised with respect to the total length arc length at that location. This means that the location of the struts in the plots will vary with x-location, since the total length used for the normalisation varies with x-location. For the cases where the results of the LEI wing with and without struts are compared, corrections have been applied to account for the differences in lower surface arc length.

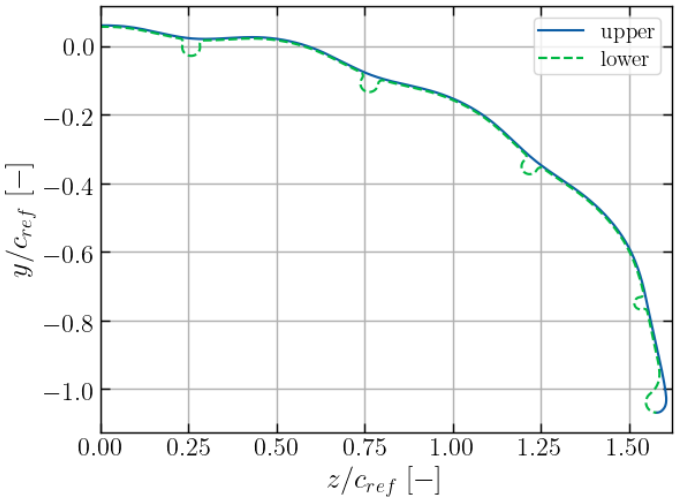

Figure 5.2: Upper and lower surface outline of the LEI wing at x = 0.5.

There are a few variables that will be reoccurring during the aerodynamic analysis in this chapter. The velocity components do not require an introduction, as these are defined through the coordinate system. The same holds true for the vorticity vector components. However, there are other variables for which the used definition should be clarified. One of these variables is the x-component of the skin friction coefficient $C_{f,x}$. It is defined by Eq. (5.1), where $\tau_{w,x} = \mu \frac{\partial U_x}{\partial y}\Big|_{y=0}$. By using the x-component of the skin friction coefficient, regions with recirculation or separation can be identified as negative or very low $C_{f,x}$. In addition to this, laminar to turbulent transition can be identified by a sudden strong increase in $C_{f,x}$.

$$C_{f,x} = \frac{\tau_{w,x}}{\frac{1}{2}\rho U_\infty^2} \tag{5.1}$$

Another variable that will be used often is the total pressure coefficient, which is defined by Eq. (5.2). The first term after the = sign on the left represents the static pressure coefficient and the second term the dynamic pressure coefficient. Since the density and freestream velocity are unity, the relation can be simplified. With the total pressure coefficient, it is possible to visualise regions of high energy, such as the freestream, and regions where there are energy losses or energy exchange takes place. By definition, in the freestream, the total pressure coefficient will be equal to one. The regions that can show up as having a lower total pressure coefficient can be boundary layers, separation/recirculation regions and vortices.

$$C_{p,T} = \frac{p}{\frac{1}{2}\rho U_\infty^2} + \frac{\|\mathbf{U}\|^2}{U_\infty^2} = 2\left(p + \frac{1}{2}\|\mathbf{U}\|^2\right) \tag{5.2}$$

Last, in some parts of the analysis, the Lambda2 criterion is used. The Lambda2 criterion can be used to detect vortex cores in three-dimensional space. It does so by computing the eigenvalues of the sum of the squared symmetric and antisymmetric parts of the velocity gradient tensor. At locations where there are two or more negative eigenvalues, part of a vortex core could be present. For the mathematical foundations behind this method, the reader is referred to [104]. In OpenFOAM, the results of this method are multiplied by a negative sign, which results in only positive λ_2 values. It is also possible to compute the Lambda2 criterion on a flow field slice, i.e. a plane, and highlight areas where a vortex could be present. This is what has been done in the current study.

5.2. Aerodynamic performance of the LEI wing ($\beta = 0°$)

In this section, the aerodynamic performance of the LEI wing under zero degree sideslip angle conditions will be discussed. This starts with presenting the aerodynamic force coefficients in Section 5.2.1. In Section 5.2.2, deeper analysis based on the aerodynamic force coefficient observations is done. Following this, general flow field analysis is presented in Section 5.2.3. Lastly, the impact of the struts under zero degree sideslip angle conditions is analysed in Section 5.2.4.

5.2.1. Aerodynamic force coefficients

In Fig. 5.3, the lift curve, drag curve, drag polar and aerodynamic efficiency of the LEI wing at different Reynolds numbers are presented. As can be observed from these graphs, the Reynolds number has a strong influence on the performance of the LEI wing. At the lowest Reynolds number of $0.1 \cdot 10^6$, there is severe separation for $\alpha > 6°$. Due to this, the drag coefficient increases very strongly too. However, the lift curve flattens off rather than having a strong drop as seen at the other Reynolds numbers post-stall. It is interesting to see that even at the lower angles of attack, the lowest Reynolds number gives the highest drag-coefficient. At the lowest Reynolds number, one would expect laminar flow effects to be more present. Normally, a laminar boundary layer will have a smaller displacement thickness and lower skin friction, however, this does not seem to result in lower overall drag coefficient. One reason for this could be due to a difference in recirculation zone size behind the leading edge on the pressure side of the wing. This was reported by both Folkersma et al.[19] and Demkowicz [20] to be a strong contributor to the drag coefficient. Since a transition model is used, this can play a big role in the separation behaviour, as a laminar boundary layer is more prone to separation than a turbulent one.

This is the reason that generally speaking, the higher the Reynolds number, the more resistant the boundary layer is to separation. However, it had already been noted before by Folkersma et al.[19] in 2D and Demkowicz [20] in 3D that this general trend does not hold for a LEI wing when using a transition model. Some of their other observations regarding a laminar separation bubble on the suction side and drag crisis over the circular leading edge will be verified at the end of Section 5.2.2 as well. The maximum stall angle for this study is not achieved at the highest Reynolds number of $15 \cdot 10^6$, but rather at Re = $1 \cdot 10^6$. However, once the LEI wing stalls, the drop in the lift is much more severe at Re = $1 \cdot 10^6$. This can be for several reasons, which will be discussed in more detail later in Section 5.2.2. One can also see that post-stall, the drag coefficient increase is much higher when compared to the other cases. Another observation that can be made based on these graphs is that at the highest Reynolds number of $15 \cdot 10^6$, there is a clear off-set with respect to the lift and drag curves at the other Reynolds numbers. The lift coefficient for the Re = $15 \cdot 10^6$ case is higher for lower angles of attack, but the maximum lift-coefficient matches the Re = $3 \cdot 10^6$ case. Similarly, at the lower end of the angle of attack range, the drag coefficient of the Re = $15 \cdot 10^6$ case is lower than the others, but from $\alpha = 9°$ onwards the drag coefficient matches the Re = $1 \cdot 10^6$ and Re = $3 \cdot 10^6$ cases. The drag polar also shows this very distinct offset at lower drag coefficient values between the cases.

The last parameter considered is the aerodynamic efficiency L/D. There does seem to be a trend of increasing aerodynamic efficiency with increasing Reynolds number. Also the angle of attack at which the maximum L/D occurs changes with Reynolds number. For Re = $0.1 \cdot 10^6$, the maximum $L/D \approx 8$ and occurs $\alpha = 6°$. Both at Re = $1 \cdot 10^6$ and Re = $3 \cdot 10^6$, the maximum $L/D \approx 10.5$. However, for the former, this is at $\alpha = 6°$ and for the latter, it is at $\alpha = 9°$. For Re = $15 \cdot 10^6$, the maximum $L/D \approx 11.5$ and occurs at $\alpha = 6°$.

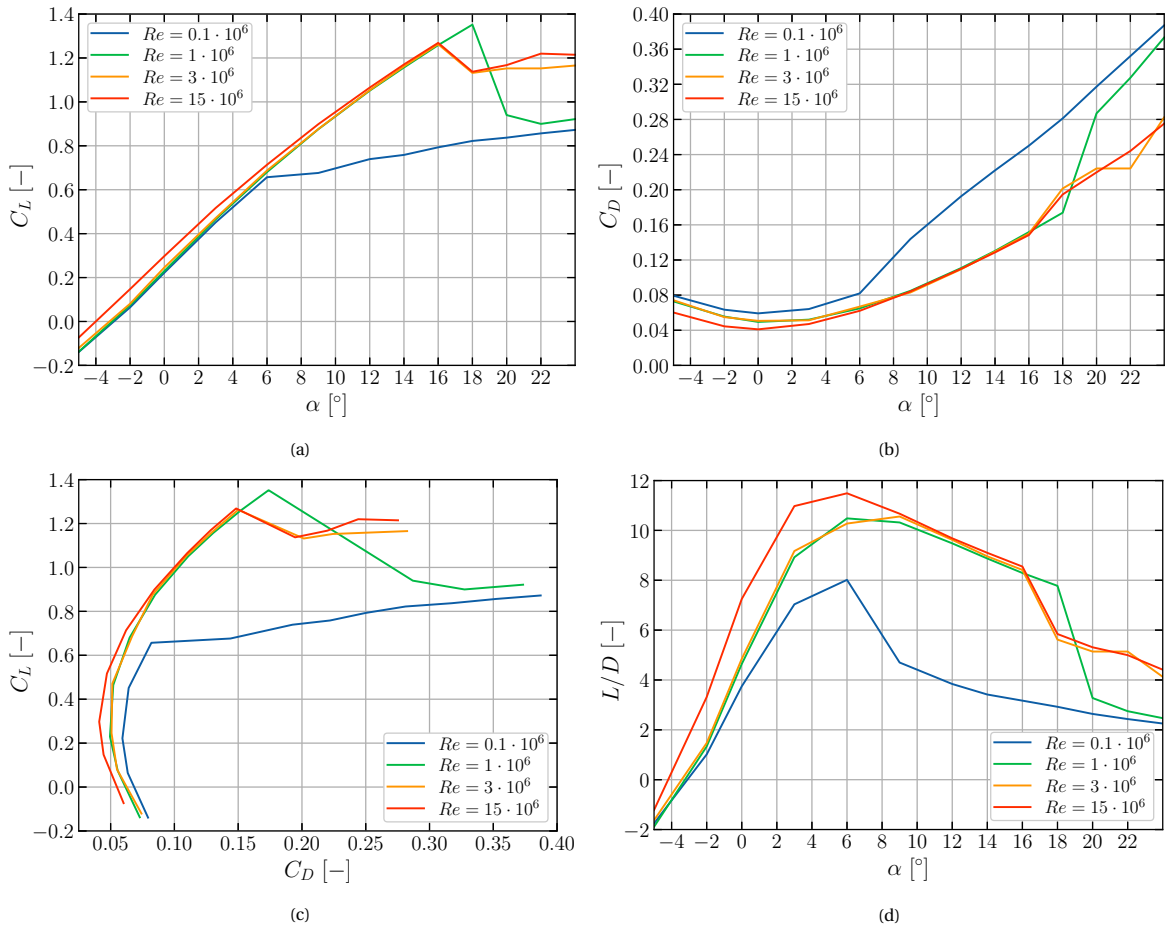

Figure 5.3: The lift curve (a), drag curve (b), drag polar (c) and aerodynamic efficiency (d) for different Reynolds numbers.

5.2.2. Analysis of aerodynamic force coefficient observations

In this section, some of the observations made based on the aerodynamic force coefficients in the previous section will be analysed in more detail. Starting with the observations for the Re = $1 \cdot 10^5$ case, where severe separation occurred for $\alpha > 6°$. To assess the aerodynamic changes, pressure distributions, skin friction distributions and the total pressure coefficient of the flow field will be compared. Before doing so, it has to be noted that the performance of RANS models post-separation is generally not strong. Therefore, it is important to realise that without experimental data of a reference case, one might be analysing nonphysical results. The pressure distributions for $\alpha = 6°$ and $\alpha = 9°$ in the vicinity of the symmetry plane are shown in Fig. 5.4. As can be seen, the peak load on the suction side of the LEI wing is much lower post-separation at $\alpha = 9°$. However, after approximately $x/c = 0.4$, there is a stronger load on the suction side for this angle of attack. The pressure for $\alpha = 6°$ does recover to $C_p = 0$ at $x/c = 1.0$ whereas the $\alpha = 9°$ case only recovers to $C_p = -0.25$. This phenomenon is what is also referred to as 'off-the-surface pressure recovery'. In this case, a detached fluid travels into a higher pressure region, such as the wake, and the recovery to freestream pressure can be more efficient than the pressure recovery for an attached boundary layer [105]. This, combined with the fact that the adverse pressure gradient is much smaller due to the lower peak load, is why at $\alpha = 9°$ the wing able to sustain a higher aft-loading. Furthermore, at $\alpha = 6°$ there is the leading edge loading peak, a short pressure recovery, a second smaller peak and subsequently the conventional pressure recovery.

In Fig. 5.5, the chordwise skin friction coefficient $C_{f,x}$ is plotted for both cases. Since only the x-component in chorwise direction is taken into account, negative $C_{f,x}$ indicates regions of reversed flow, whereas a strong positive increase indicates transition from laminar to turbulent. From these plots, it can be concluded that the majority of the suction side is separated at $\alpha = 9°$. At $\alpha = 6°$, it seems like there is a laminar separation bubble, since the $C_{f,x}$ is negative only within a certain range of the suction surface. This region coincides with the second small pressure peak seen in Fig. 5.4. When a laminar separation bubble has a considerable size, it

can cause the pressure to stay constant between the separation point and the transition point of the bubble. However, it seems that in this case, the laminar separation bubble is very small, hence only causing a small peak in pressure. The $C_{f,x}$ over the pressure side of the wing is fairly similar, as both cases show separation off the circular leading edge and a recirculation region from $x/c = 0.15$ to $x/c = 0.5$. What might seem odd is that the $C_{f,x}$ has a small positive spike at the trailing edge, but this can be explained easily. As the CAD model has a finite and circular shaped trailing edge, part of the flow still accelerates around this circular edge. This accelerating flow means that the gradient of velocity at the surface is higher, thereby increasing the wall shear stress.

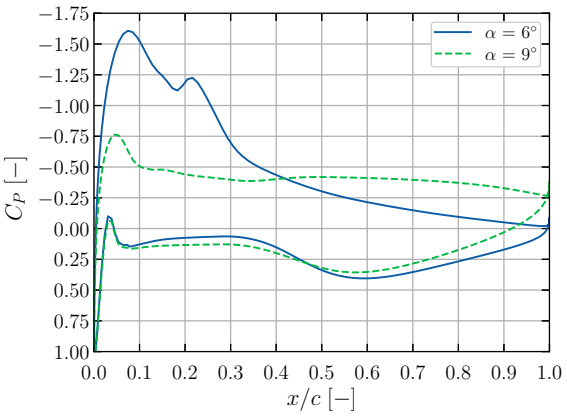

Figure 5.4: Chordwise C_p distribution near the symmetry plane: $\mathrm{Re} = 1 \cdot 10^5$, $\beta = 0°$.

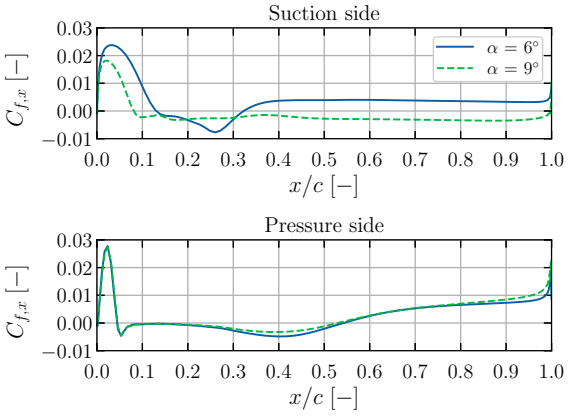

Figure 5.5: Chordwise $C_{f,x}$ distribution near the symmetry plane: $\mathrm{Re} = 1 \cdot 10^5$, $\beta = 0°$.

In Fig. 5.6 and Fig. 5.7, flow field slices at the same location of the plots in Fig. 5.4 and Fig. 5.5 are shown. As can be seen from these figures, in both cases there is a very low $C_{p,T}$ region behind the leading edge on the pressure side of the wing. This shows up as blue in the plots. These losses propagate further downstream along the pressure side but are strongest just behind the leading edge. The losses on the pressure side are largest at $\alpha = 6°$, which most likely has to do with the alignment of the circular leading edge with the incoming flow. For increasing angle of attack, the lower side of the leading edge becomes more aligned with the flow, meaning the separation in this region becomes less severe. Over the suction side of the wing, the extent of the separation at $\alpha = 9°$ becomes evident.

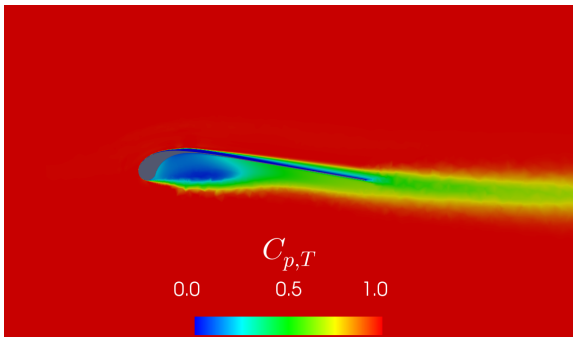

Figure 5.6: $C_{p,T}$ near the symmetry plane: $\mathrm{Re} = 1 \cdot 10^5$, $\alpha = 6°$, $\beta = 0°$.

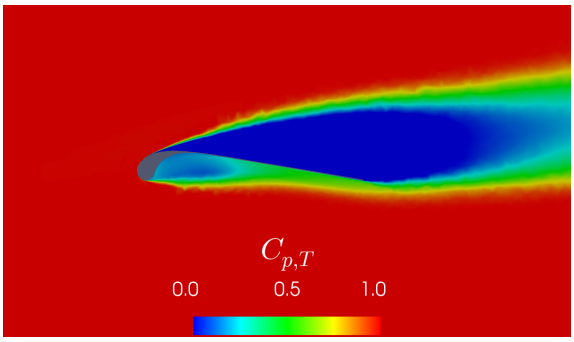

Figure 5.7: $C_{p,T}$ near the symmetry plane: $\mathrm{Re} = 1 \cdot 10^5$, $\alpha = 9°$, $\beta = 0°$.

As the simulations are three-dimensional, just observing one slice at a certain spanwise location cannot be used to draw conclusions on the overall flow field around the wing. Therefore, in Fig. 5.8 and Fig. 5.9, the total pressure coefficient is plotted on spanwise slices at $x = 0.5$. Comparing these two plots clearly shows that all along the span the separation at the suction side is much worse at $\alpha = 9°$. Again, the pressure side seems to have fewer losses at $\alpha = 9°$, which was explained previously by the better alignment of the lower side of the circular leading edge with the incoming flow.

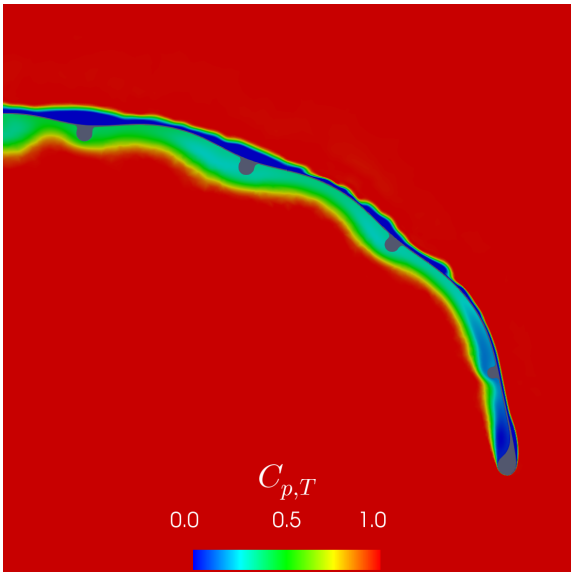

Figure 5.8: $C_{p,T}$ at x = 0.5: Re = $1 \cdot 10^5$, $\alpha = 6°$, $\beta = 0°$.

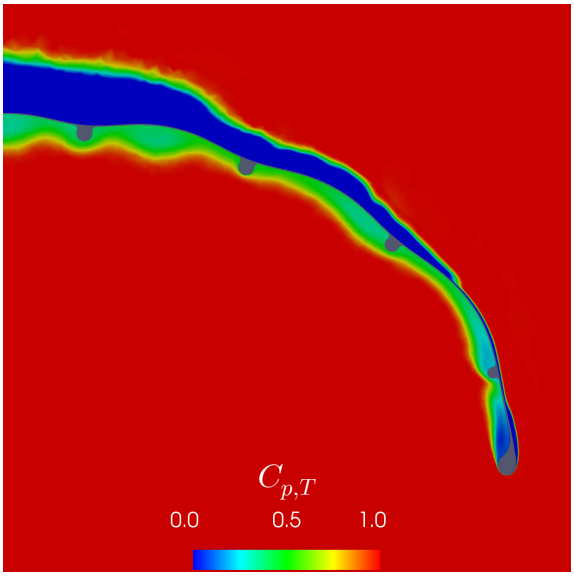

Figure 5.9: $C_{p,T}$ at x = 0.5: Re = $1 \cdot 10^5$, $\alpha = 9°$, $\beta = 0°$.

In Fig. 5.10, the spanwise pressure distribution is presented. This plot makes several things clear. First, for this specific x location, the spanwise loading over the suction side is much higher at $\alpha = 9°$. This corresponds well with the chordwise pressure distributions shown in Fig. 5.4 at $x/c = 0.5$. Second, there is a strong negative C_p loading in the tip region and around the leading edge of the tip on the suction side of the wing. Third, when looking at the pressure side, there is a much higher positive pressure along the majority of the span at $\alpha = 9°$. This is a result of the different inflow angle. A detailed discussion about the pressure distribution around the struts will be given in Section 5.2.4, but the vertical lines indicate their locations on the pressure side.

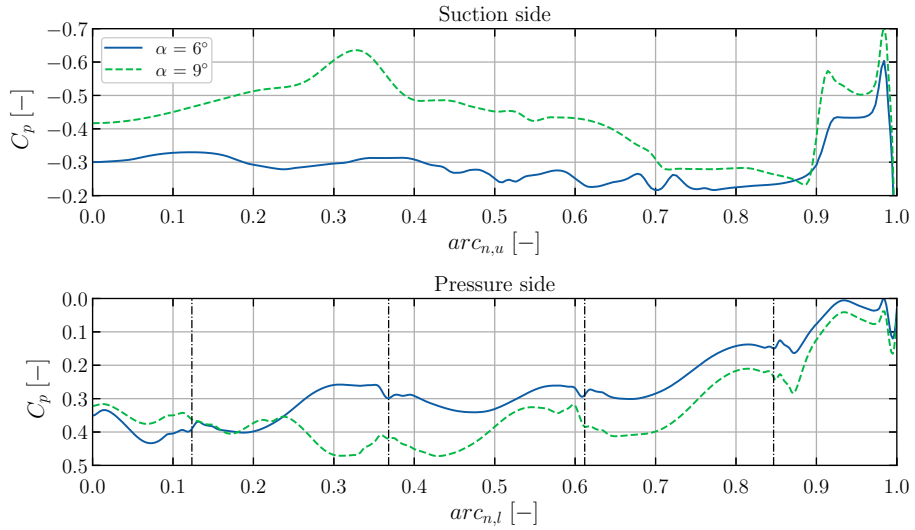

Figure 5.10: Spanwise C_p distribution at x = 0.5: Re = $1 \cdot 10^5$, $\beta = 0°$.

Another clear difference between the cases Re = $1 \cdot 10^6$ and Re = $3 \cdot 10^6$ was the maximum lift-coefficient. A higher maximum lift-coefficient was achieved at the lower Reynolds number. However, in that case, the post-stall lift drop was much more severe, which is something that will be analysed now.

In Fig. 5.11 and Fig. 5.12, the pressure distribution and skin friction distribution at the maximum lift coefficient angle of attack near the symmetry plane is plotted for both cases. In Fig. 5.13 and Fig. 5.14, the pressure distribution and the skin friction distribution at the next considered angle of attack post-stall near the symmetry plane are plotted. Please note that the angles of attack at which this happens are different for both

cases. The reason for comparing them this way is to get insight into the different mechanisms at play around their respective maximum lift conditions.

For the pressure distributions at the maximum lift condition in Fig. 5.11, there is not much difference to be observed. Given that Re = $1 \cdot 10^6$ had a higher maximum lift-coefficient it was expected that there was a higher suction peak. However, when observing the skin friction distribution in Fig. 5.12, some very clear differences appear. At Re = $3 \cdot 10^6$, laminar to turbulent transition takes place at approximately $x/c = 0.06$, as the $C_{f,x}$ exhibits a strong increase. At Re = $1 \cdot 10^6$, there is a higher initial $C_{f,x}$ peak, which is most likely down to the flow accelerating more rapidly at $\alpha = 18°$. After that, there is a strong drop in $C_{f,x}$ and it even becomes negative momentarily, before increasing again. This could be a very small laminar separation bubble, but the relative rate at which it drops and bounces back makes it seem more likely that the laminar boundary layer is on the verge of separation. The skin friction distribution on the pressure side shows that the recirculation zone is smaller at Re = $3 \cdot 10^6$, which is due to the better alignment at that angle of attack.

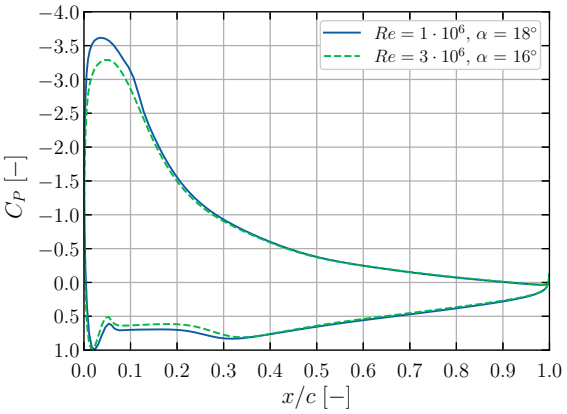

Figure 5.11: Chordwise C_p distribution near the symmetry plane pre-stall: $\beta = 0°$.

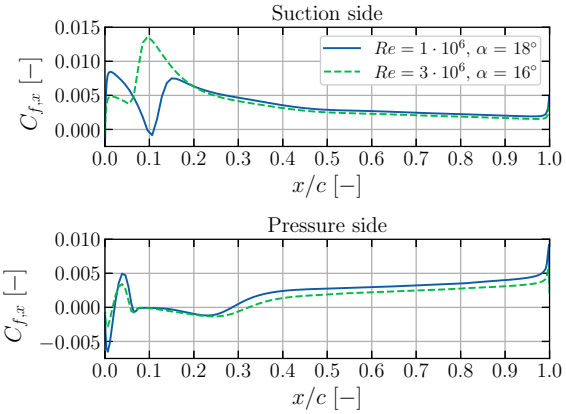

Figure 5.12: Chordwise $C_{f,x}$ distribution near the symmetry plane pre-stall: $\beta = 0°$.

When comparing the post-stall pressure distributions in Fig. 5.13, it shows a result in line with the severity of the drop in lift coefficient. At Re = $1 \cdot 10^6$, the drop is much more severe and it seems as if it is almost instant leading edge stall. When looking at the skin friction distributions in Fig. 5.14, the situation can be understood better. At Re = $3 \cdot 10^6$, the skin friction distribution looks quite similar to the pre-stall case. The transition from laminar to turbulent happens early on, after which the $C_{f,x}$ drops below zero around $x/c = 0.6$. This indicates that trailing edge separation occurs at this specific spanwise location. When comparing this to the case at Re = $1 \cdot 10^6$, it becomes clear where the differences in the lift and drag coefficient come from. There is almost instant leading edge separation and the flow stays separated over the whole chord length. This shows the vulnerability of the laminar boundary layer to more sudden and severe separation due to adverse pressure gradients. In this post-stall scenario, the recirculation region on the pressure side is larger at Re = $1 \cdot 10^6$.

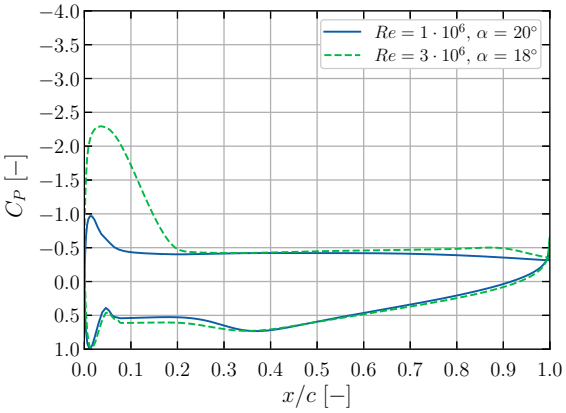

Figure 5.13: Chordwise C_p distribution near the symmetry plane post-stall: $\beta = 0°$.

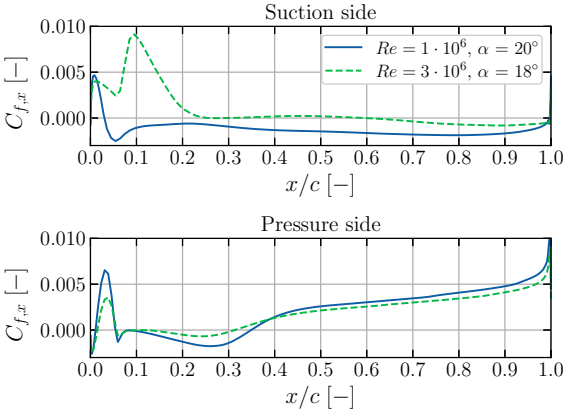

Figure 5.14: Chordwise $C_{f,x}$ distribution near the symmetry plane post-stall: $\beta = 0°$.

In Fig. 5.15 and Fig. 5.16, the pre-stall $C_{f,x}$ is plotted on the surface of the wing. In addition to this, a total pressure coefficient slice is shown in the vicinity of the symmetry plane. As can be seen, for Re = $3 \cdot 10^6$ there is a strong increase in $C_{f,x}$ at the start of the suction surface of the wing. This strong increase corresponds to the transition of the boundary layer from laminar to turbulent that was also observed previously in Fig. 5.12. After this peak, the $C_{f,x}$ gradually becomes less towards the trailing edge. The only region where there seems to be very low, or even negative, $C_{f,x}$ is just after the leading edge of the tip. When comparing this to the case at Re = $1 \cdot 10^6$, the results vary widely. To start, the $C_{f,x}$ over the leading edge is much higher, which is to be expected when the angle of attack increases and the flow accelerates. However, it seems as if this pressure gradient is too strong for the boundary layer to sustain, as there are patches of very low or negative $C_{f,x}$. The outboard region of the wing seems to suffer most from this. After these regions, the $C_{f,x}$ increases again, but there are more low $C_{f,x}$ regions along the chordwise direction of the suction surface.

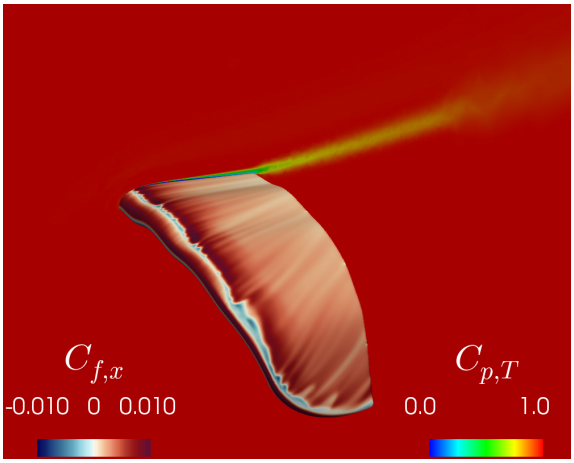

Figure 5.15: $C_{f,x}$ on the surface and $C_{p,T}$ near the symmetry plane: Re = $1 \cdot 10^6$, $\alpha = 18°$, $\beta = 0°$.

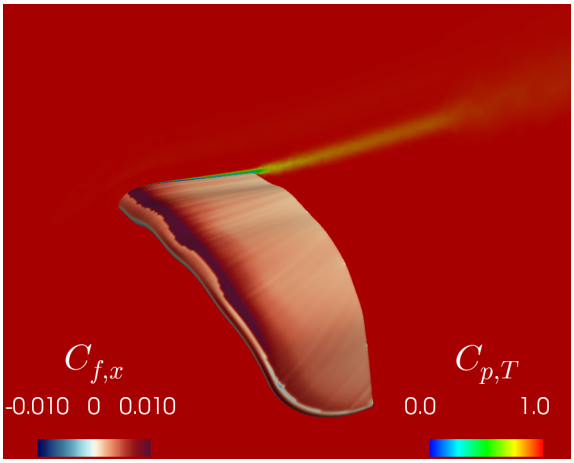

Figure 5.16: $C_{f,x}$ on the surface and $C_{p,T}$ near the symmetry plane: Re = $3 \cdot 10^6$, $\alpha = 16°$, $\beta = 0°$.

These plots can be compared to the post-stall results in Fig. 5.17 and Fig. 5.18. Starting with the case at Re = $3 \cdot 10^6$. It can be seen that is mainly the centre section of the suction surface where the separation takes place. Furthermore, it is also clearly not leading edge separation. There is still a similar transition line, which means the separation happens from a turbulent boundary layer. This is most likely the reason why the separation starts from the trailing edge and progresses forward. An increase in the angle of attack, at this Reynolds number, will cause an even greater adverse pressure gradient and will most likely move the separation point upstream. In addition to this, it will cause the separation region to increase in size and move further outboard as well. Again, when looking at the case at Re = $1 \cdot 10^6$, the results are very different. This is a

case with a very large region of leading edge stall. This becomes clear from the very low $C_{f,x}$ right at the start of the suction surface. It can be seen that the region of separated flow on the flow field slice is much larger. This comparison has shown how the separation behaviour of the LEI wing is affected by the transition of the boundary layer.

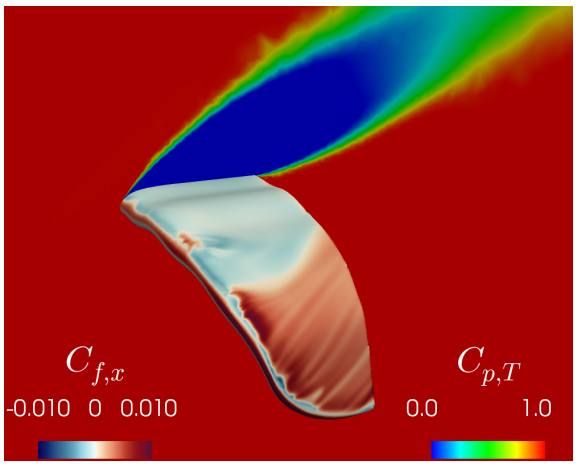

Figure 5.17: $C_{f,x}$ on the surface and $C_{p,T}$ near the symmetry plane: Re = $1 \cdot 10^6$, $\alpha = 20°$, $\beta = 0°$.

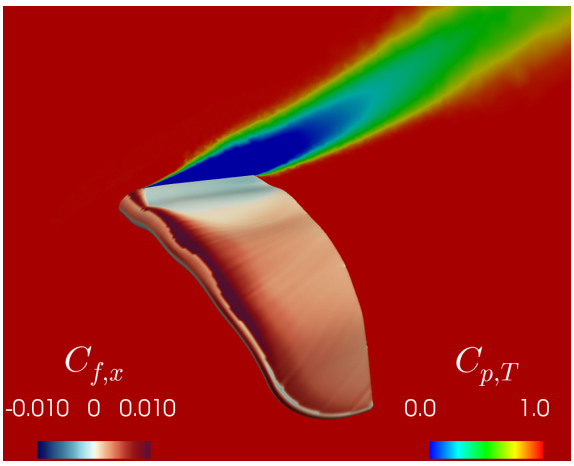

Figure 5.18: $C_{f,x}$ on the surface and $C_{p,T}$ near the symmetry plane: Re = $3 \cdot 10^6$, $\alpha = 18°$, $\beta = 0°$.

To conclude this section, some previous observations by Folkersma et al.[19] and Demkowicz [20] will be verified. In both their studies, they observed a laminar separation bubble over the suction surface of the wing at certain Reynolds numbers. In Fig. 5.19 and Fig. 5.20, the velocity magnitude and streamlines around the wing are shown at $\alpha = 6°$ for Re = $0.1 \cdot 10^6$ and Re = $3 \cdot 10^6$, respectively. As can be seen, a laminar separation bubble is present on the suction surface at Re = $0.1 \cdot 10^6$ and it fully disappeared at Re = $3 \cdot 10^6$. Furthermore, the size of the recirculation zone has decreased drastically with increasing Reynolds number. This is in line with the observations of the previous studies.

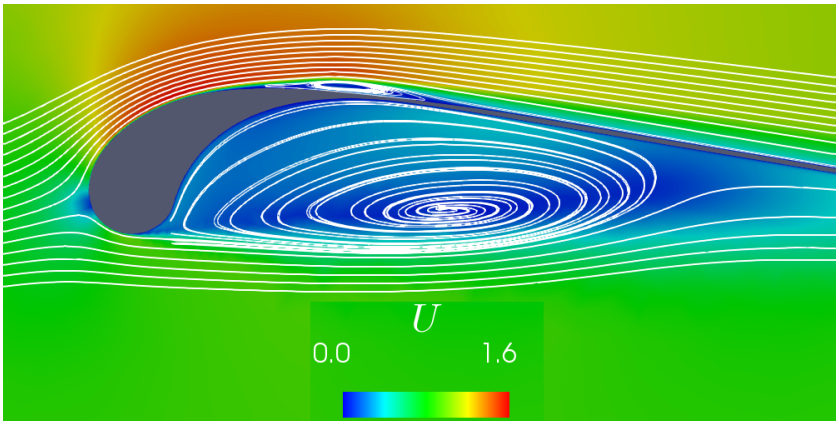

Figure 5.19: Velocity magnitude and streamlines around the LEI wing near the symmetry plane: Re = $0.1 \cdot 10^6$, $\alpha = 6°$, $\beta = 0°$.

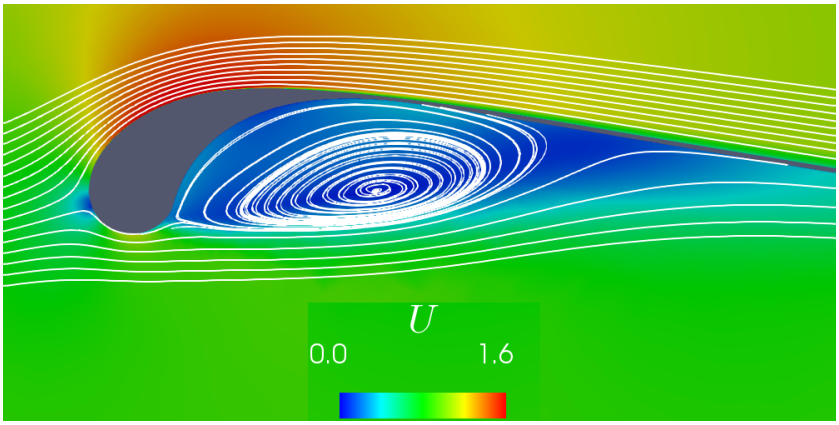

Figure 5.20: Velocity magnitude and streamlines around the LEI wing near the symmetry plane: Re = $3 \cdot 10^6$, $\alpha = 6°$, $\beta = 0°$.

In addition to this, both studies observed drag crisis over the pressure side of the circular leading edge. Drag crisis can result in early transition of the boundary layer, which will reduce the separation. Folkersma et al.[19] argued that this was the reason for the increase in lift coefficient and decrease in drag coefficient at lower angles of attack at some of the higher Reynolds numbers. As was shown in Section 5.2.1, at Re = $15 \cdot 10^6$ there was an offset in lift and drag coefficient at lower angles of attack compared to other Reynolds numbers. Therefore, to verify if in this case, drag crisis is also at play, comparisons of the pressure distribution and skin friction distribution are plotted in Fig. 5.21 and Fig. 5.22. This is done for Re = $3 \cdot 10^6$ and Re = $15 \cdot 10^6$ at $\alpha = 0°$. Over the suction side, the pressure distribution is similar for both Reynolds numbers. However, the pressure side shows a clear difference over the circular leading edge. A more negative C_p peak can be observed for Re = $15 \cdot 10^6$, with a higher C_p along the remained of the chord length. Looking at the skin friction distribution for $C_{f,x}$ shows clearly that early transition takes place at Re = $15 \cdot 10^6$ on the suction side of the wing. However, one can also observe transition over the circular leading edge on the pressure side of the wing. A clear increase in $C_{f,x}$ is present at $x/c = 0.025$ for Re = $15 \cdot 10^6$. This results in a smaller recirculation zone, which can be identified by the negative $C_{f,x}$. To conclude, the drag crisis is clearly observable at Re = $15 \cdot 10^6$ and this leads to a decrease in the recirculation zone size. Furthermore, the C_p is higher on the pressure side of the wing because of this. This is the reason for the higher lift coefficient and lower drag coefficients observed for Re = $15 \cdot 10^6$ at lower angles of attack.

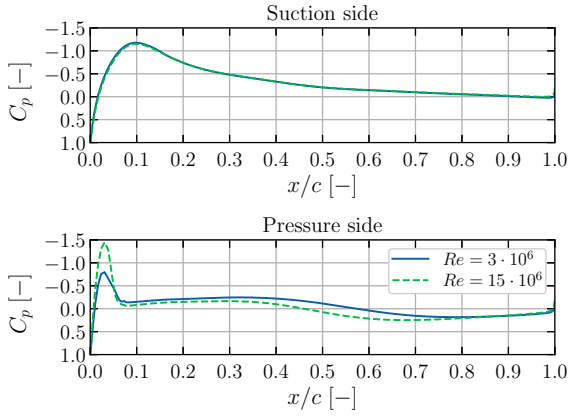

Figure 5.21: Chordwise C_p distribution near the symmetry plane: $\alpha = 0°$, $\beta = 0°$.

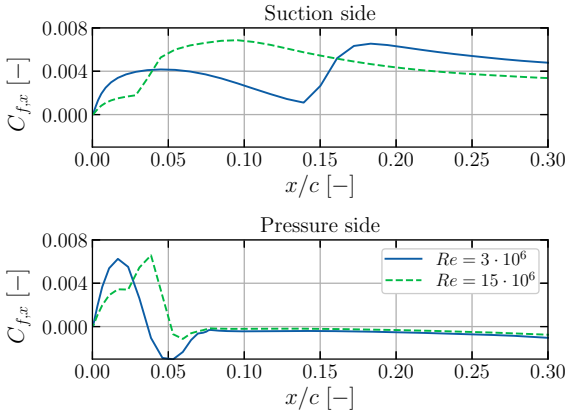

Figure 5.22: Chordwise $C_{f,x}$ distribution near the symmetry plane: $\alpha = 0°$, $\beta = 0°$.

5.2.3. Flow field analysis

Where the previous section mainly focused on several specific comparisons based on differences in force coefficients, this section will give a general overview of the flow features and characteristics of the LEI wing. The flow field around the LEI wing is complex and very dependent on the inflow conditions and Reynolds

number. This section will give an in-depth analysis of the flow field around the rigid LEI wing at $\alpha = 12°$ and $Re = 3 \cdot 10^6$. The Reynolds number and angle of attack are chosen based on experimental data presented in [21].

In Fig. 5.23, streamlines emanating from lines in front of the LEI wing are shown. Please note that for these plots, the wing and flow field are mirrored with respect to the symmetry plane. The pressure coefficient is plotted over the surface of the wing. The streamlines are coloured by the z-component of velocity U_z, which is normal the symmetry plane. The shape of the wing, combined with the loading on the suction side of the wing, cause the flow to be pulled inboard around the tips. On the pressure side, the pressure differential causes the flow to move outboard. This is essentially a stronger version of the tip vortex interaction that is usually seen on airplane wings. The effect on the aerodynamics of such a low aspect ratio wing will be much larger than on a high aspect ratio aircraft wing. This roll-up of the flow causes an increase of vorticity in the wake and the formation of a tip vortex. The pressure coefficient shows that the leading edge at the centre of the wing experiences the highest loading. This also comes back to the observed centre section separation discussed in detail in Section 5.2.2. If the centre section has the highest load, it will also have the largest adverse pressure gradient, hence the highest chance of separating the earliest.

The loading along the leading edge of the tip is much lower than the rest of the wing's leading edge loading, as can be seen in Fig. 5.24. This is a result of the curved shape that effectively bends the leading edge away from the incoming flow. The skin friction coefficient $C_{f,x}$ is plotted over the lower surface of the wing in Fig. 5.25. The regions with negative $C_{f,x}$ indicate the recirculation of the flow behind the leading edge. It can be seen that the three most inboard sections, when considering the struts as dividers, have the largest recirculation zones in terms of chordwise length. After the first three sections, the wing starts to curve downwards more strongly and this clearly impacts the recirculation regions. As was shown by the streamlines, the pressure side of the tip area causes a strong outwash. When observing the $C_{f,x}$ in this area, it is higher than at the centre sections of the wing. It seems as if this outwash and pressure loading on the tip decreases the recirculation behind the leading edge in this area. Last, close to the trailing edge of the struts the $C_{f,x}$ briefly increases strongly before the flow separates. A similar interaction happens of the trailing edge of the wing itself. This is due to the flow accelerating around the trailing edge of the struts and the wing, which momentarily increases the velocity and thus wall shear stress. It is comparable to the brief load peak over the rear of an Ahmed body, which is a numerical and experimental test case often used in the automotive industry [106]. However, the boundary layer is unable to stay attached along such a sharp corner, especially in the case of the capped off rear of the struts. This shows on the rear of the struts as $C_{f,x}$ is close to zero or negative in this area.

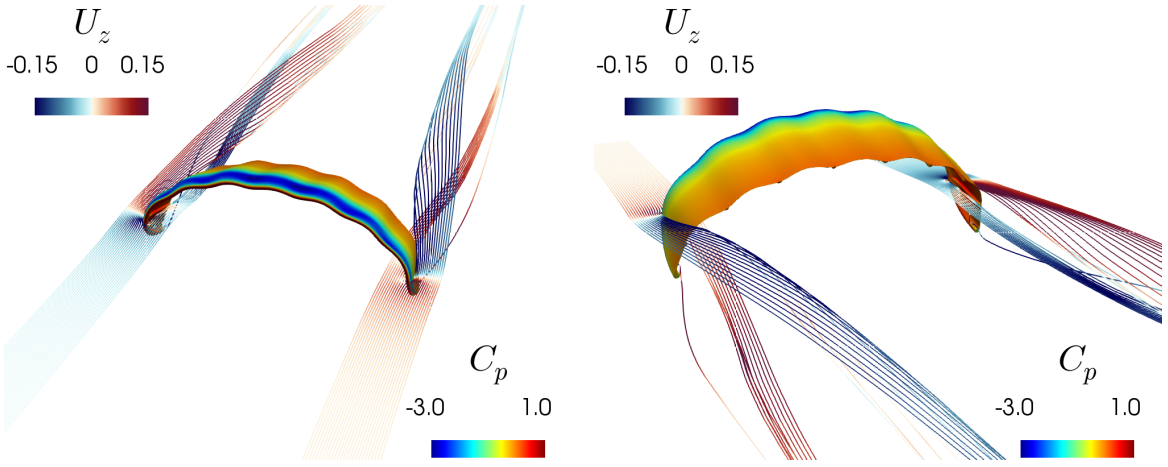

Figure 5.23: Front view (a) and rear view (b) of the C_p on the surface and the streamlines around the wing coloured by U_z: $Re = 3 \cdot 10^6$, $\alpha = 12°$, $\beta = 0°$.

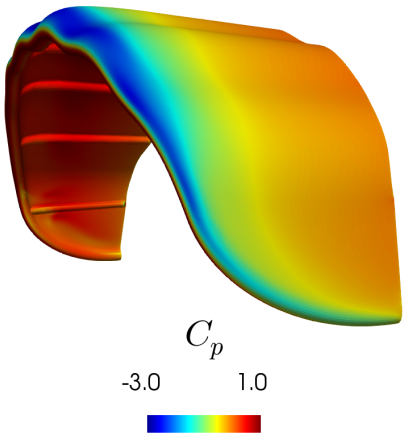

Figure 5.24: C_p on the surface of the wing: Re = $3 \cdot 10^6$, $\alpha = 12°$, $\beta = 0°$.

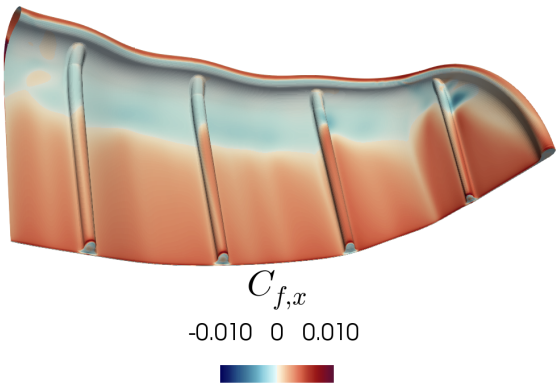

Figure 5.25: $C_{f,x}$ on the pressure side of the wing: Re = $3 \cdot 10^6$, $\alpha = 12°$, $\beta = 0°$.

The recirculation zones will have a large impact on the flow field around the LEI wing. In this section, only a few flow field slices will be presented and discussed. In Fig. 5.26 and Fig. 5.27, the x-component of velocity U_x and z-component of velocity U_z are presented. The x-component of velocity visualises the extent of the recirculation zone away from the wing. It shows that close to the surface of the wing, the negative x-component of velocity is highest, indicating the strongest flow reversal. Further away from the surface of the wing this effect diminishes. The z-component of velocity shows that the dominant flow direction on the pressure side is outwards and on the suction side is inwards. Around the most inboard and most outboard strut, one can see several regions which do not have a defined flow direction. Regions of positive and negative z-component of velocity alternate over small areas which can indicate that the flow circulates here in a spanwise direction as well, or that vortices influence the local flow field velocity distribution.

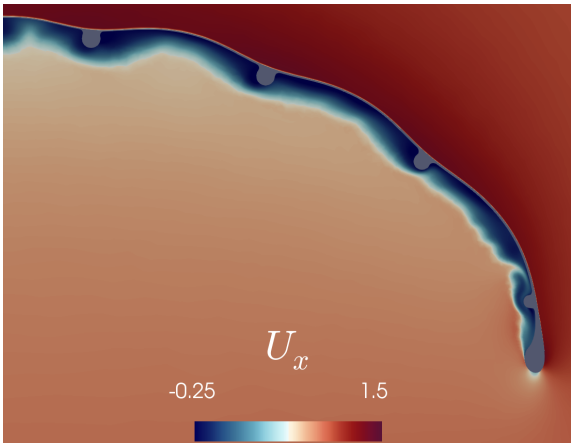

Figure 5.26: U_x at x = 0.3: Re = $3 \cdot 10^6$, $\alpha = 12°$, $\beta = 0°$.

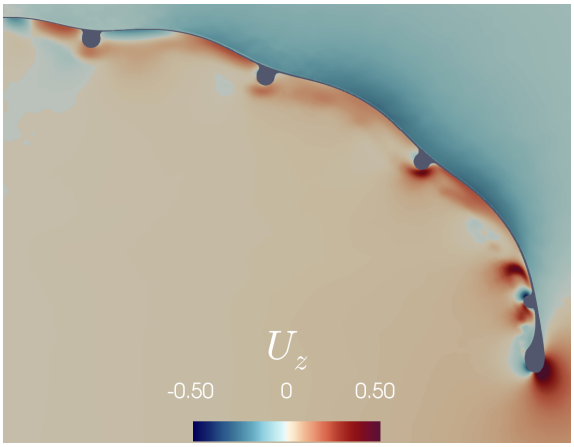

Figure 5.27: U_z at x = 0.3: Re = $3 \cdot 10^6$, $\alpha = 12°$, $\beta = 0°$.

In Fig. 5.28, the x-component of vorticity Ω_x is shown. Positive vorticity indicates a clockwise curl of the velocity field and negative vorticity indicates a counter-clockwise curl. Since the vorticity is by definition the curl of the velocity field, it is to be expected that certain trends of U_z and Ω_x relate to each other. This shows, as general trends in flow field directions match. However, one downside of only considering vorticity is that the curl of a velocity field can also be strong in a shear layer or boundary layer, resulting in regions that are flagged as high vorticity without having a large impact on the flow field. To overcome this, it is useful to also consider the Lambda2 criterion. In Fig. 5.29, the λ_2 vortex structures are plotted. As can be seen, it leads to a different visual result than the vorticity does. However, since this computation is within the recirculation region, it still shows diffused and spread out regions of positive λ_2. This will be different when moving further downstream, as will be shown in Section 5.2.4. Nonetheless, the Lambda2 criterion does highlight some

stronger vortex cores in the tip region and around the most outboard strut.

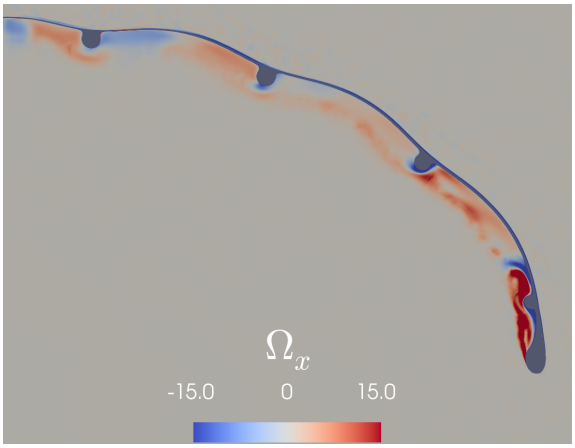

Figure 5.28: Ω_x at x = 0.3: Re = $3 \cdot 10^6$, $\alpha = 12°$, $\beta = 0°$.

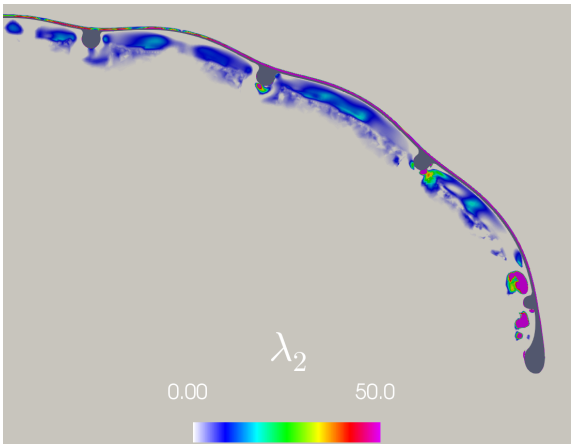

Figure 5.29: λ_2 structures at x = 0.3: Re = $3 \cdot 10^6$, $\alpha = 12°$, $\beta = 0°$.

In-depth analysis of the flow field slices and surface variable plots will require a considerable amount of figures. Therefore, it has been decided to do this concurrently with the comparison to the study done by Demkowicz [20]. As such, Section 5.2.4 will present the elaborate analysis of the flow field around the LEI wing and at the same time assess the impact of the struts on the flow field.

5.2.4. The impact of the struts

In this section, the impact of the struts on the aerodynamic performance of the LEI wing will be assessed for $\beta = 0°$. The results of the current study will be compared to the results of Demkowicz [20]. However, there were several challenges when comparing these results. Demkowicz [20] used a different scaling convention, which meant that the Reynolds numbers at which the simulations were done are not matching the current study exactly. This different scaling convention also meant a different LEI wing size and a different domain size. Furthermore, insufficient refinement of the volume mesh around the LEI wing and wake region could also impact the comparison. Therefore, it has been decided to perform a new simulation for just the flow condition discussed later in this section. This is done with the same geometry as used in Demkowicz's study and involved adding volumetric refinements, using the corrected Reynolds number and after solving, rescaling the domain. Only volumetric refinements regions have been added to the mesh, the surface mesh and all mesh settings such as first cell height are as used by Demkowicz [20]. The results of this newly done simulation will therefore still be referred to as Demkowicz's study in this section.

For the comparison of the force coefficients, however, this was not possible as it would require redoing all simulations done by Demkowicz. Comparisons of the force coefficients between the current study and Demkowicz's study [20] are shown in Fig. 5.30. The Reynolds number indicated in these plots corresponds to the current study. The Reynolds numbers in Demkowicz's study were 18% higher due to the different scaling. However, based on the curves it can be concluded that this difference in Reynolds number does not cause observable differences in trends. Looking at the force coefficient curves, it seems that the struts do not have a substantial impact. Before the maximum lift coefficient is reached, the lift curves of both studies almost fall on top of each other. There is also hardly any observable difference in the maximum lift coefficients, which occur at the same angles of attack. Arguably one of the only small differences in lift coefficient trends occurs post-stall. With the exception of Re = $15 \cdot 10^6$, the lift coefficients of Demkowicz's study are higher at the same angles of attack post-stall. For Re = $3 \cdot 10^6$, the lift-coefficient of the current study is lower between for $0° < \alpha < 16°$. When comparing the drag coefficients, the trends between the two studies are also quite comparable. However, there are some minor differences to be observed. First, for Re = $15 \cdot 10^6$ and Re = $1 \cdot 10^6$ the drag coefficient of the current study is lower post-stall. Second, for Re = $3 \cdot 10^6$, the drag coefficient of the current study is lower between for $0° < \alpha < 16°$. These drag coefficient differences can most likely be explained by the differences in the lift and the associated changes in lift-induced drag. Last, for Re = $0.1 \cdot 10^6$, the drag is slightly higher for the current study in the attached flow regime ($\alpha < 6°$). This could be an effect of the difference in Reynolds number since this is known to be a Reynolds number where are larger part of

the flow is laminar. This could mean that the higher Reynolds number case by Demkowicz has slightly less pressure drag. The drag polar highlights a bit more clear that the differences between the two studies appear to be largest for Re = $3 \cdot 10^6$. Considering the L/D shows that the aerodynamic efficiencies of both studies are fairly equal. The only exception to this is the difference at Re = $3 \cdot 10^6$, where the aerodynamic efficiency of the current study appears to be higher for $0° < \alpha < 16°$.

Based on this comparison, it can be concluded that there are no clear differences in trends between the two studies. As such, the impact of the struts on the force coefficients seems small. However, the flow fields will be compared next and it is still expected to observe differences there.

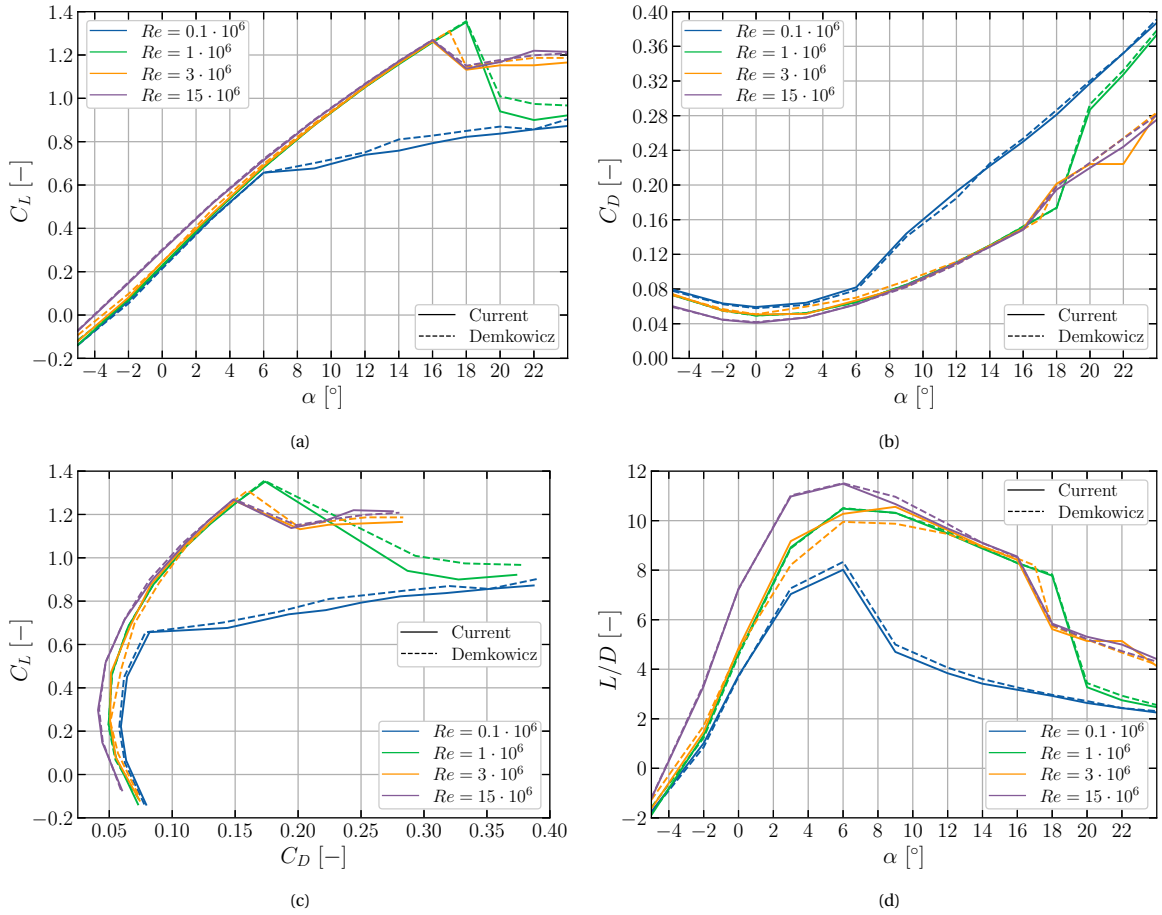

Figure 5.30: Comparison of the lift curve (a), drag curve (b), drag polar (c) and aerodynamic efficiency (d) between the current study and Demkowicz's study [20] for different Reynolds numbers.

The rest of this section will be spent on the comparison of the flow field and surface variables between the two studies. This is done at Re = $3 \cdot 10^6$ and $\alpha = 12°$. In terms of flow field, this will mainly be done based on two planes at x-locations x = 0.3 and x = 0.6. The reason for choosing these two locations is that x = 0.3 resides inside the recirculation region on the pressure side and x = 0.6 just behind it. This way it is also possible to assess how differences upstream propagate downstream. Starting the comparison with the analysis of the total pressure coefficient $C_{p,T}$ at x = 0.3 in Fig. 5.31. The struts will be referred to by the numbers 1 to 4, starting counting from the side of the symmetry plane. First comparing the regions between the symmetry plane and strut 1 and strut 1 and strut 2. It can be seen that the regions of losses in the study by Demkowicz show a much more upward and downward variation. Most notably between strut 1 and strut 2, Demkowicz study has a high $C_{p,T}$ region much closer to the surface. Between strut 2 and strut 3, the high $C_{p,T}$ region also approaches the surface closer in Demkowicz's study. It is likely that the struts forming blockage and restricting the flow in these regions cause this difference. In the tip region around strut 4 it can also be seen that the losses are stronger in the study by Demkowicz. The suction side of the wing shows no visible differences between the two studies for this location and flow field variable.

Further downstream at x = 0.6, the presence of the struts also has an impact on the flow field, as shown in Fig. 5.32. If one would only look at the results of the current study, it could be argued that some of the losses are caused by the struts. When also considering the result of Demkowicz, one can see that many of the losses already appear in approximately similar places. The loss around strut 1 seems to be split up by the strut, but there is still a loss observed at the same location in Demkowicz's study. Around strut 2 and 3 this changes slightly, as it seems that there is more of a build-up of loss in the vicinity of the strut, whereas it is more spread out in the study of Demkowicz. It is likely that the struts impact the recirculation regions and therefore steer the losses into more defined directions. In the tip region, there are clear losses at strut 4 which do not appear in Demkowicz's study. However, in Demkowicz's study the region behind the leading edge of the tip has more losses on the pressure side. Finally, there are no differences on the suction side of the wing.

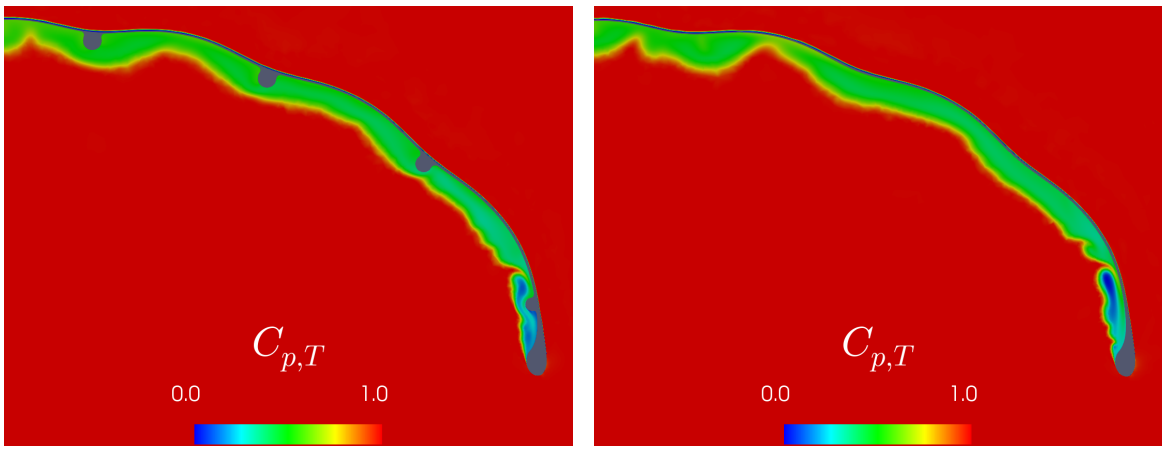

(a) (b)

Figure 5.31: $C_{p,T}$ at x = 0.3 for the current study (a) and Demkowicz's study [20] (b): Re = $3 \cdot 10^6$, $\alpha = 12°$, $\beta = 0°$.

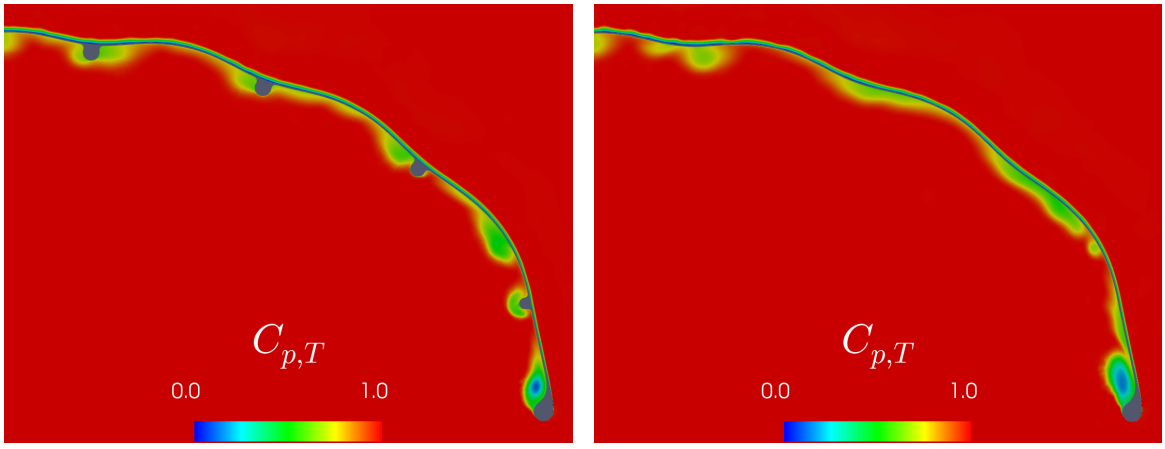

(a) (b)

Figure 5.32: $C_{p,T}$ at x = 0.6 for the current study (a) and Demkowicz's study [20] (b): Re = $3 \cdot 10^6$, $\alpha = 12°$, $\beta = 0°$.

The next variable for which a comparison will be done is the z-component of velocity U_z. This is shown in Fig. 5.34 at x = 0.3, which is inside the recirculation zone behind the leading edge. First considering the regions around strut 1 and strut 2. It can be seen that in Demkowicz's study, the z-component of velocity magnitudes are higher in the regions where otherwise the struts block the crossflow. This is especially true for the negative velocity region immediately to the right of strut 1 and the positive velocity region to the left of strut 2. When moving further outboard to the area around strut 3, similar observations can be made. There is a higher positive velocity in the study by Demkowicz, whereas the flow is slowed down more in the present study. However, it is interesting to note that it seems that in the current study, the flow accelerates over strut

3. This can be deduced by the high peak velocity, which also seems to cause a higher positive velocity to the right of strut 3. The cluster of positive and negative velocity just above strut 4 could indicate the presence of a vortex in this region. Similarly, at the bottom side of strut 4, there is a high positive peak velocity, which does not exist in that location in Demkowicz's study.

At x = 0.6 there are similar differences, as can be seen in Fig. 5.34. First, it is interesting to note that the flow field interaction around the area of strut 1 seems very similar. In both studies, there seems to be a region close to the surface of the wing where positive and negative velocity regions meet. Therefore, this interaction seems more dominated by the shape of the wing, rather than the presence of the strut. However, it also shows that the struts do influence the position of the crossflow regions, as clear differences can be seen around strut 2 and strut 3. For the current study, the regions with positive velocity have shifted to the left, due to the strut limiting the crossflow. This also creates a very different velocity field to the right of strut 3. There are clear variations in velocity direction around strut 4, these variations do not occur in Demkowicz's study. Some conclusions can also be drawn when comparing the flow field at x = 0.3 with x = 0.6. Where at x = 0.3 it seems there is very strong outwashing crossflow, this is no longer present at x = 0.6. This could mean several things. First, the crossflow may be induced by the shape of the wing at the leading edge. Once the flow then propagates further downstream it is more dominated by other local effects which cause this strong crosslow to diffuse. Second, since there are recirculation regions on the pressure side behind the leading edge, it is possible that these dominate the crossflow in this area. Once these recirculation regions cease to exist, at x = 0.6, the crossflow also decreases. Third, the downstream flow field will have an effect on the upstream flow field. As Fig. 5.23 showed, there is quite some down- and inwash behind the wing. As it is an incompressible flow field, the flow situation downstream will influence the situation upstream and vice versa. There is no visible difference in U_z over the suction surface of the wing when comparing the two studies. However, it can be observed that further downstream the negative velocity becomes stronger over the suction side of the wing. This is to be expected due to the anhedral shape of the wing combined with the design of the airfoil section.

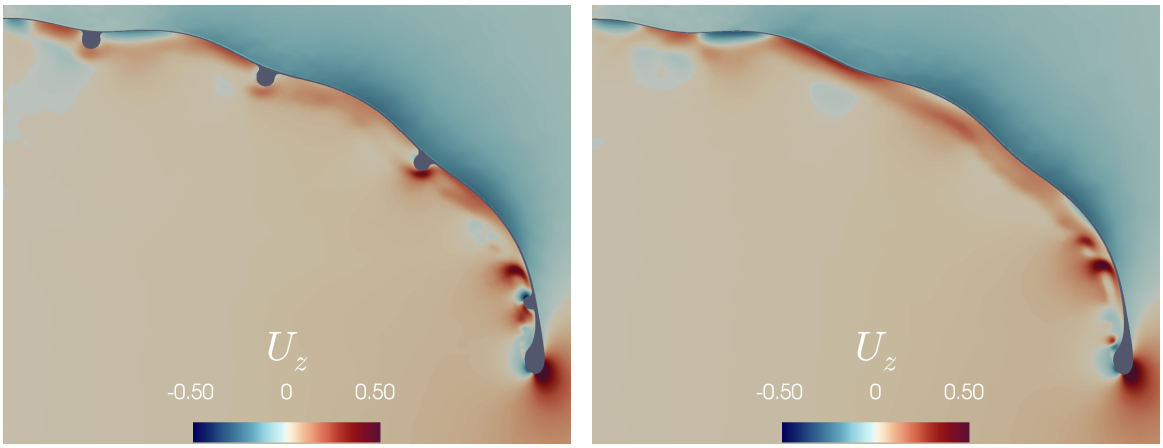

(a) (b)

Figure 5.33: U_z at x = 0.3 for the current study (a) and Demkowicz's study [20] (b): Re = $3 \cdot 10^6$, $\alpha = 12°$, $\beta = 0°$.

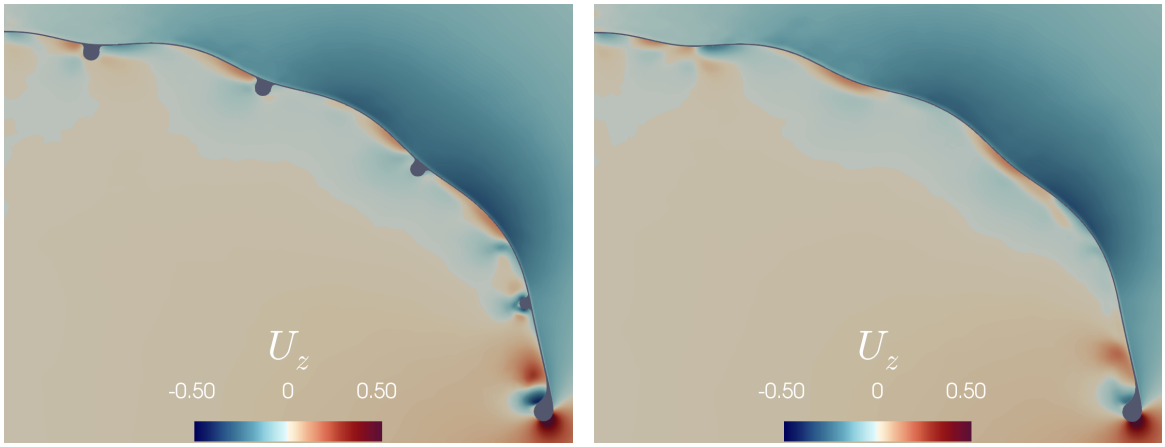

(a) (b)

Figure 5.34: U_z at x = 0.6 for the current study (a) and Demkowicz's study [20] (b): Re = $3 \cdot 10^6$, $\alpha = 12°$, $\beta = 0°$.

The plots for the x-component of vorticiy Ω_x at x = 0.3 are shown in Fig. 5.35. Again, positive vorticity indicates clockwise rotation and negative vorticity counterclockwise rotation. It can be seen that around strut 1, the blockage formed by the strut causes a region of positive vorticity to be directed around the lower side of the strut. This redirecting does not occur in the study by Demkowicz. Nonetheless, the main topology of vorticity regions is similar around strut 1, albeit slightly offset. First, there exists a negative vorticity region near the symmetry plane, next to this a positive region and then again a negative region of vorticity. Below strut 2, there is a small region of negative vorticity, something which does not occur in Demkowicz's study. Because of this, the negative region of vorticity observed in Demkowicz's study, between strut 2 and strut 3, does not appear in the present study. Over the lower side of strut 3, there is again a region of negative vorticity. Between strut 3 and strut 4, the vorticity distribution is also visibly different between the two studies. In the current study, the majority of this region consists of positive vorticity, whereas in Demkowicz's study the positive vorticity has a much lower magnitude, especially close to the surface of the wing. This relates back to the z-component of velocity presented earlier. Both studies have a region of high positive vorticity from the extreme of the tip upwards.

The differences in Ω_x at x = 0.6 are plotted in Fig. 5.36. It can be seen that for the current study, the vorticity regions around strut 1 and strut 2 have a higher magnitude. It seems that in Demkowicz's study, the vorticity is more distributed over a larger area and, therefore, has a lower magnitude. Between strut 3 and strut 4, it gets even more interesting. In the current study, there is a positive and a negative region which seem to collide causing high vorticity magnitudes at the point where they meet. The boundary layer at this collision location could be compromised by the counter-rotating vorticity regions pulling it off the surface. When looking back at Fig. 5.32, one can see an accumulation of losses at this exact location, which could indicate the boundary layer losses being pulled of the surface. Again, for Demkowicz's study, the magnitude of vorticity is much lower and more distributed over this region. Around strut 4, there are two very defined regions of positive and negative vorticity which are non-existent in Demkowicz's study. These will have a strong effect on the local flow field and this could be the reason for the strong differences in the area between strut 3 and strut 4. The high positive vorticity region at the extremity of the tip has again a larger magnitude and seems to be pushed down towards the tip. This can be a direct result of this negative vorticity at the bottom of strut 4. In Demkowicz's study, non of these effects occur and it can be seen that the positive vorticity at the tip is more distributed and less strong. From comparing the x-component of vorticity, it is clear that there are differences between the flow field of the two studies on the pressure side which are caused by the struts. At x = 0.3 the flow field seems to be more dominated by what happens upstream and by the shape of the wing, but at x = 0.6 the impact of the struts on the local flow field becomes clear further outboard.

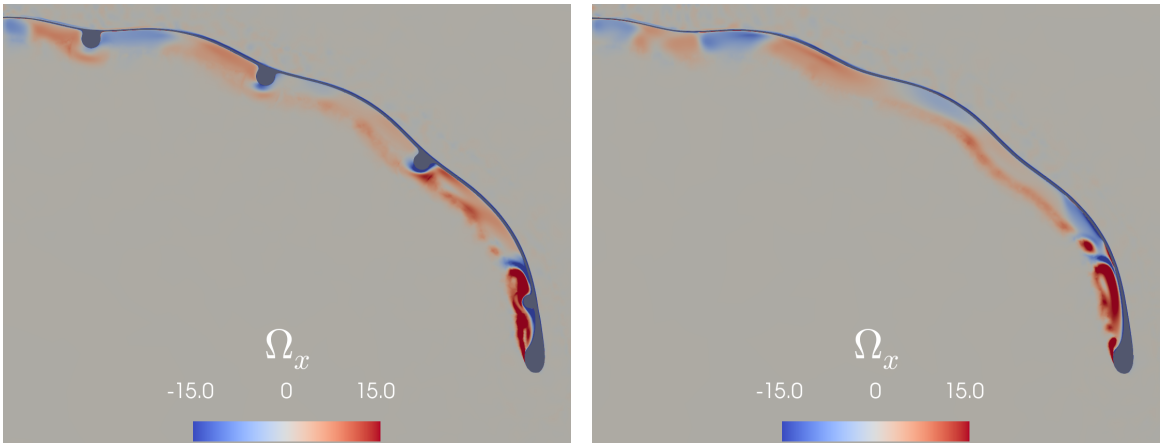

(a) (b)

Figure 5.35: Ω_x at x = 0.3 for the current study (a) and Demkowicz's study [20] (b): Re = $3 \cdot 10^6$, $\alpha = 12°$, $\beta = 0°$.

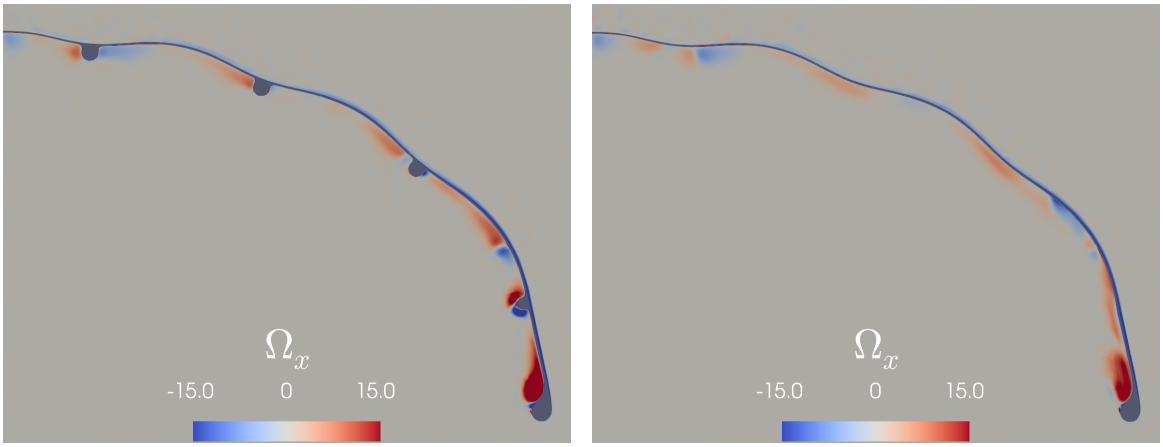

(a) (b)

Figure 5.36: Ω_x at x = 0.6 for the current study (a) and Demkowicz's study [20] (b): Re = $3 \cdot 10^6$, $\alpha = 12°$, $\beta = 0°$.

In Fig. 5.37, the skin friction coefficient $C_{f,x}$ on the pressure side of the wing is plotted for both studies. First, it is interesting to note some observations that can be made based on Demkowicz's study. When considering the region where the $C_{f,x}$ is positive, downstream of the recirculation region, it can be seen that for the locations where strut 1 to strut 3 are in the current study, there are straight lines with close to zero $C_{f,x}$. As the analysis of the x-component of vorticity showed, there were multiple regions where positive and negative vorticity would collide below the surface of the wing. The locations where this happens correspond to the straight lines with close to zero $C_{f,x}$ as seen in Fig. 5.37 (b). The fact that these locations match so closely with the locations of the struts indicates very clearly how much the flow field is dominated by the shape of the wing. In Demkowicz's study, the recirculation region has a much more wavy pattern in the spanwise direction, clearly caused by the fact that the flow can move around unrestricted below the wing.

When considering the region from strut 3 to the tip, the differences between the two studies are larger, which was also the case for the flow field slices discussed previously. It can be seen that between the location of strut 3 and strut 4, the shape of the recirculation zone is different. To the right of strut 4, the recirculation region is much smaller for the current study. This could be caused by the blockage of strut 4, as this results in stronger vorticity being contained in this region. This stronger vorticity also causes the higher $C_{f,x}$ on the surface of the current study. The comparison of the $C_{f,x}$ plotted on the surface shows that there are several mechanisms at play. First, there is the shape of the LEI wing itself, which seems to strongly influence the main distribution. Second, there is the impact of the struts, which influence the recirculation region shapes and cause differences in the tip region.

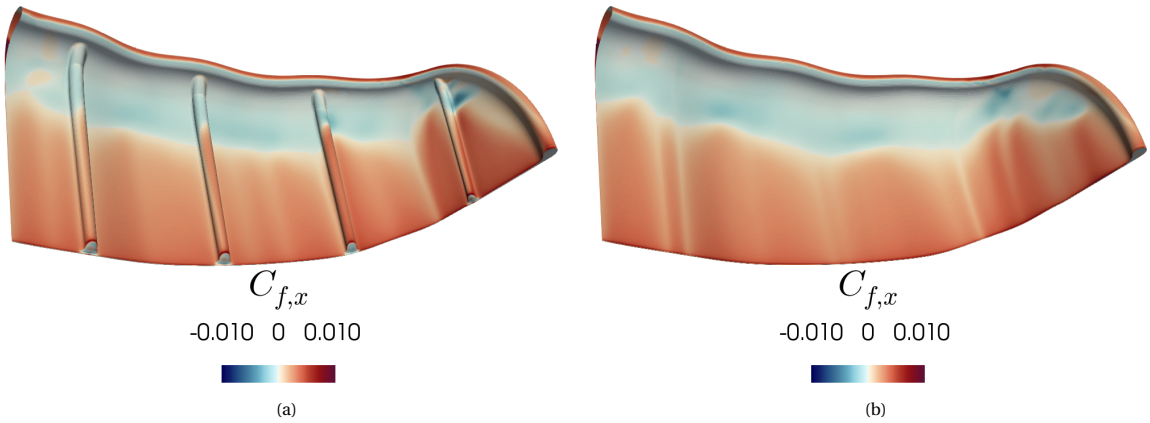

Figure 5.37: $C_{f,x}$ on the pressure side of the wing for the current study (a) and Demkowicz's study [20] (b): Re = $3 \cdot 10^6$, $\alpha = 12°$, $\beta = 0°$.

To assess the differences in a more detailed manner, the pressure and skin friction distributions have been computed for both cases. Starting with the chordwise pressure distribution near the symmetry plane in Fig. 5.38. What this shows is that there is no difference over the suction surface of the wing. The pressure surface, however, does show some differences. These differences were already observed from the $C_{f,x}$ plotted in Fig. 5.37, but can be more quantitatively compared now. The plot shows that at this specific location, for $0.18 < x/x < 0.35$ the C_p is higher in the current study.

Comparing $C_{f,x}$ in Fig. 5.39, more differences can be observed. For both studies, the transition happens at approximately the same point on the suction side, indicated by the rapid increase of $C_{f,x}$ starting around $x/c = 0.08$. After this, there is a slight offset between the two lines, although they do follow the same trend. Since there were no observable differences in the flow field on the suction side of the LEI wing, this offset could be caused by the differences in $y+$ between the two cases. Demkowicz [20] used $y+ < 1$ as a condition for the first cell height, whereas the current study uses $y+ \ll 1$. This will influence the velocity gradient near the wall and, therefore, also the boundary layer profile and computation of the velocity gradient at the wall. The fact that the pressure distributions over the suction surface match each other exactly shows that this difference in $C_{f,x}$ does not have an impact on the loading of the LEI wing. As also observed in Fig. 5.37, the $C_{f,x}$ on the pressure side does show some more defined differences. As can be seen, in Demkowicz's study there is a larger recirculation region which starts later and the $C_{f,x}$ over the remainder of the pressure side is higher. For the current study, there is a very small recirculation region, followed by a region where the $C_{f,x}$ stays very close to zero, until it recovers. The $C_{f,x}$ of Demkowicz's study is higher from approximately $x/c = 0.36$ onwards, which on this side is most likely caused by the differences in the flow field, rather than $y+$.

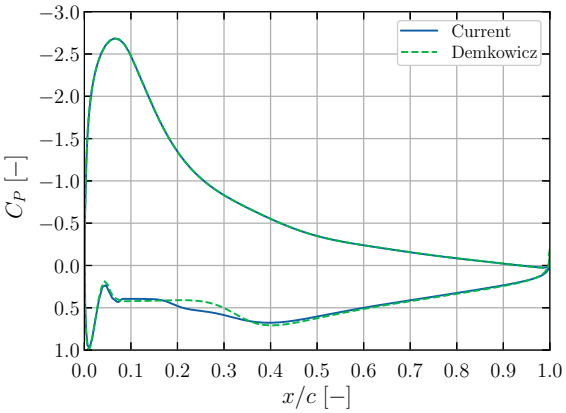

Figure 5.38: Comparison of the chordwise C_p distribution to Demkowciz's study [20] near the symmetry plane: Re = $3 \cdot 10^6$, $\alpha = 12°$, $\beta = 0°$.

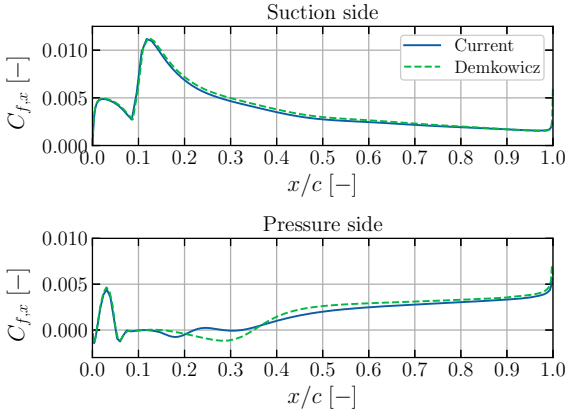

Figure 5.39: Comparison of the chordwise $C_{f,x}$ distribution to Demkowciz's study [20] near the symmetry plane: Re = $3 \cdot 10^6$, $\alpha = 12°$, $\beta = 0°$.

Similar to the chordwise distributions, it is possible to compute the spanwise distributions of selected variables. This will be done at the same locations as the earlier discussed flow field slices. The definitions of the x-axes variables $arc_{n,u}$ and $arc_{n,l}$ were given in Section 5.1.

Starting with the spanwise distribution at x = 0.3, as shown in Fig. 5.40. As can be seen, the loading on the suction side of the wing is similar between the two cases. The peak load that can be close to $arc_{n,u} = 1.0$ is caused by the flow the accelerating around the leading edge of the tip due to the pressure differential. High positive U_z was observed at the leading edge of the tip in Fig. 5.33. For the pressure side, there is much more variation, which is in line with other observations done so far. The approximate locations of the struts are indicated by vertical lines. It can be seen that at many locations the pressure coefficient exhibits different behaviour. One thing that becomes clear is how the pressure drops over the first two struts. This makes sense since the crossflow will cause the flow to accelerate over the bottom side of the struts. The higher pressure will then be in the area of the fillets near the struts, as the flow is more restricted here. This interaction clearly shows for strut 1 and strut 2. At strut 3, it can be seen that the pressure drop does not occur at the approximate normal centre line of the strut. This can be explained by the fact that the main shape of the wing starts to bend downwards here, meaning the centre line of the strut is no longer the lowest point in y-direction. This causes the pressure drop to shift to a location slightly off-centre. When relating this back to Fig. 5.33, it can be seen that U_z velocity peak also occurs more to the right. The plots, therefore, correspond very well to what was seen in the flow field analysis. A strong increase in C_p can also be seen to the left of strut 4, with a very strong drop until the approximate centre line of the strut. This large variation in C_p is caused by the strong vorticity observed in this region in Fig. 5.35.

Comparing this to the pressure distribution of Demkowicz's study shows the clear impact the struts have on the loading on the pressure side. For Demkowicz's study, most of the inboard pressure distribution is very gradual with only a strong increase in C_p around $arc_{n,l} = 0.25$. For $arc_{n,l} > 0.8$, there is a slight increase before a strong drop in C_p. This drop also happens for the current study, but due to the strut, it occurs further outboard. Additionally, the pressure drop in this region is much smaller for Demkowicz's study but spread out over a larger region. Generally, the differences between the two studies are the largest in the tip region on the pressure side. This corresponds well with the flow field observations, where the tip region on the pressure side showed the largest differences.

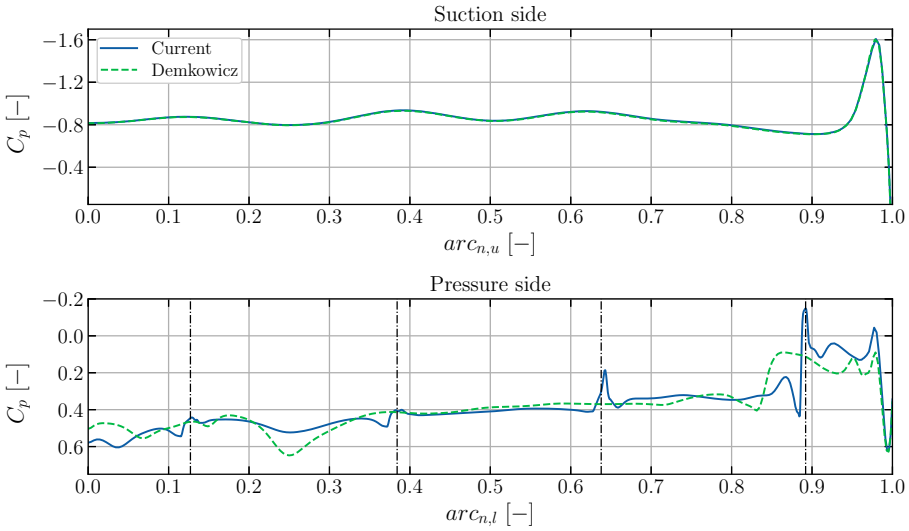

Figure 5.40: Comparison of the spanwise C_p dstribution to Demkowicz's study [20] at x = 0.3: Re = $3 \cdot 10^6$, $\alpha = 12°$, $\beta = 0°$.

The spanwise pressure distribution plots at x = 0.6 are shown in Fig. 5.41. Before focusing on the comparison of the two studies, some general remarks about the differences between the two x-locations can be made. What can be seen is that the C_p on the suction side of the wing at x = 0.6 is higher than at x = 0.3, indicating less load. This was also observed in Fig. 5.24, which highlighted the fact that close to the leading edge, the strongest loading occurred. Moving further downstream over the suction surface of the wing, the loading dropped rapidly. In addition to this, the pressure side loading is much more gradual at x = 0.6 and less extreme peaks occur. This also relates back well to the more muted U_z velocity field in Fig. 5.33 at x = 0.6, when compared to the U_z velocity at x = 0.3 in Fig. 5.34.

It can be seen that loading wise, the two studies show much more comparable results at x = 0.6. The previously seen influence of strut 1 and strut 2 on the local loading is much more benign than at x = 0.3. This results in a much closer match in these regions between the two studies. There is no longer a peak loading over strut 3, which caused such a clear observable difference in the previous plot. The first clear difference between the two studies occurs in the region around strut 4. There are small peaks on either side of strut 4, which correspond well with the high negative U_z observed in Fig. 5.34 and the vorticity in Fig. 5.36. Again, it is the tip region where the largest differences between the two studies are observed. However, the differences are much smaller in this case. Similar as at x = 0.3, the C_p in Demkowicz's study is higher and spread out over a larger area. In the current study, there is a stronger and more defined pressure peak. These differences in the tip region are in agreement with the observations made on the flow fields.

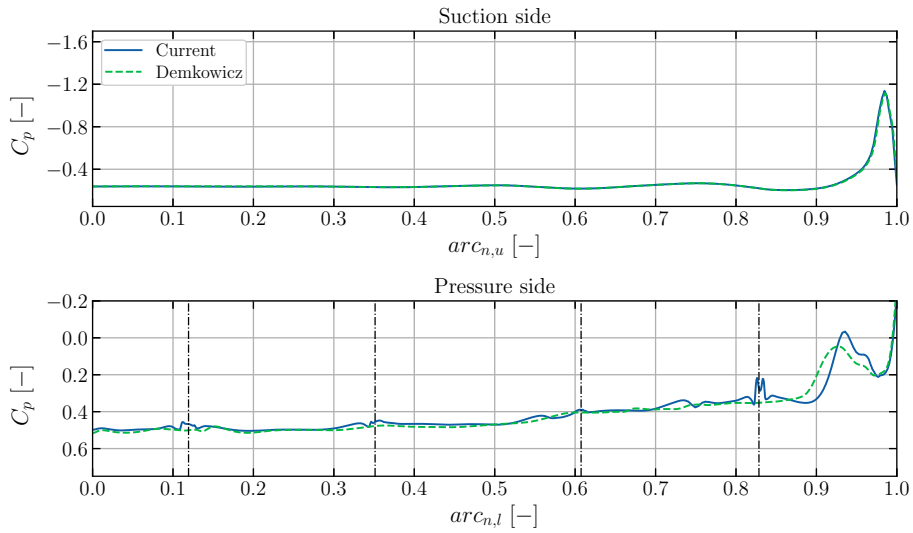

Figure 5.41: Comparison of the spanwise C_p dstribution to Demkowicz's study [20] at x = 0.6: Re = $3 \cdot 10^6$, $\alpha = 12°$, $\beta = 0°$.

In this section, the impact of the struts on the aerodynamic performance of the LEI has been analysed for $\beta = 0°$. For these cases, only half of the domain needed to be considered, assuming the flow would be fully symmetric around the symmetry plane. The results of the current study have been thoroughly analysed and compared to a newly run case based on the geometry used in Demkowicz's study [20]. The comparison has been done based on force coefficients, flow field data and surface variables. These are all used to build a better picture of the impact the struts have on the overall aerodynamic performance of the LEI wing. The following observations and conclusions were made about the impact of the struts:

- The addition of the struts did not have a major impact on the force coefficients. For both the lift and drag coefficient, the current study and Demkowicz's study [20] showed very comparable results. The maximum lift coefficients were all matching closely and occurred at the same angle of attack. Post-stall, the lift coefficients of Demkowicz's study are higher at all Reynolds numbers with the exception of Re = $15 \cdot 10^6$. For Re = $3 \cdot 10^6$, the lift coefficient of the current study was slightly lower for $0° < \alpha < 16°$. This led to the drag coefficient being lower in this range as well. The drag coefficients post-stall were lower in the current study for Re = $1 \cdot 10^6$ and Re = $15 \cdot 10^6$. As the differences between the lift- and drag coefficients were not large, no strong changes in the aerodynamic efficiency were observed. These mixed observations and no consistent trend between the differences between the studies show that the struts do not have a clearly defined impact on the aerodynamic force coefficients.

- Comparisons between the flow fields of the two studies have been made at x = 0.3 and x = 0.6. Comparison of the total pressure coefficient showed that the blockage of the struts did impact the locations and size of the recirculation regions. They also caused more loss build-up, whereas in Demkowicz's study [20] the losses were more freely distributed along the surface of the wing. Comparison of the z-component of velocity showed that at x = 0.3, less strong crossflow was present in the regions in between the struts. However, the flow accelerated over strut 3, causing a much higher positive crossflow there. There was also a strong influence of strut 4 on the local velocity field observed. At x = 0.6, the strong crossflow was no longer present and differences were more benign. The struts impacted the vorticity distribution at x = 0.3 and x = 0.6. The largest differences were observed to be from strut 3 outboard, which is in line with the differences seen for the z-component of velocity. The blockage of strut 4 caused counter-rotating vorticity regions on the sides of the strut. This had a larger impact on the flow field around the tip area. In the current study, the vorticity regions seemed smaller in size but stronger in magnitude. Since for Demkowicz's study, no blockage of the struts was present, the vorticity field was distributed more freely. In general, the flow field seemed to be mainly dominated by the shape of the wing itself, with the struts causing local changes.

- Comparison of the skin friction coefficient $C_{f,x}$ on the pressure side of the LEI wing further highlighted the influence of the LEI wing shape over the impact of the struts. For Demkowicz's study [20], there were several straight lines of low $C_{f,x}$ observed on the pressure side. These were caused by alternating

vorticity fronts colliding and seemed to occur at similar locations as the struts. This is an important observation as it highlights the strong influence the LEI wing shape has on the flow field. If these locations align with the locations of the struts, it partly explains why the results between the two studies are fairly similar. Even though the flow field mechanisms at play might not be exactly the same, they do lead to a quite similar flow field. This especially goes for the part of the wing inboard of strut 3. Outboard of strut 3, the differences were larger and this changed the regions with negative $C_{f,x}$ considerably.

- The pressure distributions over the LEI wing have been compared in chordwise and spanwise direction. For the chordwise direction at a location near the symmetry plane. This showed that there was no visible difference in the loading over the suction surface of the wing at that specific location. The pressure side did show some differences, which was to be expected due to the differences in the recirculation regions. Considering the spanwise pressure distribution at both x = 0.3 and x = 0.6, supported the flow field observations made earlier. At x = 0.3, the presence of the struts had a clear influence on the pressure distribution. With the largest differences observed around the tip area, where there was a more negative pressure loading for the current study. The observation that the vorticity seemed more distributed, with lower peak loads, in Demkowicz's study was also backed up by the pressure distribution. At x = 0.6, the differences were much smaller, with only the region from strut 4 outboard showing similar differences as at x = 0.3. At both locations, the pressure distribution over the suction side was the same.

5.3. Aerodynamic performance of the LEI wing ($\beta \neq 0°$)

In this section, the analysis of the aerodynamic performance of the LEI wing under sideslip conditions will be presented. For this it is necessary to use a full-domain without symmetry plane. First, a comparison between the half-domain and full-domain cases will be in discussed in Section 5.3.1. After this, the impact of the sideslip angle on the aerodynamic force coefficients will be discussed in Section 5.3.2. This is followed by a flow field analysis in Section 5.3.4 and the comparison of the impact of the struts under sideslip conditions in Section 5.3.4.

5.3.1. Half-domain vs. full-domain

In this subsection, a comparison between a half-domain and full-domain case will be done at $\beta = 0°$. This to assess the impact of the symmetry assumption. The reference condition at which this comparison is done is $Re = 3 \cdot 10^6$ and $\alpha = 12°$. In Table 5.1, the aerodynamic coefficients are compared. As can be seen from this, the difference in force coefficients between these two cases is minimal. Nonetheless, it is still worth comparing the flow fields.

Table 5.1: Comparison of the force coefficients between the half- and full-domain cases.

	Half-domain	Full-domain	Δ [%]
C_L [−]	1.05320	1.05158	-0.15
C_D [−]	0.10947	0.10966	+0.17

In Fig. 5.42, the total pressure coefficient, $C_{p,T}$ is shown for the half-domain and full-domain, respectively. As can be seen, the flow field for the full domain case is not symmetrical. The struts will be referred to numbered from left to right based on the full-domain case, this means the struts from the half domain case start at number 5. The first difference can be observed around the location of the symmetry plane and strut 4 and 5. In this area, there seem to be much more losses underneath the struts in the half-domain case. This could be the result of the symmetry plane impacting the recirculation region between the symmetry plane and strut 5. In the full domain case, the flow is able to move freely in this region and since the recirculation region is three-dimensional, it is to be expected that this will lead to differences. The other differences can be observed in the tip region, especially when comparing the left-hand side of the full-domain case to the half-domain case. The right-hand side of the full-domain case matches relatively well with the half-domain case. Since the geometry is entirely symmetrical, one would expect the flow fields to be entirely symmetrical. It could be that underlying instability of the flow field causes issues with convergence, hindering the solver to converge to a fully symmetrical flow field. Even when running this full domain case for 20000 iterations, instead of 6000, it did not lead to a symmetrical averaged flow field.

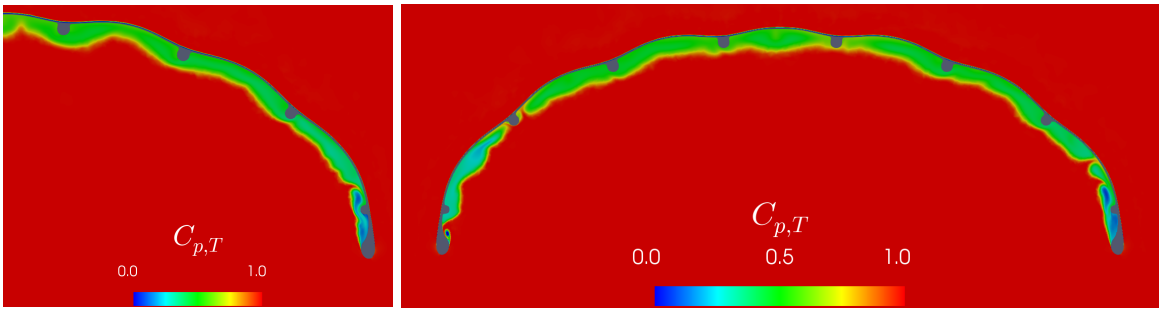

(a) (b)

Figure 5.42: $C_{p,T}$ at x = 0.3 for the half-domain (a) and full-domain (b): Re = $3 \cdot 10^6$, $\alpha = 12°$, $\beta = 0°$.

It is interesting to see that the force coefficients are still so similar for the differences in flow fields observed. However, such an observation was also made when analysing the impact of the struts for the half domain cases. Therefore, no further in-depth analysis will be done on the comparison between the half-domain and full-domain cases. It can be concluded that there are differences between the half-domain and full-domain cases, but that these do not lead in significant changes in force coefficients. As such, when taking factors such as time and computational resources into account, the usage of the half-domain cases is justified for cases where $\beta = 0°$. However, if it would be possible to obtain quantitative flow field data from experimental tests, rather than just force coefficients, the full-domain case is preferred for correlation.

5.3.2. Aerodynamic force coefficients

In this section, the aerodynamic force coefficients under sideslip conditions will be analysed. The force coefficients curves are presented in Fig. 5.43. Since these simulations have been done at a fixed angle of attack $\alpha = 12°$, the plots have the sideslip angle β on the x-axis. Plotted are the lift, drag and sideforce coefficient and the aerodynamic efficiency. The sideslip angle ranges from 0° to 12° with intervals of 4°. This sideslip range has been chosen based on the experimental data of Oehler et al [18].

First, some observations can be made about the effect of the Reynolds number on the aerodynamic force coefficients under sideslip conditions. As can be seen, the lift coefficient increases with Reynolds number at all sideslip angles considered. However, the differences between the curves are minimal and up to and including $\beta = 8°$, the differences are in the order of 1%. At $\beta = 12°$, the case at Re = $1 \cdot 10^6$ stalls, as a strong drop in lift coefficient can be observed. While at other Reynolds numbers the lift coefficient also drops, it is not as severe. The drag coefficient shows an inverse relationship with the Reynolds number, as the drag coefficient decreases with increasing Reynolds number. Again, at $\beta = 12°$ it can be seen that the case at Re = $1 \cdot 10^6$ has stalled, as the drag rises much more than at the other two Reynolds numbers. The Reynolds number seems to have little effect on the sideforce coefficient. What is interesting to note is that also the sideforce coefficient drops off at $\beta = 12°$ for the case at Re = $1 \cdot 10^6$. This means that the stall occurs at both the centre section of the wing as well as the tip regions since the tips are the largest contributor to the sideforce coefficient. The changes in aerodynamic efficiency are a result of the differences in lift and drag coefficient. Therefore, the effect of the Reynolds number on this variable is as expected.

Now taking the case at Re = $3 \cdot 10^6$ as a reference condition and analysing it in more detail. Starting by looking at the lift coefficient curve, which shows a clear trend. As can be seen, the lift coefficient drops for increasing sideslip angle. The loss is not constant for each increase in sideslip angle but rather increases with each subsequent interval. Therefore, for this LEI wing at this specific flow condition, it is clear that the relationship between the lift coefficient and sideslip angle is non-linear. The loss in lift coefficient at $\beta = 12°$, relative to $\beta = 0°$, is 11.2%. When considering the drag coefficient curve, there seems to be an opposite trend. For each subsequent sideslip angle increase, the increase in drag coefficient becomes larger. The increase in drag is much more substantial than the loss in the lift. The increase in drag coefficient at $\beta = 12°$, relative to $\beta = 0°$, is 61.0%. It can be seen that at $\beta = 0°$, the sideforce coefficient is zero. In Section 5.3.1 it was shown that the flow field on the pressure side of the wing at x = 0.3 was asymmetrical for $\beta = 0°$. However, when considering the full flow field around the LEI wing, there is no net sideforce present at $\beta = 0°$. This also further supports the usage of a half-domain when the sideslip angle is zero. Contrary to the lift and drag coefficient, the relationship between the sideforce and the sideslip angle seems to be linear. For an increase

in the sideslip angle, there is also an increase in the sideforce, which is as expected. While the lift coefficient does not decrease too much during sideslip, the drag coefficient sees a strong increase. This means that the aerodynamic efficiency of the LEI wing will decrease. The aerodynamic efficiency is plotted in Fig. 5.43 as well. It shows that the decrease in L/D at $\beta = 12°$, relative to $\beta = 0°$, is 44.8%.

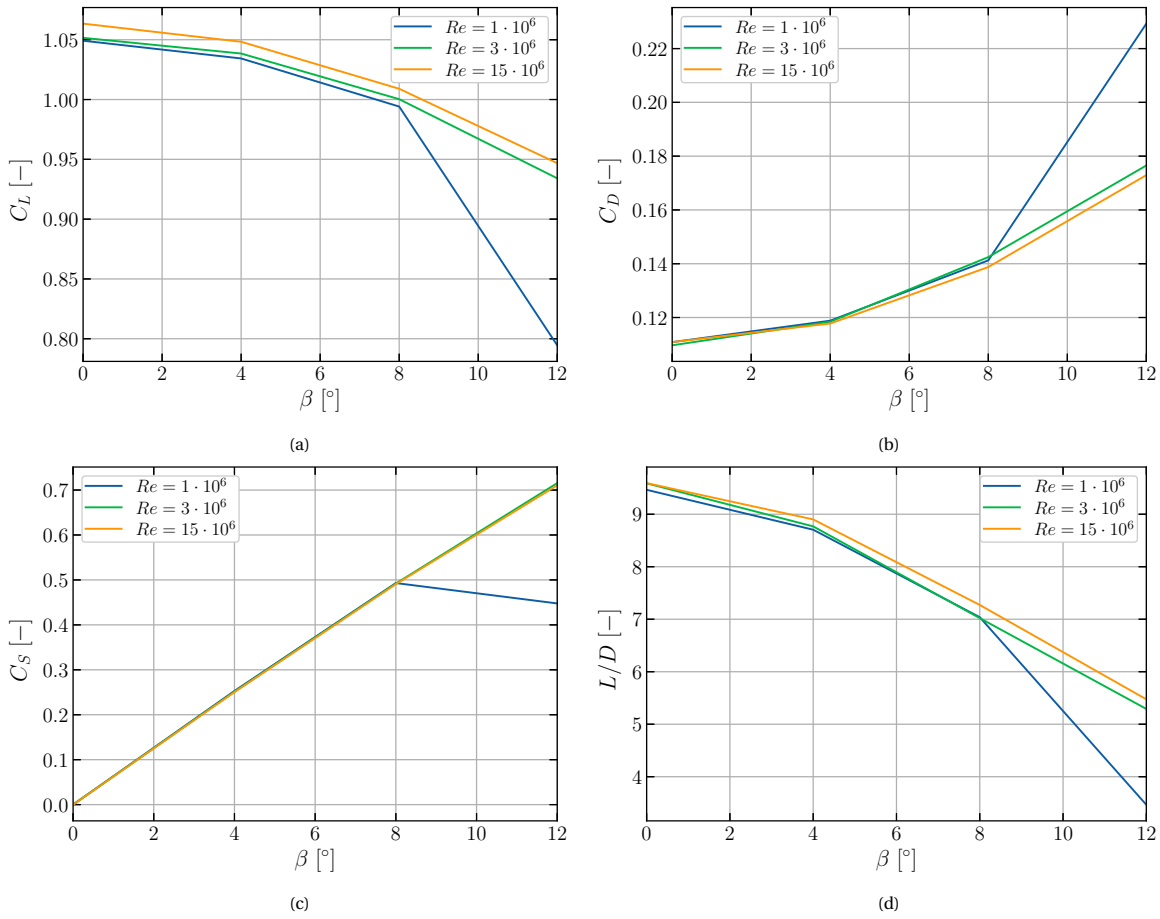

Figure 5.43: The lift (a), drag (b) and sideforce (c) coefficients and L/D (d) as a function of β for different Reynolds numbers.

5.3.3. Flow field analysis

In this section, the main flow features and surface variables of the LEI wing will be analysed for different sideslip angles. As the previous section showed, a change in sideslip angle can have a considerable impact on the aerodynamic performance of a LEI wing. Similarly to Section 5.2.4, most of the analysis will be done at x = 0.3 and x = 0.6. In addition to this, some extra visualisation of the flow field will be given. When referring to regions around the wing, the left-hand side is used to indicate the left-hand side in the plots and figures. When non-zero sideslip angles are considered, the left-hand side can also be referred to as the windward side, since this is the side which is upstream for the positive sideslip angles. The right-hand side is used to indicate the right-hand side in the plots and figures. When non-zero sideslip angles are considered, the right-hand side can also be referred to as the leeward side, since this is the side which is downwind for the positive sideslip angles.

Starting with some general flow field observations based on the plots in Fig. 5.44. In these plots, the z-component of velocity U_z is plotted on a plane in the wake behind the wing. The pressure coefficient C_p is plotted over the surface of the wing and streamlines are emanating from upstream. The streamlines visualise the difference between the inflow angle of $\beta = 0°$ and $\beta = 12°$. In addition to this, they highlight the interaction of the flow around the tip and the propagation downstream in the wake. The C_p on the surface of the wing indicates the symmetric loading at $\beta = 0°$ and asymmetric loading at $\beta = 12°$. Based on the flow field plane placed in the wake, the strong change in inwash and outwash behaviour can be observed. At $\beta = 0°$,

the upper portions of the wake tend the turn inwards, whereas the lower portions of the wake move outwards with respect to the centre of the wing. At $\beta = 12°$, the regions were positive U_z was seen at $\beta = 0°$ have become stronger, whereas the negative U_z regions have become more positive. This is the result of the change in inflow angle.

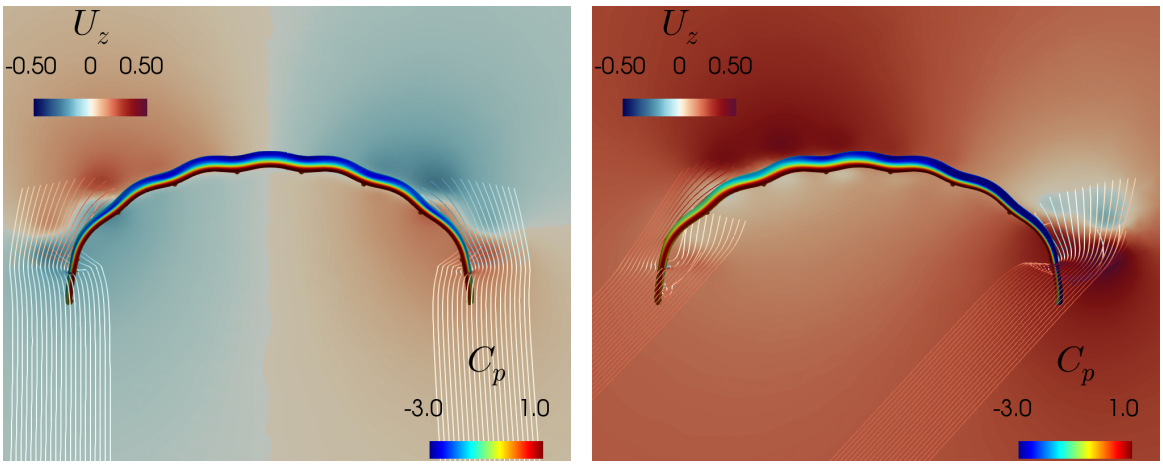

(a) $\beta = 0°$ (b) $\beta = 12°$

Figure 5.44: Overview of the flow field around the LEI wing for different sideslip angles β: Re = $3 \cdot 10^6$, $\alpha = 12°$.

Contrary to the approach in Section 5.2.4, the spanwise pressure distributions over the wing will be discussed first, as they give a good overview of the load changes. Starting at x = 0.3, for which the plot is shown in Fig. 5.45, where the dashed vertical lines indicate the locations of the struts. As can be seen from the plot of the suction side, there is a very clear trend in terms of pressure distribution. On the left-hand side of the plot, the C_p gets higher for every increase in sideslip angle. This increase in C_p starts at the centre of the wing and gradually becomes more towards the tip at $arn_{n,u} = -0.5$. The higher the sideslip angle, the greater the increase in C_p. This is amplified around the tip leading edge region where the negative pressure peak drops from $C_p = -1.6$ at $\beta = 0°$ to $C_p = -0.35$ at $\beta = 12°$. For the positive $arn_{n,u}$ locations on the right-hand side, there is an opposite trend. Now at the highest sidelsip angle of $\beta = 12°$, the negative peak load is $C_p = -3.75$, whereas for $\beta = 0°$ the negative peak load is still $C_p = -1.6$. On the pressure side of the wing, there is more variation between the different cases. However, there are also clear examples of similarities in the trends. Starting with the left-hand side of the wing. It can be seen that for $\beta = 0°$, the C_p is highest along the left-hand side of the wing. For increasing sideslip angle, the C_p drops on this side. At $\beta = 12°$, there is always a pressure drop to the right of each strut on the left-hand side, indicating acceleration of the flow over the lower side of the strut. The high negative C_p peaks in the tip region can most likely be explained by the presence of vortices, but this will be further analysed later in this section. On the right-hand side of the wing, the trend is again the opposite. The $\beta = 0°$ case has the lowest C_p along this side of the wing, with each increase in β leading to a higher C_p. This can be explained by the fact that the inflow angle becomes more perpendicular to the pressure side surface. A similar trend was seen on the left-hand side of the suction side, for which the same argumentation holds.

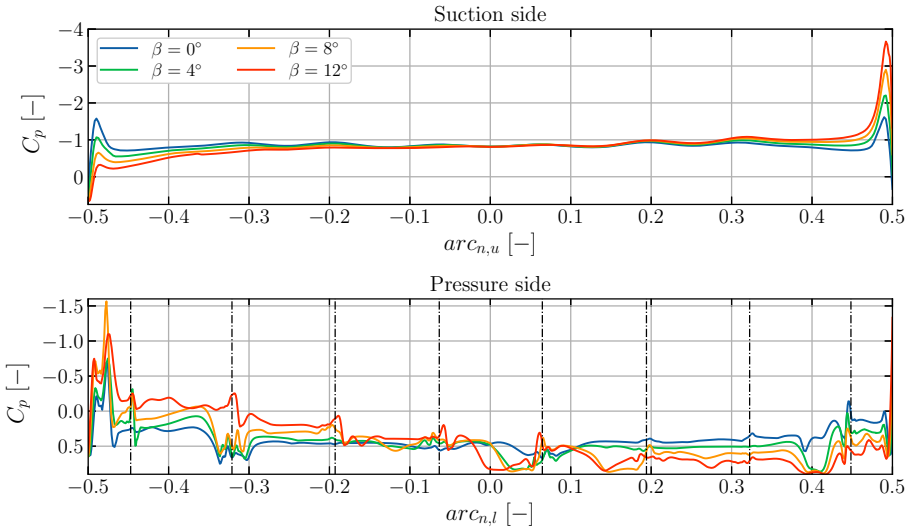

Figure 5.45: Spanwise C_p distribution at x = 0.3 for different sideslip angles β: Re = $3 \cdot 10^6$, $\alpha = 12°$.

At x = 0.6, the differences are much more muted, as can be seen in Fig. 5.46. This was also the case when looking at the impact of the struts in Section 5.2.4 and explained by a decrease in crossflow on the pressure side of the wing. This then also leads to less variation in the pressure distribution between the different sideslip angles. On the suction side of the wing, the divergence between the loading of the different cases starts further outboard than at x = 0.3. This shows that further downstream, the effect of the sideslip angle is most dominant near the tip regions. Similarly as previously observed, on the left-hand side the C_p increases with each increase in sideslip angle. The negative C_p peak close to $arn_{n,u} = -0.5$ increases from $C_p = -1.2$ at $\beta = 0°$ to $C_p = -0.18$ at $\beta = 12°$. On the right-hand side, the negative pressure peak decreases from $C_p = -1.18$ at $\beta = 0°$ to $C_p = -3.6$ at $\beta = 12°$. The pressure side also shows less variation around the centre of the wing compared to x = 0.3. On the left-hand side, the C_p seems to drop with increasing sideslip angle. This can be due to the presence of vortices that become stronger at higher sideslip angles. On the right-hand side, the differences are even smaller. Up to the most outboard strut, the C_p gets slightly higher with increasing sideslip angle. Further outboard in the tip region, the differences become larger and close to the tip at $\beta = 12°$, a completely different distribution is observed.

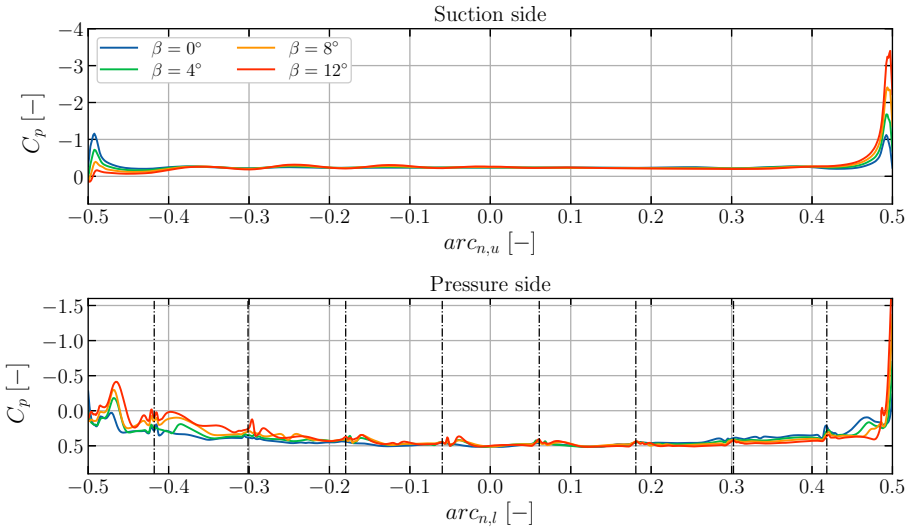

Figure 5.46: Spanwise C_p distribution at x = 0.6 for different sideslip angles β: Re = $3 \cdot 10^6$, $\alpha = 12°$.

Now that the differences in pressure distributions have been highlighted, a closer look at the flow field around

the LEI wing will be necessary to explain some of these differences. This will be done at x = 0.3 and x = 0.6. However, since there will also be an analysis of the impact of the struts during sideslip conditions in Section 5.3.4, not all variables will be considered at both x-locations here.

In Fig. 5.47, the total pressure coefficient is shown at x = 0.3 for the different sideslip angles. As was already noted before, the $\beta = 0°$ case does not have a symmetric flow field on the pressure side of the wing. From these flow field slices, it is clear that there are two main trends in terms of $C_{p,T}$. First, there is the left-hand side in the plots, which is dominated by regions of low $C_{p,T}$. This could either be larger recirculation zones, thus more separation, or higher energy exchange in the form of vortices. The regions with low $C_{p,T}$ that start around the tip gradually become larger and move further inboard for each increase in sideslip angle. In addition to this, the losses around strut 2, 3 and 4 become larger and can be seen to move to the right-hand side of the wing as well. This is to be expected given the fact that the inflow angle directs the flow there. On the right-hand side, with exception of the region around strut 5, the losses have decreased. Around strut 5, one can still see a large zone with low $C_{p,T}$. This can be a result of the inflow angle having the most detrimental effect in this region. When looking to the right of strut 4, a similar region of larger losses exists. These losses could also be associated with vortices, but this will be analysed later. Further outboard the $C_{p,T}$ increases, with the right-hand side tip region barely showing any loss at $\beta = 12°$ when compared to $\beta = 0°$.

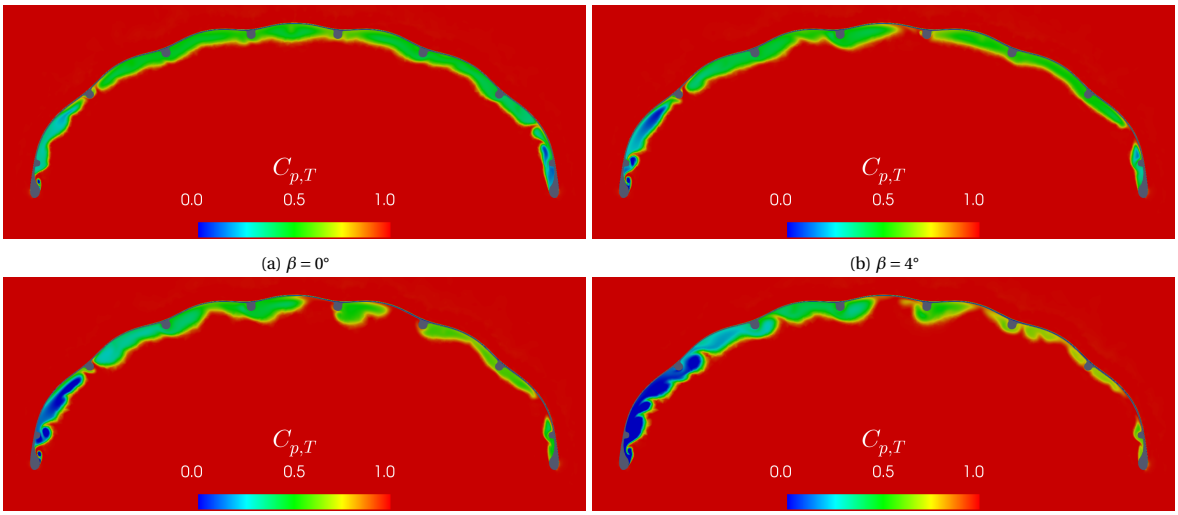

(a) $\beta = 0°$ (b) $\beta = 4°$

(c) $\beta = 8°$ (d) $\beta = 12°$

Figure 5.47: $C_{p,T}$ at x = 0.3 for different sideslip angles β: Re = $3 \cdot 10^6$, $\alpha = 12°$.

Moving further downstream to x = 0.6, the sideslip angle has a similar effect on the flow field around the wing. However, the losses are in general much less further downstream. Therefore, only $\beta = 0°$ and $\beta = 12°$ are compared in Fig. 5.48, as these have the largest delta. As can be seen, on the left-hand side the losses increased strongly again. There is a vortex forming close behind the leading edge of the tip, as also will be shown in more detail later. On the right-hand side, the losses are again much lower. At this x-location, there is almost no loss, with only a clear region of loss to the right of strut 5.

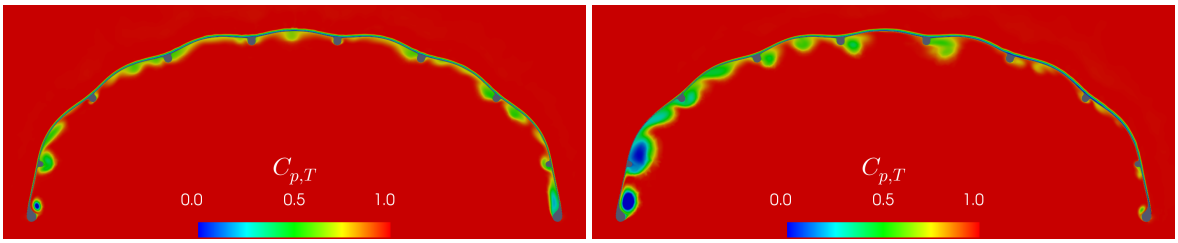

(a) $\beta = 0°$ (b) $\beta = 12°$

Figure 5.48: $C_{p,T}$ at x = 0.6 for different sideslip angles β: Re = $3 \cdot 10^6$, $\alpha = 12°$.

In Fig. 5.49, the z-component of velocity U_z is shown at x = 0.3 for different sideslip angles. Before looking at the differences between the velocity fields during sideslip, some observations about the $\beta = 0°$ flow field can be made. As was already note before, the flow field is not symmetric on the pressure side of the wing. However, one region which seems to appear almost symmetrical is the region between the two most inboard struts. The z-component of velocity close to the surface to the right of strut 4 is positive, whereas it is negative to the left of strut 5. There is a clear line close to the centre of the wing where the z-component of velocity rather abruptly changes from positive to negative or vice versa. Just below these regions exists a region with the velocity component in opposite direction. This could be a sign of two recirculations region in the lateral direction.

Comparing the velocity fields above the suction side of the wing for increasing sideslip angle, it can be seen that on the left-hand side, U_z becomes increasingly positive. This is to be expected since the positive sideslip angle will cause the fluid to move more from left to right in the plane considered. On the right-hand side, one can see that the negative U_z region gets more positive for increasing sideslip angle. However, the anhedral shape of the wing will always result in a region of negative velocity over the outboard region of the suction side. With increasing sideslip angle, the seemingly lateral recirculation regions at the centre of the wing no longer exist. However, it can be seen that for each positive sideslip angle, a recirculating region exist to the right of strut 5. Furthermore, there are regions on the pressure side of the wing where U_z negative close to the surface. Since the inflow has an increasing positive z-component for increasing sideslip angle, this means this recirculation goes against the incoming flow. More on these recirculation regions will be discussed later on when analysing the x-component of vorticity. Around the leading edge of the tips, one can see the impact of the sideslip angle as well. On the left-hand side, the negative velocity peak keeps getting more positive. On the right-hand side, one can see an increasing positive velocity around the leading edge of the tip. Both these observations correlate very well to the decrease and increase in pressure peaks around the tips observed in Fig. 5.45.

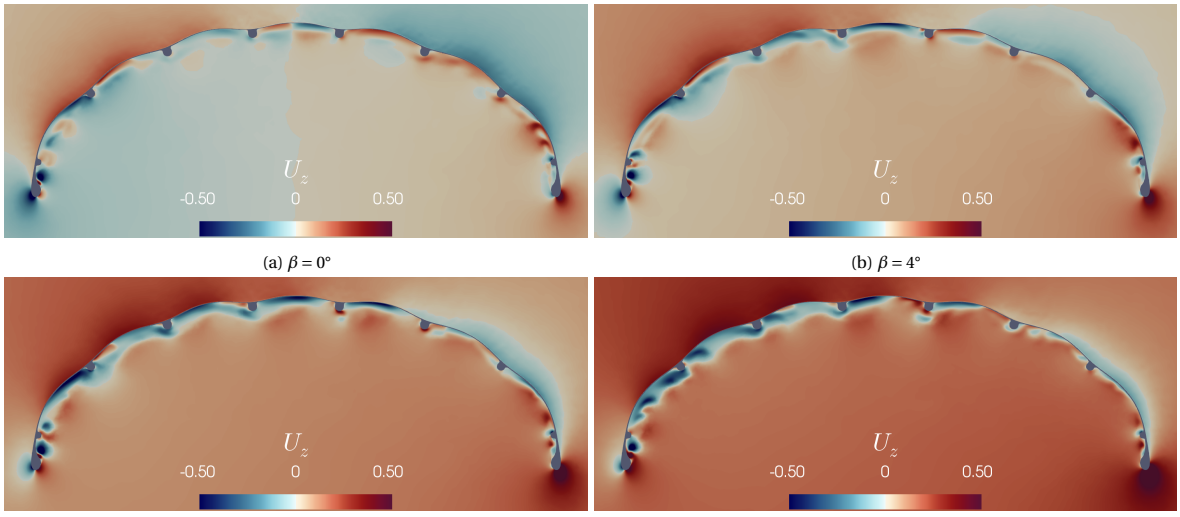

(a) $\beta = 0°$ (b) $\beta = 4°$

(c) $\beta = 8°$ (d) $\beta = 12°$

Figure 5.49: U_z at x = 0.3 for different sideslip angles β: Re = $3 \cdot 10^6$, $\alpha = 12°$.

In Fig. 5.50, the z-component of velocity is shown at a y-normal plane located at y = -0.5. This further highlights the change in inwash and outwash discussed earlier. Furthermore, it also shows the changes in velocity over the leading edge on both sides of the wing. On the left-hand side, it can be seen that at $\beta = 12°$, the flow no longer has a strong negative U_z peak at the leading edge. On the right-hand side, the positive U_z peak has increased further as the effective angle of attack at this location has increased.

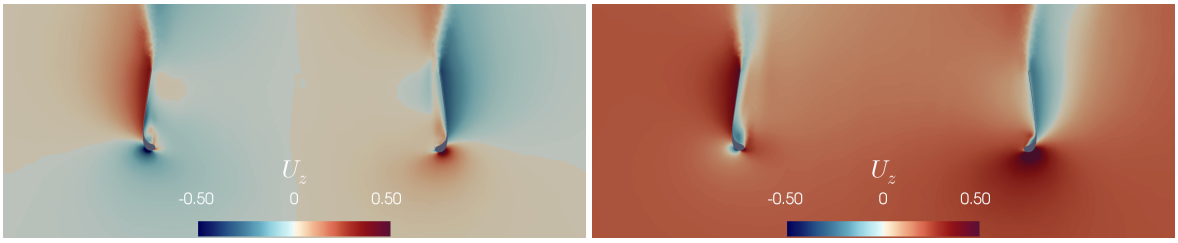

(a) $\beta = 0°$ (b) $\beta = 12°$

Figure 5.50: U_z at y = -0.5 for different sideslip angles β: Re = $3 \cdot 10^6$, $\alpha = 12°$.

In Fig. 5.51, the x-component of vorticity Ω_x is shown at x = 0.3 for different sideslip angles. For $\beta = 0°$, the two lateral recirculation regions at the centre on the pressure side of the wing are visible. The positive vorticity indicates clockwise circulation and the negative vorticity indicates counter-clockwise circulation. When comparing the vorticity regions between the two cases, it is clear what influence the sideslip angle has. For example, to the right of strut 4, there is a clear negative vorticity region at $\beta = 12°$. Given the inflow angle, this indicates a recirculation that is either the result of separation or a vortex. Comparing this to the $C_{p,T}$ plot shown in Fig. 5.47, one can see that the region of recirculation matches the region where the large losses occur. Especially on the left-hand side of the wing for $\beta = 12°$, there are several of these negative vorticity regions to the right of the struts. On both sides of the wing, there are high positive vorticity regions to the left of the struts. The clearest example of this is at strut 5. This is due to the fact that for this inflow angle, the struts cause blockage. This blockage will in turn force the flow to be redirected along the strut, inducing the positive circulation. The positive vorticity in the right-hand side tip region also decreases strongly with increasing sideslip angle. On the left-hand side, the opposite happens with an increase in negative vorticity regions.

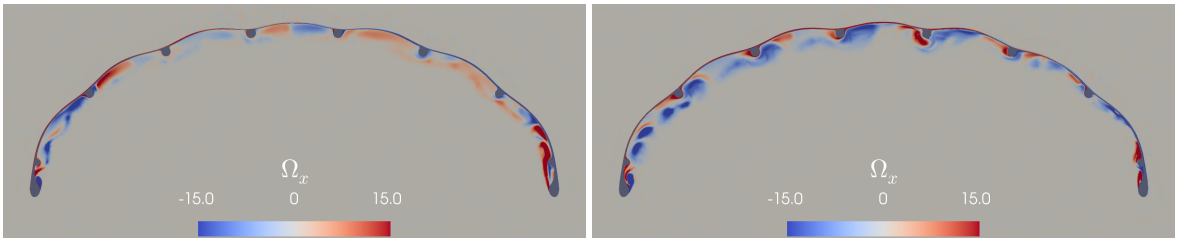

(a) $\beta = 0°$ (b) $\beta = 12°$

Figure 5.51: Ω_x at x = 0.3 for different sideslip angles β: Re = $3 \cdot 10^6$, $\alpha = 12°$.

In Fig. 5.52, the Lambda2 criterion vortex structures are shown at x = 0.6 for different sideslip angles. As explained earlier, the Lambda2 criterion is a vortex core line detection method. It only says something about the presence of vortices and their strength, not about the rotation direction. However, based on the Ω_x plots like Fig. 5.51, it is easy to argue the rotational direction. Since at $\beta = 0°$ the flow field is not symmetrical, one can see that this leads to clear differences in vortex structures being formed on each side. In the tip region on the left-hand side, a clear vortex forms behind the leading edge of the tip. At strut 1, there is also a vortex on either side of the strut. When comparing this to the same region on the right-hand side, one can see a less strong and more spread out vortex structure. Also, the vortex structure at strut 8 is not comparable to the stronger structures seen at strut 1. The strength and position of several vortices follow a clear trend with increasing sideslip angle. Starting the comparison on the left-hand side near the tip. It can be seen that the vortex that resides behind the leading edge of the tip has increased in size and strength. Also the vortices on the sides of strut 1 are larger and stronger. This correlates well with the pressure distributions shown in Fig. 5.45 and Fig. 5.46, where a higher negative peak loading could be observed for increasing sideslip angle. Generally speaking, a vortex has formed to the right of the struts on the left-hand side of the wing. This is caused by the flow accelerating over the strut from left to right and then separating. On the right-hand side of the wing, there are a few new vortices such as to the right of strut 5 and strut 6, the vortex near the tip has decreased in size and strength.

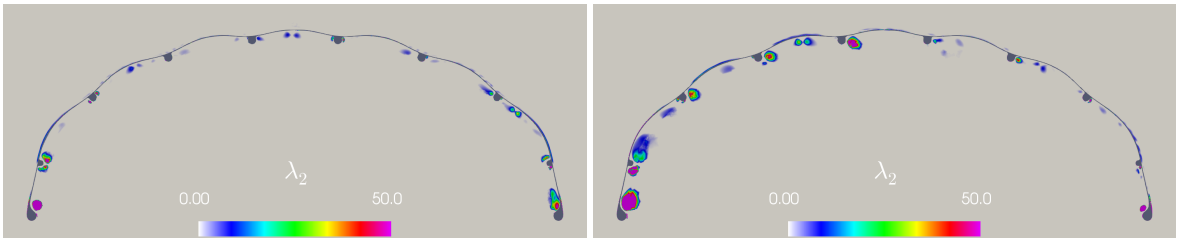

(a) $\beta = 0°$ (b) $\beta = 12°$

Figure 5.52: λ_2 criterion vortex structures at x = 0.6 for different sideslip angles β: Re = $3 \cdot 10^6$, $\alpha = 12°$.

In Fig. 5.53, the skin friction coefficient $C_{f,x}$ on the pressure side of the wing is shown for different sideslip angles. For $\beta = 0°$, the centre sections show a fairly symmetrical distribution. The recirculation regions, indicated by negative $C_{f,x}$, have a similar shape and length. As already became clear from the flow field planes, further outboard the flow field symmetry no longer holds. It can be seen that towards the tip the recirculation regions have a different shape and size as a result of the different flow field interactions. For $\beta = 12°$, one can see that the symmetry no longer holds, as expected. On the left-hand side, the regions with negative $C_{f,x}$ are less uniform. This is because on the left-hand side of the wing, vortices have formed to the right of most struts, as was shown before. These vortices have reduced the recirculation zones in their vicinity. However, there are also areas where the recirculation zone has become larger, such as to the left of strut 2. The right-hand side of the wing shows a decrease in the size of the recirculation regions. This was also seen as a decrease in losses in Fig. 5.47 and caused by the change in inflow angle.

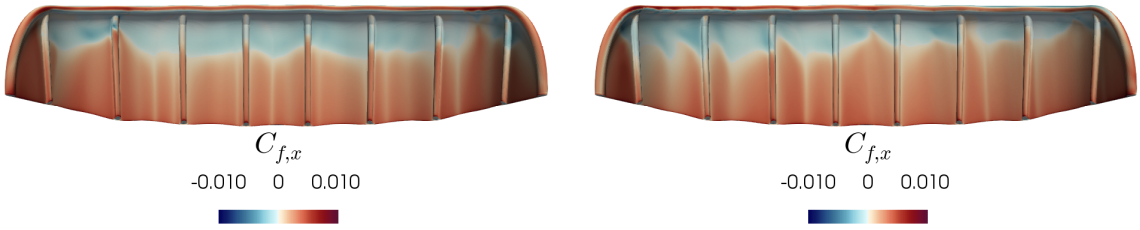

(a) $\beta = 0°$ (b) $\beta = 12°$

Figure 5.53: $C_{f,x}$ on the pressure side of the wing for different sideslip angles β: Re = $3 \cdot 10^6$, $\alpha = 12°$.

In this section, the aerodynamic performance of the LEI wing during sideslip conditions is analysed. This has been done based on force coefficients, flow field analysis and surface variables. Based on this analysis, there are several conclusions that can be drawn. These are as follows:

- Changes in sideslip angle β had a strong impact on the force coefficients of the LEI wing. The force coefficients considered were the lift, drag and sideforce coefficient. The lift coefficient decreased non-linear in relation to the sideslip angle, with every increment leading to an increased loss in lift coefficient. At $\beta = 12°$ the loss in lift coefficient is 11.2% compared to $\beta = 0°$. For the drag coefficient, an inverse relation holds. Every increment of the sideslip angle leads to a stronger increase in the drag coefficient. At $\beta = 12°$, the drag coefficient is 61.0% higher. The sideforce coefficient seems to have a positive linear relation with increasing sideslip angle. The aerodynamic efficiency of the LEI wing decreases with 44.8% at $\beta = 12°$.
- The spanwise pressure distributions on the suction side of the wing showed clear trends at both x = 0.3 and x = 0.6. At both x-locations, the C_p on the windward side increased and the C_p on the leeward side decreased. The difference was largest close to the leading edge of the tip at both the locations considered. On the pressure side, the trend was inverted. Generally speaking, the C_p decreased on the windward side and increased on the leeward side. The lower C_p on the windward side was caused by stronger vortices forming and the impact they had on the flow field.
- Analysis of the flow fields has been predominantly done for $\beta = 0°$ and $\beta = 12°$ at x = 0.3 and x = 0.6. The analysis of the total pressure coefficient showed that in general on the pressure side, the low $C_{p,T}$ re-

gions increased on the windward side and decreased on the leeward side. The z-component of velocity has been considered at x = 0.3 but also at a y-normal plane at y = -0.5. At x = 0.3, below the left-hand side of the wing, the U_z became increasingly negative with an increase in sideslip angle. Since the inflow has a positive z-component, the negative U_z can indicate recirculation against the mean flow direction. On the right-hand side, the biggest change was a strong negative U_z velocity near the surface of the wing to the right of strut 5. Around the leading edge of the tip, the U_z kept increasing at the leeward side and decreasing at the windward side, in line with the spanwise pressure coefficient. At y = -0.5, the effect of the inflow angle on the z-component of velocity around the LEI wing was shown to be strong. The x-component of vorticity showed an increase in counter-clockwise vorticity regions. The analysis of Lambda2 vortex structures showed that these vorticity regions corresponded to strong vortices that formed with increasing sideslip angle.

- Analysis of the $C_{f,x}$ on the pressure side of the wing showed changes in the recirculation regions, associated with negative $C_{f,x}$, on both sides of the wing. On the windward side, these changes were mainly dominated by vortices that formed for increasing sideslip angle. These vortices decreased the recirculation regions in their vicinity. On the windward side, the recirculation regions decreased due to a more favourable inflow angle.

5.3.4. The impact of the struts

In this section, the impact of the struts during sideslip condition will be analysed. This will start with a comparison of the force coefficients, after which a comparison of the flow fields is done. As Section 5.2.4 focused on the case where $\beta = 0°$, in this section the flow field comparison will only be done for $\beta = 12°$. This decision was made because the differences in flow field were highest at this sideslip angle. Furthermore, also considering the other sideslip angles that were simulated would lead to a lot of overlap in the comparison. The considered reference flow condition is $\alpha = 12°$, Re = $3 \cdot 10^6$ and $\beta = 12°$. For the simulations without the struts, the geometry as used in Demkowicz's study [20] has been used. This is made into a full-domain, without symmetry plane, and including the same volumetric refinements as previously mentioned in Section 4.3. However, the surface mesh and other mesh settings have been left unchanged. Nonetheless, the results for the geometry without the struts will no longer be referred to as Demkowicz's study. This is due to the fact that Demkowicz did not consider any sideslip angle in his study and, therefore, referring to the results as being his would lead to confusion.

In Fig. 5.54, one can see the relevant force coefficients plotted for both the geometries. The lift coefficient curves follow the same trend. However, for the case without the struts, the curve is consistently higher. Still, the differences are very minimal, with the maximum difference occurring at $\beta = 12°$ leading to a 0.6% difference in lift coefficient. The drag coefficients also match very well between the two cases. At $\beta = 0°$, the geometry without the struts has a slightly higher drag coefficient. For the other sideslip angles, the drag coefficient is lower for the geometry without the struts. The largest difference in values occurs at $\beta = 8°$, but is still only 1.3%. The sideforce coefficient does not show any observable differences. Both geometries lead to exactly the same increase in sideforce coefficient with sideslip angle. Last, the differences in aerodynamic efficiency are small. The small differences here are a direct result of the marginal differences in lift- and drag coefficients. The largest difference occurs at $\beta = 8°$, which is 1.6%. This comparison shows that similar to the half-domain cases, the impact of the struts on the force coefficient is very small.

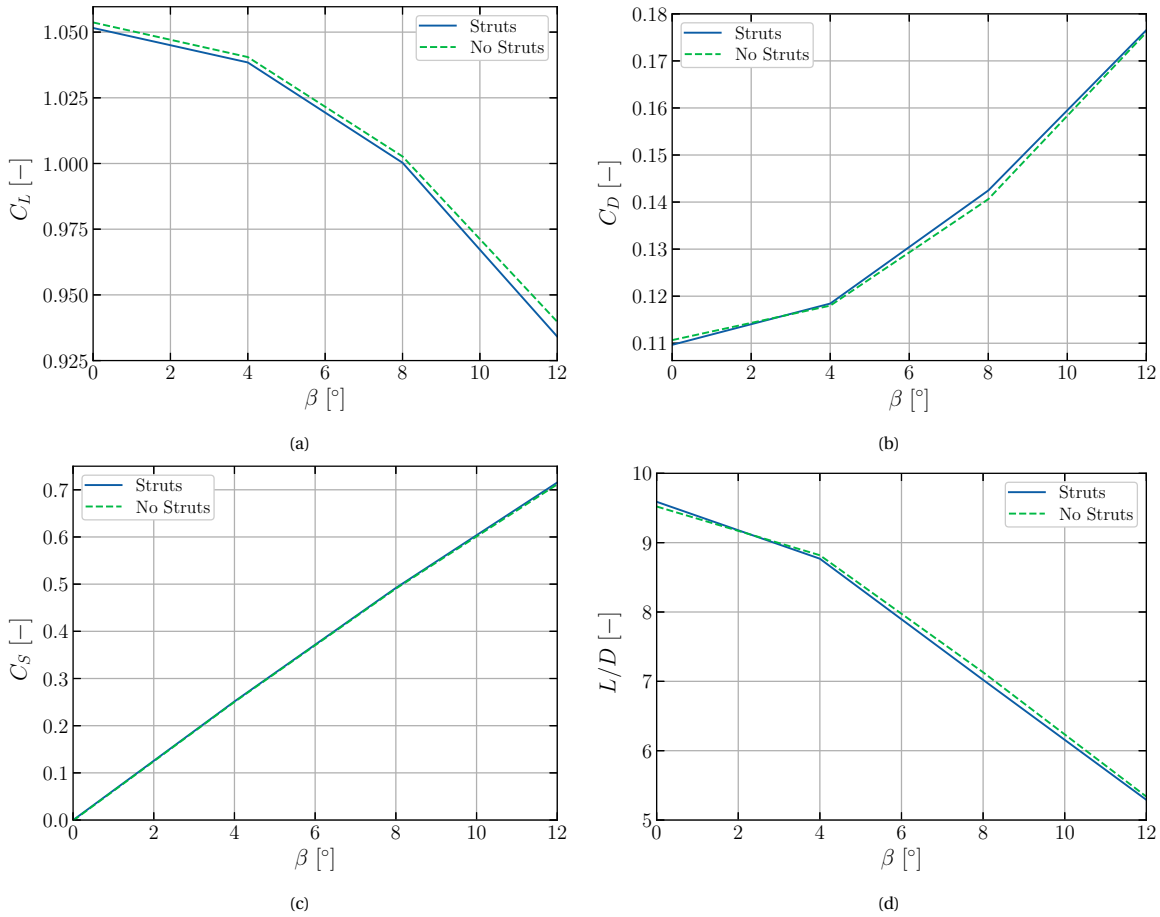

Figure 5.54: Comparison of the lift (a), drag (b) and sideforce (c) coefficients and L/D as a function of β for the wing with and without struts: Re = $3 \cdot 10^6$, $\alpha = 12°$.

Up next is the comparison of the flow fields at x = 0.3 and x = 0.6. As was mentioned before, these two locations have been specifically chosen to assess how upstream flow field differences propagate downstream. Later on in this section, the spanwise pressure distributions will be compared and related back to the flow fields.

In Fig. 5.55, the total pressure coefficient is shown at x = 0.3 for both geometries. Again, for the full-domain, there are eight struts in total, which will be referred to numbered from left to right. Comparing the general distribution of losses around the wing, one can see that the flow fields are quite comparable. Both have the largest losses on the left-hand side due to the inflow angle and decreased losses on the right-hand side. However, while the general flow field is in quite good agreement, locally there are some differences. For the geometry without the struts, the low $C_{p,T}$ region on the left-hand side is much more spread out and uniform. When the struts are included, it can be seen that this loss region becomes less uniform. This is due to the blockage that is caused by the struts. The struts will redirect the incoming flow causing larger velocity and pressure differentials. This could then lead to stronger vorticity regions forming, as will be discussed later on. For now, it is clear that the struts have an impact on the regions with larger $C_{p,T}$ losses on the left-hand side. On the right-hand side, in the region of strut 7 and 8, the case without the struts again has a much more spread out and uniform region of losses. However, losses in this region are generally lower for the case with the struts. Around the centre of the wing, it can be seen that the losses seem more restricted for the case with the struts. For example, around the symmetry centre section of the wing, there is less loss because strut 4 and strut 5 have restricted the recirculation regions behind the leading edge.

In Fig. 5.56, the comparison for $C_{p,T}$ is shown at x = 0.6. On the left-hand side, a similar difference can be observed as at x = 0.3. Close to the region of the tip and the location of strut 1, there is a much larger region of low $C_{p,T}$ for the case without the struts. The tip region of the case with the struts shows two fairly round

regions of low $C_{p,T}$, which can be related back to the presence of vortices. These vortices will greatly impact the local flow field, leading to the differences observed. It can be seen that there are more regions of low $C_{p,T}$ to the right of the struts on the left-hand side, most of these correspond to vortices as well. On the right-hand side, the flow fields are very similar with no strong impact of the struts visible. It is interesting to note again that the majority of the flow field seems to be dominated by the shape of the wing, even under sideslip. The suction side of the wing is not affected at both of the x-locations.

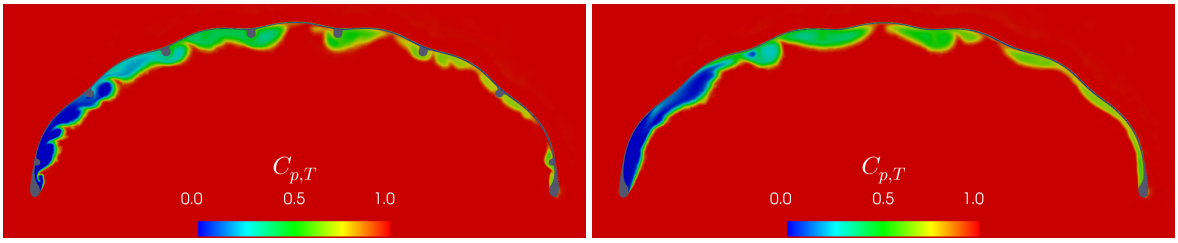

(a) (b)

Figure 5.55: $C_{p,T}$ at x = 0.3 for the LEI wing with (a) and without struts (b): Re = $3 \cdot 10^6$, $\alpha = 12°$, $\beta = 12°$.

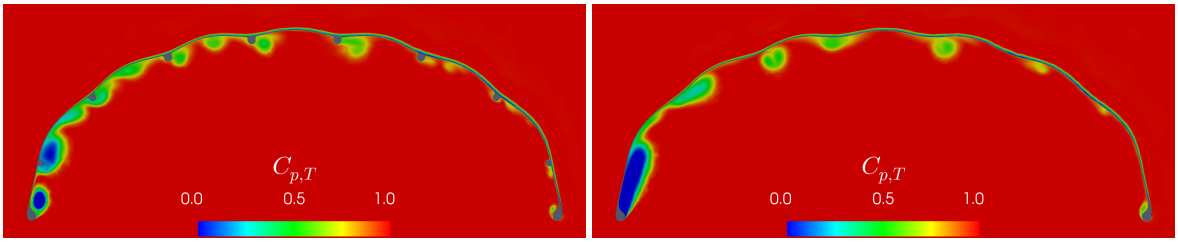

(a) (b)

Figure 5.56: $C_{p,T}$ at x = 0.6 for the LEI wing with (a) and without struts (b): Re = $3 \cdot 10^6$, $\alpha = 12°$, $\beta = 12°$.

In Fig. 5.57, the z-component of velocity is shown at x = 0.3. On the left-hand side, one can see most of the differences again occur in the tip region and around strut 1 and strut 2. For the case with struts, it can be seen that there is a lot of positive and negative U_z variation. For the case without the struts, the velocity distribution is very gradual and uniform. This clearly shows how the velocity field changes locally due to the presence of the struts. However, what is also interesting to note is how similar the velocity fields are from strut 2 till strut 5. While the magnitude of U_z in these regions might be different, there seems to be a matching trend in terms of alternating velocity direction. If one would only see the case with the struts, it could be easy to conclude that the struts cause this variation, but side-by-side it shows how much the wing shape influences the velocity field. Around strut 5, the velocity field is also remarkably similar to the case without the struts. In the region of strut 6, it can be seen that the strut has formed blockage for the flow. The case without the struts has a much higher positive U_z. Despite this, the flow field still shows similar interactions. Only at the locations of the struts, there are local differences, which do not seem to impact the general flow field as much as on the left-hand side.

In Fig. 5.58, the comparison of the U_z velocity fields is shown at x = 0.6. The general velocity field looks very similar with and without struts. A clear example of this is the regions around strut 3, 4 and 5. While the magnitude might be different, they do show the same trends in terms of alternating negative and positive U_z. On the right-hand side, there are also no large differences in the velocity field. The only region where still clear differences can be observed is the tip region on the left-hand side. There seems to be strong velocity variation for the case with the struts. For the case without the struts, one can see a smooth velocity field without strong variation in this area. For both x-locations, the suction side of the wing does not show clear observable differences.

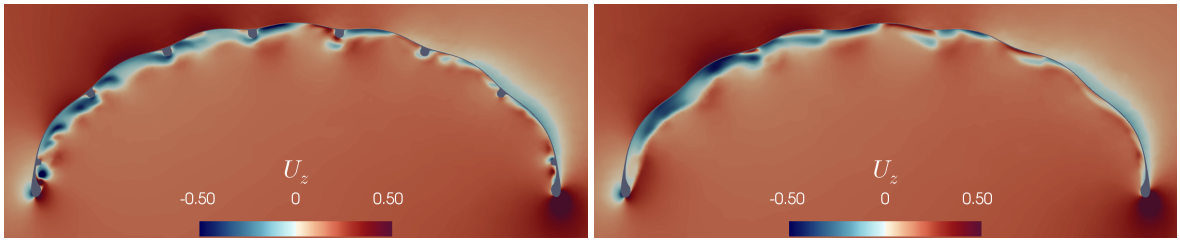

(a) (b)

Figure 5.57: U_z at x = 0.3 for the LEI wing with (a) and without struts (b): Re = $3 \cdot 10^6$, $\alpha = 12°$, $\beta = 12°$.

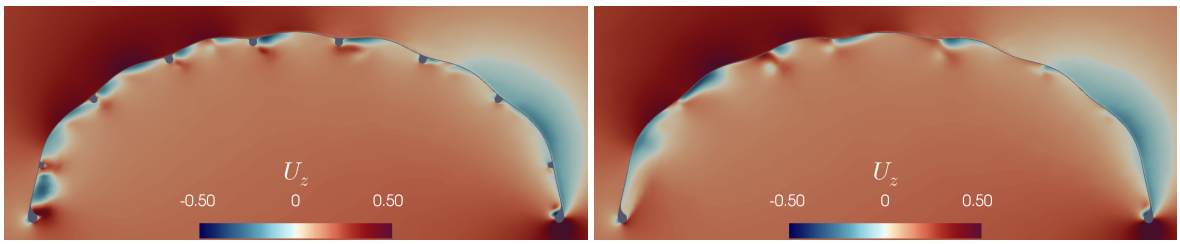

(a) (b)

Figure 5.58: U_z at x = 0.6 for the LEI wing with (a) and without struts (b): Re = $3 \cdot 10^6$, $\alpha = 12°$, $\beta = 12°$.

In Fig. 5.59, the x-component of vorticity is compared at x = 0.3. The previously shown flow field variables already highlighted the areas which are similar or different for the different geometries. However, the vorticity will still be included in the discussion here, as it can underline that in fact many of the flow field interactions stem from the shape of the wing, rather than the struts. When looking at the location of strut 3 in the case without struts, an interesting observation can be made. There is a strong positive vorticity region visible at the exact location of the strut. This vorticity region seems to influence the vorticity field in a similar way as the strut does for the other case. While around strut 4 and 5 the vorticity field shows higher peak values, again the case without struts has a similar pattern of alternating vorticity regions. They are much more spread out and uniform, simply because there are no struts causing blockage. The same can be concluded for the other struts further to the right. In Fig. 5.59, the Ω_x at x = 0.6 is shown. Similar conclusions can be drawn for this x-location as for x = 0.3, but it will be used as a reference for the next variable that will be discussed.

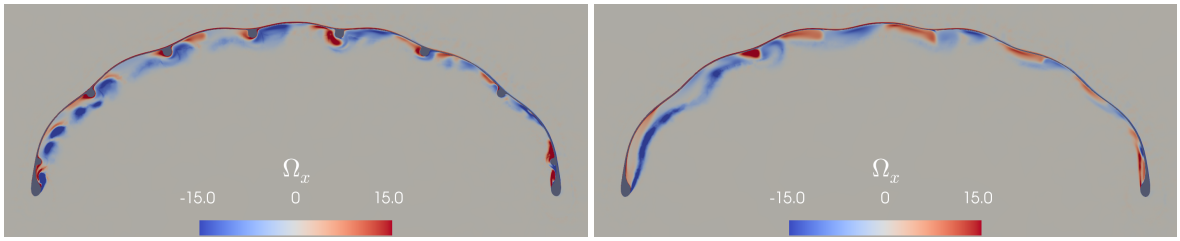

(a) (b)

Figure 5.59: Ω_x at x = 0.3 for the LEI wing with (a) and without struts (b): Re = $3 \cdot 10^6$, $\alpha = 12°$, $\beta = 12°$.

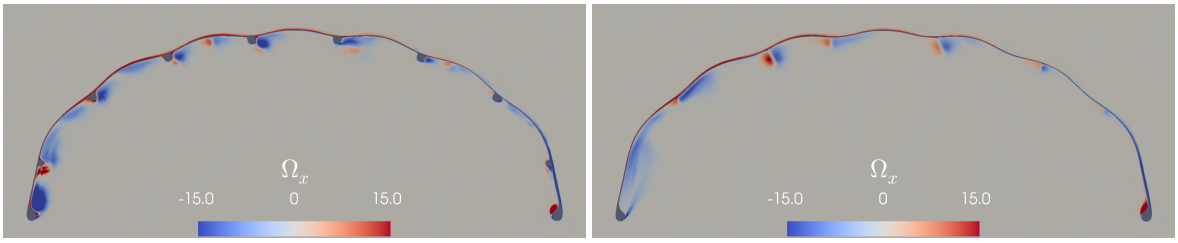

(a) (b)

Figure 5.60: Ω_x at x = 0.6 for the LEI wing with (a) and without struts (b): Re = $3 \cdot 10^6$, $\alpha = 12°$, $\beta = 12°$.

In Fig. 5.61, the Lambda2 vortex structures are plotted at x = 0.3. What this comparison highlights is the difference in vortex structures on the left-hand side of the wing. Especially in the region close to the tip, several vortices exist in the case with struts. As these vortices will have an influence on the local flow field, the reason for the previously observed differences becomes clear. In the case without the struts, there are some very weak vortices in this region and they reside much further away from the pressure surface of the wing. As previously shown in the $C_{p,T}$ and U_z plots, there were considerable differences in flow fields in this area. These differences can now be traced back to the presence of the strong vortices in the case with the struts. However, the case without struts also shows several vortices underneath the wing, but they are more spread out and with lower magnitude. This is a reoccurring observation made for all the flow fields.

In Fig. 5.62, the Lambda2 vortex structures are plotted at x = 0.6. Starting with the vortex in the tip region on the left-hand pressure side of the wing. For the case with struts, there is a strong and clearly defined vortex. When looking at the vorticity field in Fig. 5.60 it can be seen it is rotating counter-clockwise. In the case without struts, there is no vortex in this area. However, for that case, there are several pairs of vortices underneath the wing. What is most remarkable about these pairs of vortices is that they occur relatively close to the locations where the struts are for the other case. This shows that most of the structures would also be there without the struts, but that the struts alter the local flow field. This underlines once more that the main flow field is dominated by the shape of the wing and that the struts have a secondary impact.

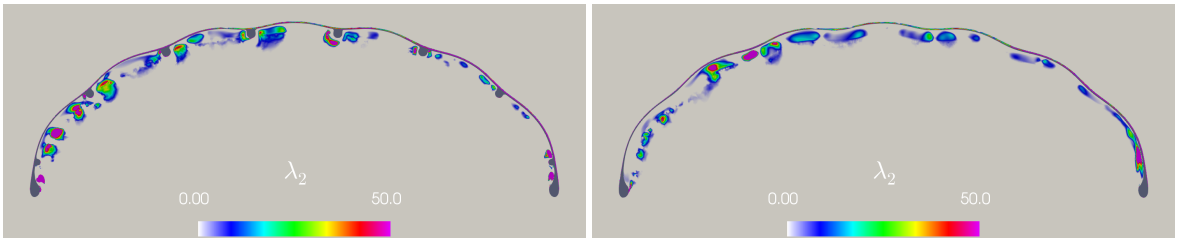

(a) (b)

Figure 5.61: λ_2 criterion vortex structures at x = 0.6 for the LEI wing with (a) and without struts (b): Re = $3 \cdot 10^6$, $\alpha = 12°$, $\beta = 12°$.

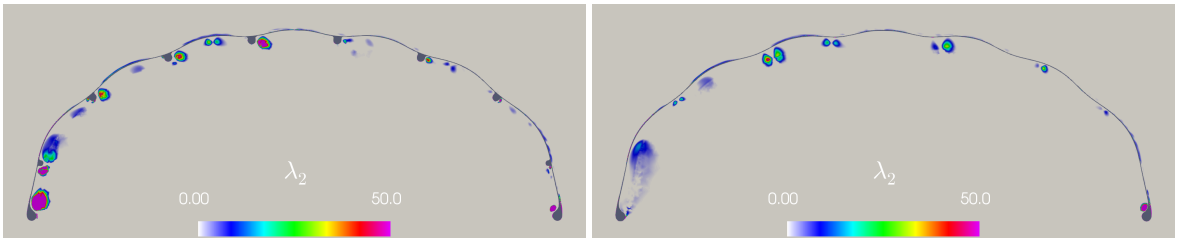

(a) (b)

Figure 5.62: λ_2 criterion vortex structures at x = 0.6 for the LEI wing with (a) and without struts (b): Re = $3 \cdot 10^6$, $\alpha = 12°$, $\beta = 12°$.

In Fig. 5.63, a comparison between $C_{f,x}$ on the pressure side is made for the geometry with and without struts. First, it can be seen that the general trends in response to the sideslip angle are comparable. For both cases,

the recirculation regions are larger on the left-hand side and smaller on the right-hand side. On the right-hand side of the geometry without the struts, one can see the clear low $C_{f,x}$ lines over the surface. These lines of low, close to zero, $C_{f,x}$ correspond to vorticity fronts meeting. For the half-domain comparison of Section 5.2.4, the locations of these lines corresponded very well with the location of the struts. In this case, this is slightly less, which is mainly due to the change in inflow angle. It is interesting to see that in this case, these lines with low $C_{f,x}$ appear in comparable locations for both geometries. On the left-hand side, it is clear that the recirculation regions for the case without the strut are larger and $C_{f,x}$ is more negative at several places. As was shown before, there are fewer vortices and they are less strong compared to the case with the struts. These vortices seemed to have decreased the severity of the recirculation on the left-hand side for the case with the struts.

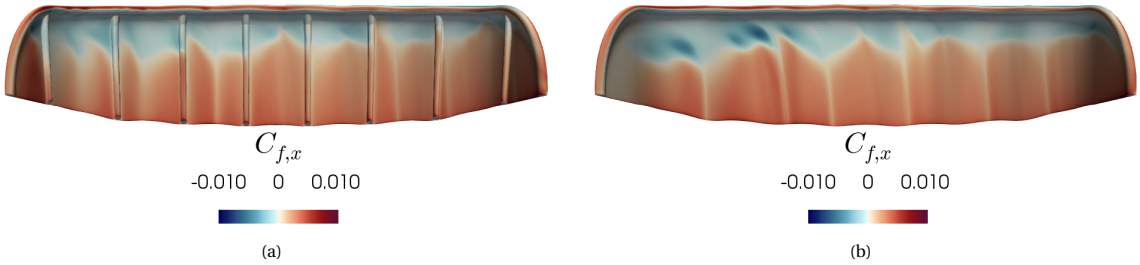

Figure 5.63: $C_{f,x}$ on the pressure side of the LEI wing with (a) and without struts (b): Re = $3 \cdot 10^6$, $\alpha = 12°$, $\beta = 12°$.

In Fig. 5.64, the comparison of the spanwise pressure distribution at x = 0.3 is shown. As can be seen, the suction side of the wing has the same distribution with no observable differences. However, this was also already observed from the flow field analysis. On the pressure side, there are larger differences, similar to the flow field observations. Again, the vertical lines indicate the position of the struts. It can be seen that on the left-hand side, there are slightly stronger negative C_p peaks at the locations of the struts. This is due to the acceleration of the flow over the struts. At $arc_{n,l} \approx -0.25$, the C_p is more negative in the case without struts. When this is related back to Fig. 5.61, it shows that there is a strong vortex present in this area. There are larger difference in C_p from strut 1 further outboard to the tip. As was shown in Fig. 5.61, there are many vortices present for the case with struts, this leads to stronger negative C_p in this region. On the right-hand side, similar observations can be made. One area which is still interesting to highlight is around $arc_{n,l} = 0.4$, since there the C_p is so clearly more negative for the case without the struts. Looking at Fig. 5.61, it can be seen that there are stronger vortex structures in this region.

Last, the spanwise pressure distribution for both cases at x = 0.6 is shown in Fig. 5.65. Again, on the suction side there are no differences observed between the two cases. On the pressure side, only the left-hand side shows some differences. Similar to the distribution at x = 0.3, the pressure distribution for the case without struts is very gradual without real peaks. For the case with the struts, more variation can be observed due to the presence of vortices, albeit very muted at this x-location. In addition to this, the pressure variations caused by the struts can be seen at their respective locations as well.

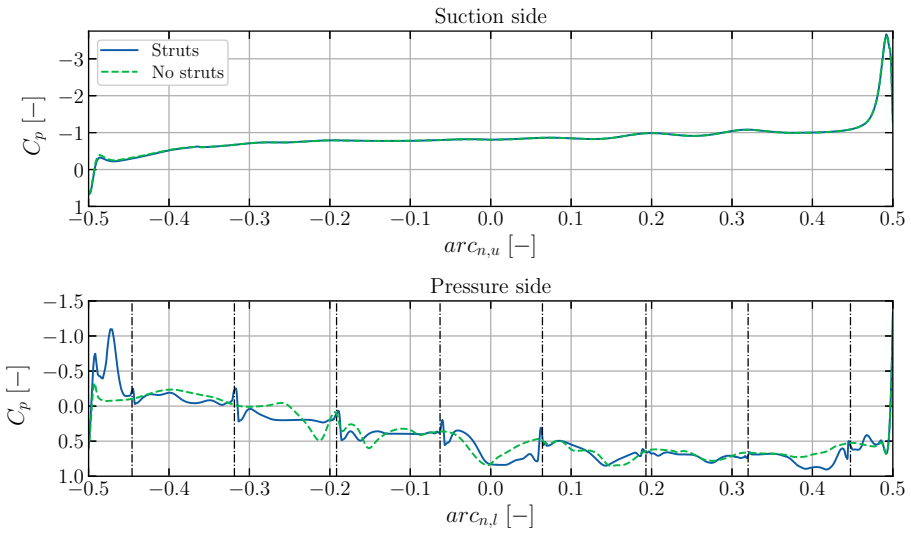

Figure 5.64: Comparison of the spanwise C_p distribution at x = 0.3 for the LEI wing with and without struts: Re = $3 \cdot 10^6$, $\alpha = 12°$, $\beta = 12°$.

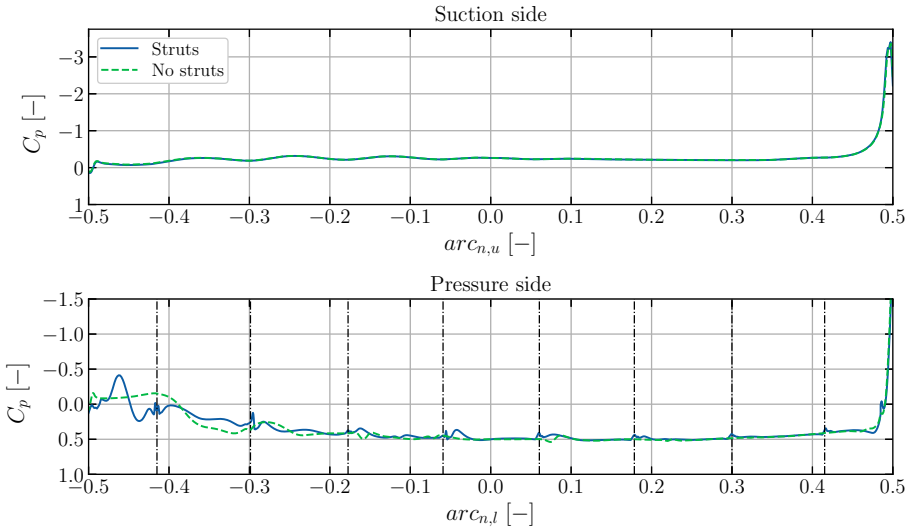

Figure 5.65: Comparison of the spanwise C_p distribution at x = 0.6 for the LEI wing with and without struts: Re = $3 \cdot 10^6$, $\alpha = 12°$, $\beta = 12°$.

In this section, the impact of the struts on the aerodynamic performance of the LEI wing during sideslip conditions has been analysed. Since Demkowicz's study [20] did not consider sideslip conditions, it was necessary to set up full-domain simulations based on his geometry. For this, mesh settings of the original study where left unchanged and only volumetric refinement regions were added. The comparison has been done for force coefficients, flow field data and surface variables. The flow field data and surface variables have been compared at Re = $3 \cdot 10^6$, $\alpha = 12°$ and $\beta = 12°$. The conclusions and observations based on this are as follows:

- Similar to the half-domain comparison done in Section 5.2.4, the struts did not have a strong impact on the force coefficients. For all coefficients considered, the trends of the curves were the same. The lift coefficient for the case without the struts was slightly higher at all sideslip angles considered. The drag coefficient was lower at most of the sideslip angles for the case without struts, with the exception of $\beta = 0°$. The sideforce coefficient did not show any observable differences. The aerodynamic efficiency was slightly higher at most of the sideslip angles for the case without the struts, with the exception of $\beta = 0°$. Thus, only for the lift coefficient there is a consistent difference, all other variables do show a mixed response. Based on this it can be concluded that the struts do not impact the aerodynamic force

coefficients much for the flow conditions considered.

- The flow field comparisons have been done at x = 0.3 and x = 0.6. For the total pressure coefficient, the same general flow field trends were observed during sideslip. The windward side saw an increase in low $C_{p,T}$ and the leeward side a decrease. Low $C_{p,T}$ regions are more restricted by the struts, whereas for the geometry without the struts, losses are more freely and uniformly distributed along the wing. The $C_{p,T}$ flow field seemed to be dominated mostly by the shape of the wing, with the impact of the struts coming in second place. The struts also impacted the local velocity field when considering the z-component of velocity U_z. On the windward side, the case with the struts has multiple regions with alternating U_z direction, whereas the case without the struts has a fairly uniform and smooth velocity distribution. This is caused by the blockage of the struts resulting in vortex structures being formed. Analysis of the x-component of vorticity Ω_x further underlined the influence of the shape of the wing. The alternating positive and negative vorticity regions on the pressure side of the wing seemed to follow a similar pattern. The case with the struts had many strong vortices forming in the windward side tip region. These vortices are responsible for the observed U_z velocity variations. For the geometry without struts, vortices seemed to be present in the regions where otherwise the struts would be placed.
- Comparison of the skin friction coefficient $C_{f,x}$ showed that the general response to sideslip conditions is the same. In both cases, recirculation regions were larger on the windward side and smaller on the leeward side. However, in the case with struts, the vortices that were present led to a decrease in the recirculation regions in their vicinity. For the case without struts, the recirculation regions were larger and seemed more severe on the windward side of the wing. This is a direct result of having fewer vortices in this region.
- Analysis of the spanwise pressure distributions led to conclusions in line with the observations done for the force coefficients and flow field. Over the suction side of the wing, no differences were observed in the C_p distribution. On the pressure side, differences were largest near the tip regions. Over the majority of the pressure side, the C_p distributions followed the same trends. At x = 0.3, the differences were larger than at x = 0.6, which was also shown in Section 5.2.4 for the cases at $\beta = 0°$. The case with the struts showed stronger C_p variations locally in the vicinity of the struts. The C_p distribution of the case without struts showed some variations due to vortices, but was overall much more uniform and gradual.

5.4. Comparison with literature

In this section, the results will be compared to several existing numerical and experimental studies. First, the comparison to numerical studies is done in Section 5.4.1. After this, the numerical results are compared to experimental studies in Section 5.4.2.

5.4.1. Numerical studies

The most important numerical reference study that is used for comparison has been done by Demkowicz [20]. This study used a similar LEI wing model with a simplified geometry without struts. The simulation setup of Demkowicz's study has been used for the current study as well. This means that both studies used the $\gamma - Re_{\theta t}$ transition model to perform steady-state RANS simulations. In doing so, a vast amount of numerical data was available to do an almost like-for-like comparisons between the two geometries. These comparisons have been done for the force coefficients, flow fields and surface variables. In the previous sections, this in-depth comparison has been discussed elaborately. The comparison focused on two different aspects. First, analysing the impact of the struts for cases where $\beta = 0°$. The conclusions of this were summarised at the end of Section 5.2.4. Second, the impact of the struts during sideslip conditions was assessed. The conclusions of this were summarised at the end of Section 5.3.4.

Demkowicz's study [20] was an extension to 3D of the 2D LEI wing airfoil study done by Folkersma et al.[19]. Demkowicz performed a comparison of all the aerodynamic features and trends between his study and Folkserma's study. Some of these aerodynamic features were also verified for the present study at the end of Section 5.2.2. Therefore, the author decided to not compare the results of the current study to the results presented by Folkersma et al.[19] in further detail. For a more elaborate discussion on the aerodynamic differences between the 2D LEI wing airfoil study and a 3D LEI wing study the reader is referred to [20].

Another study that focused specifically on a LEI wing was done by Deaves [35]. This study used the LEI V2 wing, which is the predecessor of the V3A used in this study. However, even with different designs, it is possible to compare the trends between the two studies. Therefore the lift and drag coefficient are compared in Fig. 5.66. The simulations by Deaves were only done at Re = $6 \cdot 10^6$ and they are compared to the closest Reynolds number of the current study which is Re = $3 \cdot 10^6$. As can be seen, the slope of the lift curve is much steeper for the current study. In addition to this, the current study reaches a much higher maximum lift coefficient. For Deaves study, the lift curve seems to flatten off, rather than stall, even at very high angles of attack. The drag coefficient of the current study is also consistently higher, with the difference increasing with the angle of attack. This can be caused by the higher lift-induced drag. However, there were several problems with the study done by Deaves both in terms of mesh quality and convergence. The computational mesh was of quite a low quality, which led to poor convergence at most of the angles of attack. This means that differences in results could also be due to these factors, rather than just the different LEI wing model. Therefore, no further in-depth comparison of, for example, skin friction coefficients or pressure distributions is done.

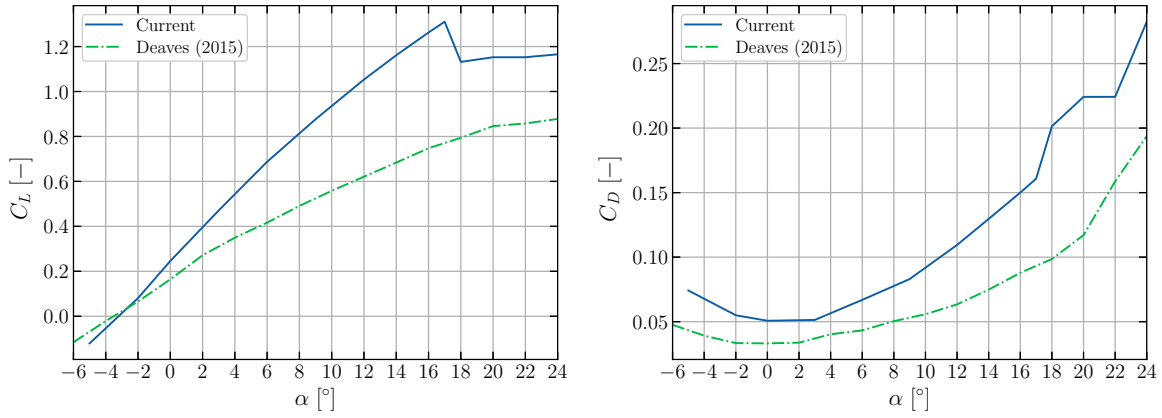

(a) (b)

Figure 5.66: Comparison of the lift (a) and drag (b) curves to the study by Deaves [35].

Gaunaa et al.[48] studied the aerodynamic performance of a simple kite geometry. This is the only study that performed simulations for both zero sideslip angle, as well as non-zero sideslip angles. Unfortunately, for the zero sideslip angle cases, a rather unconventional α_{pitch} has been used instead of just the angle of attack α. Since no relation is given for how this α_{pitch} relates to α it is not possible to compare the lift and drag coefficient curves. In addition to this, no further details about the flow variables such as the Reynolds number are given. This, combined with the fact that it concerns a simple kite geometry makes it impossible to compare absolute values. However, it is still possible to compare the trends of the two studies. Specifically, the trends for a kite or LEI wing under sideslip conditions, for which the lift and drag coefficient are shown in Fig. 5.67. The difference in absolute values does not only come from the different shapes of the wings, but also from different angles of attack. The current study used a fixed $\alpha = 12°$ for the cases where sideslip angle was simulated. Gaunaa et al.[48] used an $\alpha_{pitch} = 0°$ in his study. Looking beyond this, one can see that the impact of increasing the sideslip itself on the force coefficients is similar. For both studies, the drop in lift coefficient becomes worse with every increment in β. Similarly, the increase in drag coefficient becomes stronger with every increment in β for both studies.

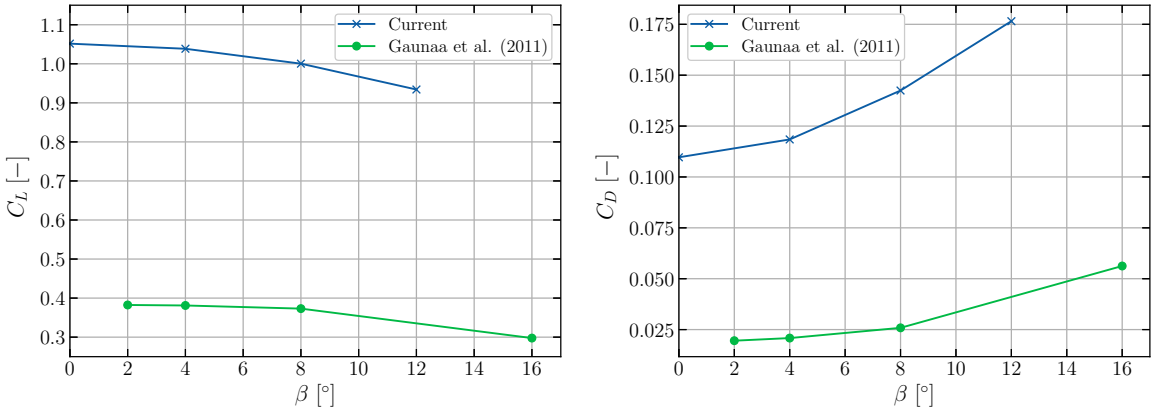

(a) (b)

Figure 5.67: Comparison of the lift (b) and drag (b) coefficients as a function of sideslip angle to the study by Gaunaa et al.[48].

The current study only focused on modelling the aerodynamics of the LEI wing including the struts. In doing so, it neglected other elements which are part of a complete pumping kite power system such as the tether, the bridle line system and the KCU. It is expected that these elements will negatively impact, i.e. increase, the drag coefficient. Studies using dynamic models often use assumptions or approximations to account for the effect of these elements on the system as a whole. Therefore, to compare the aerodynamic force coefficients and performance of the LEI wing to those studies, a correction should be used. One way of doing this is by computing a parasitic drag coefficient. In order to do this, the drag of the bridle line system itself has to be approximated, which can be done through the superposition of both a normal and axial drag component [107]. However, only a normal component of drag is assumed for this approximation, which is calculated through Eq. (5.3) [108]. In this equation, V_n is the normal velocity component, which is for simplicity set to equal the freestream velocity. $A_{e,bridle}$ represents the effective area of the complete bridle line system. To estimate this, the total length of the bridle line system and the diameter of the bridle lines are used. The V3A has a total bridle line system length of $L_{bridle} = 95.726m$ and the diameter is assumed to be equal to $d = 2.5mm$, these are the values used by Demkowicz [20]. The drag coefficient of the cylinder $C_{D,cyl}$ depends on factors such as the Reynolds number and the roughness of the cylinder surface. For this estimation, it is assumed to be equal to 1, which is a common average value.

$$D_{bridle} = \frac{1}{2}\rho V_n^2 A_{e,bridle} C_{D,cyl} \tag{5.3}$$

Using Eq. (5.3) as input for Eq. (5.4), the bridle drag coefficient was determined to be $C_{D,bridle} = 0.0122$, using $A_{V3A} = 19.6m^2$ as area of the LEI wing.

$$C_{D,bridle} = \frac{2D_{bridle}}{\rho U_\infty^2 A_{V3A}} \tag{5.4}$$

Next to this, there is also the impact of the tether drag and KCU, which were shown to be non-negligible by Roullier [39]. In his thesis, Roullier states using $d_T = 0.01m$ as tether diameter, $C_{D,T} = 0.96$ as tether drag coefficient and $L_{tet} = 300m$ as average tether length. Now the total tether drag can be determined by using these coefficients in Eq. (5.3). The normal velocity V_n is corrected for an assumed elevation angle of 30°, but the velocity variation with altitude is neglected. This leads to a total tether drag coefficient of $C_{D,T_{tot}} = 0.0367$. Last, the drag of the KCU is estimated. Roullier assumed $A_{KCU} = 1.6m^2$ as the area of the KCU and $C_{D,KCU} = 1$ as the drag coefficient. Assuming that V_n is equal to the freestream velocity at the KCU gives a total KCU drag coefficient of $C_{D,KCU_{tot}} = 0.0816$. Now the total parasitic drag can be determined through Eq. (5.5), which leads to $C_{D,par} = 0.131$.

$$C_{D,par} = C_{D,bridle} + C_{D,T_{tot}} + C_{D,KCU_{tot}} \tag{5.5}$$

The lift- and drag coefficients of the dynamic models are usually averages and, therefore, an average of the coefficients of the current study will also be determined. This is done by taking the average for the range $6° < \alpha < 16°$ at $\text{Re} = 3 \cdot 10^6$. This range has been chosen based on the experimental data presented in [18]. The same has been done for Demkowicz's results [20], but using the parasitic drag as estimated in this study to keep this consistent. The results of this and four other studies are presented in Table 5.2.

As can be seen, there four additional studies included in the table. The first study is by van der Vlugt et al [22] (2013), which computed the variables by statistical analysis of the experimental data gathered by Ruppert [50]. Ruppert's study has been discussed in Chapter 2 and it made use of the LEI V2 wing developed by Kitepower. This is the design that was also used by Deaves [35] in his numerical study. Second, the study by Fechner et al.[37] (2015), which proposed a new dynamic modelling framework for a pumping kite power system including a four-point kite model. The system was validated by using experimental data of a Hydra kite owned by the Delft University of Technology. Third, the study by Faggiani and Schmehl [109] (2018), which focused on the design and economics of a pumping kite wind park using representative kite parameters. Fourth, in the most recent study by van der Vlugt et al.[38] (2019) a quasi-steady pumping kite power system modelling framework was introduced. This study used time-averaged input parameters based on experimental data of a redesigned Genetrix Hydra kite.

The differences between the averaged results of the current study and Demkowicz's study [20] are minimal. Both the lift and drag coefficient are almost exactly the same. However, this was already shown in detail in Section 5.2.4. Compared to van der Vlugt et al.[22], the lift coefficient is exactly matching, but the drag coefficient is 19.5% higher. The differences with Fechner et al.[37] are comparable, with a 2% higher lift coefficient and a 13.8% higher drag coefficient. Both the study Faggiani and Schmehl [109] and van der Vlugt et al.[38] reported lower lift coefficients. This resulted in the lift coefficient of the current study being 25% and 69% higher, respectively. Comparing the drag coefficient to these two studies shows that it is 19.5% and 59.3% higher, respectively.

Table 5.2: Comparison of the averaged force coefficients and aerodynamic efficiencies between different numerical studies.

Study	C_L	C_D	L/D
Current study averaged	1.00	0.108	9.25
Current study averaged with $C_{Dp} = 0.131$	1.00	0.239	4.18
Demkowicz (2019) [20] averaged	1.00	0.109	9.25
Demkowicz (2019) [20] averaged with $C_{Dp} = 0.131$	1.00	0.240	4.16
van der Vlugt et al. (2013) [22]	1.0	0.2	5.0
Fechner et al (2015) [37] - Sim. II	0.98	0.21	4.64
Faggiani and Schmehl (2018) [109]	0.8	0.2	4.0
van der Vlugt et al. (2019) [38]	0.59	0.15	3.6

The available reference studies are all different in their approach and have varying lift and drag coefficients. The current study is on the high end of the lift coefficient range and seems to overestimate the drag coefficient compared to the reference studies. However, the aerodynamic efficiency, L/D, falls well within the range of the reference studies. The difficulty in comparing the results is the very simplified and general approximations that are made for the parasitic drag. Since the parasitic drag accounts for a large part of the total drag coefficient in the current calculation, the sensitivity to this correction is very high. A more sophisticated aerodynamic drag correction study can be done to estimate the necessary drag corrections. For example, using the data and model developed by Roullier [39] to make such estimations, however, this was beyond the scope of this thesis work. In addition to this, it is also unclear how reliable some of the input data of the dynamic models is. As some of these inputs are based on experimental data, the data processing can have a strong impact on the computed coefficients.

5.4.2. Experimental studies

As the research aim was to improve the correlation of the simulation results to experimental data, this section will discuss this correlation. First, some remarks about acquiring experimental data will be made. After this, several aerodynamic correlations of different methods will be compared. Lastly, the correlation to the study by Roullier [39] is presented.

Before discussing the comparisons to experimental studies, some remarks will made about several relevant

considerations. First, the effective angle of attack at the wing is not a variable that can be measured directly during experimental tests. Van der Vlugt et al.[38] showed that, in theory, the angle of attack does not vary along the flight path if the angle between the wing and tether is kept constant. This would be the case for a massless kite without steering input and a sideslip component. However, the in-flight operation of the LEI wing deviates from this idealised case. As was already shown in Chapter 2, the L/D, angle of attack and heading of the kite flying figure-of-eight manoeuvres are related. During these manoeuvres, there are changes in velocity induced by the gravity which in turn affects the angle of attack and aerodynamic performance of the wing. As Van der Vlugt et al.[38] also discusses, the effect of gravity leads to a deviation from the idealised case, as the tether alignment and therefore tether force changes. As the angle of attack is determined through geometrical relations, this can also lead to offsets between the numerical and experimental data. The geometric model used by Oehler et al.[18] for determining the angle of attack was shown in Fig. 2.2. Now this can be considered as the geometric angle of attack. An underlying assumption for determining the lift and drag curve as a function of this geometric angle of attack is that at maximum constant power setting, the wing does not deform. If this is the case, variations in lift and drag coefficient are solely dependent on the changes in the geometric angle of attack. However, since the LEI wing has a flexible membrane, that has been observed to change under loading, this could lead to an effective angle of attack at the wing that is different from the geometric angle of attack. However, the effects of this potential fluid-structure interaction have not been quantified yet and are, therefore, not accounted for in the experimental data processing.

Secondly, there are large differences in the statistical quality of the data between the experimental studies by Oehler et al.[18] and Roullier [39]. Oehler et al.[18] only used the data of 5 whole pumping cycles and, among others, filtered out the data points with strong steering input. Furthermore, testing was done using an asymmetric bridle lay-out which impacted data processing as well. Roullier [39] developed a more extensive model and used the data of 128 full pumping cycles, significantly increasing the statistical quality. In addition to this, only specific data points with the LEI wing in upward direction for straight flight segments were taken into account. This brings the condition of the experimental data points of Roullier [39] much closer to the simulated CFD conditions. Because of this, the results of Roullier's study [39] will be taken as most important experimental reference.

In Fig. 5.68, L/D curves of several studies are plotted over the filtered experimental data by Oehler et al.[18]. Filtering was necessary to exclude data points with strong steering input and lower than 1 power setting. Both the results of the present study and the study by Demkowicz [20] are at $\mathrm{Re} = 3 \cdot 10^6$ and have been corrected with the parasitic drag as computed in Section 5.4.1. Ruppert [50] and Fechner et al.[37] used two-dimensional sail wing section data to derive the correlation of the lift and drag coefficient with angle of attack. These correlations were then used in their respective dynamic pumping kite power models. However, both studies were corrected in [18] to better fit the newly acquired experimental data. Ruppert [50] used several experimental data sets of the LEI V2 kite and LEI Hyrdra V5 kite, whereas Fechner et al.[37] used airfoil data with several adjustments based on experience for LEI wings. Only the traction phase for $6° < \alpha < 16°$ will be considered and the comparison will focus on comparing the CFD studies to the models by Ruppert [50] and Fechner et al.[37]. As can be seen, Fechner et al.[37] estimates the highest L/D throughout the considered traction phase range, with a very gradual decrease from $\alpha > 10°$ onwards. Ruppert [50] predicts a similar maximum L/D, but there is a much more distinct decrease at higher angles of attack. Last, the present study for the LEI wing struts and Demkowicz's study [20] for the LEI wing without struts. It can be seen that both studies do not predict a decrease in the L/D within the considered traction phase angle of attack range. Thus, the correlation to the models considered here has not changed since the impact of the struts on the aerodynamics force coefficients was proven to be minimal. Comparisons to the experimental study by Oehler et al.[18] will not be done since these results differed strongly from the results obtained by Roullier [39]. As was discussed in the previous paragraph, the statistical quality of the data by Roullier is much higher and, therefore, this will be taken as reference.

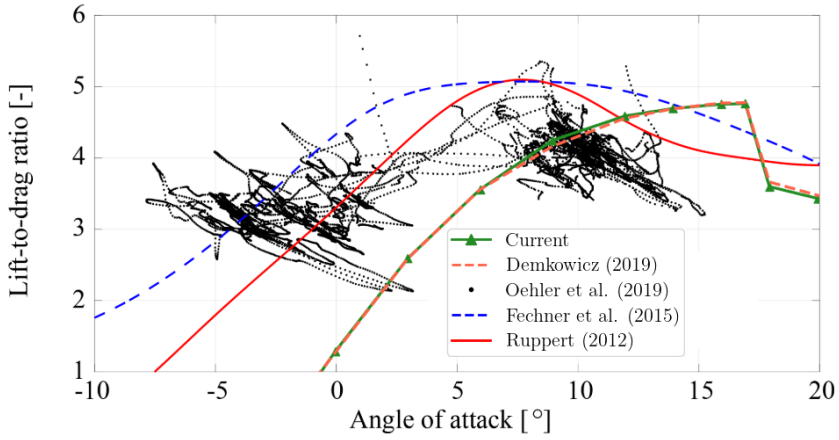

Figure 5.68: Comparison of the lift-to-drag ratio between several aerodynamic models and CFD studies. (reproduced and edited figure from Oehler et al.[18])

The lift and drag curves based on the study by Roullier [39] are presented in Fig. 5.69. This experimental study used the same LEI V3A wing as the current study. The experimental data has been filtered to only represent the straight-flight sections in upwards direction during the traction phase of the pumping kite power system. For details on how these experimental lift and drag coefficient data points were determined the reader is referred to [39]. Both the results of the present study and the study by Demkowicz [20] are at $Re = 3 \cdot 10^6$. As can be seen, the lift slope of the numerical data is much steeper than the spread of experimental data points. The experimental data points seem to have a very flat response to change in angle of attack. The numerical data shows a strong linear relation with the angle of attack which reaches much higher lift coefficient values. Correlation between experimental and numerical lift coefficient values is best for $3° < \alpha < 10°$. For the drag coefficient, the opposite trend can be observed. The average of the experimental data points seem to have a steeper slope than the numerical data. Due to this, the discrepancy between the experimental and numerical drag coefficient values increases with angle of attack. The absolute values of the drag coefficient of the experimental and numerical study are closest for $0° < \alpha < 6°$. As was already concluded before, the struts have no impact on the correlation to experimental data.

Since the experimental data presented is obtained for a constant power setting, the changes in angle of attack can be considered flow induced. However, such a flow induced angle of attack variation could also change the loading of the wing itself along the figure-of-eight manoeuvre. Since the centre section at the rear of the wing is not well supported by the rear bridle system, a potential aero-elastic response of the wing could follow. If this centre section of the wing experiences an increase in loading, the rear could be pulled upwards, thereby decreasing the effective angle of attack at this section. Additionally, this could result in tips of the wing being pulled more inboard, increasing the drag coefficient. This aero-elastic interaction could be one explanation for the rather flat lift curve and more steep drag curve of the experimental data, however, a study on the deformation of the wing in-flight would be needed to test this hypothesis.

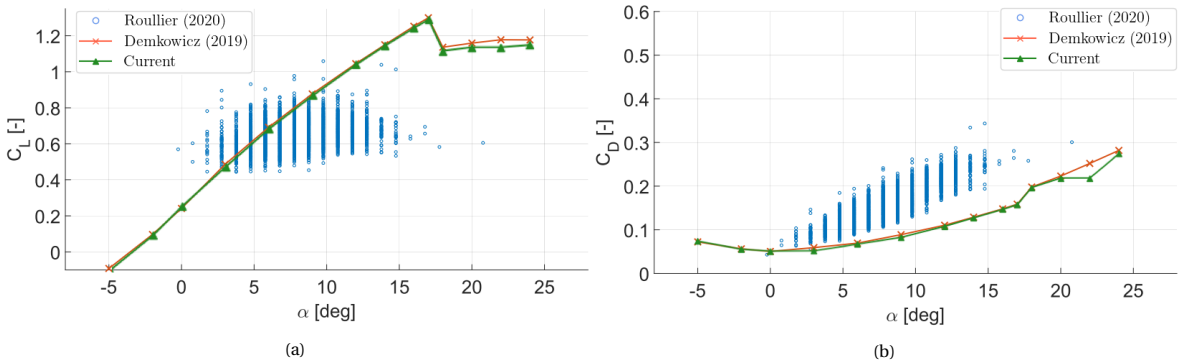

(a) (b)

Figure 5.69: Comparison of the lift (a) and drag (b) coefficients computed by Roullier [39] to CFD studies. (reproduced and edited figure from Viré et al.[110])

Viré et al.[110] discussed the correlation of Demkowicz's [20] numerical results to the same experimental data set and also posed several reasons for the discrepancies. First, the fact that during operation, the wing will deform considerably under the aerodynamic loading. This deformation is not taken into account in the current numerical reference studies. Second, out of plane movements of the wing, such as roll and yaw motion components to compensate for gravity, will cause a sideforce component, which leads to a decrease in the effective lift force component in tether direction and an increase in the drag force.

From the discussion on experimental studies in this section, several conclusions can be drawn. First, the results of the present numerical study and the experimental study by Roullier [39] match within a narrow range of flow conditions. Roullier filtered the data in such a way that the considered data points were as close as possible to the condition simulated in CFD. However, there are still uncertainties such as the experimentally determined angle of attack. Second, next to the experimental data processing methods, factors such as the wing deformation and steering actuation are expected to have a strong impact on the aerodynamic performance and correlation. Third, since the impact of the struts on the aerodynamic force coefficients is proven to be minimal, this can be out ruled as reason for earlier observed discrepancies to experimental data by Demkowicz [20].

6

Conclusions and recommendations

Characterising the aerodynamic performance of a LEI wing that operates as part of a pumping kite power system is a complex problem. Throughout its operation, it will experience a wide range of constantly changing flow conditions. Furthermore, the flexible membrane of the LEI wing will deform based on the aerodynamic loads applied to it. This makes the optimisation of such a wing a challenging FSI problem. In the present study, efforts have been focused on enhancing the understanding of the aerodynamic side of this problem, not taking the structural coupling into consideration. This has been done by performing CFD simulations of a fixed shape geometry of the LEI V3A wing. In Section 6.1, the conclusions of this study will be summarised. The recommendations for future studies and additional improvements are given in Section 6.2.

6.1. Conclusions

There have been several studies that focused on numerically modelling the aerodynamics of LEI wings. Points of improvement for the most recent study by Demkowicz [20] were found to be the inclusion of the chordwise struts and considering the aerodynamic performance of the LEI wing during sideslip conditions. The chordwise struts have been included in the present study, bringing the simulated geometry closer to the real in-flight wing. Pointwise meshing software has been used to generate a high-quality hybrid volume mesh. An elaborate mesh convergence study has been done which showed that the sensitivity of the aerodynamic force coefficients to changes in mesh refinement was low. After this, CFD simulations were performed using the open source CFD toolbox OpenFOAM. These simulations were done using a steady-state RANS solver with the $\gamma - \widetilde{\mathrm{Re}}_{\theta t}$ transition model. A wide range of flow conditions has been considered with varying Reynolds number, angle of attack and sideslip angle.

The aerodynamic analysis was split-up into two main parts, the first part focused on flow conditions where the sideslip angle was zero. For these cases, the Reynolds number range was chosen to be from $0.1 \cdot 10^6$ to $15 \cdot 10^6$ and the angle of attack ranged from $-5°$ to $24°$. It was shown that early stall occurred for $\mathrm{Re} = 0.1 \cdot 10^6$ at $\alpha > 6°$, which was concluded to be due to the separation of a laminar boundary layer. Furthermore, no consistent scaling of the maximum lift coefficient with Reynolds number was observed. The maximum lift coefficient was observed for $\mathrm{Re} = 1 \cdot 10^6$ at $\alpha = 18°$. In addition to this, the angle of attack for which the highest aerodynamic efficiency was achieved varied with Reynolds number, with the maximum occurring for $\mathrm{Re} = 15 \cdot 10^6$ at $\alpha = 6°$. At Reynolds numbers below $3 \cdot 10^6$ and low angles of attack, a laminar separation bubble was present on the suction side of the wing. For $\mathrm{Re} = 15 \cdot 10^6$, drag crisis was observed over the pressure side of the circular leading edge. This led to a decrease in the drag coefficient and increase in the lift coefficient. These findings were in line with the observations made in previous studies by Folkersma et al.[19] and Demkowicz [20].

For the cases at non-zero sideslip angle, the Reynolds number ranged from $1 \cdot 10^6$ to $15 \cdot 10^6$, but the angle of attack was fixed to 12°. The sideslip angle was varied from 0° to 12°. Based on these simulations, the research question "*How does the aerodynamic performance of a LEI wing change as a function of the sideslip angle?*" can be answered. The lift coefficient decreased with sideslip angle and the drag coefficient increased with sideslip angle. The changes in these two force coefficients were observed to be non-linear, with every incre-

ment in the sideslip angle leading to a larger change in the coefficients. A positive linear relation between the sideforce coefficient and sideslip angle was observed. With increasing Reynolds number, the lift coefficient increased and the drag coefficient decreased. The sideforce coefficient was unaffected by changes in the Reynolds number. At Re = $1 \cdot 10^6$, the wing stalls at a sideslip angle of 12°, leading to a stronger drop in the lift coefficient, increase in the drag coefficient and drop in the sideforce coefficient. A clear shift of loading was observed on the spanwise pressure distributions. For the suction side, the pressure coefficient over the windward side of the wing increased with every increment in sideslip angle. Over the leeward side, the pressure coefficient decreased with every increment in sideslip angle. The largest load differences were observed close to the leading edge of the tips. For the pressure side of the wing, generally the inverse held true, with a decrease in pressure coefficient on the windward side and an increase in pressure coefficient on the leeward side. Below the pressure side of the wing, the windward side saw an increase in the losses associated with recirculation, stronger vorticty regions and stronger vortices. On the leeward side, the losses associated with the recirculation decreased and most of the vorticity regions changed from clockwise to counter-clockwise rotation.

The other main research question "*What is the impact of the inclusion of the chordwise struts on the aerodynamic performance and the flow field around a LEI wing when employing a 3D RANS CFD simulation?*" can now be answered for both zero and non-zero sideslip angle flow conditions. The impact of the struts on the force coefficients for zero sideslip angle conditions proved to be minimal throughout the Reynolds number and angle of attack range. However, a comparison of the flow fields and surface variables still showed local differences. The flow field around the wing without the struts was observed to be more gradual and uniform as the flow was able to move around more freely. The blockage of the struts caused more restriction of the recirculation losses, stronger variations in velocity and vorticity, and more vortices to be present below the pressure side of the wing. However, the general flow field layout stayed the same between the two geometries and seemed to be more dominated by the shape of the wing itself. Comparison of the pressure distributions in chordwise and spanwise direction showed that there is a negligible influence on the loading over the suction side of the wing. On the pressure side, most of the variation was observed on the outboard portion of the wing. For the cases at non-zero sideslip angles, the impact was in line with the observations at zero sideslip angle, with no substantial differences in force coefficients. The general response of the flow field to increasing sideslip angle was observed to be the same. Again, below the pressure side of the wing there were local differences, mainly on the windward side. The largest differences were observed in terms of velocity variations and the presence of stronger vortices. Based on the present work, it can be concluded that the struts do not have a substantial impact on the aerodynamic performance of the LEI wing.

Next to the in-depth comparison to the numerical study done by Demkowicz [20], the results have been compared to several other numerical studies. The study by Deaves [35] analysed the aerodynamics of the LEI V2 wing, which was the predecessor of the LEI V3A subject of the present study. This showed that the lift curve of the LEI V3A was much steeper, achieving a considerably higher maximum lift coefficient. In addition to this, the drag coefficient of the LEI V3A was also observed to be consistently higher. In the study by Gaunaa et al.[48], non-zero sideslip angle simulations of a simple kite geometry were conducted. The trends in terms of lift and drag coefficient changes as a function of the sideslip angle were observed to be the same. To compare averaged lift and drag coefficients to the input data used in several numerical kite power system models, an estimation of the parasitic drag coefficient of the bridle system, KCU and tether was made. The averaged lift coefficient fell within the range of the other numerical studies and the averaged drag coefficient appeared to be slightly overestimated. Comparison of the lift coefficient to the experimental study by Roullier [39] showed agreement for an angle of attack range from 3° to 10°. The drag coefficient was underestimated for all angles of attack considered. Based on this comparison, it was concluded that the struts have no influence on the correlation to experimental data. Furthermore, it was discussed that the comparison to experimental data is challenging because of the uncertainties in the experimental data processing methods. Factors such as wing deformation and steering actuation are expected to have a strong impact on the correlation but still need to be further studied and quantified.

6.2. Recommendations

Based on the results of this work, and the experience gained throughout this project, there are several recommendations for future studies. These recommendations will be discussed in this section.

At the moment, the CAD model of the LEI wing is based on a shape that is called the design shape. While it is clear that this shape is different from the shape of the in-flight wing, it is not well assessed how large this discrepancy is. The present study showed that much of the flow field around the wing is predominantly influenced by the shape of the wing and that the struts play a secondary role. Any discrepancies between the simulated wing geometry and the in-flight wing are, therefore, expected to have a strong impact on the correlation. Currently, some efforts within the AWE research group are being put into measuring wing deformation in-flight through the use of IMU sensors. The results of this study could be used to adjust the shape of the simulated wing accordingly.

Experimental methods used are equally vulnerable to the impact of the assumptions that are used to obtain the lift and drag coefficients. As video material of the LEI V3A wing in operation has shown, the tip regions of the wing tend to flatten out at high power settings. This will increase the effective projected area which should, in theory, be accounted for in the experimental data processing. However, as such corrections would most likely introduce even more uncertainties, the problem could also be approached from the numerical modelling side. Even without knowing the exact deformation, it is possible to run a numerical sensitivity study on tip deformation. Several CAD packages are known to have the capability to morph and deform surfaces. By morphing the tips of the wing, but keeping the actual dimensions of the geometry the same, it would be possible to set up simulations with different tip deflection angles. As attempts with shape morphing based on the physics and structural properties of the wing have proven to be difficult in the past, this method could provide a more accessible way of gaining insight into the sensitivity of the force coefficients to the wing shape.

While the taken meshing approach has proven that a high-quality volume mesh can be generated for a LEI wing including chordwise struts, the current process is very labour intensive. Since it involves a multitude of manual operations and user involvement, the usage of this approach within an actively iterating design department would be costly. Mainly because the efforts of researchers put into this are not being spent on actually improving the design or performance of the wing. Therefore, efforts put into automating parts of this process could lead to large returns on the time invested. There are several macros freely available from the Pointwise repository on Github that could handle small tasks, such as creating a domain of a common shape, e.g. a sphere. In addition to this, own macros can be programmed within Pointwise. The programming language used is Glyph and Pointwise provides an extensive user guide on programming in Glyph. Furthermore, there are several articles available on their website providing practical examples on this topic. Thus, even if not the whole meshing approach from start to finish can be automated, significant time savings could be made here.

Performing an experimental study solely focused on acquiring data for correlation to CFD would be highly valuable. While the current numerical setup was validated in a previous study for a 2D sail wing, correlation only based on force coefficients leaves too many unknowns and uncertainties. There are several aspects that can be further studied such as the turbulence model, the turbulence model parameters and defined boundary conditions. However, without having quantitative flow field data, it is not possible to critically assess and judge why some settings are leading to better correlation than others. As wind tunnel testing of LEI wings was shown to be not feasible, the author would propose a different approach. Since the technology of 3D printers has matured in the past decade, it would be possible to produce a scaled model based on the shape that is used for CFD simulations. With this model, a series of wind tunnel tests could be conducted at, for example, the low turbulence tunnel of the Delft University of Technology. This tunnel has an octagonal test section of $1.80m \times 1.25m$, meaning it could most likely fit a 1:15 scale model of the LEI V3A. The maximum velocity in the test section is approximately $120m/s$. Assuming the kinematic viscosity in CFD can be set to the tunnel's value, this would translate to a maximum Reynolds number that is well above 1 million. Since the wind tunnel is equipped with a Particle Image Velocimetry system, not only force coefficients can be extracted but also quantitative flow field data can be obtained. This could be taken at several planes of interest. Based on this data, CFD settings can be optimised to better represent the flow physics and interactions around the wing. Following this, the change in correlation to in-flight experimental force coefficient data can be assessed.

With the data of the simulations done in the present study, there are still several post-processing operations which can be useful for other numerical models. One of these would be computing the force coefficients for separate sections of the wing. Since there are dynamic models that divide a LEI wing up into, for example, one centre section and two outboard sections, comparison of these local force coefficients could provide insight

in the local discrepancy between the models. In addition to this, it would be possible to do a comparison of the moment coefficients between the CFD model and other dynamic models. Furthermore, the estimation of the parasitic drag coefficient could be improved. Currently, the estimation is done in a simple way for the bridle line system, KCU and tether. As the estimation for the parasitic drag is just added on top of the drag coefficient value, it causes an offset of the drag curve. Therefore, the corrected drag coefficient is very sensitive to this offset. Improving the fidelity of this estimation can improve the confidence in the correction and reduce the uncertainty that is currently present.

In terms of numerical modelling, there are several steps that could be taken next. First, a numerical study of the unsteady flow features around the wing could be conducted using URANS. The flexible membrane of the wing, constantly changing inflow conditions and aerodynamic loads make the flow field around the wing highly unsteady in-flight. Even though a rigid wing geometry is used and no coupling with a structural solver is employed, URANS simulations could still provide insights into the transient flow features around the wing. While research using URANS has been initiated during the current study, several simulation settings still require further attention before drawing conclusions based on those results. Second, it could be an option to model both the aerodynamics and structural side of the problem through FSI simulations. In this way, a better understanding of the coupling between the aerodynamic loads and structural deformation in flight could be obtained. Based on these simulations, averaged force coefficients could be computed and compared to the rigid wing results. Last, simulations using higher fidelity CFD methods, such as DES and LES, could be performed. However, while in theory they are resolving more of the real flow physics, there are many additional uncertainties that come along. Therefore, this last option might be best to do once quantitative flow field data is available.

Bibliography

[1] M. Folkersma, R. Schmehl, and A. Viré. “Steady-state aeroelasticity of a ram-air wing for airborne wind energy applications”. In: *Journal of Physics: Conference Series*. Volume 1618. 3. IOP Publishing. 2020.

[2] H. E. Murdock et al. *Renewables 2019 Global Status Report*. REN21, 2019.

[3] E. Dupont, R. Koppelaar, and H. Jeanmart. “Global available wind energy with physical and energy return on investment constraints”. In: *Applied Energy* 209 (2018), pages 322–338.

[4] M. M. Hoogwijk. “On the global and regional potential of renewable energy sources”. PhD thesis. Utrecht University, 2004.

[5] C. L. Archer and M. Z. Jacobson. “Evaluation of global wind power”. In: *Journal of Geophysical Research: Atmospheres* 110.D12 (2005).

[6] D. Honnery and P. Moriarty. “Estimating global hydrogen production from wind”. In: *International Journal of Hydrogen Energy* 34.2 (2009), pages 727–736.

[7] IRENA. *Future of wind: Deployment, investment, technology, grid integration and socio-economic aspects*. Technical report. International Renewable Energy Agency, 2019.

[8] M. Diehl. “Airborne wind energy: Basic concepts and physical foundations”. In: *Airborne wind energy*. Springer, 2013, pages 3–22.

[9] U. Zillmann and P. Bechtle. “Emergence and economic dimension of airborne wind energy”. In: *Airborne Wind Energy*. Springer, 2018, pages 1–25.

[10] M. L. Loyd. “Crosswind kite power (for large-scale wind power production)”. In: *Journal of Energy* 4.3 (1980), pages 106–111.

[11] S. Watson et al. “Future emerging technologies in the wind power sector: A European perspective”. In: *Renewable and Sustainable Energy Reviews* 113 (2019), page 109270.

[12] U. Ahrens, M. Diehl, and R. Schmehl. *Airborne wind energy*. Springer Science & Business Media, 2013.

[13] A. Cherubini et al. “Airborne Wind Energy Systems: A review of the technologies”. In: *Renewable and Sustainable Energy Reviews* 51 (2015), pages 1461–1476.

[14] R. Schmehl. *Airborne wind energy: advances in technology development and research*. Springer, 2018.

[15] T. Stehly et al. *2017 Cost of Wind Energy Review*. Technical report. National Renewable Energy Laboratory, 2018.

[16] V. Salma et al. “Current and expected airspace regulations for airborne wind energy systems”. In: *Airborne Wind Energy*. Springer, 2018, pages 703–725.

[17] L. Bruinzeel et al. “Ecological impact of airborne wind energy technology: current state of knowledge and future research agenda”. In: *Airborne Wind Energy*. Springer, 2018, pages 679–701.

[18] J. Oehler and R. Schmehl. “Aerodynamic characterization of a soft kite by in situ flow measurement”. In: *Wind Energy Science* 4.1 (2019), pages 1–21.

[19] M. Folkersma, R. Schmehl, and A. Viré. “Boundary layer transition modeling on leading edge inflatable kite airfoils”. In: *Wind Energy* 22.7 (2019), pages 908–921.

[20] P. Demkowicz. “Numerical analysis of the flow past a leading edge inflatable kite wing using a correlation-based transition model”. Master’s thesis. Delft University of Technology, 2019.

[21] J. Oehler, R. Schmehl, and M. van Reijen. “Experimental investigation of soft kite performance during turning maneuvers”. In: *Journal of Physics: Conference Series*. Volume 1037. 5. IOP Publishing. 2018, page 052004.

[22] R. van der Vlugt, J. Peschel, and R. Schmehl. “Design and experimental characterization of a pumping kite power system”. In: *Airborne wind energy*. Springer, 2013, pages 403–425.

[23] U. Fechner. “A methodology for the design of kite-power control systems”. PhD thesis. Delft University of Technology, Delft, the Netherlands, 2016.

[24] U. Fechner and R. Schmehl. “Model-based efficiency analysis of wind power conversion by a pumping kite power system”. In: *Airborne wind energy*. Springer, 2013, pages 249–269.

[25] B. Houska and M. Diehl. “Optimal control of towing kites”. In: *Proceedings of the 45th IEEE Conference on Decision and Control*. IEEE. 2006, pages 2693–2697.

[26] H. Hu and Z. Yang. “An experimental study of the laminar flow separation on a low-Reynolds-number airfoil”. In: *Journal of Fluids Engineering* 130.5 (2008).

[27] B. G. Newman and H. T. Low. “Two-dimensional impervious sails: experimental results compared with theory”. In: *Journal of Fluid Mechanics* 144 (1984), pages 445–462.

[28] M. Jahanmiri. *Laminar separation bubble: its structure, dynamics and control*. Technical report. Chalmers University of Technology, 2011.

[29] H. P. Horton. “Laminar separation bubbles in two and three dimensional incompressible flow.” PhD thesis. Queen Mary University of London, 1968.

[30] P. Wen and W. Qiu. “Investigation of drag crisis phenomenon using CFD methods”. In: *Applied Ocean Research* 67 (2017), pages 306–321.

[31] H. Hu, M. Tamai, and J. T. Murphy. “Flexible-membrane airfoils at low Reynolds numbers”. In: *Journal of Aircraft* 45.5 (2008), pages 1767–1778.

[32] R. G. den Boer. “Low speed aerodynamic characteristics of a two-dimensional sail wing with adjustable slack of the sail”. In: *Technische Hogeschool Delft, Luchtvaart-en Ruimtevaarttechniek, Report LR-307* (1980).

[33] M. R. Waszak, L. N. Jenkins, and P. Ifju. “Stability and control properties of an aeroelastic fixed wing micro aerial vehicle”. In: AIAA Atmospheric Flight Mechanics Conference. 2001.

[34] R. C. Leuthold. “Multiple-Wake Vortex Lattice Method for Membrane Wing Kites”. Master’s thesis. Delft University of Technology, 2015.

[35] M. E. Deaves. “An Investigation of the Non-Linear 3D Flow Effects Relevant for Leading Edge Inflatable Kites”. Master’s thesis. Delft University of Technology, 2015.

[36] T. Coudou. “Numerical modeling of inflatable airborne wind energy systems”. Master’s thesis. Université de Mons, 2017.

[37] U. Fechner et al. “Dynamic model of a pumping kite power system”. In: *Renewable Energy* 83 (2015), pages 705–716.

[38] R. van der Vlugt et al. “Quasi-steady model of a pumping kite power system”. In: *Renewable energy* 131 (2019), pages 83–99.

[39] A. Roullier. “Experimental analysis of a kite system’s dynamics”. Master’s thesis. Delft University of Technology, 2020.

[40] J. Breukels. “An engineering methodology for kite design”. PhD thesis. Delft University of Technology, 2011.

[41] A. M. Kuethe, C. Y. Chow, and Y. C. Fung. *Foundations of Aerodynamics, Bases of Aerodynamics Design*. Wiley, 1987.

[42] J. Katz and A. Plotkin. *Low-speed aerodynamics*. Volume 13. Cambridge university press, 2001.

[43] J. J. Chattot and M. M. Hafez. *Theoretical and applied aerodynamics*. Springer, 2015.

[44] J. D. Anderson Jr. *Fundamentals of aerodynamics*. Tata McGraw-Hill Education, 2010.

[45] D. D. Joseph. “Potential flow of viscous fluids: Historical notes”. In: *International Journal of Multiphase Flow* 32.3 (2006), pages 285–310.

[46] F. A. Dvorak and F. A. Woodward. *A viscous potential flow interaction analysis method for multi-element infinite swept wings, volume 2*. NASA, 1974.

[47] R. Vaithiyanathasamy. “Double wake model for separated flows over airfoils”. Master’s thesis. University of Twente, 2017.

[48] M. Gaunaa et al. “A computationally efficient method for determining the aerodynamic performance of kites for wind energy applications”. In: *EWEA Annual Event 2011*. European Wind Energy Association (EWEA). 2011.

[49] B. J. C. Horsten and L. L. M. Veldhuis. “A New Hybrid Method to Correct for Wind Tunnel Wall-and Support Interference On-line”. In: *World Academy of Science, Engineering and Technology* 58 (2009).

[50] M. B. Ruppert. “Development and validation of a real time pumping kite model”. Master’s thesis. Delft University of Technology, 2012.

[51] B. van Leer and K. G. Powell. “Introduction to computational fluid dynamics”. In: *Encyclopedia of Aerospace Engineering* (2010).

[52] H. K. Versteeg and W. Malalasekera. *An introduction to computational fluid dynamics: the finite volume method*. Pearson education, 2007.

[53] J. H. Ferziger, M. Perić, and Robert L. Street. *Computational methods for fluid dynamics*. Volume 3. Springer, 2002.

[54] S. B. Pope. *Turbulent flows*. IOP Publishing, 2001.

[55] G. N. Coleman and R. D. Sandberg. *A primer on direct numerical simulation of turbulence-methods, procedures and guidelines*. University of Southampton, 2010.

[56] J. Fröhlich and W. Rodi. “Introduction to Large Eddy Simulation of Turbulent Flows”. In: *Closure Strategies for Turbulent and Transitional Flows*. Cambridge University Press, 2002, pages 267–298.

[57] G. Alfonsi. “Reynolds-averaged Navier–Stokes equations for turbulence modeling”. In: *Applied Mechanics Reviews* 62.4 (2009).

[58] D. Cappelli and N. N. Mansour. “Performance of Reynolds averaged Navier-Stokes models in predicting separated flows: study of the hump flow model problem”. In: *31st AIAA Applied Aerodynamics Conference*. 2013, page 3154.

[59] J. Yao et al. “Unsteady RANS calculation of flow over Ahmed car model”. In: *IUTAM Symposium on Unsteady Separated Flows and their Control*. Springer. 2009, pages 471–476.

[60] L. Schiavetta, K. Badcock, and R. Cummings. “Comparison of DES and URANS for unsteady vortical flows over delta wings”. In: *45th AIAA Aerospace Sciences Meeting and Exhibit*. 2007.

[61] F. Menter. “Zonal Two Equation k-w Turbulence Models For Aerodynamic Flows”. In: *23rd Fluid Dynamics, Plasmadynamics, and Lasers Conference*. 1993.

[62] R. B. Langtry and F. R. Menter. “Correlation-based transition modeling for unstructured parallelized computational fluid dynamics codes”. In: *AIAA journal* 47.12 (2009), pages 2894–2906.

[63] A. Bruining. “Aerodynamic characteristics of a curved plate airfoil section at Reynolds numbers 60000 and 100000 and angles of attack from-10 to+ 90 degrees”. In: *Delft University of Techology, Department of Aerospace Engineering, Report LR-281* (1979).

[64] G. J. Walker. “The Role of Laminar-Turbulent Transition in Gas Turbine Engines: A Discussion”. In: *Journal of Turbomachinery* 115.2 (1993), pages 207–216.

[65] A. K. Kundu. *Aircraft design*. Volume 27. Cambridge University Press, 2010.

[66] S. Jain, N. Sitaram, and S. Krishnaswamy. “Effect of Reynolds number on aerodynamics of airfoil with Gurney flap”. In: *International Journal of Rotating Machinery* (2015).

[67] M. Kaushik. *Theoretical and Experimental Aerodynamics*. Springer, 2019.

[68] Pointwise. *T-Rex Hybrid Meshing in Pointwise*. Accessed: 08-06-2020. 2011. URL: `https://www.pointwise.com/theconnector/2011-July/T-Rex-Hybrid-Meshing-Pointwise.html`.

[69] C. D. Cone. *The theory of induced lift and minimum induced drag of nonplanar lifting systems*. National Aeronautics and Space Administration, 1962.

[70] N. G. Verhaagen and S. H. J. Naarding. “Experimental and numerical investigation of vortex flow over a sideslipping Delta wing”. In: *Journal of Aircraft* 26.11 (1989), pages 971–978.

[71] M. Shields and K. Mohseni. “Effects of sideslip on the aerodynamics of low-aspect-ratio low-Reynolds-number wings”. In: *AIAA journal* 50.1 (2012), pages 85–99.

[72] D. C. Forbes et al. “Computational study of wake structure and base pressure on a generic SUV model”. In: *The International Vehicle Aerodynamics Conference*. Woodhead Publishing. 2014.

[73] J. B. Barlow, W. H. Rae, and A. Pope. *Low-speed wind tunnel testing*. John Wiley & Sons, 1999.

[74] A. de Wachter. “Deformation and Aerodynamic Performance of a Ram-Air Wing”. PhD thesis. Delft University of Technology, 2008.

[75] D. Costa. “Experimental Investigation of Aerodynamic and Structural Properties of a Kite”. Master’s thesis. ETH Zurich, 2011.

[76] J. Hummel, Dietmar Göhlich, and R. Schmehl. “Automatic measurement and characterization of the dynamic properties of tethered membrane wings”. In: *Wind Energy Science* 4.1 (2019), pages 41–55.

[77] J. Stevenson, K. Alexander, and P. Lynn. “Kite performance testing by flying in a circle”. In: *The Aeronautical Journal* 109.1096 (2005), pages 269–276.

[78] ANSYS Inc. *Lecture 6: Turbulence Modeling, Introduction to ANSYS FLUENT*. Accessed: 12-10-2020. URL: https://imechanica.org/files/fluent_13.0_lecture06-turbulence.pdf.

[79] P. Catalano and M. Amato. “An evaluation of RANS turbulence modelling for aerodynamic applications”. In: *Aerospace science and Technology* 7.7 (2003), pages 493–509.

[80] W. P. Jones and B. E. Launder. “The prediction of laminarization with a two-equation model of turbulence”. In: *International journal of heat and mass transfer* 15.2 (1972), pages 301–314.

[81] B. E. Launder and D. B. Spalding. “The numerical computation of turbulent flows”. In: *Numerical prediction of flow, heat transfer, turbulence and combustion*. Elsevier, 1983, pages 96–116.

[82] D. C. Wilcox et al. *Turbulence modeling for CFD*. Volume 2. DCW industries La Canada, CA, 1998.

[83] F. R. Menter, M. Kuntz, and R. Langtry. “Ten years of industrial experience with the SST turbulence model”. In: *Turbulence, heat and mass transfer* 4.1 (2003), pages 625–632.

[84] A. Ramezani, G. Stipcich, and I. Garcia. “Introduction to Computational Fluid Dynamics by the Finite Volume Method”. In: *Lecture, BCAM–Basque Center for Applied Mathematics* (2016).

[85] O. Kolditz. “Finite volume method”. In: *Computational Methods in Environmental Fluid Mechanics*. Springer, 2002, pages 173–190.

[86] Wolf Dynamics. *Finite Volume Method: a crash introduction*. Accessed: 12-10-2020. URL: http://www.wolfdynamics.com/wiki/fvm_crash_intro.pdf.

[87] L. S. Caretto et al. “Two calculation procedures for steady, three-dimensional flows with recirculation”. In: *Proceedings of the third international conference on numerical methods in fluid mechanics*. Springer. 1973, pages 60–68.

[88] S. V. Patankar and D. B. Spalding. “A calculation procedure for heat, mass and momentum transfer in three-dimensional parabolic flows”. In: *International Journal of Heat and Mass Transfer* 15.10 (1972), pages 1787–1806.

[89] J. P. Van Doormaal and G. D. Raithby. “Enhancements of the SIMPLE method for predicting incompressible fluid flows”. In: *Numerical heat transfer* 7.2 (1984), pages 147–163.

[90] OpenCFD Ltd. *OpenFOAM: User Guide v2006, SIMPLE algorithm*. Accessed: 12-10-2020. URL: https://www.openfoam.com/documentation/guides/latest/doc/guide-applications-solvers-simple.html.

[91] M. Morgut and E. Nobile. “Comparison of hexa-structured and hybrid-unstructured meshing approaches for numerical prediction of the flow around marine propellers”. In: *The First International Symposium on Marine Propulsors smp*. Volume 9. 2009.

[92] Envenio. *Top 6 Reasons to Choose Structured Grids in CFD*. Accessed: 06-09-2020. URL: https://www.design-engineering.com/cfd-automeshing-1004028397-1004028397/.

[93] Pointwise. *T-Rex Hybrid Meshing in Pointwise*. Accessed: 06-09-2020. URL: https://www.pointwise.com/theconnector/2011-July/T-Rex-Hybrid-Meshing-Pointwise.html.

[94] A. Bakker. *Lecture 7 - Meshing: Applied Computational Fluid Dynamics*. Accessed: 10-09-2020. URL: http://www.bakker.org/dartmouth06/engs150/07-mesh.pdf.

[95] Pointwise. *Area and Volume Ratio*. Accessed: 07-09-2020. URL: https://www.pointwise.com/doc/user-manual/examine/functions/area-volume-ratio.html.

[96] Pointwise. *Equiangle Skewness*. Accessed: 07-09-2020. URL: https://www.pointwise.com/doc/user-manual/examine/functions/equiangle-skewness.html.

[97] J. Rhoads. *OpenFOAM Workshop 2014: Effects of grid quality on solution accuracy*. Accessed: 08-09-2020. URL: https://afinemesh.files.wordpress.com/2014/07/ofw20141.pdf.

[98] D. Schroeder. *Increasing the chance of convergence: Treatement of Non-orthogonality with solvers and relaxation factors*. Accessed: 08-09-2020. URL: https://www.simscale.com/forum/t/increasing-the-chance-of-convergence-treatement-of-non-orthogonality-with-solvers-and-relaxation-factors/88850.

[99] Pointwise. *Centroid Skewness*. Accessed: 10-09-2020. URL: https://www.pointwise.com/doc/user-manual/examine/functions/centroid-skewness.html.

[100] B. Fabritius and G. Tabor. "Improving the quality of finite volume meshes through genetic optimisation". In: *Engineering with Computers* (2015).

[101] C. L. Rumsey and S. X. Ying. "Prediction of high lift: review of present CFD capability". In: *Progress in Aerospace Sciences* 38.2 (2002), pages 145–180.

[102] ESI Group. *ESI-OpenCFD*. Accessed: 23-09-2020. URL: https://www.openfoam.com/about/.

[103] OpenFOAM. *OpenFOAM v8 User Guide: 4.5 Numerical schemes*. Accessed: 21-09-2020. URL: https://cfd.direct/openfoam/user-guide/v8-fvschemes/.

[104] J. Jeong and F. Hussain. "On the identification of a vortex". In: *Journal of fluid mechanics* 285 (1995), pages 69–94.

[105] A. M. O. Smith. "High-Lift Aerodynamics". In: *Journal of Aircraft* 12.6 (1975), pages 501–530.

[106] G. Rossitto et al. "Wake structure and drag of vehicles with rounded rear edges". In: *50th 3AF International Conference on Applied Aerodynamics*. 2015.

[107] S. F. Hoerner. "Fluid-dynamic drag". In: *Hoerner Fluid Dynamics* (1965).

[108] S. Dunker. "Tether and bridle line drag in airborne wind energy applications". In: *Airborne Wind Energy*. Springer, 2018, pages 29–56.

[109] P. Faggiani and R. Schmehl. "Design and economics of a pumping kite wind park". In: *Airborne Wind Energy*. Springer, 2018, pages 391–411.

[110] A. Viré et al. "Reynolds-Averaged Navier-Stokes simulations of the flow past a leading edge inflatable wing for airborne wind energy applications". In: *Journal of Physics: Conference Series*. Volume 1618. 3. IOP Publishing. 2020.